

# Radiative corrections for the two-pion contribution to the hadronic vacuum polarization contribution to the muon $g - 2$

Inaugural dissertation  
of the Faculty of Science,  
University of Bern

presented by  
Joachim MONNARD  
from Attalens (Fribourg)

Supervisor of the doctoral thesis:  
Prof. Dr. Gilberto COLANGELO  
Institute for Theoretical Physics  
Albert Einstein Center for Fundamental Physics  
University of Bern



# Radiative corrections for the two-pion contribution to the hadronic vacuum polarization contribution to the muon $g - 2$

Inaugural dissertation  
of the Faculty of Science,  
University of Bern

presented by  
Joachim MONNARD  
from Attalens (Fribourg)

Supervisor of the doctoral thesis:  
Prof. Dr. Gilberto COLANGELO  
Institute for Theoretical Physics  
Albert Einstein Center for Fundamental Physics  
University of Bern

Accepted by the Faculty of Science.

Bern, June 21, 2021

The Dean

Prof. Dr. Zoltán Balogh



# Contents

<b>Introduction</b>	<b>1</b>
<b>1 The anomalous magnetic moment of the muon <math>(g - 2)_\mu</math></b>	<b>3</b>
1.1 Physical definition of $(g - 2)_\ell$	3
1.2 $(g - 2)_\ell$ in the standard model	5
1.3 $g - 2$ as a test of the standard model	6
1.4 Current status of $(g - 2)_\mu$	7
1.5 Sector contributions	10
1.6 Hadronic contributions	11
1.7 HVP	12
1.8 $\pi\pi$ channel in HVP	15
<b>2 Unitarity and analyticity</b>	<b>17</b>
2.1 S-matrix unitarity	17
2.2 Scattering amplitude and partial-wave expansion	19
2.3 Watson's theorem	22
2.4 Unitarity applied on Feynman graphs	22
2.5 Analyticity and crossing symmetry	23
2.6 Fixed-t dispersion relation	25
2.7 Subtractions	27
2.8 Sum rules	29
2.9 Mandelstam representation	30
2.10 The Omnès-Muskhelishvili problem	30
<b>3 Chiral perturbation theory</b>	<b>33</b>
3.1 Effective field theory	33
3.2 Chiral symmetry	33
3.3 Transformation of the Goldstone boson fields	36
3.4 Chiral Lagrangian	37
3.5 Mass corrections and external sources	38
3.6 Weinberg's power counting	40
3.7 Electromagnetic contribution	41
3.8 Next-to-leading order Lagrangian	42
3.9 Resonance saturation	43
<b>4 Pion-pion scattering</b>	<b>45</b>
4.1 Kinematics	45
4.2 Multipion states	45
4.3 Isospin amplitudes	47

4.4	Partial-wave representation . . . . .	48
4.5	Phenomenological amplitude . . . . .	51
4.6	Radiative corrections of the $\pi\pi$ -scattering amplitude in ChPT . . . . .	52
<b>5</b>	<b>The pion vector form factor . . . . .</b>	<b>55</b>
5.1	Purely hadronic form factor in ChPT . . . . .	55
5.2	Dispersive representation of $F_V^\pi(s)$ . . . . .	56
5.3	Radiative corrections in ChPT . . . . .	57
<b>6</b>	<b>Radiative corrections to the process <math>e^+e^- \rightarrow \pi^+\pi^-</math> . . . . .</b>	<b>59</b>
6.1	Divergences in radiative corrections . . . . .	59
6.2	Cross section . . . . .	60
6.3	Leading-order cross section . . . . .	61
6.4	Types of radiative correction . . . . .	62
6.4.1	Initial-state radiation . . . . .	62
6.4.2	Final-state radiation . . . . .	63
6.4.3	Interference contribution . . . . .	64
<b>7</b>	<b>Final-state radiation . . . . .</b>	<b>66</b>
7.1	Model-dependent estimation . . . . .	66
7.2	Dispersive method . . . . .	69
7.3	General unitarity relation . . . . .	70
<b>8</b>	<b>Building block <math>\gamma^* \rightarrow \pi\pi\gamma</math> . . . . .</b>	<b>72</b>
8.1	Pion-pole contribution . . . . .	72
8.2	Two-pion contribution . . . . .	73
<b>9</b>	<b>Building block <math>\pi\pi \rightarrow \pi\pi\gamma</math> . . . . .</b>	<b>75</b>
9.1	Derivation of the gauge-invariant amplitude . . . . .	75
9.2	Charged channels . . . . .	78
9.3	Ambiguity in the pion-pole contribution . . . . .	80
9.4	Rescattering effects . . . . .	81
9.5	Cross section $\sigma(\gamma\pi \rightarrow 3\pi)$ . . . . .	84
<b>10</b>	<b>Building block <math>T_{\pi\pi}^\alpha</math> . . . . .</b>	<b>87</b>
10.1	Topologies . . . . .	87
10.2	Tree-level photon exchange (topology 10.1a) . . . . .	88
10.3	Direct triangle (topology 10.1b) . . . . .	91
10.3.1	P-wave contribution . . . . .	92
10.3.2	S-wave contribution . . . . .	95
10.3.3	The process $\pi^+\pi^+ \rightarrow \pi^+\pi^+$ . . . . .	99
10.4	Crossed triangles (topologies 10.1c and 10.1d) . . . . .	100
10.5	Many-loop topologies (10.1e - 10.1g) . . . . .	104
10.5.1	P-wave projection . . . . .	107
10.5.2	S-wave projection . . . . .	109
10.5.3	Contribution to the process $\pi^+\pi^+ \rightarrow \pi^+\pi^+$ . . . . .	114
10.5.4	Ambiguity due to homogeneous solution . . . . .	114
10.6	Contribution from many-loop topologies in the crossed channels . . . . .	116
10.7	Summary of the chapter . . . . .	118

<b>11 Radiative corrections to the pion vector form factor <math>F_\pi^{V,\alpha}</math></b>	<b>120</b>
11.1 Topologies . . . . .	120
11.2 Triangle correction (diagram 11.1a) . . . . .	121
11.3 Many-loop topologies . . . . .	122
11.4 Numerical solution of the implicit integral equation . . . . .	126
11.5 Contribution from many-loop topologies in the crossed channels . . . . .	127
11.6 Summary of the chapter . . . . .	129
<b>12 Impact on <math>(g - 2)_\mu</math></b>	<b>130</b>
12.1 Corrections to the cross section . . . . .	130
12.2 Ambiguity in the extraction of FSR . . . . .	131
12.3 Numerical contribution to $(g - 2)_\mu$ . . . . .	133
<b>13 Outlook</b>	<b>135</b>
<b>Appendix A Kinematics</b>	<b>137</b>
A.1 $2 \rightarrow 2$ process . . . . .	137
A.2 $2 \rightarrow 2 \rightarrow 2$ process . . . . .	138
A.3 $2 \rightarrow 3 \rightarrow 2$ process . . . . .	139
<b>Appendix B Phase-space differentials</b>	<b>141</b>
<b>Appendix C Regularization of the infrared phase-space integrals</b>	<b>143</b>
<b>Appendix D Omnès functions</b>	<b>145</b>
<b>Appendix E Angular integration</b>	<b>148</b>
<b>Appendix F Numerical solution of the implicit integral equation</b>	<b>152</b>
<b>Appendix G Dictionary of the different topologies</b>	<b>154</b>
<b>Bibliography</b>	<b>156</b>





# Introduction

Throughout the second half of the twentieth century, physicists achieved one of the most impressive successes in science. They elaborated a predictive theory describing three of the four fundamental interactions. The so-called standard model of particle physics brings together electromagnetism and the strong and weak interactions in one single theory. Even though the fourth fundamental interaction, gravity, is not included, the standard model has been experimentally confirmed by the physics community as the theory of particle physics which best describes a multitude of experiments which have thoroughly tested it.

In the last decade, many discrepancies between standard-model predictions and experimental measurements were spotted. Two of them that are particularly important concern flavour lepton universality and, directly related to this thesis, the anomalous magnetic moment of the muon,  $(g - 2)_\mu$ . If the significance of those anomalies is confirmed, this would be a direct hint towards new physics. It is therefore very important that the precision of the prediction of those quantities is as high as possible.

At the current level of precision, radiative corrections to the process  $e^+e^- \rightarrow \pi^+\pi^-$  play an important role in the theoretical determination of  $(g - 2)_\mu$ . In particular, the contribution from final-state radiation (FSR) can not be calculated in a model-independent way and may represent a dangerous and difficult to estimate systematic uncertainty. At low energy, Chiral perturbation theory (ChPT) including electromagnetism is a good framework to deal with such effects [1, 2]. Such corrections have been calculated in ChPT at next-to-leading order [3] and at the two-loop level in the low-energy expansion in the presence of isospin breaking effects [4]. Note that while the former includes corrections due to virtual-photon exchanges, the latter only includes corrections due to pion-mass difference. Moreover, the correction amplitude evaluated at a center-of-mass energy below 1GeV is particularly important [5]. At such high energy, the chiral expansion breaks down and ChPT does not provide an accurate description anymore. In order to estimate the size of the corrections, one must therefore use alternative methods.

So far, those radiative corrections at the typical hadronic scale have been calculated in a model-dependent way based on scalar QED [6]. Even though such a method allows one to calculate the corrections in a perturbative framework, without introducing any free parameter, its model dependence also induces a systematic uncertainty that is hard to estimate. In this thesis we aim at calculating the final-state radiative corrections to the process  $e^+e^- \rightarrow \pi^+\pi^-$  in a model-independent way. To that end, we rely on unitarity and analyticity and use dispersion relations to express those corrections in terms of integrals of well-defined purely hadronic states. We emphasize that this is the first time that such a framework is used for the calculation of those radiative corrections. In this thesis, we will prove that the calculation is doable (even though with some well-controlled approxi-

mations) and explain the method in detail.

We will see that within our dispersive method, the radiative corrections to the  $\pi\pi$ -scattering amplitude are also needed as input in the calculation. Those have been calculated at the one-loop level in ChPT in [7, 8]. In order to extend the validity of those calculations to higher energy, we apply the same dispersive framework to the partial waves of the  $\pi\pi$ -scattering amplitude. This is also the first time that such a model-independent method is applied to evaluate radiative corrections.

The thesis is organized as follows: chapter 1 introduces the anomalous magnetic moment of the muon, its current theoretical and experimental status and underlines the importance of the contribution from FSR in the process  $e^+e^- \rightarrow \pi^+\pi^-$ . In chapter 2, we introduce the concepts of unitarity and analyticity which, coupled with complex analysis, provide the central tools used in the calculations of the thesis. Chapter 3 is a brief introduction to chiral perturbation theory that is used later on for the fixing of subtraction constants at low energy. Chapters 4 and 5 introduce the purely-hadronic quantities that are the central building blocks of this project. Those are respectively the  $\pi\pi$ -scattering amplitude and the pion vector form factor. In chapter 6, we introduce in more detail the radiative corrections to  $e^+e^- \rightarrow \pi^+\pi^-$ , their different types and how they contribute to the cross section. We then focus on the FSR in chapter 7. We explain the model-dependent method used so far for the determination of those radiative corrections. We then describe our dispersive method, specifying the related approximations and the quantities needed as input. In particular, it is shown that some building blocks are required in the evaluation of the discontinuity in the unitarity relation of the pion vector form factor. Those are then discussed in the next chapters. Chapter 8 refers to the process  $\gamma^* \rightarrow \pi\pi\gamma$  that has been extensively treated in the literature. In chapter 9, we calculate the amplitude for the process  $\pi\pi \rightarrow \pi\pi\gamma$ . It is shown that the pion-pole approximation is dominant in the energy range of interest. In chapter 10, we discuss the radiative corrections to the  $\pi\pi$ -scattering amplitude. To that end, a finite number of topologies is identified and various methods are used for their evaluation. In particular, we encounter a new type of implicit integral equation which is solved numerically. In chapter 11, we discuss the radiative corrections to the pion vector form factor. We also identify a finite set of topologies contributing as radiative corrections and the same kind of implicit integral equation is encountered. Finally, we use our results to calculate the contribution to  $(g-2)_\mu$  in chapter 12. The technical details of the calculation can be found in the different appendices.

# Chapter 1

## The anomalous magnetic moment of the muon $(g - 2)_\mu$

In this chapter, we introduce the anomalous magnetic moment of the muon and explain how it is calculated in the standard model. We review the current status of the anomaly between its theoretical prediction and its measurement. At the end of the chapter, we address the contributions dominating the theoretical uncertainty and explain the importance of radiative corrections.

### 1.1 Physical definition of $(g - 2)_\ell$

Classically, the magnetic dipole moment of a charged particle is defined by the torque it undergoes in an external magnetic field. As an illustration, let us consider an orbiting particle with mass  $m$  and charge  $q$  as displayed in figure 1.1. Given its position  $\mathbf{r}$  and velocity  $\mathbf{v}$ , the circular motion generates an angular momentum

$$\mathbf{L} = m\mathbf{r} \times \mathbf{v}. \quad (1.1)$$

Since the particle is charged, its motion also induces a magnetic dipole moment. The latter can be expressed in terms of the angular momentum:

$$\boldsymbol{\mu}_L = \frac{q}{2mc} \mathbf{L} = \frac{q}{2c} \mathbf{r} \times \mathbf{v}. \quad (1.2)$$

The fact that the system carries a magnetic dipole moment means that it does interact with external magnetic fields. This interaction appears at the level of the Hamiltonian in the form

$$H_\mu = -\boldsymbol{\mu}_L \cdot \mathbf{B}. \quad (1.3)$$

This magnetic dipole moment can thus be measured. Note that for simplicity, we assumed no external electric field. Otherwise, an electric dipole moment coupled to the external electric field must also be included in the Hamiltonian.

In quantum mechanics, additionally to their masses and electromagnetic charges  $e$ , particles have a well-defined spin. Spin can be thought of as an intrinsic angular momentum. The usual representation for its quantum mechanical operator is given by

$$\mathbf{S} = \frac{\hbar}{2} \boldsymbol{\sigma}, \quad (1.4)$$

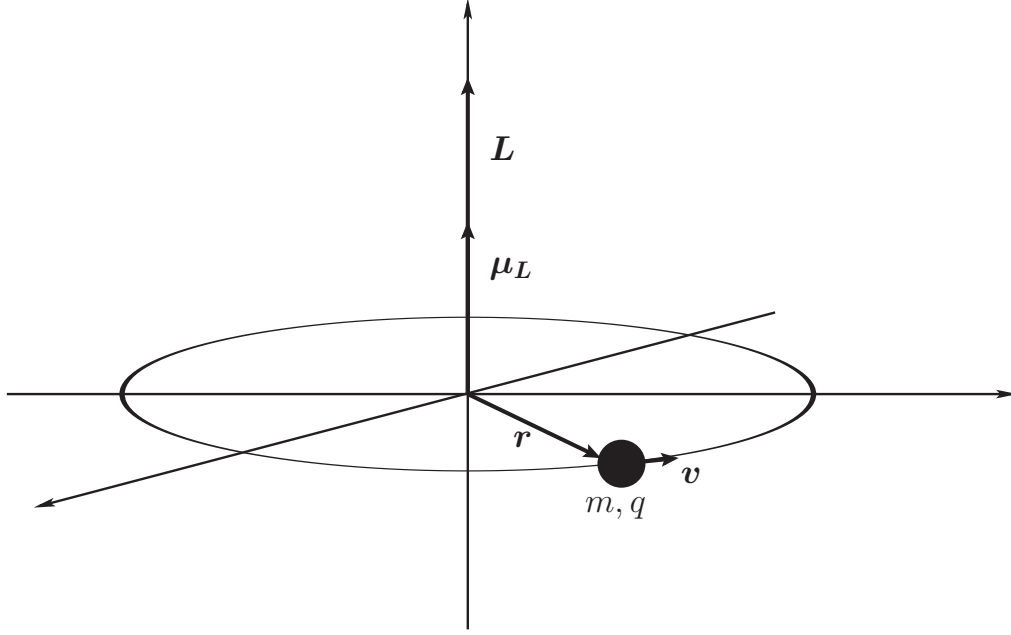


Figure 1.1: classical example of a charged orbiting particle

where the three components of  $\boldsymbol{\sigma} = (\sigma_x, \sigma_y, \sigma_z)$  are the Pauli matrices. Relation (1.2) can be generalized to the spin, giving rise to a magnetic dipole moment

$$\boldsymbol{\mu}_S = \frac{e}{2mc} \mathbf{S} = g \frac{Q\mu_0}{2} \boldsymbol{\sigma}, \quad (1.5)$$

where  $Q = \pm 1$  for leptons and antileptons respectively. Also, the definition of the Bohr magneton,  $\mu_0 = e\hbar/2mc$  has been used. Note that the magnetic dipole moment induced by the spin and angular momentum of a lepton is responsible for the splitting of its energy levels in the presence of an external magnetic field. This is the well-known Zeeman effect.

The main difference between  $\boldsymbol{\mu}_S$  and  $\boldsymbol{\mu}_L$  is the presence of the gyromagnetic ratio  $g$  or  $g$ -factor. At first, phenomenological estimations established  $g = 2$ . This was confirmed by Dirac, who was the first to theoretically predict a numerical value to  $g$ . It turns out that the non-relativistic limit of the Dirac equation for an electron in the presence of an electromagnetic field naturally leads to a Hamiltonian containing a term similar to (1.5). To be exact, this term is

$$H_D = -Q\mu_0 \boldsymbol{\sigma} \cdot \mathbf{B}. \quad (1.6)$$

In order for the two equations to agree, we must set  $g = 2$ . In other words, the  $g$ -factor for the spin takes twice the value associated with the angular momentum. However, this result does not take into account the full standard-model contribution. In the case of the nucleons, for instance, the magnetic dipole moment differs drastically from the Dirac prediction. It is only with the development of the quark model that this deviation was understood. In the real world, leptons also interact with different quantum fields. Quantum fluctuations are therefore responsible for additional corrections to the magnetic dipole moment of the leptons. All of those deviations from  $g = 2$  go under the name of

anomalous magnetic moment of the corresponding lepton. Conventionally, the quantity of interest is defined as

$$a_\ell := \frac{g_\ell - 2}{2}, \quad \ell \in \{e, \mu, \tau\}. \quad (1.7)$$

Note that  $a_\ell$  has no dimension and is a pure number.

## 1.2 $(g - 2)_\ell$ in the standard model

In order to calculate the different contributions to the anomalous magnetic moment of a lepton in the standard model, one has to consider the matrix element of the electromagnetic current for the scattering of an incoming lepton  $\ell(p_1)$  to an outgoing lepton  $\ell(p_2)$ . Using translational invariance, the latter can be expressed in momentum space as

$$\begin{aligned} \tilde{M}^\mu(q; p) &:= \int d^4x e^{iqx} M^\mu(x; p), \\ &= \int d^4x e^{-iqx} \langle \ell(p_2) | j^\mu(x) | \ell(p_1) \rangle, \\ &= \int d^4x e^{i(p_2 - p_1 - q)x} \langle \ell(p_2) | j^\mu(0) | \ell(p_1) \rangle, \\ &= (2\pi)^4 \delta^{(4)}(p_2 - p_1 - q) \langle \ell(p_2) | j^\mu(0) | \ell(p_1) \rangle. \end{aligned} \quad (1.8)$$

In QED, the T-matrix element has a convenient covariant decomposition involving only two different Dirac structures. This is due to the fact that QED conserves parity and is gauge invariant. We have

$$\langle \ell(p_2) | j^\mu(0) | \ell(p_1) \rangle = (-ie) \bar{u}(p_2) \left[ \gamma^\mu F_1(q^2) + i \frac{\sigma^{\mu\nu} q_\nu}{2m_\ell} F_2(q^2) \right] u(p_1), \quad (1.9)$$

where  $u(p_i)$  and  $\bar{u}(p_i)$  describe the lepton spinors and  $\gamma^\mu$  the Dirac matrix. We also defined the commutator of two Dirac matrices as  $\sigma^{\mu\nu} = i[\gamma^\mu, \gamma^\nu]$ .  $F_1(q^2)$  and  $F_2(q^2)$  are respectively the Dirac and the Pauli form factors. In the static limit ( $q^2 = 0$ ), the first one fulfils the charge renormalization condition

$$\lim_{q^2 \rightarrow 0} F_1(q^2) = 1, \quad (1.10)$$

whereas in the same limit, the second one is the anomalous magnetic moment of the muon itself

$$\lim_{q^2 \rightarrow 0} F_2(q^2) = a_\ell. \quad (1.11)$$

Note that parity is in general not conserved in the standard model. This means that further Lorentz structures involving the  $\gamma_5$  matrix are also allowed. In general, one can reduce the T-matrix element above to a sum of four different terms:

$$\begin{aligned} \langle \ell(p_2) | j^\mu(0) | \ell(p_1) \rangle &= (-ie) \bar{u}(p_2) \Pi^\mu(q) u(p_1), \\ \Pi^\mu(q) &= \left[ \gamma^\mu F_1(q^2) + i \frac{\sigma^{\mu\nu} q_\nu}{2m_\ell} F_2(q^2) + \left( \gamma^\mu + \frac{2m_\ell q^\mu}{q^2} \right) \gamma_5 F_3(q^2) \right. \\ &\quad \left. + \frac{\sigma^{\mu\nu} q_\nu}{2m_\ell} \gamma_5 F_4(q^2) \right]. \end{aligned}$$

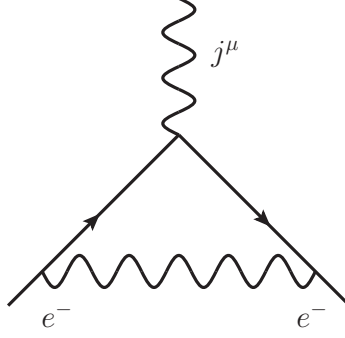


Figure 1.2: First order electromagnetic correction in  $\alpha$  to the matrix element in (1.8)

The two additional form factors  $F_3(q^2)$  and  $F_4(q^2)$  are respectively the anapole moment and the electric dipole moment. They both vanish in the limit  $q^2 \rightarrow 0$ . Those are beyond the scope of this thesis and we shall focus on  $F_2(q^2)$  only.

Historically, the first and dominant correction to the anomalous magnetic moment of the electron has been calculated by Schwinger in 1948 [9]. This contribution involves the calculation of the Feynman diagram depicted in figure 1.2. The corresponding famous result

$$a_e = \frac{\alpha}{2\pi} \quad (1.12)$$

is universal, in the sense that it is identical for the three lepton generations. This is by far the largest contribution to the anomalous magnetic moment of the leptons, since it is the leading-order correction to the perturbative expansion in  $\alpha$ . Today, the pure QED contributions to  $a_e$  and  $a_\mu$  are known up to  $\mathcal{O}(\alpha^5)$  [10, 11]. This amounts to the calculation of over 15'000 Feynman diagrams. This gives a flavour of the immense effort invested into the theoretical determination of the anomalous magnetic moment of both the electron and the muon.

### 1.3 $g - 2$ as a test of the standard model

Among the three charged leptons of the standard model, the muon is potentially the best candidate to provide hints towards new physics. This is due to the mass hierarchy and the very different order of magnitude of their lifetimes.

Assuming that unknown degrees of freedom exist, their interactions with the particles present in the standard model could potentially have an effect on the anomalous magnetic moments of the leptons. It has been noticed [12] that if those degrees of freedom are very heavy compared to the lepton ( $\Lambda \gg m_\ell$ ) their contribution  $\delta a_\ell$  would scale as

$$\frac{\delta a_\ell}{a_\ell} \sim \frac{m_\ell^2}{\Lambda^2}. \quad (1.13)$$

Since the typical energy scale of potential new physics is around the electroweak scale ( $\Lambda \approx 100\text{GeV}$ ), this kind of contribution is heavily suppressed and thus hard to detect. Note however the quadratic dependence in the lepton mass. The contribution from such

degrees of freedom is therefore more important for heavier leptons.

The electron is essentially stable, which makes it easy to scrutinize experimentally. However, its light weight ( $m_e = 0.511 \text{ MeV}$ ) makes the mass ratio above extremely small. The precision required to detect this kind of contribution is therefore out of reach. For a long time, the electron  $g - 2$  has been the most precisely measured observable. The good agreement between its theoretical prediction and experimental result has been a strong check of the validity of QED. Note however that recently, a new method for the measurement of the fine-structure constant  $\alpha$  based on atomic interferometry indicates an anomaly of about  $2\sigma$  [13].

The  $\tau$ , on the other hand is by far the heaviest of the three lepton generations ( $m_\tau = 1776.86 \text{ MeV}$ ), which makes the ratio (1.13) more favourable. Unfortunately, it also has the shortest lifetime ( $\tau_\tau = 2.906 \times 10^{-13} \text{ s}$ ). It is therefore not possible with our current level of technology to measure its anomalous magnetic moment in a precise way.

This is why the muon is the best candidate for testing the standard model via its anomalous magnetic moment. By a coincidence in nature, it happens to be just in the middle of the hierarchy, being about 200 times heavier than the electron ( $m_\mu = 105.658 \text{ MeV}$ ) and living long enough to be studied in today's experimental facilities ( $\tau_\mu = 2.197 \times 10^{-6} \text{ s}$ ). Those nice properties of the muon explain why its anomalous magnetic moment has received so much attention in the past years.

## 1.4 Current status of $(g - 2)_\mu$

The anomalous magnetic moment of the muon has been predicted and measured at an impressive level of precision. For a long time, the most precise measurement came from experiment E821 in Brookhaven National Laboratory [14]. The results from this measurement and from the theory are the following:

$$\begin{aligned} a_\mu^{\text{exp}} &= 116\,592\,089(63) \times 10^{-11}, \\ a_\mu^{\text{SM}} &= 116\,591\,810(43) \times 10^{-11}, \\ a_\mu^{\text{exp}} - a_\mu^{\text{SM}} &= 279(76) \times 10^{-11}. \end{aligned}$$

Despite being very small relatively to their absolute value, the difference between both numbers is still substantial in comparison to the uncertainty. Those two results correspond to a  $3.8\sigma$  discrepancy between the standard-model prediction  $a_\mu^{\text{SM}}$  and the experimental measurement  $a_\mu^{\text{exp}}$ . In these results,  $a_\mu^{\text{SM}}$  receives contributions exclusively from the particles in the standard model by definition. The experimental number, on the other hand, contains all possible contributions provided by nature. This can be any physics that has not yet been uncovered. The fact that the difference between the two numbers does not vanish hints therefore directly towards such unknown contributions.

A new experimental measurement of  $(g-2)_\mu$  going under the name of E989 is in progress at Fermilab [15]. Its planned accuracy of 140 ppb would amount to an improvement by a factor 4 compared to Brookhaven's 500 ppb. It is interesting to notice that, assuming the central value of the result remains untouched, the anomaly would increase to about 7  $\sigma$  as can be seen on figure 1.3 [5]. This new experiment is thus of great importance and

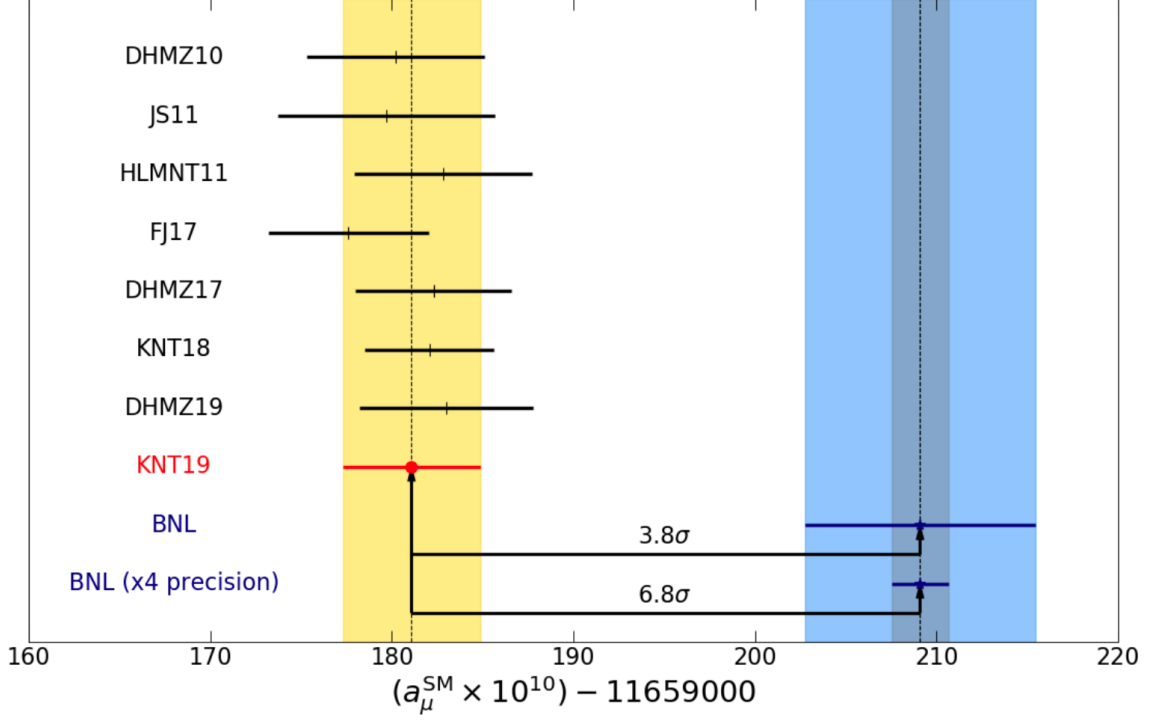


Figure 1.3: Comparison of different evaluations of  $a_\mu^{\text{SM}}$  and the experimental result [5]. The light blue band corresponds to the uncertainty on the experimental measurement from E821. The light grey band corresponds to the hypothetical final result by Fermilab, assuming the central value remains unchanged and the four-fold reduction in uncertainty is achieved

will provide crucial information about the anomaly. Recently, Fermilab disclosed a first result, based on the first run of the experiment. This result agrees well with the result from Brookhaven, as shown in figure 1.4 [16]. The four-fold planned reduction of the uncertainty is not yet achieved, but this should be the case after inclusion of the data from further runs, improving the statistics. Nevertheless, the combination of both measurements leads to a refinement of the experimental result and the current status is a  $4.2\sigma$  anomaly with the theoretical prediction. The new combined result is the following:

$$\begin{aligned} a_\mu^{\text{exp}} &= 116\,592\,061(41) \times 10^{-11}, \\ a_\mu^{\text{exp}} - a_\mu^{\text{SM}} &= 251(59) \times 10^{-11}. \end{aligned} \quad (1.14)$$

It is also worthwhile mentioning that a third experiment, E34, is planned at J-PARC [17]. While the BNL and Fermilab experiments both work with ultra-relativistic muons, E34 is based on an ultra-cold muon beam. An agreement between the two a priori completely different methods would be a strong cross-check of the validity of the results.

On the other hand, it is also crucially important that the theoretical prediction reaches a level of precision similar to the experiment. To that end, the *Muon g-2 theory initiative* has been founded in 2017 and a remarkable amount of work has been dedicated to the reduction of the theoretical uncertainty.



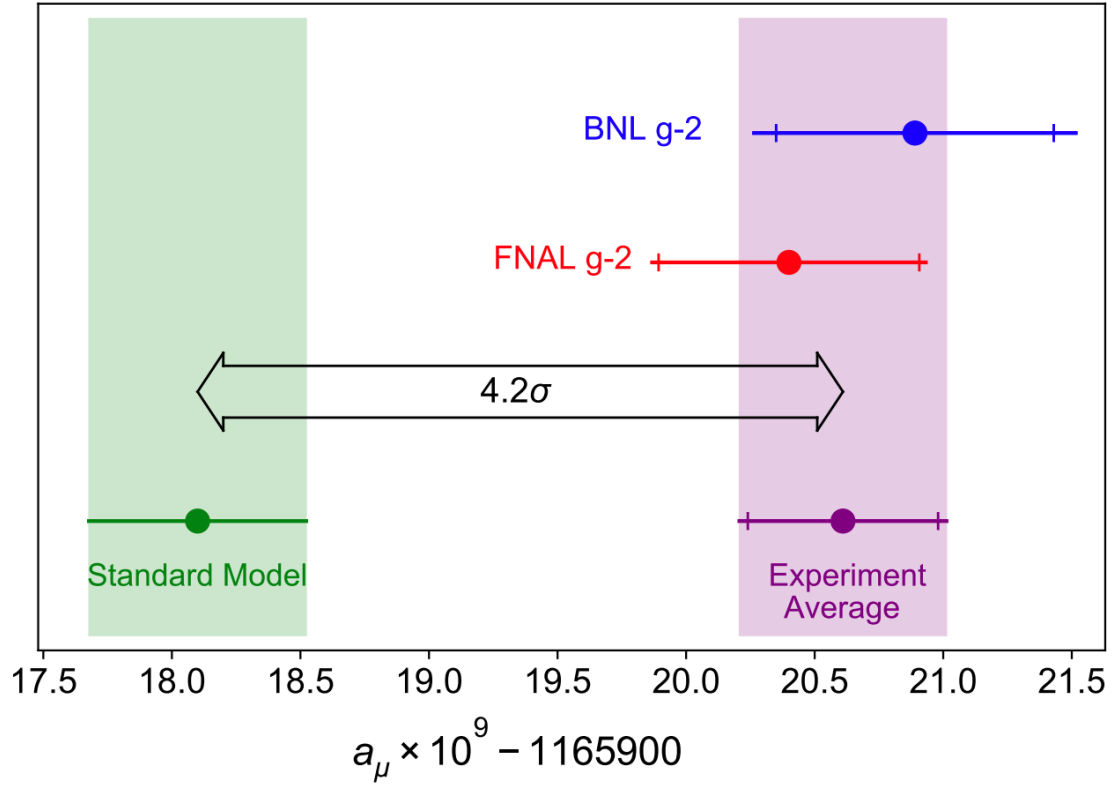


Figure 1.4: Result of the first run of E989 at Fermilab [16]. Both experimental results from Brookhaven (blue) and Fermilab (red) are combined into an average (purple) with reduced uncertainty.

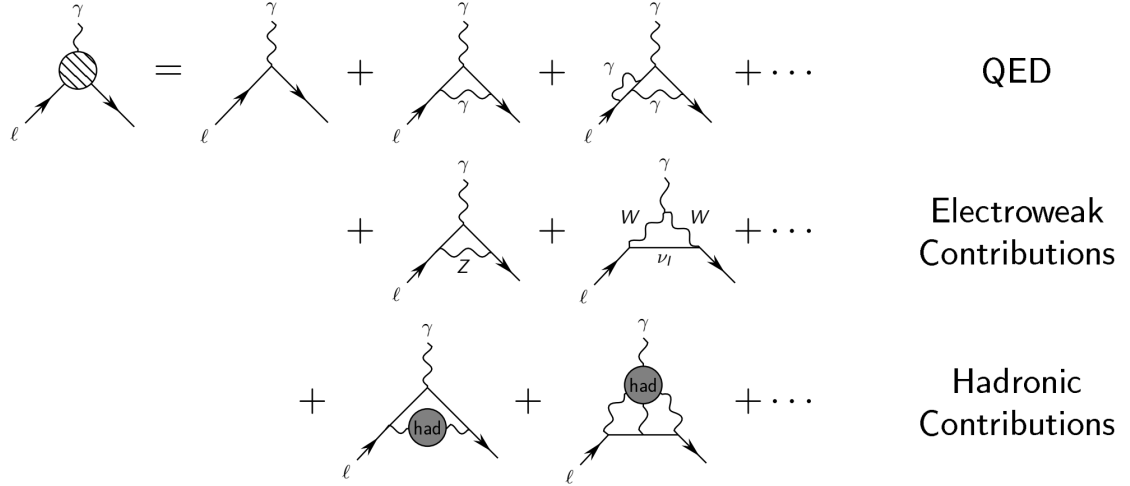


Figure 1.5: Schematic representation of the different sectors of the standard model contributing to  $a_\mu$

## 1.5 Sector contributions

All sectors of the standard model contribute to the anomalous magnetic moment of the leptons. As stated above, the latter gets corrections from all quantum fluctuations. Those can be exchanges of virtual photons or leptons (pure QED), weak W and Z bosons or even hadronic particles. Figure 1.5 <sup>1</sup> displays examples of the lowest-order topologies of each sector.

In the case of the electron, because of the ratio (1.13) the contribution from the hadronic and EW sectors are negligible compared to the contribution from QED. For the muon, however, those contributions are more important and must be carefully taken into consideration.

The numerical values for the different sectors contributing to the anomalous magnetic moment of the muon are listed in table 1.1 [18]. Numerically, the total contribution to  $a_\mu$  is highly dominated by the pure QED contributions. The corrections from the electroweak (EW) and hadronic (HVP + HLbL) sectors are several orders of magnitude smaller than QED. However, the crucial point is that the uncertainty is dominated by the strong sector. The large uncertainties on the hadronic contributions reflect the fact that quarks hadronize at low energy and QCD is not perturbative any more. It is therefore not possible to use the usual perturbative techniques, as in QED. In order to reduce the uncertainty, it is important to understand better the effect of hadronic interactions on  $a_\mu$ .

---

<sup>1</sup>I thank Laetitia Laub for providing this nice pictorial description

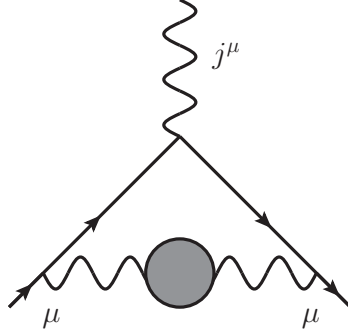


Figure 1.6: HVP contribution to  $a_\mu$ . The grey blob accounts for the hadronic vacuum polarization of the photon.

Contribution	value $\times 10^{11}$
QED	116 584 718.931(104)
EW	153.6(1.0)
HVP	6845(40)
HLbL	92(18)
theory (total)	116 591 810(43)
experiment (E821)	116 592 089(63)
discrepancy	279(76)

Table 1.1: Numerical value of the different contributions to  $a_\mu$ . HVP and HLbL are both contributions from the hadronic sector.

## 1.6 Hadronic contributions

There are two main contributions from the hadronic sector, namely hadronic vacuum polarization (HVP) and hadronic light-by-light (HLbL).

The first one, depicted in figure 1.6 appears at order  $\alpha^2$ . It consists of an insertion of the hadronic vacuum polarization in the photon line of the vertex correction of figure 1.2. Note that in addition to the HVP contribution from figure 1.6, other corrections with additional exchanges of virtual photons between the muon lines must also be taken into account. Such contributions are suppressed at least by a power of  $\alpha$  compared to the leading one. It is also possible to replace one of the internal photon lines by a neutral Z boson. This contribution is very small since suppressed by  $m_\mu^2/m_Z^2 \ll 1$ . The leading HVP correction is the object of interest in this thesis and we will specify in more details its properties in the next section.

The second one, depicted in figure 1.7 appears one order higher in  $\alpha$  than HVP, namely  $\alpha^3$ . Its calculation requires the determination of the hadronic Green's function of four electromagnetic currents in pure QCD:

$$\Pi^{\mu\nu\lambda\sigma}(q_1, q_2, q_3) := -i \int d^4x d^4y d^4z e^{-i(q_1x + q_2y + q_3z)} \langle 0 | T \{ j^\mu(x) j^\nu(y) j^\lambda(z) j^\sigma(0) \} | 0 \rangle. \quad (1.15)$$

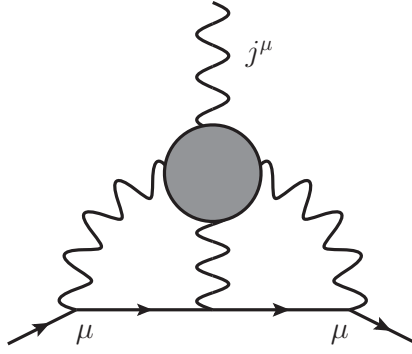


Figure 1.7: HLbL contribution to  $a_\mu$ . The grey blob accounts for hadronic interactions in the process  $\gamma\gamma^* \rightarrow \gamma^*\gamma^*$ .

The complexity of the tensorial structure makes it a very challenging task. This explains why despite the suppression by one power of  $\alpha$  compared to HVP, its uncertainty is of the same order of magnitude. Some data-driven methods based on dispersion relations [19, 20] allowed a good estimation of this quantity.

## 1.7 HVP

In what follows, we explain in more details how the HVP contribution is calculated [21]. Using Lorentz invariance, one can write the one-particle irreducible self-energy function of the photon as

$$\Pi_{\mu\nu} = ie^2 \int d^4x e^{iq \cdot x} \langle 0 | T \{ j_{\text{em}}^\mu(x), j_{\text{em}}^\nu(0) \} | 0 \rangle = (g^{\mu\nu} q^2 - q^\mu q^\nu) \Pi(q^2). \quad (1.16)$$

The Lorentz structure in front of this representation ensures that the electromagnetic current is conserved ( $q_\mu \Pi^{\mu\nu} = 0$ ). The scalar self-energy function  $\Pi(q^2)$  depends on the virtuality of the photon. To be able to compute the diagram of figure (1.6), it is convenient to make this dependence appear explicitly. Hence, we rewrite the renormalized self-energy function using a once-subtracted dispersion relation. Dispersion relations have an important place in this thesis and will be introduced in detail in the next chapters. For now, we use the formula

$$\bar{\Pi}(q^2) := \Pi(q^2) - \Pi(0) = \frac{q^2}{\pi} \int_{s_{\text{thr}}}^{\infty} \frac{ds}{s} \frac{\text{Im}\Pi(s)}{s - q^2}. \quad (1.17)$$

In pure QCD, the integral starts at the two-pion threshold. Using the optical theorem (unitarity) and taking only hadronic interactions into account, the imaginary part of the scalar function can be related to the total hadronic cross section:

$$\sigma(e^+e^- \rightarrow \text{hadrons}) = \frac{\alpha}{s} \frac{4\pi}{\sigma_e(s)} \left( 1 + \frac{2m_e^2}{s} \right) \text{Im}\Pi(s), \quad (1.18)$$

where  $\sigma_\ell = \sqrt{1 - 4m_\ell^2/s}$  is the threshold function. At this point, the  $q^2$ -dependence in (1.17) lies exclusively in the Cauchy pole  $\frac{1}{s - q^2}$ . That is, we can calculate the first order HVP contribution by computing the projection of the one-loop vertex diagram on  $g - 2$  in

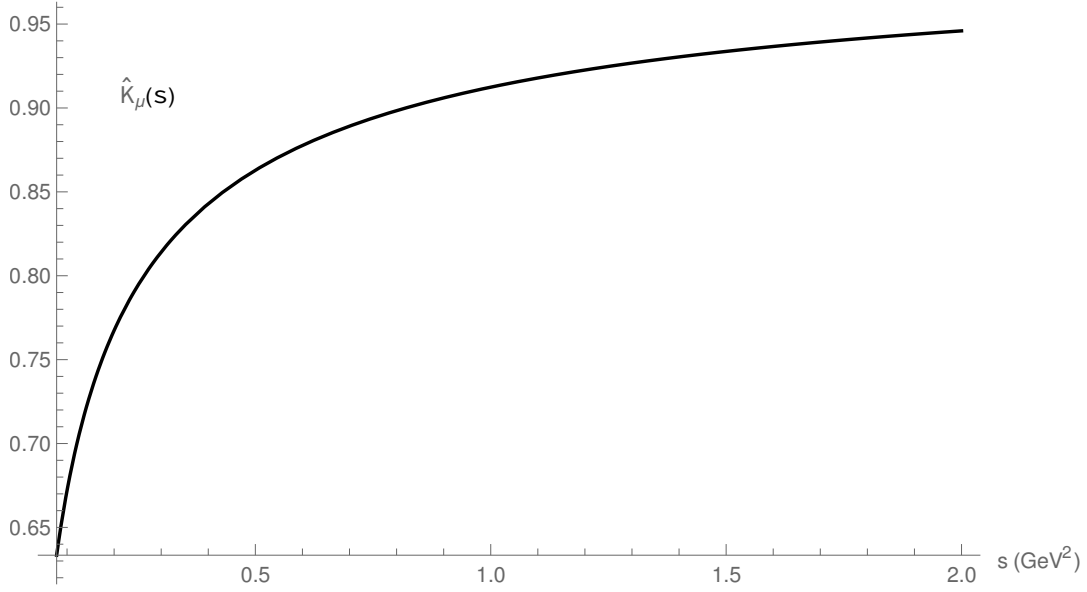


Figure 1.8: behaviour of the function  $\hat{K}_\mu(s)$  in the interval  $s \in [4m_\pi^2, 2 \text{ GeV}^2]$

the case of a photon of mass  $\sqrt{s}$ . To that end, we use the usual Feynman-parametrization technique. Then by convoluting the result with the imaginary part of  $\Pi(s)$ , and using relation (1.18) above, we arrive at the master formula

$$a_\mu^{\text{HVP}} = \left( \frac{\alpha m_\mu}{3\pi} \right)^2 \int_{4m_\pi^2}^{\infty} \frac{ds}{s^2} \hat{K}_\mu(s) R_{\text{had}}(s). \quad (1.19)$$

In this expression, the cross section is the purely hadronic one, meaning that the integral starts at the two-pion creation threshold. The function  $\hat{K}_\mu(s)$  accounts for the one-loop vertex diagram containing a massive photon and projected on  $g - 2$ . It is given by [22]

$$\hat{K}_\mu(s) = \frac{3s}{m_\mu^2} \left( \frac{z^2}{2} (2 - z^2) + \frac{(1 + z^2)(1 + z)^2}{z^2} \left( \log(1 + z) - z + \frac{z^2}{2} \right) + \frac{1 + z}{1 - z} z^2 \log(z) \right) \quad (1.20)$$

where  $z$  can be expressed in terms of the muon-threshold function

$$z = \frac{1 - \sqrt{1 - \frac{4m_\mu^2}{s}}}{1 + \sqrt{1 - \frac{4m_\mu^2}{s}}} \equiv \frac{1 - \sigma_\mu(s)}{1 + \sigma_\mu(s)}. \quad (1.21)$$

As we can see on the plot of figure 1.8, the function  $\hat{K}_\mu$  takes values between 0.6 and 1 when evaluated at  $s \in [4m_\pi^2, 2 \text{ GeV}^2]$ . Note also that the hadronic information is exclusively contained in the function

$$R_{\text{had}}(s) = \frac{3s}{4\pi\alpha^2} \frac{s\sigma_e(s)}{s + 2m_e^2} \sigma(e^+e^- \rightarrow \text{hadrons}). \quad (1.22)$$

The derivation above corresponds to the leading-order contribution from the HVP sector. Considering additional photon exchanges as for instance the diagrams depicted in figure 1.9 allows one to calculate the next orders in  $\alpha$ . The NLO contribution has been

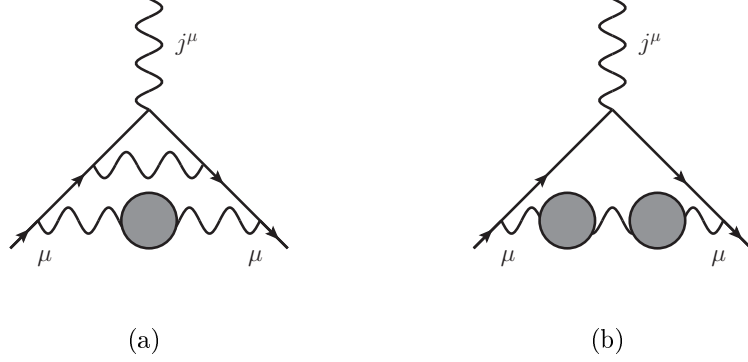


Figure 1.9: example of diagrams contributing to HVP at NLO.

calculated in [5] and the NNLO in [23]. As we can see from the table 1.2 [18], the NNLO contribution is only suppressed by one order of magnitude compared to the NLO contribution and is thus surprisingly large. This large effect is explained by the presence of large logarithms.

Contribution	value $\times 10^{11}$
HVP LO ( $e^+e^-$ )	6931(40)
HVP NLO ( $e^+e^-$ )	-98.3(7)
HVP NNLO ( $e^+e^-$ )	12.4(1)
HVP LO (lattice)	7116(184)
HVP ( $e^+e^-$ LO + NLO + NNLO)	6845(40)

Table 1.2: Numerical value of the different contributions to  $a_\mu$  from the HVP sector.

In the same table, we can see that the result from lattice QCD provides a larger contribution than the one from the data-driven analysis. Note that the uncertainty related to that prediction is also relatively large. However, a very recent publication from the Budapest-Marseille-Wuppertal (BMW) collaboration [24] confirmed the larger contribution from the lattice, reducing the uncertainty by almost a factor 4. Their result is  $a_\mu^{\text{HVP,LO}} = (7087 \pm 53) \times 10^{-11}$  and does not agree with the dispersive approach. This results would reduce the tension between the theoretical prediction and the experimental measurement of  $a_\mu$ . It is thus important to understand what causes such a large discrepancy between the result from the lattice and the dispersive approach. One possible source of error from the latter is the final state radiative correction to the process  $e^+e^- \rightarrow \pi^+\pi^-$  that, as we will see later, is not completely understood theoretically.

Another point worth mentioning is the recent project to calculate the HVP contribution from space-like data [25]. The idea is that after a manipulation of the convolution integral above, it is possible to express  $a_\mu^{\text{HVP}}$  as a function of the fine-structure constant evaluated in the space-like region:

$$a_\mu^{\text{HVP}} = \frac{\alpha}{\pi} \int_0^1 dx (1-x) \Delta\alpha_{\text{had}}[t(x)], \quad (1.23)$$

$$t(x) = \frac{m_\mu^2 x^2}{x-1} < 0 \quad (1.24)$$

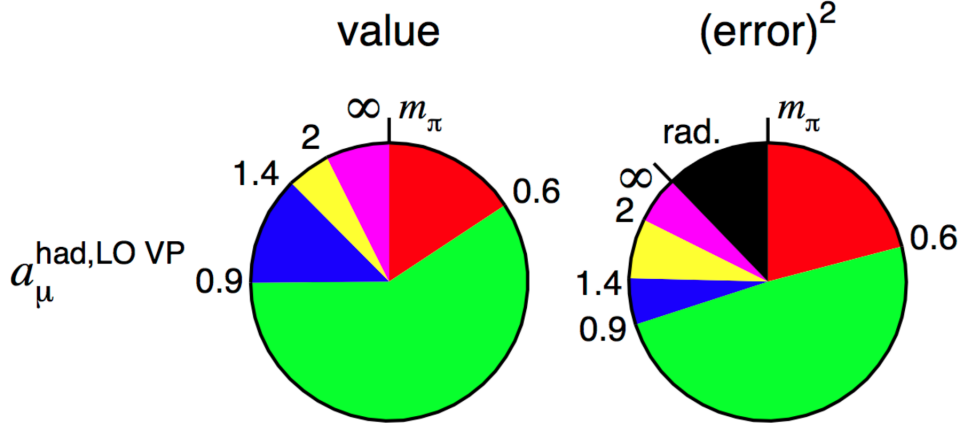


Figure 1.10: Proportions of the contributions to  $a_\mu^{\text{HVP}}$  and its uncertainty from the different regions of the integral (1.19) [26]. The cut-off energy  $\Lambda$  is evaluated in GeV. The black region in the chart on the right corresponds to the uncertainty due to radiative corrections.

In this expression,  $\Delta\alpha_{\text{had}}(t)$  is the hadronic contribution to the running of  $\alpha$ . It is integrated over a spacelike region  $t < 0$ . In order to extract it, one needs to subtract from the experimental result the QED contribution  $\Delta\alpha_{\text{QED}}(t)$  that can be calculated very precisely.

The advantage of this method is that there is no resonant structures in the space-like region. An experimental measurement based on muon-electron scattering (MUonE project) should therefore in principle provide a smooth curve with a smaller uncertainty.

## 1.8 $\pi\pi$ channel in HVP

In the master formula (1.19), the low-energy part of the spectrum is enhanced by  $1/s^2$  in the dispersive integral and is therefore of great importance. Note that, as can be seen on figure 1.8, the function  $\hat{K}_\mu(s)$  is bounded between 0.6 and 1. An interesting exercise is to apply an energy cut-off  $\Lambda^2$  to the dispersive integral and make it vary to analyse the effect on  $a_\mu^{\text{HVP}}$ . This has been done in [26]. The result is displayed in figure 1.10. We see that most of the contribution comes from the integration up to  $1 \text{ GeV}^2$ . Note that the threshold energy of the dispersive integral  $m_\pi^2$  corresponds to the intermediate state  $\pi^0\gamma$ . This is due to the fact that the photon-inclusive cross-section is considered, as explained below. Looking at the contribution to the uncertainty, the situation is roughly the same. Consequently, in order to reduce the uncertainty drastically, the precision on the low-energy spectrum of the cross section  $\sigma(e^+e^- \rightarrow \text{hadrons})$  must be improved.

At low energy, i.e. up to about  $1 \text{ GeV}^2$ , the hadronic cross section is dominated by the  $\pi^+\pi^-$  channel. As can be seen from BABAR data in figure 1.11 [27], the latter is mediated by the  $\rho(770)$ -resonance exchange and surpasses the other channels by 2 to 4 orders of magnitude. The other predominant channel,  $K\bar{K}$ , only starts at around  $1 \text{ GeV}^2$ , where the sharp  $f_0(980)$  is located. Its contribution to  $a_\mu^{\text{HVP}}$  is thus suppressed by the kernel in the integral (1.6) with respect to the  $\pi\pi$  channel. The cross section  $\sigma(e^+e^- \rightarrow \pi^+\pi^-)$  therefore plays a very important role in the determination of the HVP effect on  $a_\mu$ .

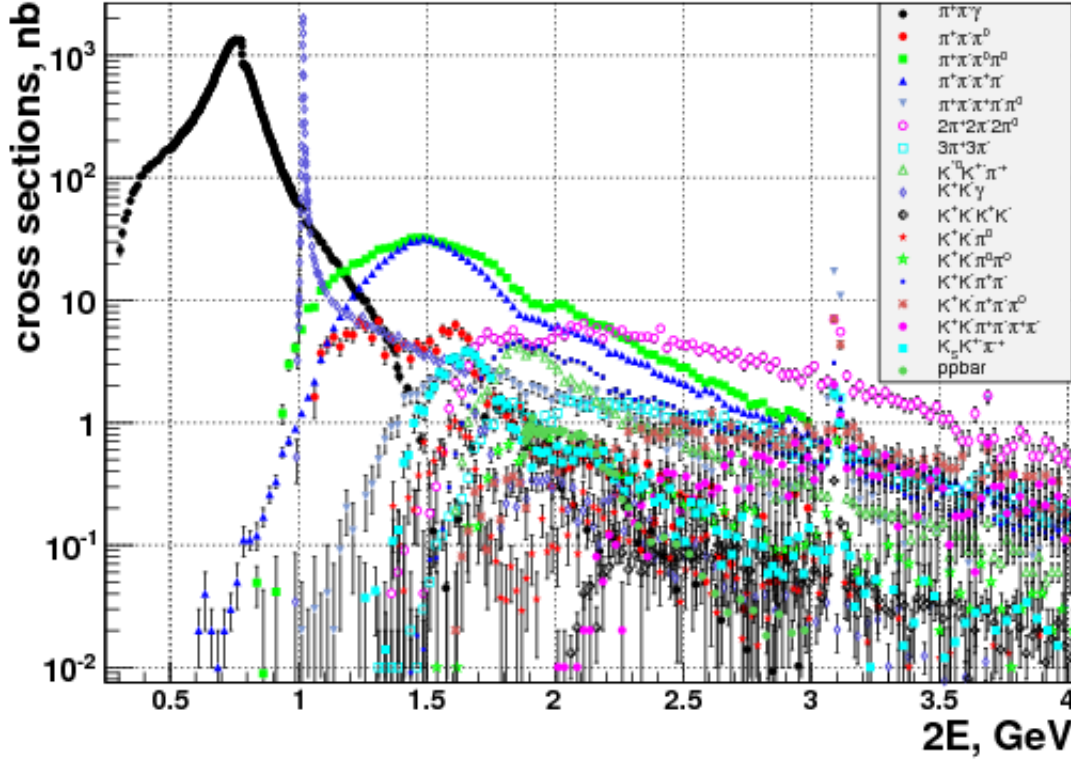


Figure 1.11: Experimental results from BABAR of the different channel contributions to the photon-inclusive hadronic cross section  $\sigma(e^+e^- \rightarrow \text{hadrons})$  [27]. The  $\rho(770)$  peak in the  $\pi^+\pi^-$  channel dominates the low-energy region.

The radiative corrections to the cross-section in (1.22) contribute significantly to the uncertainty, as can also be noted from figure 1.10. They contribute at the same order in  $\alpha$  as the HVP contribution at NLO or the HLbL contribution. One must therefore be careful and avoid double-counting. In order for the cross section to be infrared finite, virtual-photon as well as real-photon exchanges must be taken into account. This amounts to the inclusion of the full final-state radiation (FSR) into the cross section. Therefore, the prevalent convention is to include into the leading-order HVP the one-photon inclusive hadronic channel:

$$\begin{aligned} \sigma(e^+e^- \rightarrow \gamma^* \rightarrow \text{hadrons}(\gamma)) &:= \sigma(e^+e^- \rightarrow \gamma^* \rightarrow \text{hadrons}) \\ &+ \sigma(e^+e^- \rightarrow \gamma^* \rightarrow \text{hadrons} + \gamma). \end{aligned} \quad (1.25)$$

This explains why the intermediate state  $\pi^0\gamma$  must also be taken into account in the HVP contribution at LO. As will be explained later, the calculation of the virtual-photon contribution to the FSR has only been carried out in model-dependent ways so far. The goal of this thesis is to describe the FSR corrections to the process  $e^+e^- \rightarrow \pi^+\pi^-$  in a model-independent way. The method used to that end is explained in the next chapters.



## Chapter 2

# Unitarity and analyticity

In this chapter, we introduce the concepts of unitarity and analyticity and derive some tools that will be used later on in this thesis.

Unitarity is a very general property of any quantum field theory. It is related to the fact that, starting from an initial state, the probability of any outcome to happen must always be equal to one. This translates into the unitarity of the so-called  $S$ -matrix that relates any initial to any final state of a process. Together with the principle of maximal analyticity, unitarity allows one to completely determine the analytic structure of a scattering amplitude. Complex analysis can then be used to make predictions even when perturbative methods are not valid [28]. This is for instance the case in QCD at low energy.

### 2.1 $S$ -matrix unitarity

Let us consider a scattering process without specifying any particular kinematics. We denote the initial state as  $|i\rangle$ . This state is called asymptotic in the sense that long before the collision, it can be considered as free. Moreover, the set of all possible initial states form a complete basis of the so-called Fock space. From quantum mechanics, we know that the final state is a superposition of states, and can thus be written in terms of the initial state as  $|f\rangle = S|i\rangle$ .  $S$  is a linear operator called the  $S$ -matrix. It relates the asymptotic incoming states to the outgoing ones and therefore contains all the information about the dynamics of the process. Using the Born postulate, we can calculate the probability that the system ends up in an arbitrary state  $|l\rangle$  in terms of the  $S$ -matrix elements:

$$P = |\langle l|f\rangle|^2 = |\langle l|S|i\rangle|^2. \quad (2.1)$$

Since the particles forming the initial and final states may be very far from each other and not interact at all, it is convenient to introduce a matrix  $T$  and rewrite the  $S$ -matrix as

$$S = \mathbb{1} + iT. \quad (2.2)$$

The information about the interaction is contained in this so-called  $T$  matrix. It is conventional to extract the momentum-conservation constraint out of the  $T$ -matrix element in order to define the scattering amplitude [29]. Defining the momenta of the initial and final states to be respectively  $\{k_j\}$  and  $\{p_i\}$  and their sum  $P_f = \sum_j p_j$ ,  $P_i = \sum_j k_j$ , we

have

$$\langle f|T|i\rangle = (2\pi)^4 \delta^{(4)}(P_f - P_i) M_{fi}(\{p_i\}, \{k_j\}). \quad (2.3)$$

$M_{fi}(\{p_i\}, \{k_j\})$  is the transition amplitude describing the process  $i \rightarrow f$ .

The conservation of probability implies the unitarity of the  $S$ -matrix. This has interesting consequences for the transition amplitude. To show this, let us now choose a basis of states in a Fock space  $\{|n\rangle\} \in \mathcal{H}$  that is orthonormal and complete, that is

$$\langle m|n\rangle = \delta_{nm}, \quad (2.4)$$

$$\sum_n |n\rangle\langle n| = \mathbb{1}. \quad (2.5)$$

According to quantum mechanics, any state  $|\tilde{n}\rangle \in \mathcal{H}$  can be written as a superposition of states composing the basis:

$$|\tilde{n}\rangle = \sum_n a_n |n\rangle. \quad (2.6)$$

Using the fact that  $|\tilde{n}\rangle$  must be normalized and the orthonormality of the states of the basis, we see that the coefficients  $a_n$  must fulfil the constraint

$$\sum_n |a_n|^2 = 1. \quad (2.7)$$

Starting from an arbitrary initial state  $|\tilde{n}\rangle$ , the probability that the final state of the scattering process ends up in any of the states of the basis must be equal to one [30], that is, after using (2.5):

$$1 \stackrel{!}{=} \sum_n |\langle n|S|\tilde{n}\rangle|^2 = \sum_n \langle \tilde{n}|S^\dagger|n\rangle \langle n|S|\tilde{n}\rangle = \sum_{m,m'} a_{m'}^* a_m \langle m'|S^\dagger S|m\rangle. \quad (2.8)$$

In order for this relation to hold for any set of coefficients  $\{a_m\}$ , the  $S$ -matrix must obey

$$\langle m'|S^\dagger S|m\rangle = \delta_{m'm}, \quad (2.9)$$

$$S^\dagger S = \mathbb{1}. \quad (2.10)$$

On the other hand, the probability that an arbitrary final state arises from some initial state is also equal to unity. This implies

$$SS^\dagger = \mathbb{1}, \quad (2.11)$$

and thus, the conclusion is that the  $S$  matrix is unitary.

In order to understand what are the consequences for the transition amplitudes, we decompose the  $S$ -matrix according to (2.2). The unitarity of the  $S$ -matrix (2.10) implies for the  $T$  matrix

$$-i(T - T^\dagger) = T^\dagger T. \quad (2.12)$$

Sandwiching this relation between the initial and final states, and assuming time-reversal invariance ( $\langle f|T|i\rangle = \langle i|T|f\rangle$ ), we use the completeness relation  $\sum_n |n\rangle\langle n| = \mathbf{1}$  to rewrite

$$2\text{Im}\langle f|T|i\rangle = \langle f|T^\dagger T|i\rangle = \sum_n \langle f|T^\dagger|n\rangle\langle n|T|i\rangle. \quad (2.13)$$

Using the expression above, this translates directly into a relation for the transition amplitude. We simplify the Dirac  $\delta$  functions and write explicitly the phase-space integration to get

$$2\text{Im}M_{fi} = (2\pi)^4 \sum_n \int d\Phi_n(P_f, k_1, \dots, k_n) M_{nf}^* M_{ni}. \quad (2.14)$$

Note that the sum accounts for all possible intermediate states  $|n\rangle$  with total momentum  $P_n = P_f$ . Also,  $\int d\Phi_n$  represents the full phase-space integration

$$d\Phi_n(P; k_1, \dots, k_n) := \delta^{(4)}\left(P - \sum_n k_n\right) \prod_{i=1}^n \frac{d^3 k_i}{(2\pi)^3 2k_i^0}. \quad (2.15)$$

The explicit form of its differential in the case of  $n$  particles with momenta  $\{k_1, \dots, k_n\}$  is given in Appendix B.

In the case of a two-particle scattering process, in the limit where the initial and final state are identical,  $|f\rangle = |i\rangle$ , the phase-space integral of the amplitude squared  $|M_{ni}|^2$  can be related to the total cross section for the process  $i \rightarrow i$ . In this limit, relation (2.14) is the well-known optical theorem relating the cross-section to the imaginary part of the forward-scattering amplitude:

$$\text{Im}M(i \rightarrow i) = 2E_{\text{c.m.}} p_{\text{c.m.}} \sigma_{\text{tot}}(i \rightarrow i). \quad (2.16)$$

The two quantities evaluated in the center-of-mass frame  $E_{\text{c.m.}}$  and  $p_{\text{c.m.}}$  are respectively the total energy of the system and the modulus of the three-momentum of any of the two external particles.

From relation (2.14), we see that in order to obtain the imaginary part of a given transition amplitude  $M_{fi}$ , we need to sum over all intermediate states allowed by the symmetries of the process. There might be an infinite number of them and this is of course impossible in practice. The idea is to understand which intermediate states are dominant in the process. There is only a finite number of them to be considered. We can then truncate the series and ignore the rest.

## 2.2 Scattering amplitude and partial-wave expansion

The unitarity of the S-matrix has nice consequences when restricted on 2-body scattering processes. Let us therefore consider the process  $\phi_1(p_1)\phi_2(p_2) \rightarrow \phi_3(p_3)\phi_4(p_4)$  depicted in figure 2.1. The particles  $\phi_i$  have masses  $m_i$  and four-momenta  $p_i = (E_i, \mathbf{p}_i)$   $i \in \{1, 2, 3, 4\}$ . For simplicity, they are chosen to have no spin. The four particles are on-shell:

$$p_i^2 = m_i^2 = E_i^2 - \mathbf{p}_i^2 \quad i \in \{1, 2, 3, 4\}. \quad (2.17)$$

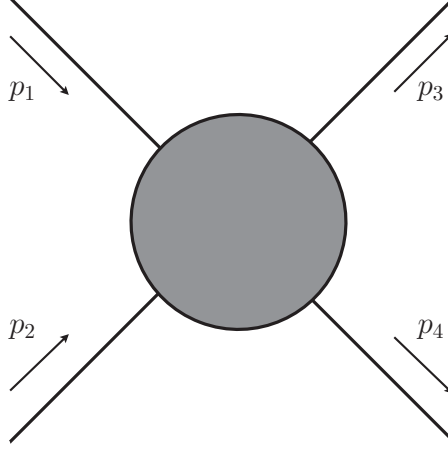


Figure 2.1: Scattering process  $\phi_1(p_1)\phi_2(p_2) \rightarrow \phi_3(p_3)\phi_4(p_4)$

The Mandelstam variables of the scattering process are

$$\begin{aligned} s &= (p_1 + p_2)^2 = (p_3 + p_4)^2 \\ t &= (p_1 - p_3)^2 = (p_2 - p_4)^2 \\ u &= (p_1 - p_4)^2 = (p_2 - p_3)^2. \end{aligned} \quad (2.18)$$

Because of the on-shell relation

$$s + t + u = \sum_{i=1}^4 m_i^2, \quad (2.19)$$

the scattering amplitude depends on two out of the three invariant Mandelstam variables additionally to the masses of the particles. We can choose to express the amplitude in terms of the squared center-of-mass energy and momentum transfer  $s$  and  $t$ . The latter can be expressed in terms of the scattering angle  $\theta_s$  between an incoming and an outgoing particle in the center of-mass-frame of  $s$  (see Appendix A for an explicit parametrization of the kinematics of this process). For this particular process, relation (2.3) becomes

$$\langle \phi_3(p_3)\phi_4(p_4) | T | \phi_1(p_1)\phi_2(p_2) \rangle = (2\pi)^4 \delta^{(4)}(p_1 + p_2 - p_3 - p_4) M(s, t(\theta_s)). \quad (2.20)$$

It is very useful to express such a scattering amplitude as a partial-wave expansion. This representation is based on angular momentum conservation and is possible because the Legendre polynomial  $P_\ell(z)$  form a complete orthogonal set. We thus write the amplitude as

$$M(s, t(\theta_s)) = \sum_{\ell} (2\ell + 1) P_\ell(\cos \theta_s) f_\ell(s). \quad (2.21)$$

Note that this particular representation corresponds to a scattering amplitude where all particles are spinless. For particles with arbitrary spins, this relation can be generalized using Wigner  $d_{mm'}^J(\theta)$  functions.

The partial waves  $f_\ell(s)$  only depend on the center-of-mass energy squared. They represent transition amplitudes between states of identical angular momentum  $\ell$ . In order to

single out a well-defined partial wave, one can simply project the amplitude by integrating over  $z_s := \cos \theta_s$ :

$$f_\ell(s) = \frac{1}{2} \int_{-1}^1 dz_s M(s, z_s) P_\ell(z_s). \quad (2.22)$$

This relation holds because the Legendre polynomials form an orthogonal basis that is normalized as

$$\int_{-1}^1 dz_s P_\ell(z_s) P_{\ell'}(z_s) = \frac{2}{2\ell + 1} \delta_{\ell\ell'}. \quad (2.23)$$

The unitarity relation of the partial waves can be written in a very compact form. This is especially true in the elastic region, where the only intermediate state considered is identical to the final state. Let us start by calculating the imaginary part in  $s$  of the scattering amplitude. For simplicity, we restrict ourselves to intermediate states with only two particles with masses  $m_{n_{1,2}}$ . We define by  $M_{fi}$  the amplitude with initial state  $|i\rangle = |\phi_1\phi_2\rangle$  and final state  $|f\rangle = |\phi_3\phi_4\rangle$ . We write the unitarity relation according to the derivation above and expand the two amplitudes in partial waves.

$$\begin{aligned} \text{Im} M(s, t) &= (2\pi)^4 \sum_n \frac{1}{2} \int_{\mathbf{k}} d\Phi_2^n(\mathbf{k}) M_{ni} M_{fn}^* \\ &= \sum_n \frac{\lambda^{1/2}(s, m_{n_1}^2, m_{n_2}^2)}{64\pi^2 s} \int d\Omega(\mathbf{k}) M_{ni}(s, \hat{\mathbf{p}}_1 \cdot \hat{\mathbf{k}}) M_{fn}^*(s, \hat{\mathbf{p}}_3 \cdot \hat{\mathbf{k}}) \\ &= \sum_n \sum_{\ell\ell'} \frac{(2\ell + 1)(2\ell' + 1)}{64\pi^2} \frac{\lambda^{1/2}(s, m_{n_1}^2, m_{n_2}^2)}{s} f_\ell^{ni} f_{\ell'}^{fn*} \\ &\quad \times \int d\Omega(\hat{\mathbf{k}}) P_\ell(\hat{\mathbf{p}}_1 \cdot \hat{\mathbf{k}}) P_{\ell'}(\hat{\mathbf{p}}_3 \cdot \hat{\mathbf{k}}). \end{aligned} \quad (2.24)$$

We used the Källén function  $\lambda(a, b, c) := a^2 + b^2 + c^2 - 2(ab + bc + ac)$ . The differential  $d\Phi_2^n$  accounts for the 2-body phase-space integral of the intermediate state  $|n\rangle$ . Its explicit form can be found in appendix B. Also, the partial waves  $f_\ell^{ni}$  correspond to the scattering amplitude  $M_{ni}$ . In order to calculate explicitly the phase-space integral, one can expand the Legendre polynomials in spherical harmonics as

$$P_\ell(\hat{\mathbf{p}} \cdot \hat{\mathbf{k}}) = \frac{4\pi}{2\ell + 1} \sum_{m=-\ell}^{\ell} Y_{\ell m}(\hat{\mathbf{p}}) Y_{\ell m}(\hat{\mathbf{k}}). \quad (2.25)$$

The orthonormality of the spherical harmonics,

$$\int d\Omega(\hat{\mathbf{k}}) Y_{\ell m}(\hat{\mathbf{k}}) Y_{\ell' m'}(\hat{\mathbf{k}}) = \delta_{\ell\ell'} \delta_{mm'} \quad (2.26)$$

allows to project (2.24) on the partial wave of interest:

$$\begin{aligned} \text{Im} f_\ell(s) &= \frac{1}{2} \int_{-1}^1 dz \text{Im} M(s, z) P_\ell(z) \\ &= \sum_n \frac{\lambda^{1/2}(s, m_{n_1}^2, m_{n_2}^2)}{16\pi s} f_\ell^{ni} f_\ell^{fn*}. \end{aligned} \quad (2.27)$$

## 2.3 Watson's theorem

A very interesting conclusion can be drawn for the partial waves of an amplitude, once only purely elastic final state scattering is considered. This means that the only intermediate state in the unitarity relation is  $|n\rangle = |f\rangle$ . Let us write the partial-wave expansion of the process  $f \rightarrow f$  as

$$M_{ff}(s, z) = \sum_{\ell} (2\ell + 1) t_{\ell}(s) P_{\ell}(z). \quad (2.28)$$

Then, assuming  $|f\rangle$  to be the only intermediate state in the sum of relation (2.27), the imaginary part of a given partial wave  $f_{\ell}(s)$  is reduced to

$$\text{Im} f_{\ell}(s) = \frac{\lambda^{1/2}(s, m_3^2, m_4^2)}{16\pi s} f_{\ell}(s) t_{\ell}^*(s). \quad (2.29)$$

The Källén function  $\lambda(s, m_3^2, m_4^2)$  depends on the masses of the two particles composing the state  $|f\rangle$  defined above. The important point is that the imaginary part of the partial wave must be a real quantity. This means that the imaginary part of the product  $f_{\ell}(s) t_{\ell}^*(s)$  must vanish exactly. Writing the partial waves in a complex exponential form

$$f_{\ell}(s) = |f_{\ell}(s)| e^{i\delta_f(s)}, \quad (2.30)$$

$$t_{\ell}(s) = |t_{\ell}(s)| e^{i\delta_t(s)}, \quad (2.31)$$

the relation above implies that the phase  $\delta_f(s)$  must be identical to the phase  $\delta_t(s)$  up to integer factors of  $\pi$ . Of course, this is only true in the limit of purely elastic rescattering. Generally, this assumption is good at low energy. At higher energies, inelasticities must be accounted for as corrections to this relation.

The knowledge of the phase of a partial wave in the physical region turns out to be very useful. The related Omnès problem is explained in the next chapters.

## 2.4 Unitarity applied on Feynman graphs

It was shown by Cutkosky in 1960 [31] that there is a direct relation between the unitarity relation (2.14) and Feynman diagrams. The so-called Cutkosky cutting rule amounts to cut the diagram in the channel of interest in all possible ways. For each cut, all crossed propagators are replaced according to

$$\frac{1}{q^2 - M^2 + i\epsilon} \rightarrow \begin{cases} -2\pi i \theta(q^0) \delta^{(1)}(q^2 - M^2) & q \text{ flows upwards,} \\ -2\pi i \theta(-q^0) \delta^{(1)}(q^2 - M^2) & q \text{ flows downwards.} \end{cases} \quad (2.32)$$

The  $\theta$  function simply keeps track of the sign of the energy of the particle in the loop, depending on the flow direction.

In order to illustrate that feature, let us consider the simple example of the diagram in figure 2.2. The dashed line represents a scalar insertion with momentum  $q$ . We assume for simplicity that the internal masses are identical to the external ones  $p_1^2 = p_2^2 = m^2$ . Also, the vertices have no particular structure and we set the coupling constants to 1. This diagram is therefore identical to the Passarino-Veltman  $C_0$  function [32]

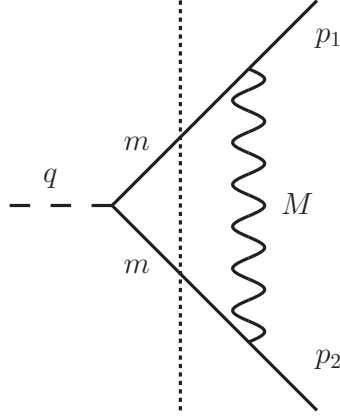


Figure 2.2: Triangle scalar diagram

$$C_0(q^2, p_1^2, p_2^2, m_1^2, m_2^2, m_3^2) = \frac{1}{i} \int \frac{d^4 k}{(2\pi)^4} \frac{1}{[k^2 - m_1^2][(k - p_1)^2 - m_2^2][(k + p_2)^2 - m_3^2]} \quad (2.33)$$

in the particular case  $m_2^2 = m_3^2 = p_1^2 = p_2^2 = m^2$  and  $m_1^2 = M^2$ .

The dotted line represents the only possible cut in this situation. Its contribution to the imaginary part is

$$\begin{aligned} \text{Im} M(q^2) &= \frac{(2\pi)^2}{2} \int \frac{d^4 k}{(2\pi)^4} \frac{1}{[k^2 - M^2]} \delta^{(1)}((k - p_1)^2 - m^2) \delta^{(1)}((k + p_2)^2 - m^2) \\ &\quad \times \theta((k - p_1)^0) \theta(k + p_2)^0 \\ &= \frac{1}{2} (2\pi)^4 \int d\Phi_2 \frac{1}{[(k_1 - p_2)^2 - M^2]} \\ &= \frac{1}{16\pi q^2 \sqrt{1 - 4m^2/q^2}} \log \frac{M^2 + q^2 - 4m^2}{M^2}. \end{aligned} \quad (2.34)$$

In summary, we see that the imaginary part of the diagram of interest can be calculated as the phase-space integral of the product of the two sub-amplitudes. In fact, this result can be generalized to any diagram. The Cutkosky cutting rule amounts to cutting the diagram in all possible ways and integrating the product of the sub-amplitudes separated by the cut over the full phase space.

## 2.5 Analyticity and crossing symmetry

The analytic properties of a scattering amplitude in one of its Mandelstam variables play a central role in this thesis. They can be obtained from unitarity, together with the principle of maximal analyticity. The latter follows from causality and assumes that all singularities of an amplitude must have a dynamical origin. To understand why unitarity allows to identify the singularities of the amplitude, we must review the kind of processes contributing to the scattering amplitude.

The first one is the exchange of a single particle of mass  $m$ . It can be any fundamental particle or bound state whose quantum numbers are consistent with the initial and final state of the process. The exchange is described in the momentum space by a propagator  $1/(s-m^2)$ . Consequently, it contributes to the amplitude as a simple pole in  $s$ .

The second possibility is the contribution from loop diagrams: Cutkosky's rule or, more generally, unitarity, implies that any Feynman diagram that can be cut through a multi-particle state contributes to the amplitude. When  $s$  is larger than the creation threshold, that is, large enough for the creation of the particles in the intermediate states,  $s > s_{\text{thr}}$ , this contribution gets an imaginary part. In the case  $s < s_{\text{thr}}$ , the contribution is real and is a simple polynomial. This is one of the two conditions that must be fulfilled, in order for Schwarz reflection principle to be valid. The latter states that if there exists a domain  $D$ , whose intersection with the real axis is  $\Lambda$  and a function  $f(s)$  that is analytic in  $D$  and such that  $\text{Im}f(s) = 0$  for  $s \in \Lambda$ , then

$$f(s^*) = f(s)^* \quad (2.35)$$

for  $s$  and  $s^*$  belonging to  $D$ . Choosing a small parameter  $\epsilon > 0$ , we can therefore conclude that for  $s > s_{\text{thr}}$

$$\lim_{\epsilon \rightarrow 0} T(s + i\epsilon, t) - T(s - i\epsilon, t) = \lim_{\epsilon \rightarrow 0} T(s + i\epsilon, t) - T^*(s + i\epsilon, t) \neq 0. \quad (2.36)$$

This shows the presence of a cut from the energy threshold to infinity. The discontinuity on this cut can directly be related to the imaginary part of the amplitude evaluated on the upper rim of the cut:

$$\begin{aligned} \frac{1}{2i} \text{Disc } T(s, t) &= \frac{1}{2i} \lim_{\epsilon \rightarrow 0} [T(s + i\epsilon, t) - T(s - i\epsilon, t)] \\ &= \lim_{\epsilon \rightarrow 0} \text{Im } T(s + i\epsilon, t). \end{aligned} \quad (2.37)$$

In that sense, poles in the complex plane are associated with bound states, i.e. intermediates states with only one particle. Cuts are associated with intermediate states in the unitarity relation. Their branch point is the threshold energy, or the minimal energy for the creation of the intermediate particles.

As already explained above, a 2-body scattering amplitude depends on two out of the three Mandelstam variables  $s$ ,  $t$  and  $u$ . For each of these three variables, there exists a kinematical region in the Mandelstam plane corresponding to the physical process. In the case of the process depicted in figure 2.1, the physical region of  $s$  corresponds to the process  $\phi_1\phi_2 \rightarrow \phi_3\phi_4$ , whereas the physical region of  $t$  corresponds to the process  $\phi_1\phi_3 \rightarrow \phi_2\phi_4$  and the physical region of  $u$  corresponds to the process  $\phi_1\phi_4 \rightarrow \phi_2\phi_3$ . Those processes are thus related by crossing symmetry. This means that singularities can arise from the unitarity relation from either of the three variables. Moreover, the Mandelstam hypothesis [33] assumes that the scattering amplitude evaluated in the physical region of one of the variables can be related to the two others by an analytic continuation.

As an illustration, the Mandelstam plane of the  $\pi\pi$ -scattering process is depicted in figure 2.3. In the  $s$ -channel center-of-mass frame, those can be expressed in terms of the kinematic variables

$$\begin{aligned} s &= p_1^2 + p_2^2 + 2p_1 \cdot p_2 = 2m_\pi^2 + 2(E_1 E_2 + |\mathbf{p}_1||\mathbf{p}_2|), \\ t &= p_1^2 + p_3^2 - 2p_1 \cdot p_3 = 2m_\pi^2 - 2(E_1 E_3 - \cos\theta |\mathbf{p}_1||\mathbf{p}_3|), \\ u &= p_1^2 + p_4^2 - 2p_1 \cdot p_4 = 2m_\pi^2 - 2(E_1 E_4 + \cos\theta |\mathbf{p}_1||\mathbf{p}_4|). \end{aligned} \quad (2.38)$$



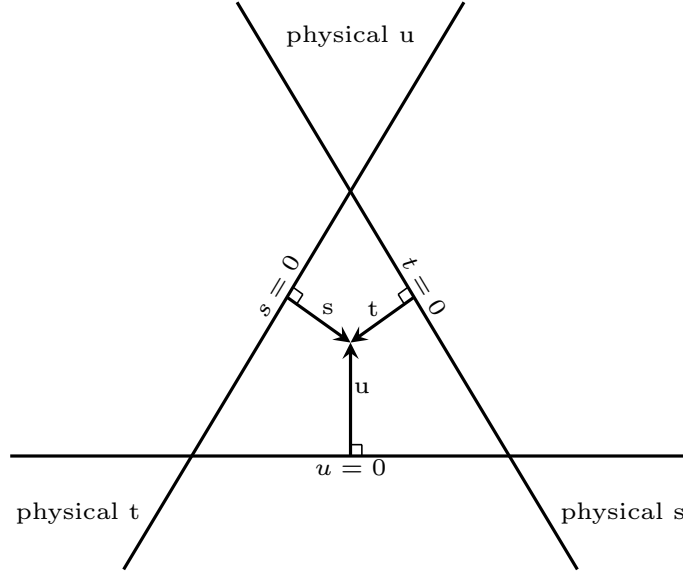


Figure 2.3: Mandelstam plane for  $\pi\pi$  scattering

The energy and three-momentum of each particle is given by

$$E_i = \frac{\sqrt{s}}{2} \quad (2.39)$$

$$|\mathbf{p}_i| = \frac{\sqrt{s - 4m_\pi^2}}{2} = \frac{\sqrt{s}}{2} \sigma_\pi(s) \quad (2.40)$$

The s-channel physical region is defined for  $s \geq 4m_\pi^2$  and  $-1 < \cos\theta < 1$ . This is equivalent to  $t < 0$  and  $u < 0$ . Similarly, if we choose the t- or u-channel center-of-mass frame, the physical region is defined respectively for  $t > 4m_\pi^2$ ,  $s < 0$ ,  $u < 0$  or  $u > 4m_\pi^2$ ,  $s < 0$ ,  $t < 0$ . According to the Mandelstam hypothesis, the transition amplitude evaluated in the t and u physical regions is the analytic continuation of the amplitude in the s region. In other words, the amplitude for the processes  $\pi(p_1)\pi(-p_3) \rightarrow \pi(-p_2)\pi(p_4)$  and  $\pi(p_1)\pi(-p_4) \rightarrow \pi(-p_2)\pi(p_3)$  can be directly related to  $\pi(p_1)\pi(p_2) \rightarrow \pi(p_3)\pi(p_4)$ .

Those singularities are therefore all identified by unitarity and crossing symmetry. Once all singularities are known, maximal analyticity ensures that the amplitude is analytic everywhere else in the complex plane. Therefore, the powerful mathematical theorems of complex analysis can be used and lead to dispersion relations. As stated in [30], "*One of the most important discoveries in elementary particle physics has been that of the complex plane*". This shows the importance of the work by Mandelstam in the late 1950's in various fields of particle physics [34].

## 2.6 Fixed-t dispersion relation

The dispersion relation is a powerful tool that relates an amplitude evaluated on an arbitrary point of the complex plane to an integral over its imaginary part. It is based on the analytic properties of the amplitude. For a nice and detailed introduction about this

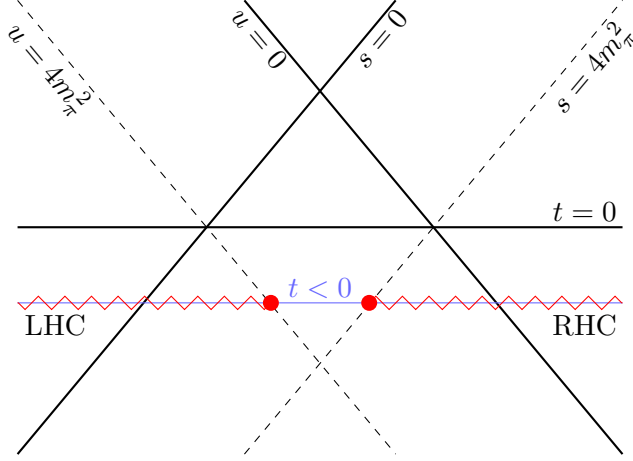


Figure 2.4: Analytic property of the  $\pi\pi$  scattering amplitude on the Mandelstam plane. The blue line accounts for a fixed  $t < 0$ . The red twisted line represents the cuts starting at the two-pion threshold.

topic, see [35, 36].

Because of the on-shell relation, the scattering amplitude depends on two out of the three Mandelstam variables that we choose to be  $s$  and  $t$ . We describe the amplitude as  $T(s, t, \Sigma - s - t)$ , where  $\Sigma = \sum_i m_i^2$ . In order to study its analytic property in  $s$  on the Mandelstam plane, we fix  $t$ . According to the principle of maximal analyticity, the amplitude is analytic in the whole complex plane, except for the singularities originating from the unitarity relation. In the case of the example of the previous section, the  $\pi\pi$ -scattering amplitude in the isospin limit the amplitude has no pole. This is due to the fact that there is no three-pion vertex. The  $\pi\pi$ -rescattering implies that there is a right-hand cut (RHC) starting at the pion threshold  $s_{thr} = 4m_\pi^2$ . The amplitude also has a left-hand cut (LHC) due to the on-shell relation  $u = 4m_\pi^2 - s - t$ . When  $s < t$ ,  $u$  is large enough for the creation of a pair of pions. The situation is depicted on figure 2.4.

Let us assume that the amplitude has an analytic structure similar to the example above. Knowing that the amplitude is analytic everywhere on the complex plane, except for those two cuts, we can use Cauchy's integral formula. This allows us to express the amplitude evaluated at an arbitrary point of the complex plane as a contour integral whose closed path is entirely contained in the analytic region. We define this contour by  $\Gamma$  and write

$$T(s, t) = \frac{1}{2\pi i} \oint_{\Gamma} ds' \frac{T(s', t)}{s' - s} \quad (2.41)$$

This situation is depicted in figure 2.5a in the case of an arbitrary circular contour. The analyticity of the amplitude everywhere on the complex plane except for the cuts then allow to deform the contour  $\Gamma$  into a new one,  $\Gamma'$ , as shown in figure 2.5b. Before the next step, we must assume that  $T(s, t)$  vanishes in the limit  $|s| \rightarrow \infty$ . This is of course not generally the case and subtractions must sometimes be introduced to address this issue. Assuming this nonetheless, the integration over the edge of the circle vanishes once the radius of  $\Gamma'$  is sent to infinity. We are thus left with only the integrals over the two cuts. This corresponds to figure 2.5c.

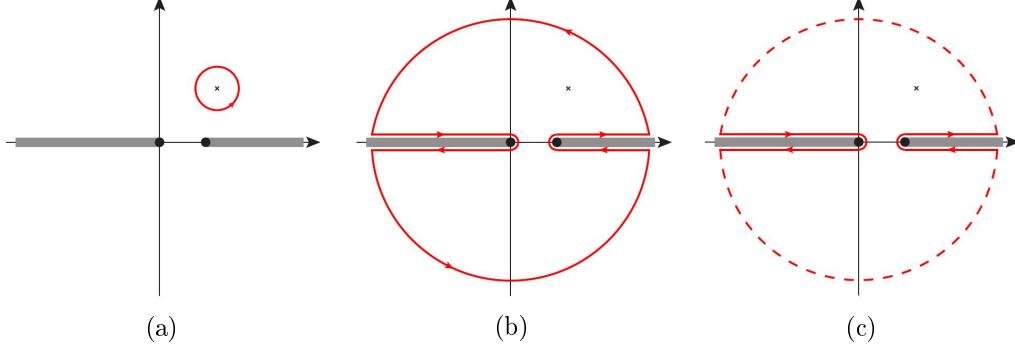


Figure 2.5: Deformation of the contour in the derivation of the dispersion relation. The cross indicates the point in the complex plane at which we evaluate the amplitude. The grey lines represent the left and right-hand cuts. The red line corresponds to the closed path of integration.

At this point, we can invoke the Schwarz reflection principle (2.35) to rewrite the difference between the amplitude evaluated on the upper and lower rim of the cut according to (2.37). This allows to write the contour integral along the two cuts in terms of the imaginary part of the amplitude:

$$T(s, t) = \frac{1}{\pi} \left\{ \int_{-\infty}^{-t} ds' \frac{\text{Im}T(s', t)}{s' - s} + \int_{4m_\pi^2}^{\infty} ds' \frac{\text{Im}T(s', t)}{s' - s} \right\}. \quad (2.42)$$

Note that the  $i\epsilon$  term has been dropped in that expression. However, the imaginary part is understood to be expressed slightly above the real axis. In order to evaluate explicitly the integral with the Cauchy pole, we can use the relation

$$\frac{1}{s' - (s \pm i\epsilon)} = P \frac{1}{s' - s} \pm i\pi \delta^{(1)}(s' - s), \quad (2.43)$$

where  $P$  means the Cauchy principal value of the integral. Equation (2.42) can then be rewritten as a relation between the real and imaginary part of  $T$ . For  $s > 0$ , we have

$$\text{Re } T(s, t) = \frac{1}{\pi} \left\{ \int_{-\infty}^{-t} ds' \frac{\text{Im}T(s', t)}{s' - s} + P \int_{4m_\pi^2}^{\infty} ds' \frac{\text{Im}T(s', t)}{s' - s} \right\}. \quad (2.44)$$

Note that there is no need to take the principal value in the first of the two integrals, since the integration variable  $s'$  is smaller than  $s$ . The contribution from the left-hand cut is thus purely real.

## 2.7 Subtractions

The derivation above was valid provided that the amplitude vanishes on the dashed circle of figure 2.5c. If the asymptotic behaviour of the amplitude does not fulfil this condition, one has to introduce subtractions. To that end, we choose  $n$  subtraction points  $\{s_1, \dots, s_n\}$

and write the contour integral for the ratio  $T(s, t)/P_n(s)$  where  $P_n(s)$  is the following polynomial of order  $n$ :

$$P_n(s) := \prod_{i=1}^n (s - s_i). \quad (2.45)$$

Asymptotically, the new integrand is damped by an additional factor  $s^n$ , where  $n$  is chosen large enough such that the integral over the circle vanishes when  $|s'| \rightarrow \infty$ . If all the poles are different, one can directly use the residue theorem to evaluate the integral. In the case where some poles have a higher multiplicity, one has to expand around this point first to extract the corresponding residue.

The drawback is the introduction of a priori unknown constants, one for each pole. Their number is equal to the multiplicity of the pole. Those are the so-called subtraction constants.

As an illustration, let us consider the case of two subtractions at different points. In the case of  $\pi\pi$  scattering, because of Froissard bound [37], two subtractions are enough for the integral on the circle to vanish. We choose  $s_1, s_2 \in \mathbb{R}$  and calculate

$$\begin{aligned} \frac{1}{2\pi i} \oint ds' \frac{T(s', t)}{(s' - s)(s' - s_1)(s - s_2)} &= \frac{T(s, t)}{(s - s_1)(s - s_2)} + \frac{T(s_1, t)}{(s_1 - s)(s_1 - s_2)} \\ &+ \frac{T(s_2, t)}{(s_2 - s)(s_2 - s_1)}. \end{aligned} \quad (2.46)$$

We can follow the previous steps to deform the contour and write

$$\begin{aligned} T(s, t) &= T(s_1, t) \frac{s - s_2}{s_1 - s_2} + T(s_2, t) \frac{s - s_1}{s_2 - s_1} \\ &+ \frac{(s - s_1)(s - s_2)}{\pi} \int_{-\infty}^{-t} ds' \frac{T(s', t)}{(s' - s)(s' - s_1)(s' - s_2)} \\ &+ \frac{(s - s_1)(s - s_2)}{\pi} \int_{s_{thr}}^{\infty} ds' \frac{T(s', t)}{(s' - s)(s' - s_1)(s' - s_2)}. \end{aligned} \quad (2.47)$$

In this case, the knowledge about the amplitude at  $s = s_1$  and  $s = s_2$  is required. Those are precisely the subtraction constants that must be introduced. Note that they still depend on the fixed  $t$ . This is important, since the  $t$ -channel cut of the amplitude is encoded in those. In the derivation of the system of Roy equations, for instance, such constants are rewritten as fixed- $s$  dispersive integrals in  $t$ .

We could also choose both subtractions at the same point  $s_1$ . In this case, we must expand around  $s = s_1$ . We find

$$\frac{T(s', t)}{s' - s} = \frac{T(s_1, t)}{s_1 - s} + \left[ \frac{\partial_s T(s, t)|_{s \rightarrow s_1}}{s_1 - s} - \frac{T(s_1, t)}{(s_1 - s)^2} \right] (s' - s_1) + \mathcal{O}((s - s_1)^2). \quad (2.48)$$

Because of the factor  $1/(s' - s_1)^2$  in the integral, only the term in bracket, proportional to  $(s' - s_1)$  has a simple pole. Using the residue theorem, we then find

$$\begin{aligned} T(s, t) &= T(s_1, t) + \partial_s T(s, t)|_{s \rightarrow s_1} (s - s_1) \\ &+ \frac{(s - s_1)^2}{\pi} \left\{ \int_{-\infty}^{-t} ds' \frac{T(s', t)}{(s' - s)(s' - s_1)^2} + \int_{s_{thr}}^{\infty} ds' \frac{T(s', t)}{(s' - s)(s' - s_1)^2} \right\}. \end{aligned} \quad (2.49)$$

In this case, not only the amplitude evaluated at  $s = s_1$  is required, but also its derivative in  $s$ . Consequently, two subtraction constants are needed.

In order to determine the subtraction constants required by subtracted dispersion relations, we will rely on a low-energy description of QCD. This effective field theory is called chiral perturbation theory and will be described in the next chapter.

## 2.8 Sum rules

According to the previous section, we are free to subtract a dispersive integral more times than required by the asymptotic behaviour of the imaginary part. This can for instance be useful in order to suppress the high-energy tail of the imaginary part in the dispersive integral contributing to the real part. As noticed in the previous section, the drawback is the introduction of as many subtraction constants as there are subtractions. Choosing  $n$  as the number of subtractions, we can write an arbitrary amplitude  $f(s)$  depending on only one variable as

$$f(s) = P(s) + \frac{s^n}{\pi} \int_{s_{thr}}^{\infty} ds' \frac{\text{Im}f(s')}{s'^n(s' - s)} \quad (2.50)$$

where  $P(s)$  is a subtraction polynomial of order  $n - 1$ . Of course, the asymptotic behaviour of  $f(s)$  is fixed and must be independent of the additional number of subtractions introduced. This means that if  $f(s) \xrightarrow{s \rightarrow \infty} s^m$ , with  $m < n$ , the highest powers of  $s$  in the subtraction polynomial must be cancelled at high energy by the dispersive integral. This leads to a constraint on  $f(s)$  that is commonly called sum rule.

Let us illustrate this with a simple example. We consider an amplitude  $f(s)$  going asymptotically at most as a constant:  $f(s) \xrightarrow{s \rightarrow \infty} c$ . Defining the exact value of the real part of  $f(s)$  at two energy points  $s_1$  and  $s_2$  as  $R_{1,2} = \text{Re}f(s_{1,2})$ , we can write

$$f(s) = P(s) + D(s), \quad (2.51)$$

$$P(s) = (R_1 - D(s_1)) \frac{s - s_2}{s_1 - s_2} + (R_2 - D(s_2)) \frac{s - s_1}{s_2 - s_1} \quad (2.52)$$

$$D(s) = \frac{s^2}{\pi} \int_{s_{thr}}^{\infty} ds' \frac{\text{Im}f(s')}{s'^2(s' - s)}. \quad (2.53)$$

In this case, the linear part of the polynomial  $P(s)$  must be cancelled by  $D(s)$  in the large- $s$  limit. We expand the  $s$ -dependent part of  $D(s)$  as

$$\frac{s^2}{s' - s} = -s - s' + \mathcal{O}(s^{-1}) \quad (2.54)$$

and impose that the part of (2.51) linear in  $s$  vanishes. The result can be expressed in the following form:

$$R_1 - R_2 = \frac{s_1 - s_2}{\pi} \int_{s_{thr}}^{\infty} ds' \frac{\text{Im}f(s')}{(s' - s_1)(s' - s_2)}. \quad (2.55)$$

Assuming that the asymptotic constant  $c$  is zero, we could also impose that the high-energy limit of (2.51) vanishes, leading to an additional sum rule.

In this thesis, we will also encounter the particular case of a three-times subtracted dispersion relation of an amplitude going asymptotically at most as a constant. We define respectively as  $s_i$  and  $R_i$ ,  $i \in \{1, 2, 3\}$  the three subtraction points and the corresponding value of the amplitude. Following the same steps as above, we get the two sum rules

$$\sum_{\substack{i=1 \\ i \neq j \neq k}}^3 \frac{R_i}{(s_i - s_j)(s_i - s_k)} = \frac{1}{\pi} \int ds' \frac{\text{Im}f(s')}{(s' - s_1)(s' - s_2)(s' - s_0)}, \quad (2.56)$$

$$\sum_{\substack{i=1 \\ i \neq j \neq k}}^3 \frac{R_i(s_j + s_k)}{(s_i - s_j)(s_i - s_k)} = \frac{1}{\pi} \int ds' \frac{(s_0 + s_1 + s_2 - s')}{(s' - s_1)(s' - s_2)(s' - s_0)} \text{Im}f(s'). \quad (2.57)$$

As we will see later, these will turn out to be useful.

## 2.9 Mandelstam representation

Fixing  $t$  and writing the dispersion relation for  $s$  is evidently not the only choice we could make. We could also have done the opposite: fixing  $s$  and dispersing  $t$ . Or we could have chosen any other trajectory in the complex plane, fixing for instance the product  $us$  to a parameter and writing an hyperbolic dispersion relation [38].

We can go one step further and write the dispersion relation for two variables simultaneously. This so-called double-spectral representation has been formulated first by Mandelstam in 1958. Its general form,

$$\begin{aligned} T(s, t, u) = & \int_{s_{thr}}^{\infty} ds' \int_{t_{thr}}^{\infty} dt' \frac{\rho_{st}(s', t')}{(s' - s)(t' - t)} + \int_{s_{thr}}^{\infty} ds' \int_{u_{thr}}^{\infty} du' \frac{\rho_{su}(s', u')}{(s' - s)(u' - u)} \\ & + \int_{u_{thr}}^{\infty} du' \int_{t_{thr}}^{\infty} dt' \frac{\rho_{ut}(u', t')}{(u' - u)(t' - t)} \end{aligned} \quad (2.58)$$

is a sum of integrals over the three regions of the Mandelstam plane where two of the variables are larger than the energy threshold of the corresponding channels. The three functions  $\rho_{st}$ ,  $\rho_{su}$  and  $\rho_{ut}$  are the corresponding densities defined on these regions.

It can also be that the double-spectral densities do not have the appropriate asymptotic behaviour for the representation (2.58). In order for the integrals to be finite, one must therefore also subtract, similarly to the previous section. In this case, the subtraction terms have the form of single-variable dispersive integrals instead of constants.

## 2.10 The Omnès-Muskhelishvili problem

It was remarked in a previous section that in certain cases, the complex phase of a scattering amplitude can be obtained from the Watson theorem. Let us define such an amplitude by  $F(s)$  and assume it is analytic on the whole complex plane, except for a branch-cut on the positive real axis. The Omnès-Muskhelishvili method allows one to find the most general solution for this function, provided that its phase is known on the cut. This method has been developed by Omnès in 1958 [39], based on some previous analysis by Muskhelishvili [40].

The solution to this problem is not unique. Provided  $\Omega(s)$  is a solution normalized at  $s = 0$  ( $\Omega(0) = 1$ ), for any function  $P(s)$  analytic on the whole complex plane,  $F(s) = P(s)\Omega(s)$  is also a solution. One thus needs to add further constraints on  $F(s)$  to fix  $P(s)$ . Let us assume that the cut starts at some branch-point  $s_{thr} > 0$ . The phase along this cut is given by

$$\text{Arg}(\Omega(s)) = \delta(s) \quad s \in [s_{thr}, \infty]. \quad (2.59)$$

There are two different ways to calculate the discontinuity of  $\Omega(s)$  on the upper edge of the cut. The first one is to use the formal definition

$$\text{Disc}(\Omega(s)) = \Omega(s + i\epsilon) - \Omega(s - i\epsilon). \quad (2.60)$$

We can also use the direct relation between the discontinuity and the imaginary part of the amplitude along the cut. Moreover, our knowledge of the phase implies that

$$\begin{aligned} \text{Disc}(\Omega(s)) &= 2i|\Omega(s + i\epsilon)| \sin \delta(s) = 2i\Omega(s + i\epsilon)e^{-i\delta(s)} \sin \delta(s) \\ &= \Omega(s + i\epsilon)e^{-i\delta(s)} \left( e^{i\delta(s)} - e^{-i\delta(s)} \right) = \Omega(s + i\epsilon) \left( 1 - e^{-2i\delta(s)} \right). \end{aligned} \quad (2.61)$$

Equating (2.60) and (2.61) leads to

$$\text{Disc}(\log \Omega(s)) = \log \Omega(s + i\epsilon) - \log \Omega(s - i\epsilon) = 2i\delta(s). \quad (2.62)$$

From here, we assume that the phase converges asymptotically to a multiple of  $\pi$ :  $\delta(s) \xrightarrow{s \rightarrow \infty} \alpha\pi =: \delta(\infty)$ . Of course, this is an approximation and one could also use an incomplete Omnès-Muskhelishvili method [41, 35] to get closer to the reality. However, this goes behind the scope of this thesis. This assumption allows one to write  $\Omega(s)$  as a once-subtracted dispersive integral. The subtraction constant is fixed by the normalization condition  $\Omega(0) = 1$ :

$$\Omega(s) = \exp \frac{s}{\pi} \int_{s_{thr}}^{\infty} ds' \frac{\delta(s')}{s'(s' - s)}. \quad (2.63)$$

In order to determine the function  $P(s)$ , we need to know more about the asymptotic behaviour of  $\Omega(s)$ . To that end, we write

$$\begin{aligned} \Omega(s) &= \exp \left[ \frac{s}{\pi} \int_{s_{thr}}^{\infty} ds' \frac{\delta(s') - \delta(s) + \delta(s)}{s'(s' - s)} \right] \\ &= \exp \left[ \frac{s}{\pi} \int_{s_{thr}}^{\infty} ds' \frac{\delta(s') - \delta(s)}{s'(s' - s)} + \frac{\delta(s)}{\pi} \log \frac{s_{thr}}{s - s_{thr}} + i\delta(s) \right] \\ &\xrightarrow{s \rightarrow \infty} \exp \left[ -\frac{1}{\pi} \int_{s_{thr}}^{\infty} ds' \frac{\delta(s') - \alpha\pi}{s'} + \alpha \log \frac{s_{thr}}{s} + i\alpha\pi \right] \\ &\propto \left( \frac{s_{thr}}{s} \right)^{\alpha} \end{aligned} \quad (2.64)$$

Hence, we see that the asymptotic limit of the phase determines the asymptotic behaviour of the Omnès solution. For instance, in the case of meson form-factors, the Brodsky-Farrar counting rule states that

$$F(s) \underset{\sim}{\stackrel{s \rightarrow \infty}{\leq}} \frac{C}{s \log s^{\nu}} \quad \nu > 0. \quad (2.65)$$

In this case, the only analytic function  $P(s)$  that grows slower than exponentially in  $s$  is a polynomial. A particularly important application of the Omnès-Muskhelishvili method is the determination of the pion vector form factor that will be explained in the corresponding section. Also, the so-called modified Omnès-Muskhelishvili method explained later will be used and is a central point of this thesis.



## Chapter 3

# Chiral perturbation theory

Chiral perturbation theory (ChPT) is a low-energy description of QCD formalized in the pioneering work of Weinberg [42], and Gasser and Leutwyler [43, 44]. For excellent introductions into the topic, see for instance [45, 46, 47]. The aim of this section is to summarize the most important steps in the construction of the formalism of the theory.

### 3.1 Effective field theory

An effective field theory aims at describing a certain energy region (usually the low-energy part) of an underlying, more fundamental theory. According to Weinberg's conjecture, a quantum field theory has no content besides analyticity, unitarity, cluster decomposition and symmetry [42]. Thus, the Lagrangian of a so-called bottom-up effective theory must be invariant under the symmetry transformation of the system. The operators composing the Lagrangian are made of all low-energy degrees of freedom present in the theory. Those come along with coefficients called low-energy constants (LEC). All the information about the underlying physics is contained into those coefficients. They must be determined by experimental data. Note that effective field theories are predictive, since once the low-energy constants are fixed by experimental data about some particular process, predictions are possible for all other processes involving the same operators.

An a priori infinite number of operators contribute to the Lagrangian. However, usually, a power-counting argument allows one to classify them. The hope is that a good precision can be reached by considering only the lowest-order ones, while all the others can be neglected. For instance, the standard model itself can be considered as an effective field theory of an underlying, more general theory. The latter is renormalizable and an arbitrarily good precision can be reached from the lowest-order Lagrangian of dimension  $n = 4$ . On the other hand, as will be explained later, chiral perturbation theory needs operators of higher orders to increase the precision and is in that respect not renormalizable any more.

### 3.2 Chiral symmetry

In the standard model, the theory corresponding to the strong interactions is quantum chromodynamics (QCD). The degrees of freedom of its Lagrangian are the quarks and gluons in the form of color triplets  $q_f$ ,  $f \in \{u, d, s, c, t, b\}$  and gauge potentials  $G_a^\mu$ . The

Lagrangian

$$\mathcal{L}_{QCD} = \sum_f \bar{q}_f (i\not{D} - m_f) q_f - \frac{1}{4} \mathcal{G}_{\mu\nu}^a \mathcal{G}_a^{\mu\nu}. \quad (3.1)$$

is invariant under local  $SU(3)_c$  gauge transformations. This corresponds to a non-Abelian transformation of the quark fields

$$q_f \rightarrow \exp \left[ -i \sum_{a=1}^8 \theta_a(x) \frac{\lambda_a}{2} \right] q_f = U(x) q_f. \quad (3.2)$$

Note that  $\lambda_a$  are the generators of the  $su(3)$  Lie algebra. There are eight of them and their representation can be chosen as the Gell-Mann matrices. This also means that there are eight gauge potentials. The covariant derivative is expressed as

$$D_\mu q_f = \partial_\mu q_f - ig_s \sum_{a=1}^8 G_\mu^a q_f, \quad (3.3)$$

where  $g_s$  is the strong-coupling constant. In order for the Lagrangian to be invariant under gauge transformation, the covariant derivative must transform as  $D_\mu q_f \rightarrow U(x) D_\mu q_f$ . This implies that the gauge-potentials transform as

$$\frac{\lambda_a}{2} G_\mu^a(x) \rightarrow U(x) \frac{\lambda_a}{2} G_\mu^a(x) U^\dagger(x) - ig_s \partial_\mu U(x) U^\dagger(x). \quad (3.4)$$

They form the non-Abelian field-strength tensor

$$\mathcal{G}_a^{\mu\nu} = \partial^\mu G_\nu^a - \partial^\nu G_\mu^a + gf_{abc} G_b^\mu G_c^\nu. \quad (3.5)$$

Note that we ignored the P- and CP-violating  $\theta$ -term. It is related to the electric dipole moment of the neutron and has been shown to be extremely small experimentally [48].

At low energy, the three heaviest quarks ( $c, b, t$ ) can be integrated out and only the two or three lightest ones ( $N_f = 2, 3$ ) are taken into account. Since they are very light compared to the QCD scale  $\Lambda_{QCD}$ , their masses can be approximated by zero. In this so-called chiral limit, the Lagrangian has an additional accidental symmetry. It is invariant under global chiral transformations

$$\begin{aligned} \left( \frac{1 - \gamma^5}{2} \right) q &= q_L \rightarrow e^{-i\theta_L^a \frac{t_a}{2}} q_L \\ \left( \frac{1 + \gamma^5}{2} \right) q &= q_R \rightarrow e^{-i\theta_R^a \frac{t_a}{2}} q_R. \end{aligned} \quad (3.6)$$

The  $t_a$  are the  $N_f^2 - 1$  generators of the  $su(N_f)$  Lie algebra and can be represented by Pauli or Gell-Mann matrices in the case  $N_f = 2$  and  $N_f = 3$  respectively. Note that this symmetry would not be satisfied in case of non-vanishing quark masses. Additionally, to this symmetry, the original Lagrangian is also invariant under a global  $U(1)$  transformation for each of the chiral components and we end up with the symmetry group

$$SU(N_f)_L \times SU(N_f)_R \times U(1)_L \times U(1)_R \equiv SU(N_f)_V \times SU(N_f)_A \times U(1)_V \times U(1)_A. \quad (3.7)$$

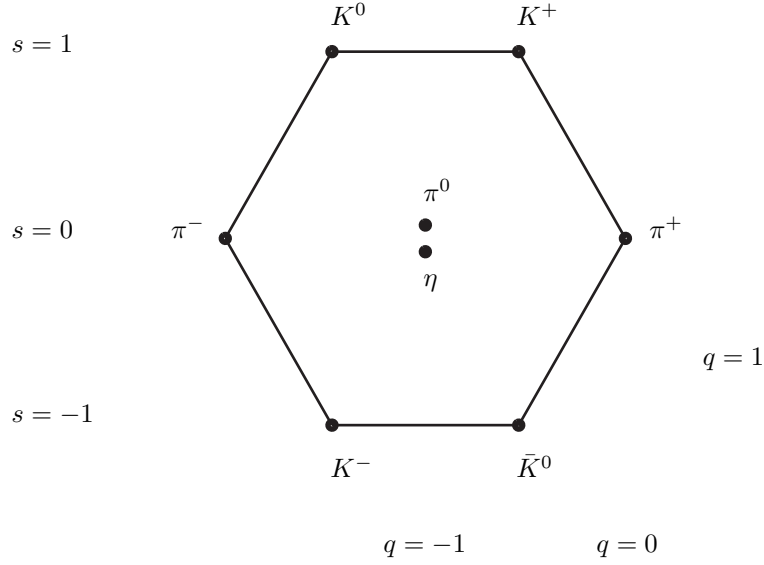


Figure 3.1: Eightfold way for the pseudo-scalar meson octet. The two axes are the strangeness (horizontal) and electric charge (diagonal).

The group  $U(1)_V$  accounts for baryon-number conservation. The group  $U(1)_A$ , however is broken by quantum corrections known as the axial anomaly [49, 50]. The remaining  $SU(N_f)_V \times SU(N_f)_A$  is the one of interest. It is spontaneously broken to the vectorial part of its group:

$$SU(N_f)_V \times SU(N_f)_A \rightarrow SU(N_f)_V. \quad (3.8)$$

The empirical indication of this spontaneous symmetry breaking is that the hadron spectrum seems to form a nice approximate  $SU(3)$  octet (see figure 3.1). This is referred to as the eightfold way [51]. Also, the physical pion masses being relatively small, they can be regarded as the Goldstone bosons of the spontaneous breaking.

Mathematically, a sufficient condition for the spontaneous symmetry breaking to happen is a non-zero quark condensate  $\langle \bar{q}q \rangle$ . If this is the case, the Goldstone theorem [52] states that there must exist a number of massless Goldstone bosons equal to the number of generators of the broken symmetry group, that is  $N_f^2 - 1$ . In our case, those are the pion triplet for  $N_f = 2$  or the meson octet for  $N_f = 3$ . In the real world, the latter are of course massive. This is due to the explicit breaking of the chiral symmetry due to non-vanishing quark masses. This breaking can be treated as a perturbation that works much better for  $N_f = 2$  than  $N_f = 3$  since the pion masses are much smaller than the typical chiral-breaking scale  $\Lambda_\chi \approx 1\text{GeV}$  compared to the other meson masses.

### 3.3 Transformation of the Goldstone boson fields

In order to construct the low-energy effective field theory of QCD we are aiming for, we must build the most general Lagrangian invariant under chiral symmetry. The operators of this Lagrangian are made of the Goldstone bosons associated with the spontaneous symmetry breaking mentioned above. It is therefore important to understand how those bosons evolve under chiral transformation.

Consider first a physical system invariant under a group  $G$  and whose ground state is only invariant under a subgroup  $H$  of  $G$ . In this situation, one can generally show that there exists an isomorphism between the Goldstone fields and the quotient  $G/H$  defined as the coset  $\{gH|g \in G\}$ . Consequently, for each of those, there is a Goldstone boson field. In our case, we have  $G = SU(N_f)_V \times SU(N_f)_A = \{(L, R)|L \in SU(N_f), R \in SU(N_f)\}$  the unbroken symmetry group and  $H = SU(2)_V = \{(V, V)|V \in SU(N_f)\}$  the subgroup of  $G$ . Let us consider one of the cosets  $\tilde{g}H = \{(\tilde{L}, \tilde{R})(V, V) = (\tilde{L}V, \tilde{R}V)|V \in H\} \in G$ . Using the unitarity of  $L$  and  $R$ , we can write

$$(\tilde{L}V, \tilde{R}V) = (\tilde{L}V, \tilde{R}\tilde{L}^\dagger\tilde{L}V) = (1, \tilde{R}\tilde{L}^\dagger) \underbrace{(\tilde{L}V, \tilde{L}V)}_{\in H}. \quad (3.9)$$

Hence we can characterize the left coset by the matrix  $U = \tilde{R}\tilde{L}^\dagger$  via the definition  $\tilde{g}H = (1, \tilde{R}\tilde{L}^\dagger)H$ . Of course, this is only a convention and we could equally well have the unity matrix in the second component. We can now analyse how the Goldstone fields evolve under  $G$  transformation by multiplying the coset with an arbitrary element  $g = (L, R) \in G$ :

$$g\tilde{g}H = (L, R\tilde{R}\tilde{L}^\dagger)H = (1, R\tilde{R}\tilde{L}^\dagger L^\dagger)H. \quad (3.10)$$

This means that the matrix of interest,  $U$  transforms as

$$U \xrightarrow{G} R\tilde{U}L^\dagger. \quad (3.11)$$

Let us now consider the building blocks of the theory. To that end, we define the following object:

$$\Phi(x) = \sum_{i=1}^{N_f^2-1} t^a \phi_a(x) \quad (3.12)$$

where the  $x$ -dependent  $\phi_a$  are the Goldstone fields and the  $t_a$  are the generators of the  $su(N_f)$  Lie algebra. In the case  $N_f = 2$ , the matrix representation of  $\Phi(x)$  is made of the Pauli matrices

$$\Phi(x) = \begin{pmatrix} \pi^0(x) & \sqrt{2}\pi^+(x) \\ \sqrt{2}\pi^-(x) & -\pi^0(x) \end{pmatrix} \quad (3.13)$$

and in the case  $N_f = 3$ , we use the Gell-Mann matrices

$$\Phi(x) = \begin{pmatrix} \pi^0(x) + 1/\sqrt{3}\eta(x) & \sqrt{2}\pi^+(x) & \sqrt{2}K^+(x) \\ \sqrt{2}\pi^-(x) & -\pi^0(x) + 1/\sqrt{3}\eta(x) & \sqrt{2}K^0(x) \\ \sqrt{2}K^-(x) & \sqrt{2}\bar{K}^0(x) & -2/\sqrt{3}\eta(x) \end{pmatrix}. \quad (3.14)$$

Note that the set of all of those Hermitian and traceless  $N \times N$  matrices with continuous components forms a vector space. Finally, we can introduce the exponential representation of  $U(x)$

$$U(x) = e^{\frac{i\Phi(x)}{F}} \quad (3.15)$$

where  $F$  has the dimension of a mass and will later turn out to be the pion decay constant. It transforms under  $G$  according to (3.11). The set composed by those matrices in exponential form is not a vector space, since the sum of two  $SU(N_f)$  matrices is not a  $SU(N_f)$  matrix. Therefore, the action of  $G$  on this space is called a non-linear realization. In fact, it is linear when restricted on the unbroken subgroup  $H$ . By expanding the exponential in (3.15) in powers of  $\Phi$  as

$$U = 1 + i\frac{\Phi}{F} - \frac{\Phi^2}{2F} + \mathcal{O}(\Phi^3), \quad (3.16)$$

the transformation under  $H$  is

$$U \xrightarrow{H} V \left( 1 + i\frac{\Phi}{F} - \frac{\Phi^2}{2F} + \dots \right) V^\dagger = 1 + i\frac{V\Phi V^\dagger}{F} - \frac{V\Phi V V^\dagger \Phi V^\dagger}{2F} + \dots \quad (3.17)$$

Therefore, we see that the Goldstone fields transform as

$$\Phi \xrightarrow{H} V\Phi V^\dagger. \quad (3.18)$$

An important remark is that the choice of parametrization of  $U$  as a function of the pseudoscalar fields is not unique. One could as well have opted for the  $\sigma$ -model parametrization for instance. In  $N_f = 2$ , the latter is

$$U = \sqrt{1 + \frac{\phi^2}{F^2}} + i\frac{\boldsymbol{\sigma} \cdot \boldsymbol{\phi}}{F}. \quad (3.19)$$

In this expression,  $\boldsymbol{\phi}$  is the three-dimensional vector made of the Goldstone boson fields  $\phi_i$  in (3.13).

### 3.4 Chiral Lagrangian

Once the building blocks of the theory and their transformation properties are known, one can construct the most general Lagrangian consistent with chiral symmetry. We want to classify each operator of the Lagrangian depending on the power of momenta they consist of. The typical momentum scale is much smaller than the chiral breaking scale  $\Lambda_\chi$  and therefore justify the expansion of our low-energy effective theory

$$\mathcal{L} = \mathcal{L}^{(2)} + \mathcal{L}^{(4)} + \dots \quad (3.20)$$

The lowest possible operator has two derivatives since without derivative,  $UU^\dagger = \mathbf{1}$  and one derivative would lead to a breaking of Lorentz invariance. At order  $p^2$ , the Lagrangian is only composed of one operator and is

$$\mathcal{L}^{(2)} = \frac{F^2}{4} \langle \partial^\mu U \partial_\mu U^\dagger \rangle. \quad (3.21)$$

The constant is fixed such that the kinetic term  $\mathcal{L}_{kin} = 1/2 \partial^\mu \phi_a \partial_\mu \phi^a$  is naturally reproduced. Also, we made use of the notation  $\langle \dots \rangle = \text{Tr}(\dots)$ , that is, we take the trace in flavour space. The constant  $F$  can be determined via the inclusion of the axial current between a one-boson state and the vacuum. The former is the Noether current associated with the transformation (3.6). We find

$$\begin{aligned} l_a^\mu &= \frac{\partial \delta \mathcal{L}}{\partial \partial_\mu \theta_L^a} = i \frac{F^2}{4} \langle \lambda_a \partial^\mu U^\dagger U \rangle, \\ r_a^\mu &= \frac{\partial \delta \mathcal{L}}{\partial \partial_\mu \theta_R^a} = -i \frac{F^2}{4} \langle \lambda_a U \partial^\mu U^\dagger \rangle. \end{aligned} \quad (3.22)$$

Thus, expanding the axial current in powers of  $\phi$ , we get

$$A_a^\mu = r_a^\mu - l_a^\mu = -i \frac{F^2}{4} \langle \lambda_a \{U, \partial^\mu U^\dagger\} \rangle = -F \partial^\mu \phi_a + \mathcal{O}(\phi^3). \quad (3.23)$$

This means that the axial current is in fact an interpolating field of the pseudoscalar bosons

$$\langle 0 | A_a^\mu | \phi_b(p) \rangle = i p^\mu \delta_{ab} F. \quad (3.24)$$

On the other hand, the partially-conserved axial-current relation (PCAC [53]) states that

$$\langle 0 | \partial_\mu A_a^\mu | \phi_b(p) \rangle = m_\phi^2 \delta_{ab} f_\phi \quad (3.25)$$

where  $m^2 = p^2$  is the mass squared of the pseudoscalar boson and  $f_\phi$  its decay constant. Comparing those two expressions, it is clear that  $F$  can be directly related to the pion decay constant  $F \approx f_\pi = 92.4 \text{ MeV}$  measurable in the process  $\pi \rightarrow \mu \nu_\mu$ . Since no more parameter is required at order  $p^2$ , expanding the Lagrangian in powers of  $\Phi$  as

$$\mathcal{L}^{(2)} = \frac{1}{2} \langle \partial_\mu \Phi \partial^\mu \Phi \rangle + \frac{1}{6F^2} \langle [\partial^\mu \Phi, \Phi] [\partial_\mu \Phi, \Phi] \rangle + \mathcal{O}(\Phi^6) \quad (3.26)$$

allows one to determine the first order contribution to any process  $\pi_1 \dots \pi_n \rightarrow \pi'_1 \dots \pi'_n$  in the chiral limit. In particular the amplitude for the process  $\pi^+(p_1) \pi^-(p_2) \rightarrow \pi^0(p_3) \pi^0(p_4)$  is given by

$$M(\pi^+(p_1) \pi^-(p_2) \rightarrow \pi^0(p_3) \pi^0(p_4))|_{m_q=0} = \frac{(p_1 + p_2)^2}{F^2} + \mathcal{O}(p^4). \quad (3.27)$$

### 3.5 Mass corrections and external sources

Even though they are very small, the quark masses are finite in nature. Those explicit chiral-breaking terms must be taken into account as well and this can be done in a perturbative way. Note that the mass term in (3.1) would be invariant under chiral transformation, provided that the mass matrix  $M = \text{diag}(m_u, m_d, m_s)$  transformed as

$$M \xrightarrow{G} R M L^\dagger. \quad (3.28)$$

This is of course not the case in reality. However, assuming it is, we can construct an invariant Lagrangian and keep track of the explicit chiral symmetry breaking in QCD.

The symmetrized lowest-order operator is  $\langle MU^\dagger + M^\dagger U \rangle$ . At order  $p^2$ , the Lagrangian is therefore

$$\mathcal{L}^{(2)} = \frac{F^2}{4} \langle \partial^\mu U \partial_\mu U^\dagger \rangle + \frac{F^2 B_0}{2} \langle MU^\dagger + M^\dagger U \rangle. \quad (3.29)$$

Note that  $B_0$  is an unknown dimensionless parameter of the theory. From this, we can read off the mass terms of the different pseudoscalars of the theory in the isospin limit ( $m_u = m_d = \hat{m}$ ):

$$m_\pi^2 = 2B_0\hat{m} \quad m_K^2 = B_0(\hat{m} + m_s). \quad (3.30)$$

We can see in this relation that in our ordering, the quark masses are  $m_q \sim \mathcal{O}(p^2)$ . The difference in the  $u$  and  $d$  quark masses causes a difference between neutral and charged pions and kaons. The size of this difference, however, is very small compared to the mass difference due to electromagnetic corrections.

Taking the mass term into account, relation (3.27) becomes

$$M(\pi^+(p_1)\pi^-(p_2) \rightarrow \pi^0(p_3)\pi^0(p_4)) = \frac{(p_1 + p_2)^2 - m_\pi^2}{F^2} + \mathcal{O}(p^4). \quad (3.31)$$

Also, at order  $p^2$ , the S-wave with  $I = 0, 2$  scattering lengths that are defined as the evaluation of the corresponding isospin amplitude at the two-pion threshold and at  $t = u = 0$  are

$$\begin{aligned} a_0^0 &= \frac{T^0(4m_\pi^2, 0, 0)}{32\pi} = \frac{7m_\pi^2}{16\pi F^2} = 0.16, \\ a_0^2 &= \frac{T^2(4m_\pi^2, 0, 0)}{32\pi} = -\frac{m_\pi^2}{16\pi F^2} = -0.045. \end{aligned} \quad (3.32)$$

The lowest-order contribution is thus a rather good approximation to the actual values  $a_0^0 = 0.220 \pm 0.005$ ,  $a_0^2 = -0.0444 \pm 0.0010$  [54].

A more general way to study the effect of non-zero mass and external sources is to couple quarks with external hermitian matrix fields  $v^\mu = l^\mu + r^\mu$ ,  $a^\mu = l^\mu - r^\mu$ ,  $s$  and  $p$  in the QCD Lagrangian:

$$\mathcal{L}_{QCD} = \mathcal{L}_{QCD}^0 + \bar{q}\gamma^\mu(v_\mu + a_\mu\gamma_5)q - \bar{q}(s - ip\gamma_5)q. \quad (3.33)$$

The external sources transform according to

$$\begin{aligned} (s + ip) &\xrightarrow{G} R(s + ip)L^\dagger \\ l^\mu &\xrightarrow{G} L l^\mu L^\dagger + iL\partial^\mu L^\dagger \\ r^\mu &\xrightarrow{G} L R r^\mu R^\dagger + iR\partial^\mu R^\dagger. \end{aligned} \quad (3.34)$$

The part of the Lagrangian  $\mathcal{L}_{QCD}^0$  is the one in (3.1), where the quark masses are set to zero. This Lagrangian must be invariant under local chiral transformation [55]. In order to take those external sources into account in the chiral Lagrangian, we define the covariant derivatives

$$D_\mu U = \partial_\mu U - ir_\mu U + iUl_\mu. \quad (3.35)$$

Also, we generalize (3.28) to  $s$  and  $p$  and the Lagrangian becomes

$$\mathcal{L}^{(2)} = \frac{F^2}{4} \langle D^\mu U D_\mu U^\dagger + \chi U^\dagger + \chi^\dagger U \rangle. \quad (3.36)$$

where  $\chi = 2B_0(s + ip)$ . At this point, the only two parameters of the theory are  $F$  and  $B_0$ . As already stated above,  $F$  can be related to the pion decay constant. In order to determine  $B_0$ , consider the QCD generating functional in the path-integral formulation [56]  $Z[v, a, s, p]$ . The Green's function can be obtained by taking the functional derivative with respect to the fields of interest. We have

$$\langle 0 | \psi \psi | 0 \rangle = \frac{\delta Z[v, a, s, p]}{\delta s} = -F^2 B_0. \quad (3.37)$$

Thus,  $B_0$  is directly related to the quark condensate. Note that relations (3.22) can be obtained in a similar way using this more general framework.

### 3.6 Weinberg's power counting

Since ChPT is a quantum field theory, loop corrections must also be taken into account. If it was not the case, only tree-level diagrams would contribute to transition amplitudes. Those would therefore be real quantities and unitarity would not be satisfied. In order for the optical theorem to be fulfilled, loop corrections can not be ignored.

There are in principle an infinite number of loops that one can imagine from the Lagrangian (3.36). Contrary to QED, each loop does not come along with a small coupling constant that can be used as a expansion parameter. The Weinberg's power counting allows to properly include those in the theory order by order in the small-momentum expansion. Let us consider an arbitrary diagram  $M$  with  $L$  loops,  $I$  internal propagators and  $V_k$  vertices of order  $2k$ . The amplitude expressed in powers of momenta is

$$M \propto \int (d^4 p)^L \left( \frac{1}{p^2} \right)^I \prod_k (p^{2k})^{V_{2k}}. \quad (3.38)$$

Consequently, Its order in the expansion is

$$\begin{aligned} D &= 4L - 2I + \sum_{k=1} 2k V_{2k} \\ &= 2 + 2L + \sum_{k=1} (2k - 2) V_{2k} \end{aligned} \quad (3.39)$$

where the topological relation  $L = I + 1 - \sum_k V_{2k}$  was used. The first conclusion is that a loop is suppressed by two powers of  $p$ . Also, we note that the three terms on the right-hand side of the equation are positive ( $k \geq 1$ ). This means that only a finite number of topologies contribute at a given order  $D$ . At order  $D = 2$ , only tree-level diagrams with vertices of order  $p^2$  appear. One order higher, one-loop diagrams with only the lowest-order vertices contribute. At that order, vertices of order  $p^4$  must also be taken into account.

In the case where the loop diagrams carry an ultraviolet divergence, the coupling constants related to the corresponding higher-order operators are needed for the absorption of



the potential loop divergences and the renormalization of that specific order of the theory. Therefore, they depend on a renormalization scale. Naturally, this dependence must vanish in any observable. This has to be the case, since such an effective field theory must be renormalizable order by order.

In conclusion, unitarity and analyticity are perturbatively satisfied in ChPT. This is in the sense of an order-by-order momentum expansion. This will be shown explicitly in the case of the pion vector form factor and the  $\pi\pi$ -scattering amplitude in the corresponding chapters.

### 3.7 Electromagnetic contribution

In the presence of external electromagnetic sources, we can introduce two spurious fields  $Q_L$  and  $Q_R$  transforming as [2]

$$Q_I \rightarrow I Q_I I^\dagger \quad I \in \{L, R\}, \quad (3.40)$$

and use them as additional building blocks for the Lagrangian. Those account for the charge matrix of the three lightest quarks.

$$Q = \frac{e}{2} \left( \lambda_3 + \frac{1}{\sqrt{3}} \lambda_8 \right) = \frac{e}{3} \begin{pmatrix} 2 & 0 & 0 \\ 0 & -1 & 0 \\ 0 & 0 & -1 \end{pmatrix}. \quad (3.41)$$

The method is therefore similar to what has been discussed above for the quark mass matrix. One direct consequence of the inclusion of electromagnetic sources is the appearance of  $L_Q^\mu = A^\mu Q_L$  and  $R_Q^\mu = A^\mu Q_R$  in the covariant derivative (3.35).

In the chiral counting scheme, the electric charge scales as

$$e, Q \sim \mathcal{O}(p). \quad (3.42)$$

At lowest order,  $p^2$ , one additional operator made of those building blocks can be included into (3.36), namely

$$\mathcal{L}_e^2 = C \langle Q U Q U^\dagger \rangle. \quad (3.43)$$

This term in the Lagrangian is responsible for a splitting of the pion masses. We have

$$\Delta_{m_\pi} := m_{\pi^\pm}^2 - m_{\pi^0}^2 = 2C \frac{e^2}{F^2} + \mathcal{O}(m_q). \quad (3.44)$$

Note that the  $\mathcal{O}(m_q)$  correction is proportional to the quark mass difference. This is however very small compared to the electromagnetic contribution. In the chiral limit, the difference between charged and neutral pions (3.44) is identical to the difference between charged and neutral kaons. This is known as Dashen's theorem [57]. Of course this is only correct at order  $p^2$  and corrections can be calculated at higher orders [2].

### 3.8 Next-to-leading order Lagrangian

In the case of  $SU(2) \times SU(2)$  at order  $p^4$ , it is possible to construct 7 independent operators. The Lagrangian in this case is

$$\begin{aligned}
\mathcal{L}_{p^4} = & \frac{l_1}{4} \langle D^\mu U^\dagger D_\mu U \rangle^2 + \frac{l_2}{4} \langle D^\mu U^\dagger D^\nu U \rangle \langle D_\mu U^\dagger D_\nu U \rangle \\
& + \frac{l_3}{16} \langle \chi^\dagger U + U^\dagger \chi \rangle^2 + \frac{l_4}{4} \langle D^\mu U^\dagger D_\mu \chi + D^\mu U^\dagger D_\mu \chi + D^\mu \chi^\dagger D_\mu U \rangle \\
& + l_5 \langle G_{\mu\nu}^R U G^{L\mu\nu} U^\dagger \rangle + \frac{il_6}{2} \langle G_{\mu\nu}^R D^\mu U D^\nu U^\dagger + G_{\mu\nu}^L D^\mu U^\dagger D^\nu U \rangle \\
& - \frac{l_7}{16} \langle \chi^\dagger U - U^\dagger \chi \rangle^2 + \frac{1}{4} (h_1 + h_3) \langle \chi^\dagger \chi \rangle \\
& + \frac{1}{2} (h_1 - h_3) \text{Re}(\det \chi) - h_2 \langle G_{\mu\nu}^R G^{R\mu\nu} + G_{\mu\nu}^L G^{L\mu\nu} \rangle.
\end{aligned} \tag{3.45}$$

The field strength tensor was introduced as

$$G_{\mu\nu}^I = \partial_\mu \bar{I}_\nu - \partial_\nu \bar{I}_\mu - i[\bar{I}_\mu^I, \bar{I}_\nu^I] \quad I \in \{L, R\} \tag{3.46}$$

and  $\bar{I}^\mu = I^\mu + Q_I A^\mu$  are the external left- or right-handed vector sources.

Those newly introduced low-energy constants effectively result from the underlying QCD dynamics. They must be fixed by experimental data. Together with  $F$  and  $B_0$ ,  $l_1, \dots, l_7$  determine the low-energy behaviour of the pseudoscalar mesons. Note that  $h_1$ ,  $h_2$  and  $h_3$  are only coupled to external fields and have no physical significance.

In the case of  $SU(3) \times SU(3)$ , instead of the 7 low-energy constants  $l_i$  above, there are 10 constants that are conventionally defined as  $L_i$ . The fact that there are fewer constants in the case of  $SU(2)$  is due to trace relations causing dependences among the different operators.

Considering external electromagnetic sources, similarly to (3.43) and following the chiral ordering explained above, the Lagrangian can be extended further at order  $p^4$ . One can mix even powers of charges as follows in the case of the  $SU(2)$  Lagrangian:

$$\begin{aligned}
\mathcal{L}_{e^2 p^2} = & F^2 \left\{ k_1 \langle D^\mu U^\dagger D_\mu U \rangle \langle Q^2 \rangle + k_2 \langle D^\mu U^\dagger D_\mu U \rangle \langle QUQU^\dagger \rangle \right. \\
& + k_3 (\langle D^\mu U^\dagger QU \rangle \langle D_\mu U^\dagger QU \rangle + \langle D^\mu U QU^\dagger \rangle \langle D_\mu U QU^\dagger \rangle) \\
& + k_4 \langle D^\mu U^\dagger QU \rangle \langle D_\mu U QU^\dagger \rangle + k_5 \langle \chi^\dagger U + U^\dagger \chi \rangle \langle Q^2 \rangle \\
& + k_6 \langle \chi^\dagger U + U^\dagger \chi \rangle \langle QUQU^\dagger \rangle \\
& + k_7 \langle (\chi U^\dagger + U \chi^\dagger) Q + (\chi^\dagger U + U^\dagger \chi) Q \rangle \langle Q \rangle \\
& + k_8 \langle (\chi U^\dagger - U \chi^\dagger) QUQU^\dagger + (\chi^\dagger U - U^\dagger \chi) QU^\dagger QU \rangle \\
& + k_9 \langle D_\mu U^\dagger [(c_R^\mu Q), Q] U + D_\mu U [(c_L^\mu Q), Q] U^\dagger \rangle \\
& + k_{10} \langle (c_R^\mu Q) U (c_{L\mu} Q) U^\dagger \rangle \\
& \left. + k_{11} \langle (c_R^\mu Q) (c_{R\mu} Q) + (c_L^\mu Q) (c_{L\mu} Q) \rangle \right\}.
\end{aligned} \tag{3.47}$$

We defined the covariant derivative of the spurious sources as

$$c_\mu^I Q_I = \partial_\mu Q_I - i[\bar{I}_\mu, Q_I] \quad I \in \{L, R\}. \tag{3.48}$$

There are also operators proportional to  $e^4$ . The corresponding Lagrangian is

$$\mathcal{L}_{e^4} = F^4 \left\{ k_{12} \langle Q^2 \rangle^2 + k_{13} \langle QUQU^\dagger \rangle \langle Q^2 \rangle + k_{14} \langle QUQU^\dagger \rangle^2 \right\}. \quad (3.49)$$

It is also important to add that the Lagrangian constructed that way contains a larger symmetry than in nature. Indeed, by construction, it is of even intrinsic parity. For instance it is not possible to describe an odd intrinsic parity process as a pion decaying into two photons. That is why we also have to include into the ChPT Lagrangian the anomalous Wess-Zumino-Witten term [58] that in the case of the decay of a pseudoscalar Goldstone boson into two vector sources is

$$\mathcal{L}_{\phi vv} = -\frac{N_C}{12\sqrt{2}\pi^2 F} \langle \partial_\mu \phi v_\nu \partial_\alpha v_\beta \rangle \epsilon^{\mu\nu\alpha\beta}. \quad (3.50)$$

### 3.9 Resonance saturation

Chiral perturbation theory works best at very low energy ( $E \ll 1 \text{ GeV}$ ). As seen above, the interaction of the Goldstone fields is determined up to some low energy constants by their non-linear realization with  $G$ .

A theory describing interactions from heavier states (resonances), later called Resonance Chiral Theory (RChT), was introduced in the seminal paper [59]. It is a useful complementary tool to ChPT to study pseudoscalar interactions. It allows to extend the region of validity of the theory, by taking into account heavier degrees of freedom consistent with the symmetry of the system [60].

We start by introducing a new field  $u$  for the Goldstone boson field. It is defined as the square root of  $U$ :  $u^2 := U$  and transforms under  $G$  as

$$u \xrightarrow{G} R u h^\dagger = h u L^\dagger. \quad (3.51)$$

The so-called compensator field  $h(L, R, U)$  depends non-trivially on  $L$ ,  $R$  and  $U$  and is the main ingredient for the non-linear realization. The additional degrees of freedom we are interested in transform either as octets or as singlets under  $G$ :

$$R \xrightarrow{G} h R h^\dagger, \quad (3.52)$$

$$R_0 \xrightarrow{G} R_0. \quad (3.53)$$

The octet fields can be chosen to be in a Gell-Mann matrix representation

$$R = \sum_{a=1}^8 \frac{\lambda_a}{\sqrt{2}} R_a. \quad (3.54)$$

For simplicity, the types of fields considered,  $R(J^{PC})$ , is restricted to the scalar, pseudoscalar, vector and axial  $S(0^{++})$ ,  $P(0^{-+})$ ,  $V(1^{--})$  and  $A(1^{++})$ . Also, the spin-1 fields are both described in term of antisymmetric tensors, following the formalism of [61].

As in the case of ChPT, one can then construct the most general Lagrangian order by order by adding all possible operators invariant under the symmetry. The RChT Lagrangian is therefore

$$\mathcal{L}_{res} = \sum_R [\mathcal{L}_{kin}(R) + \mathcal{L}_2(R) + \mathcal{L}_4(R) + \dots], \quad (3.55)$$

where the kinetic Lagrangians of the octets are

$$\mathcal{L}_{kin}(R = V, A) = -\frac{1}{2}\langle\nabla^\lambda R_{\lambda\mu}\nabla_\nu R^{\nu\mu} - \frac{1}{2}M_R^2 R_{\mu\nu}R^{\mu\nu}\rangle, \quad (3.56)$$

$$\mathcal{L}_{kin}(R = S, P) = \frac{1}{2}\langle\nabla^\mu R\nabla_{\mu\nu}R - M_R^2 R^2\rangle \quad (3.57)$$

and the lowest order interaction Lagrangians are

$$\begin{aligned} \mathcal{L}_2(V) &= \frac{F_V}{2\sqrt{2}}\langle V_{\mu\nu}f_+^{\mu\nu}\rangle + \frac{iG_V}{\sqrt{2}}\langle V_{\mu\nu}u^\mu u^\nu\rangle, \\ \mathcal{L}_2(A) &= \frac{F_A}{2\sqrt{2}}\langle A_{\mu\nu}f_-^{\mu\nu}\rangle, \\ \mathcal{L}_2(P) &= id_m\langle P\chi_- \rangle + i\tilde{d}_m P_0\langle\chi_- \rangle, \\ \mathcal{L}_2(S) &= c_d\langle Su_\mu u^\mu\rangle + c_m\langle S\chi_+ \rangle + \tilde{c}_d S_0\langle u_\mu u^\mu\rangle + \tilde{c}_m S_0\langle\chi_+ \rangle. \end{aligned} \quad (3.58)$$

In the previous relation, the following building blocks transforming as well as octets under  $G$  have been used

$$\begin{aligned} u_\mu &= i\left(u^\dagger(\partial_\mu - ir_\mu)u - u(\partial_\mu - il_\mu)u^\dagger\right), \\ \chi_\pm &= u^\dagger\chi u^\dagger \pm u\chi^\dagger u, \\ f_\pm^{\mu\nu} &= uF_L^{\mu\nu}u^\dagger \pm u^\dagger F_R^{\mu\nu}u, \\ h_{\mu\nu} &= \nabla_\mu u_\nu + \nabla_\nu u_\mu, \\ \nabla_\mu X &= \partial_\mu X + [\Gamma_\mu, X], \\ \Gamma_\mu &= \frac{1}{2}\left(u^\dagger(\partial_\mu - ir_\mu)u + u(\partial_\mu - il_\mu)u^\dagger\right), \end{aligned} \quad (3.59)$$

The different constants in (3.58) must be fixed from experimental data. For instance,  $F_V$  and  $G_V$  are respectively extracted from the decay rates  $\Gamma(\rho^0 \rightarrow e^+e^-)$  and  $\Gamma(\rho^0 \rightarrow 2\pi)$ .

One can extend the procedure at the next orders. This was done in [62] in the case of even intrinsic parity and in [63] in the case of odd intrinsic parity.

Assuming that the pseudoscalar interactions of chiral perturbation theory are only due to resonance exchanges, it was shown that the experimental value of the LECs can be well reproduced. In other words, the constants are completely saturated by those resonances reflecting the underlying dynamics at higher energy.

As an additional remark, we note that it is also possible to include baryons in the theory in a similar way. Even though those particles are very heavy, the expansion is done in their momenta which remain small at low energy. Note that in that case, odd powers of derivative are also present in the Lagrangian because of the Dirac structure (spin 1/2 particles). Such an extension of the theory is however beyond the scope of this thesis.

## Chapter 4

# Pion-pion scattering

The  $\pi\pi$ -scattering amplitude plays a central role in this thesis. At low energy, hadronic interactions are dominated by pion exchanges and rescattering effects are important. In the following chapter, we introduce the main properties of the  $\pi\pi$ -scattering amplitudes and present explicit representations used in the calculation.

### 4.1 Kinematics

Let us consider a pion-pion scattering process  $\pi(p_1)\pi(p_2) \rightarrow \pi(p_3)\pi(p_4)$ . The pions have masses  $m_\pi$  and four-momenta  $p_i = (E_i, \mathbf{p}_i)$   $i \in \{1, 2, 3, 4\}$ . All four external pions have the same mass in the isospin limit,

$$p_i^2 = m_\pi^2 = E_i^2 - \mathbf{p}_i^2 \quad i \in \{1, 2, 3, 4\}. \quad (4.1)$$

The Mandelstam variables of the scattering process are

$$\begin{aligned} s &= (p_1 + p_2)^2 = (p_3 + p_4)^2 \\ t &= (p_1 - p_3)^2 = (p_2 - p_4)^2 \\ u &= (p_1 - p_4)^2 = (p_2 - p_3)^2. \end{aligned} \quad (4.2)$$

Because of the on-shell relation

$$s + t + u = \sum_{i=1}^4 m_i^2 = 4m_\pi^2, \quad (4.3)$$

the scattering amplitude depends on two out of the three invariant Mandelstam variables additionally to the masses of the particles. This statement is very general and is valid for any two-particles scattering amplitude.

### 4.2 Multipion states

In the isospin limit, the three pion states form an isotriplet. One possible basis for their representation is the physical basis, where each of the three differently charged pions has

a well-defined  $I_3$  component. Using the notation  $|I, I_3\rangle$  where  $I$  is the total isospin and  $I_3$  its third component, we have

$$\begin{aligned} |\pi^-\rangle &= |1, -1\rangle, \\ |\pi^0\rangle &= |1, 0\rangle, \\ |\pi^+\rangle &= -|1, 1\rangle. \end{aligned} \tag{4.4}$$

It may be convenient to use an alternative basis to work in the isospin limit. The latter is formed by three elements  $|\pi^i\rangle, i \in \{1, 2, 3\}$  and their relation with the physical basis is (see for instance [64])

$$\begin{aligned} |\pi^-\rangle &= \frac{1}{\sqrt{2}}(|\pi^1\rangle - i|\pi^2\rangle) \\ |\pi^+\rangle &= \frac{1}{\sqrt{2}}(|\pi^1\rangle + i|\pi^2\rangle) \\ |\pi^0\rangle &= |\pi^3\rangle. \end{aligned} \tag{4.5}$$

Once the third isospin component of each element of the basis is known, one can construct the two-particle states. To that end, we take the direct products of two one-particle states

$$|\pi^i \pi^j\rangle = |\pi^i\rangle \otimes |\pi^j\rangle. \tag{4.6}$$

A product of states  $|j_1, m_1\rangle \otimes |j_2, m_2\rangle \equiv |j_1, j_2; m_1, m_2\rangle$  can be expressed as a linear combination of states of total isospin  $|J, m\rangle$  according to

$$|j_1, j_2; m_1, m_2\rangle = \sum_{J, M} \langle J, M | j_1, j_2; m_1, m_2 \rangle |J, M\rangle. \tag{4.7}$$

We find the decomposition by reading off the corresponding Clebsch-Gordan coefficient  $\langle J, M | j_1, j_2; m_1, m_2 \rangle$  for each of them. We find

$$\begin{aligned} |\pi^+ \pi^-\rangle &= -\sqrt{\frac{1}{6}}|2, 0\rangle - \sqrt{\frac{1}{2}}|1, 0\rangle - \sqrt{\frac{1}{3}}|0, 0\rangle \\ |\pi^-\pi^+\rangle &= -\sqrt{\frac{1}{6}}|2, 0\rangle + \sqrt{\frac{1}{2}}|1, 0\rangle - \sqrt{\frac{1}{3}}|0, 0\rangle \\ |\pi^0 \pi^0\rangle &= \sqrt{\frac{2}{3}}|2, 0\rangle - \sqrt{\frac{1}{3}}|0, 0\rangle \\ |\pi^+ \pi^0\rangle &= -\sqrt{\frac{1}{2}}|2, 1\rangle - \sqrt{\frac{1}{2}}|1, 1\rangle \\ |\pi^0 \pi^+\rangle &= -\sqrt{\frac{1}{2}}|2, 1\rangle + \sqrt{\frac{1}{2}}|1, 1\rangle \\ |\pi^-\pi^0\rangle &= \sqrt{\frac{1}{2}}|2, -1\rangle - \sqrt{\frac{1}{2}}|1, -1\rangle \\ |\pi^0 \pi^-\rangle &= \sqrt{\frac{1}{2}}|2, -1\rangle + \sqrt{\frac{1}{2}}|1, -1\rangle \\ |\pi^-\pi^-\rangle &= |2, -2\rangle \\ |\pi^+ \pi^+\rangle &= |2, 2\rangle. \end{aligned} \tag{4.8}$$

### 4.3 Isospin amplitudes

Because of isospin conservation, a process can be described in terms of the so-called isospin amplitudes  $T^I(s, t, u)$ . Let us consider the scattering process  $a + b \rightarrow c + d$  in the  $s$  channel. The corresponding amplitude can be written as

$$\begin{aligned}\langle c; d | T_s | a; b \rangle &= \sum_{I, J} \langle c; d | I, m \rangle \langle I, m | T_s | J, m \rangle \langle J, m | a; b \rangle \\ &= (2\pi)^4 \delta^{(4)} \left( \sum_i p_i \right) c_{c; d}^I c_{a; b}^I T^I(s, t, u).\end{aligned}\quad (4.9)$$

In the last line, we have defined the Clebsch-Gordon coefficients as  $\langle I, m | a; b \rangle =: c_{a; b}^I$ . Note that in the relation above, the  $T$ -matrix of the process in the  $s$ -channel has been written as  $T_s$  to avoid confusion with the isospin amplitude. We apply this method to the different two-pion states above. The physical pion-pion scattering amplitudes can then be related to the isospin amplitude as

$$\begin{aligned}T(\pi^+ \pi^+ \rightarrow \pi^+ \pi^+) &= T(\pi^- \pi^- \rightarrow \pi^- \pi^-) = T^2, \\ T(\pi^+ \pi^- \rightarrow \pi^+ \pi^-) &= \frac{1}{3}T^0 + \frac{1}{2}T^1 + \frac{1}{6}T^2, \\ T(\pi^+ \pi^0 \rightarrow \pi^+ \pi^0) &= \frac{1}{2}T^1 + \frac{1}{2}T^2, \\ T(\pi^+ \pi^- \rightarrow \pi^0 \pi^0) &= \frac{1}{3}T^0 - \frac{1}{3}T^2, \\ T(\pi^0 \pi^0 \rightarrow \pi^0 \pi^0) &= \frac{1}{3}T^0 + \frac{2}{3}T^2.\end{aligned}\quad (4.10)$$

A central property of the isospin amplitude of a  $\pi\pi$  scattering process is crossing symmetry. It is due to the fact that in the isospin limit, all of the three physical pions have the same mass. It allows to relate a process in one of the three channels to the others. Using the alternative convention for the isospin basis, the pion-pion scattering amplitude can be written as

$$\langle \pi^a(p_1) \pi^b(p_2) | T | \pi^c(p_3) \pi^d(p_4) \rangle = A(s, t, u) \delta^{ab} \delta^{cd} + B(s, t, u) \delta^{ac} \delta^{bd} + C(s, t, u) \delta^{ad} \delta^{bc}.\quad (4.11)$$

Note that because of crossing symmetry,  $B(s, t, u) = A(t, s, u)$  and  $C(s, t, u) = A(u, t, s)$ . We can directly relate the functions  $A(s, t, u)$ ,  $B(s, t, u)$  and  $C(s, t, u)$  to physical processes with the definition (4.5). We find

$$\begin{aligned}\langle \pi^+ \pi^- | \pi^0 \pi^0 \rangle &= A(s, t, u), \\ \langle \pi^+ \pi^0 | \pi^0 \pi^+ \rangle &= B(s, t, u), \\ \langle \pi^0 \pi^- | \pi^- \pi^0 \rangle &= C(s, t, u).\end{aligned}\quad (4.12)$$

Using relation (4.10) above, we can then relate the scalar functions to the isospin amplitudes  $T^I(s, t, u)$ :

$$\begin{aligned}T^0(s, t, u) &= 3A(s, t, u) + B(s, t, u) + C(s, t, u), \\ T^1(s, t, u) &= B(s, t, u) - C(s, t, u), \\ T^2(s, t, u) &= B(s, t, u) + C(s, t, u),\end{aligned}\quad (4.13)$$

and equivalently

$$\begin{aligned}
A(s, t, u) &= \frac{1}{3} (T^0(s, t, u) - T^2(s, t, u)) , \\
B(s, t, u) &= \frac{1}{2} (T^1(s, t, u) + T^2(s, t, u)) , \\
C(s, t, u) &= \frac{1}{2} (T^1(s, t, u) - T^2(s, t, u)) .
\end{aligned} \tag{4.14}$$

From there, it is possible to relate the isospin amplitudes of the  $s$ -channel to those of the  $t$ -channel by noting that  $A(s, t, u) = B(t, s, u)$  and  $C(s, t, u) = C(t, s, u)$ . We then find, using the notation  $T^I(t, s, u) = T_t^I$ ,  $T^I(u, t, s) = T_u^I$

$$\begin{aligned}
T_t^0 &= \frac{1}{3} T_s^0 + T_s^1 + \frac{5}{3} T_s^2 \\
T_t^1 &= \frac{1}{3} T_s^0 + \frac{1}{2} T_s^1 - \frac{5}{6} T_s^2 \\
T_t^2 &= \frac{1}{3} T_s^0 - \frac{1}{2} T_s^1 + \frac{1}{6} T_s^2 ,
\end{aligned} \tag{4.15}$$

or written in a more compact way using the so-called crossing matrices,

$$\begin{aligned}
T_t &= C_{st} T_s \quad , \quad C_{st} = \begin{pmatrix} 1/3 & 1 & 5/3 \\ 1/3 & 1/2 & -5/6 \\ 1/3 & -1/2 & 1/6 \end{pmatrix} , \\
T_u &= C_{su} T_s \quad , \quad C_{su} = \begin{pmatrix} 1/3 & -1 & 5/3 \\ -1/3 & 1/2 & 5/6 \\ 1/3 & 1/2 & 1/6 \end{pmatrix} , \\
T_t &= C_{ut} T_u \quad , \quad C_{ut} = \begin{pmatrix} 1 & 0 & 0 \\ 0 & -1 & 0 \\ 0 & 0 & 1 \end{pmatrix} .
\end{aligned} \tag{4.16}$$

Note that  $C_{st}^2 = C_{su}^2 = C_{ut}^2 = 1$ . Using those relations, we can also relate directly the amplitudes with well-defined isospin in  $t$ -channel to  $A(s, t, u)$ ,  $B(s, t, u)$  and  $C(s, t, u)$  as

$$\begin{aligned}
A(s, t, u) &= \frac{1}{2} (T_t^1 + T_t^2) , \\
B(s, t, u) &= \frac{1}{3} (T_t^0 - T_t^2) , \\
C(s, t, u) &= \frac{1}{2} (T_t^2 - T_t^1) .
\end{aligned} \tag{4.17}$$

## 4.4 Partial-wave representation

It is very useful to express the pion-pion scattering amplitude as a partial wave expansion. We choose the usual normalization convention and write the isospin amplitudes as

$$\begin{aligned}
T^I(s, t) &= 32\pi \sum_{\ell \text{ even}} (2\ell + 1) P_\ell(z) t_\ell^I(s) \quad , \quad I \text{ even}, \\
T^I(s, t) &= 32\pi \sum_{\ell \text{ odd}} (2\ell + 1) P_\ell(z) t_\ell^I(s) \quad , \quad I \text{ odd}.
\end{aligned} \tag{4.18}$$



The Legendre polynomials  $P_\ell(z)$  depend on the scattering angle  $\theta_s$  in the center-of-mass frame of  $s$ . The latter depends on the momentum-transfer variables  $t$  and  $u$  via the simplified relation

$$z = \cos \theta = 1 + \frac{2t}{(s - 4m_\pi^2)} = -1 - \frac{2u}{(s - 4m_\pi^2)}. \quad (4.19)$$

Because of the choice of normalization, there is an additional factor in the projection of the isospin amplitude on a particular partial wave:

$$t_\ell^I(s) = \frac{1}{64\pi} \int_{-1}^1 dz T^I(s, t(z)) P_\ell(z). \quad (4.20)$$

The unitarity relation (2.27) for the  $\pi\pi$ -scattering partial waves can be written in a very compact form. This is due to fact that the initial and final state are identical. Also the two pions in each state have the same mass, which simplifies the kinematics. In the purely elastic case, we only consider a pair of pions in the intermediate state. In that case, the fraction containing the Källén function reduces to the threshold function  $\sigma_\pi$ . Taking into account the normalization factor, the imaginary part of a partial wave is

$$\text{Im} t_\ell^I(s) = \sigma_\pi(s) |t_\ell^I(s)|^2. \quad (4.21)$$

And thus, there is a diagonal relation between the imaginary part of the partial wave and its modulus squared. Below the inelasticity threshold which is the two-kaon threshold in the case of  $\pi\pi$  scattering, the partial waves can thus be expressed as a function of their corresponding phase-shift uniquely:

$$t_\ell^I(s) = |t_\ell^I(s)| e^{i\delta_\ell^I(s)} = \frac{e^{i\delta_\ell^I(s)} \sin \delta_\ell^I(s)}{\sigma_\pi(s)} = \frac{e^{2i\delta_\ell^I(s)} - 1}{2i\sigma_\pi(s)}. \quad (4.22)$$

This relation can be generalized to the inelastic region by introducing an inelasticity function  $\eta_\ell^I(s)$  with the property  $\eta_\ell^I(s) \leq 1$ . The generalization reads

$$t_\ell^I(s) = \frac{e^{2i\delta_\ell^I(s)} \eta_\ell^I(s) - 1}{2i\sigma_\pi(s)}. \quad (4.23)$$

In the limit  $\eta_\ell^I(s) \rightarrow 1$ , we recover the elastic relation (4.22).

A parametrization of the  $\pi\pi$ -scattering partial waves  $t_\ell^I(s)$  has been calculated by different groups for  $I \in \{0, 1, 2\}$ ,  $\ell \in \{0, 1, 2, 3\}$  (see for instance [65] or [66]). Their analysis is based on a self-consistent solution of Roy equations and is valid from threshold to  $s_{max} = 1.42\text{GeV}^2$ . Above that point, they rely on a Regge description. The partial waves are reconstructed from the phase-shifts and the inelasticity functions via relation (4.23).

In this thesis, the S0- and P-waves are central building blocks since they dominate at low energy. The phase-shift and inelasticity function of the S0-wave are plotted respectively in figure 4.1 and 4.2 [67]. The inelasticity in this case becomes important around  $1\text{GeV}^2$ , at the  $K\bar{K}$  creation threshold. Concerning the P-wave, the inelasticity function differs very slightly from 1 and the phase-shift is plotted in figure 4.3. The abrupt transition at  $s \approx 0.6\text{GeV}^2$  is due to the  $\rho(770)$  resonance and is responsible for a substantial peak in the partial wave. The waves with higher angular momentum (D, F, ...) are not important at low energy.

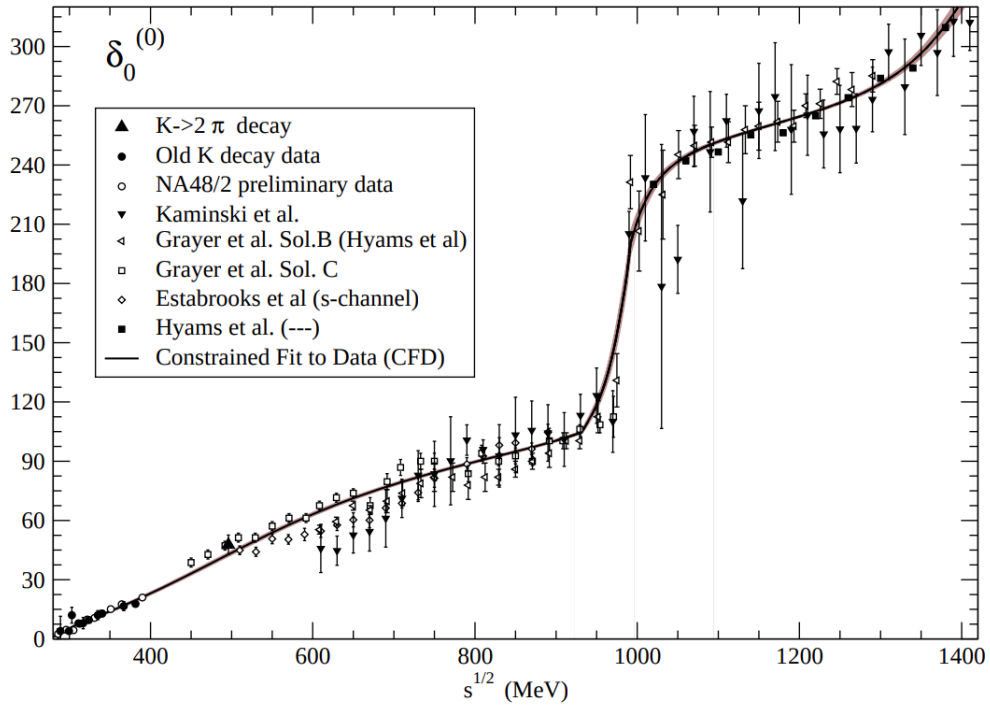


Figure 4.1: Phase-shift of the  $\pi\pi$  scattering S0-wave [65]

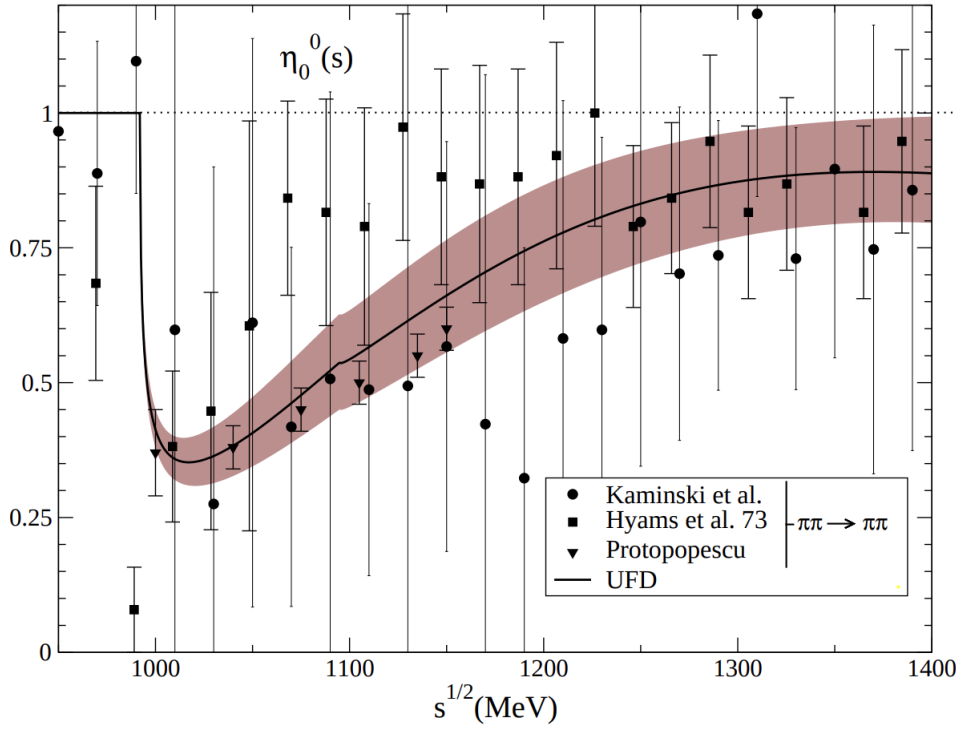


Figure 4.2: inelasticity of the  $\pi\pi$  scattering S0-wave [65]

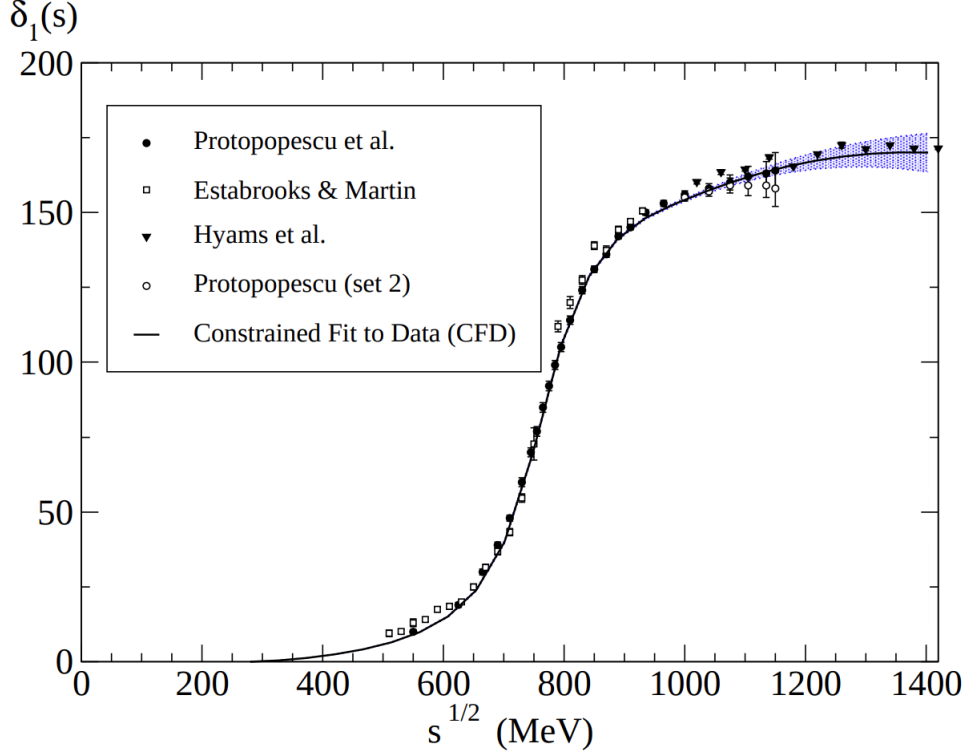


Figure 4.3: Phase-shift of the  $\pi\pi$  scattering P-wave [67]

## 4.5 Phenomenological amplitude

There is an other practical way to represent the  $\pi\pi$ -scattering amplitude. It is called phenomenological representation since based on experimental results [68]. The idea is that up to  $\mathcal{O}(p^8)$  in the chiral counting, the imaginary part of the partial waves of the two-loop representation in ChPT only gets contribution from S- and P-waves. The partial waves of the two-loop representation can be expanded into a series

$$t_\ell^I(s) = t_\ell^I(s)_2 + t_\ell^I(s)_4 + t_\ell^I(s)_6 + \mathcal{O}(p^8). \quad (4.24)$$

The first term of order  $p^2$  comes from the tree-level and is non-zero only for the S- and P-waves. The imaginary part of the partial waves is calculated from (2.24), neglecting contributions at order  $p^8$ . Plugging in the expansion (4.24) into the unitarity relation, we can calculate the imaginary part as

$$\text{Im} t_\ell^I(s) = \sigma_\pi(s) t_\ell^I(s)_2 (t_\ell^I(s)_2 + 2\text{Re} t_\ell^I(s)_4) + \mathcal{O}(p^8). \quad (4.25)$$

Note that  $t_\ell^I(s)_2 \in \mathbb{R}$ . Since  $t_\ell^I(s)_2 = 0$  for  $\ell \geq 2$ , this shows that partial waves from the D wave and above only appear at order  $p^8$ . This means that they can be expanded in Taylor series of the momenta. This is not the case for the S- and P-waves which appear in the form of unitarity corrections. Using the isospin relations (4.10), and assuming that the imaginary part of the partial waves as well as the scattering lengths  $a_0^0$  and  $a_0^2$  are known, one can write the amplitude as a function of only three single-variable functions and a

polynomial:

$$\begin{aligned}
A(s, t, u) = & 16\pi a_0^2 + \frac{4\pi}{3m_\pi^2} (2a_0^0 - 5_0^2)s + \bar{P}(s, t, u) \\
& + 32\pi \left\{ \frac{1}{3}\bar{W}^0(s) + \frac{3}{2}(s-u)\bar{W}^1(t) + \frac{3}{2}(s-t)\bar{W}^1(u) \right. \\
& \left. + \frac{1}{2}\bar{W}^2(t) + \frac{1}{2}\bar{W}^2(u) - \frac{1}{3}\bar{W}^2(s) \right\} + \mathcal{O}(p^8). \tag{4.26}
\end{aligned}$$

The functions  $\bar{W}^i$  are four-times subtracted dispersive integrals of the imaginary part of the S- and P-waves:

$$\begin{aligned}
\bar{W}^0(s) &= \frac{s^4}{\pi} \int_{4m_\pi^2}^{\infty} ds' \frac{\text{Im}t_0^0(s')}{s'^4(s' - s)}, \\
\bar{W}^1(s) &= \frac{s^3}{\pi} \int_{4m_\pi^2}^{\infty} ds' \frac{\text{Im}t_1^1(s')}{s'^3(s' - 4m_\pi^2)(s' - s)}, \\
\bar{W}^2(s) &= \frac{s^4}{\pi} \int_{4m_\pi^2}^{\infty} ds' \frac{\text{Im}t_0^2(s')}{s'^4(s' - s)}. \tag{4.27}
\end{aligned}$$

The contribution from the waves with  $\ell \geq 2$  is contained into the polynomial

$$\bar{P}(s, t, u) = \bar{p}_1 + \bar{p}_2 s + \bar{p}_3 s^2 + \bar{p}_4 (t - u)^2 + \bar{p}_5 s^3 + \bar{p}_6 s(t - u)^2, \tag{4.28}$$

where the different coefficients  $\bar{p}_i$  are given by

$$\begin{aligned}
\bar{p}_1 &= -128\pi m_\pi^4 (\bar{I}_0^1 + \bar{I}_0^2 + 2m_\pi^2 \bar{I}_1^1 + 2m_\pi^2 \bar{I}_1^2 + 8m_\pi^4 \bar{I}_2^2) \\
\bar{p}_2 &= -\frac{64\pi m_\pi^2}{3} (2\bar{I}_0^0 - 6\bar{I}_0^1 - 2\bar{I}_0^2 - 15m_\pi^2 \bar{I}_1^1 - 3m_\pi^2 \bar{I}_1^2 - 36m_\pi^4 \bar{I}_2^2 + 6m_\pi^2 H) \\
\bar{p}_3 &= -\frac{8\pi}{3} (4\bar{I}_0^0 - 9\bar{I}_0^1 - \bar{I}_0^2 - 16m_\pi^2 \bar{I}_1^0 - 42m_\pi^2 \bar{I}_1^1 + 22m_\pi^2 \bar{I}_1^2 - 72m_\pi^4 \bar{I}_2^2 + 24m_\pi^2 H) \\
\bar{p}_4 &= 8\pi (\bar{I}_0^1 + \bar{I}_0^2 + 2m_\pi^2 \bar{I}_1^1 + 2m_\pi^2 \bar{I}_1^2 - 24m_\pi^4 \bar{I}_2^2) \\
\bar{p}_5 &= -\frac{4\pi}{3} (8\bar{I}_1^0 + 9\bar{I}_1^1 - 11\bar{I}_1^2 - 32m_\pi^2 \bar{I}_2^0 + 44m_\pi^2 \bar{I}_2^2 - 6H) \\
\bar{p}_6 &= 4\pi (\bar{I}_1^1 - 3\bar{I}_1^2 + 12m_\pi^2 \bar{I}_2^2 + 2H) \tag{4.29}
\end{aligned}$$

The quantities  $\bar{I}_n^I$  and  $H$  are the following dispersive integrals

$$\begin{aligned}
\bar{I}_n^I &= \sum_{\ell=0}^{\infty} \frac{(2\ell+1)}{\pi} \int_{4m_\pi^2}^{\infty} ds \frac{\text{Im}t_\ell^I(s)}{s^{n+2}(s - 4m_\pi^2)}, \\
H &= \sum_{\ell=2}^{\infty} (2\ell+1)\ell(\ell+1) \frac{1}{\pi} \int_{4m_\pi^2}^{\infty} ds \frac{2\text{Im}t_\ell^0(s) + 4\text{Im}t_\ell^2(s)}{9s^3(s - 4m_\pi^2)} \tag{4.30}
\end{aligned}$$

In practice, we truncate the series and waves with  $\ell > 2$  are neglected. The imaginary part of the partial waves is taken from the parametrization of the previous section.

## 4.6 Radiative corrections of the $\pi\pi$ -scattering amplitude in ChPT

The radiative correction to the process  $\pi^+\pi^- \rightarrow \pi^+\pi^-$  has been calculated in [8] and is expressed as a linear combination of Passarino-Veltman loop functions. The explicit expression defined as  $A^{+-;+-}(s, t, u)$  is

$$A^{+-;+-}(s, t, u) = \left\{ \frac{s - m_{\pi^0}^2}{F^2} + B^{+-;+-}(s, t, u) + C^{+-;+-}(s, t, u) + e^2 \left( \frac{u - t}{s} \right) F_v^\pi(s)^2 \right\} + \{s \leftrightarrow t\} \quad (4.31)$$

$$\begin{aligned} B^{+-;+-}(s, t, u) &= \frac{1}{2F^4}(s - m_{\pi^0}^2)\bar{J}_{00}(s) \\ &+ \frac{1}{F^4} \left[ \frac{s^2}{4} - \frac{1}{12}(u - t)(s - 4m_\pi^2) + 2s\Delta_\pi + 4\Delta_\pi^2 \right] \bar{J}_{+-}(s) \\ &+ \frac{1}{4F^4}(u - 2m_\pi^2 - 2\Delta_\pi)(u - 2m_\pi^2 - 2\Delta_\pi - 4e^2F^2)\bar{J}_{+-}(u) \\ &+ \frac{2e^2}{F^2}(u - 2m_\pi^2 - 2\Delta_\pi) [2(s - 2m_\pi^2)G_{+-\gamma}(s) - (u - 2m_\pi^2)G_{+-\gamma}(u)] \\ &- \frac{e^2}{F^2} \left[ s + 4\Delta_\pi - 4(s - 2m_\pi^2) \left( \frac{t - u}{t + u} \right) \right] \bar{J}_{+-}(s) \end{aligned} \quad (4.32)$$

$$\begin{aligned} C^{+-;+-}(s, t, u) &= \frac{s - m_{\pi^0}^2}{F^2} \frac{e^2}{32\pi^2} \left[ -18 - 8 \left( 1 + \log \frac{m_\gamma^2}{m_\pi^2} \right) + \frac{1}{2}(K^{+-;+-} - K^{++;++}) \right] \\ &+ \frac{e^2 m_{\pi^0}^2}{32\pi^2 F^2} \left[ 10 + \frac{1}{2}(K^{+-;+-} + K^{++;++}) \right] - \frac{e^2}{2\pi^2 F^2} (s - 2m_\pi^2) \left( \frac{t - u}{t + u} \right) \\ &\frac{1}{48\pi^2 F^4} [(s - 2m_\pi^2)^2(\bar{l}_1 + \bar{l}_2) + (u - 2m_\pi^2)^2\bar{l}_2] - \frac{m_{\pi^0}^4}{32\pi^2 F^4} \bar{l}_3 \\ &+ \frac{1}{16\pi^2 F^4} \left( -\frac{5}{18}u^2 - \frac{13}{18}s^2 + \frac{2}{3}um_\pi^2 + \frac{19}{6}u\Delta_\pi + \frac{5}{18}m_{\pi^0}^4 - \frac{58}{9}m_{\pi^0}^2\Delta_\pi \right) \\ &- \frac{1}{96\pi^2 F^4} \frac{\Delta_\pi}{m_{\pi^0}^2} (-3s^2 + 16sm_\pi^2 + 2um_\pi^2 - 23m_{\pi^0}^4) \end{aligned} \quad (4.33)$$

In this expression,  $\bar{J}_{+-}(s)$  is the Passarino-Veltman function  $B_0$  with all masses equal to the charged-pion masses and subtracted at zero.

$$\begin{aligned} J_{PQ}(q^2) &\equiv B_0(s, m_P^2, m_Q^2) \\ &= \frac{1}{i} \int \frac{d^4k}{(2\pi)^4} \frac{1}{k^2 - m_P^2} \frac{1}{(k - q)^2 - m_Q^2}, \end{aligned} \quad (4.34)$$

$$\bar{J}_{PQ}(q^2) = J_{PQ}(q^2) - J_{PQ}(0). \quad (4.35)$$

The function  $G_{+-\gamma}$  is the Passarino-Veltman  $C_0$ -function already defined in (2.33) where all masses are equal to the charged-pion masses except one that is set to  $m_\gamma$ . It is infrared divergent and the term proportional to  $\log m_\gamma^2$  can be extracted. In the region  $s < 0$ , its analytic expression is

$$\begin{aligned} G_{+-\gamma}(q^2) &= C_0(q^2, m_\pi^2, m_\pi^2, m_\gamma^2, m_\pi^2, m_\pi^2) \\ &= -\frac{1}{32\pi^2 s \sigma_\pi(s)} \left\{ 4\text{Li}_2 \left( \frac{1 - \sigma_\pi(s)}{1 + \sigma_\pi(s)} \right) + \frac{\pi^2}{3} + \log^2 \left( \frac{\sigma_\pi(s) - 1}{\sigma_\pi(s) + 1} \right) \right. \\ &\quad \left. + 2 \left[ \log \left( \frac{-s}{m_\pi^2} \right) - \log \left( \frac{m_\gamma^2}{m_\pi^2} \right) + 2 \log(\sigma_\pi(s)) \right] \log \left( \frac{\sigma_\pi(s) - 1}{\sigma_\pi(s) + 1} \right) \right\}. \end{aligned} \quad (4.36)$$

The mass difference between charged and neutral pions is defined as  $\Delta_\pi = m_\pi^2 - m_{\pi^0}^2$ . Note also the presence of the scale-independent low-energy constants  $\bar{l}_i$ . Finally, the quantities  $K^{+-;+-}$  and  $K^{++;++}$  are a linear combination of electromagnetic low-energy constants  $\bar{k}_i$ . They carry a large uncertainty and their numerical value are given in [8] via the relation

$$\frac{e^2 m_{\pi^0}^2}{F^2} K^{+-;+-} = 8.6 \pm 12 \quad (4.37)$$

$$\frac{e^2 m_{\pi^0}^2}{F^2} K^{++;++} = -15 \pm 15 \quad (4.38)$$

A similar calculation has been carried out for the process  $\pi^+\pi^- \rightarrow \pi^0\pi^0$  in [7].

## Chapter 5

# The pion vector form factor

In this chapter, we introduce in more details the pion vector form factor. The latter relates an external electromagnetic current to a pair of charged on-shell pions. It describes the process effectively, without any specification about the underlying physics. It is directly related to the S-matrix element via the relation

$$\langle \pi^+(k_1)\pi^-(k_2)|j^\mu(0)|0\rangle = (-ie)F_\pi^V((k_1+k_2)^2)(k_1^\mu - k_2^\mu) \quad (5.1)$$

where  $j^\mu$  is the electromagnetic current and  $k_{1,2}$  are the pion momenta.

### 5.1 Purely hadronic form factor in ChPT

At low energy, one can use one-loop ChPT in the isospin limit to calculate [43]

$$F_\pi^V(q^2) = 1 + \frac{q^2}{6} \left\{ \frac{-6}{f_\pi^2} \left( l_6^r(\mu) - \frac{1}{96\pi^2} \left[ \log\left(\frac{m_\pi^2}{\mu^2}\right) + \frac{1}{3} + \left(1 - 4\frac{m_\pi^2}{q^2}\right) J^{(0)}\left(\frac{q^2}{m_\pi^2}\right) \right] \right) \right\} \quad (5.2)$$

The function  $J^{(0)}$  is related to the UV-finite part of the Passarino-Veltman  $B_0$ -function. It is given by

$$J^{(0)}(x) = \int_0^1 dz \log[1 + x(z^2 - z)]. \quad (5.3)$$

It gets an imaginary part when  $x > 4$ . Similarly the amplitude above has an imaginary part when  $q^2 > 4m_\pi^2$ . This corresponds to the phase-space integral of the two  $\mathcal{O}(p^2)$  sub-amplitudes. This means that unitarity and analyticity are satisfied at this order in ChPT. We can expand  $J^{(0)}(x) = -x/6 + \mathcal{O}(x^2)$  and extract the charge radius of the pion

$$\langle r^2 \rangle = 6 \frac{dF_\pi^V(q^2)}{dq^2} \Big|_{q^2=0} = \frac{-6}{f_\pi^2} \left( l_6^r(\mu) + \frac{1}{96\pi^2} \left[ 1 + \log\left(\frac{m_\pi^2}{\mu^2}\right) \right] \right). \quad (5.4)$$

The scale-dependent part in (5.2) is cancelled by the scale-dependent part of the renormalized LEC

$$l_6^r = -\frac{1}{96\pi^2} \left( \bar{l}_6 + \log \frac{m_\pi^2}{\mu^2} \right) \quad (5.5)$$

Of course, this description is good only at very low energy, close to the two-pion threshold. ChPT fails to reproduce experimental data near the  $\rho(770)$  resonance mass, even though the contribution from its low-energy tail is incorporated into the renormalized low-energy constant  $\bar{l}_6$ .

## 5.2 Dispersive representation of $F_V^\pi(s)$

In order to have a more accurate representation of the pion vector form factor evaluated at an energy of the order of magnitude of the  $\rho$  mass, one can rely on dispersion relations. We know that  $F_\pi^V(s)$  is analytic in  $s$  in the whole complex plane, except for a cut on the positive real axis, starting from the two-pion threshold. We also know that it is normalized to 1 at  $s = 0$ ,

$$F_\pi^V(0) = 1, \quad (5.6)$$

and perturbative QCD indicates that it behaves at high energy as [69]

$$F_\pi^V(s) \xrightarrow{s \rightarrow \infty} \frac{12C_F\pi f_\pi^2\alpha_s(s)}{s}. \quad (5.7)$$

In order to calculate its discontinuity on the cut, we assume elastic final state scattering. That means that the only intermediate state considered in the unitarity relation is the final state itself, that is a pair of charged pions. Also, we use our knowledge of the Lorentz structure of the matrix element (5.1). We contract the matrix element, in order to extract only the form factor. We thus have:

$$\begin{aligned} \text{Im } F_\pi^V(s) &= \text{Im } \langle \pi^+(k_1)\pi^-(k_2) | j^\mu(0) | 0 \rangle \frac{k_1^\mu - k_2^\mu}{(k_1 - k_2)^2} \\ &= \frac{1}{2} \sum_{I=0}^2 \int \frac{d\Phi_2}{(2\pi)^2} F_\pi^V(s) \frac{(p_1 - p_2) \cdot (k_1 - k_2)}{(k_1 - k_2)^2} T^{(I)}(s, t)^* \\ &= \frac{1}{2} \sigma_\pi(s) F_\pi^V(s) \sum_{I,\ell} 32\pi(2\ell+1) c_I t_\ell^I(s)^* \int_{-1}^1 \frac{dz}{2\pi} z P_\ell(z) \\ &= \sigma_\pi(s) F_\pi^V(s) t_1^1(s)^*. \end{aligned} \quad (5.8)$$

We have used the typical kinematics for a two-body scattering problem displayed in figure (A.1) of appendix A, the partial wave expansion of the  $\pi\pi$  scattering amplitude and the orthogonality of the Legendre polynomials.

This equation is nothing else than the Watson final state theorem for the pion vector form factor. Since the imaginary part must be a real number, and the threshold function  $\sigma_\pi(s)$  is purely real, the pion vector form factor must have a phase equal to the  $\pi\pi$  scattering P-wave phase shift. Of course this is exact only under our strong assumption of final state elasticity which, in practice, is good at reasonably low energy.

Since the pion vector form factor is analytic in the whole complex plane except for the positive real axis on which the phase is known, one can use the Omnès-Muskhelishvili method introduced above to calculate its energy dependence. We assume that the phase-shift of the  $\pi\pi$  scattering P-wave goes asymptotically to  $\pi$  at large energy. This means that the corresponding Omnès function goes asymptotically as  $s^{-1}$ . Therefore, because of (5.7) and (5.6), the polynomial in front of the Omnès function has to be 1 and we can write.

$$F_\pi^V(s) = \Omega_1^1(s) = \exp \frac{s}{\pi} \int ds' \frac{\delta_1^1(s')}{s'(s' - s)}. \quad (5.9)$$



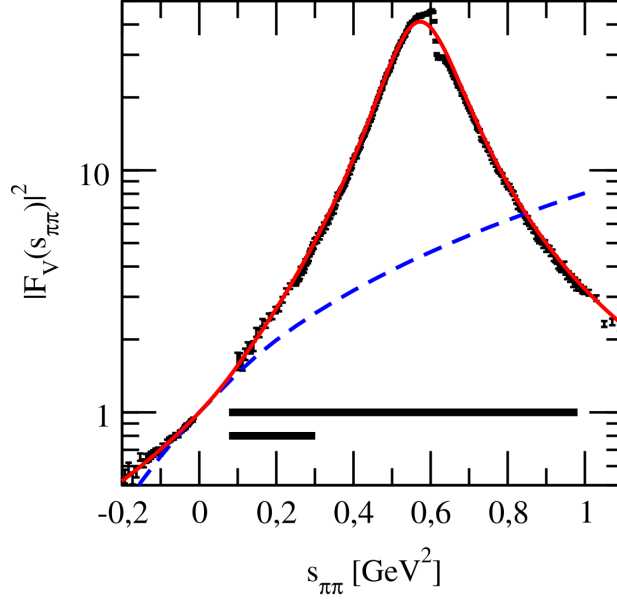


Figure 5.1: Comparison of the pion vector form factor calculated in one-loop ChPT (blue) and with a twice-subtracted Omnès function (red) in [70]. The black dots with error bands are experimental data from BABAR [71].

Comparing the one-loop result from ChPT and the dispersive result, we see on figure (5.1) that the Omnès method works very good in the intermediate energy region. The prediction from ChPT, on the other hand is only good at very low energy.

### 5.3 Radiative corrections in ChPT

The radiative corrections to the pion vector form factor  $F_\pi^V(s)$  from one-loop ChPT has been calculated in [3]. Exchanges of virtual photons are considered. The result corresponding to only the electromagnetic interactions is

$$F_{\pi,e}^V(s) = \left(\frac{e^2}{4\pi}\right)^2 \left\{ \frac{1}{3} \frac{28m_\pi^2 - 13s}{4m_\pi^2 - s} K_\pm(s) - \frac{4s}{4m_\pi^2 - s} - \frac{4}{3} \left( \frac{m_\pi^2}{s} K_\pm(s) + \frac{1}{6} \right) + \frac{s - 2m_\pi^2}{m_\pi^2} G(s) + 4 \left( \frac{s - 2m_\pi^2}{s\sigma_\pi(s)} \log \frac{\sigma_\pi(s) + 1}{\sigma_\pi(s) - 1} - 1 \right) \log \frac{m_\gamma}{m_\pi} \right\}. \quad (5.10)$$

The mass  $m_\pi$  refers to charged pions. The function  $\sigma_\pi(s)$  is the threshold function and  $K_\pm(s)$  and  $G(s)$  are related to the infrared finite part of the  $B$  and  $C$  functions in the Passarino-Veltman formalism:

$$K_\pm(s) = \int_0^1 dx \log \left( 1 - x(1-x) \frac{s}{m_\pi^2} \right) \equiv J^{(0)}(s/m_\pi^2), \quad (5.11)$$

$$G(s) = \int_0^1 dx \frac{\log \left( 1 - x(1-x) \frac{s}{m_\pi^2} \right)}{1 - x(1-x) \frac{s}{m_\pi^2}}. \quad (5.12)$$

Note the presence of a term proportional to  $\log m_\gamma$ , where  $m_\gamma$  is the photon mass regulator. This term comes from triangle topology that is infrared divergent because of the

photon line attached to two external pions and the Dyson series of the 1-particle irreducible diagrams contributing to the self energy of the pion. This logarithm is of course divergent in the limit  $m_\gamma \rightarrow 0$ . It is cancelled in any observable, as for instance the cross section, when soft-photon radiations are taken into account. Infrared divergences are omnipresent in this thesis and more technical details about the regularization procedure will be given in the next chapters.

Another feature of this expression is that it diverges at the two-pion threshold. This is due to the Coulomb pole. Near threshold, the perturbative expansion can thus not be trusted any more and one would need a resummation at all orders to have a reasonable description.

This result is only good where the momentum expansion is valid, that is, close to threshold. We have seen in the previous section that using the Omnès method allows for the description of the purely hadronic pion vector form factor at higher energy. Similarly, our goal in this thesis is to extend the result from ChPT only valid at low-energy to the intermediate energy region  $s \in [4m_\pi^2, 1\text{GeV}^2]$ .

## Chapter 6

# Radiative corrections to the process

$$e^+e^- \rightarrow \pi^+\pi^-$$

The process we are interested in is the creation of a charged pion pair from the annihilation of an electron and a positron:  $e^+(l_2)e^-(l_1) \rightarrow \pi^+(k_2)\pi^-(k_1)$ . In the standard model, this process is mediated in first approximation by a virtual photon. It also undergoes all kind of corrections due to additional virtual- and real-photon exchanges. Each of those exchanges brings a power of the electromagnetic fine-structure constant  $\alpha := \frac{e^2}{4\pi} \approx 1/137$ . These corrections can thus be treated perturbatively, order by order in  $\alpha$ . They go under the name of *radiative corrections* and are explained in more detail in this chapter.

### 6.1 Divergences in radiative corrections

Before explaining the different kinds of corrections to the process, let us make a remark about a central feature of radiative corrections. The calculation of loop diagrams in QFT causes the presence of two types of divergences that one has to take care of in order for the results to be finite and physical. Those are the infrared and ultraviolet divergences.

Ultraviolet divergences appear in the calculation of Feynman integrals of the form

$$F = \int \frac{d^4k}{(2\pi)^4} \frac{k^m}{\prod_i^n (k^2 - l_i^2)}. \quad (6.1)$$

In case  $2n \leq 4 + m$ , this integral diverges at least logarithmically. At the Lagrangian level, those divergent terms have the form of local operators. A procedure of renormalization of the constants corresponding to those operators is required, in order to absorb those divergences and make the result finite. This was already mentioned above, in the case of the low-energy constants of ChPT. In the dispersive formalism, however, such divergences never appear. The high-energy tail of the integrand in the dispersive integral can always be subtracted at the cost of introducing subtraction constants.

Infrared divergences arise because of the fact that photons are massless. In the dispersive framework, they can be related to an end-point singularity of the dispersive integral at threshold. In other cases, they can appear already at the level of the unitarity relation, in the integration over the phase space. Naturally, such divergences must disappear in any observable. The reason is that each experiment is limited in sensitivity. Photons with

energy smaller than some threshold specific to each experimental setup are undetectable. The measurement thus includes those so-called soft-photon radiations. Similarly, on the theoretical side, the inclusion of real-photon radiation leads to an infrared-finite prediction of the observable. This is because the soft-photon limit of the radiation term carries the exact same divergence as the virtual-photon contributions, up to a minus sign. Summing both contributions thus leads to a finite quantity. This explains why the sum of real- and virtual-photon contribution is needed in (6.3) in the case of the radiative corrections to  $e^+e^- \rightarrow \pi^+\pi^-$ . In practice, this can be done by introducing a regulator  $m_\gamma$  as the photon mass. Both infrared-divergent pieces are then proven to be proportional to  $\log m_\gamma$  and the cancellation can be checked analytically. These divergences are present throughout the whole project and must be dealt with carefully.

The technical details of the regularization of infrared divergences will be discussed specifically for the different cases encountered.

## 6.2 Cross section

The observable of interest is the inclusive cross section  $\sigma(e^+(l_2)e^-(l_1) \rightarrow \pi^+(k_2)\pi^-(k_1)(\gamma(k)))$ . The  $\gamma$  in brackets stands for the soft-photon emission that must be taken into account, in order for the cross section to be an infrared-finite quantity. It is defined as

$$\sigma(e^+e^- \rightarrow \pi^+\pi^-(\gamma)) = \sigma(e^+e^- \rightarrow \pi^+\pi^-) + \sigma(e^+e^- \rightarrow \pi^+\pi^-\gamma). \quad (6.2)$$

The differential cross-section for the process  $2 \rightarrow n$  where the two incoming particles have momenta  $l_1$  and  $l_2$  and the outgoing particles  $k_1, \dots, k_n$  is given by [72]

$$d\sigma(l_1l_2 \rightarrow k_1, \dots, k_n) = \frac{(2\pi)^4 |M(2 \rightarrow n)|^2}{4\sqrt{(l_1 \cdot l_2)^2 - l_1^2 l_2^2}} d\Phi_n(l_1 + l_2; k_1, k_2, \dots, k_n). \quad (6.3)$$

In that expression,  $|M|^2$  is the squared amplitude of the corresponding process. In the center of mass frame of the two incoming electrons, the so-called flux term is given by  $4\sqrt{(l_1 \cdot l_2)^2 - l_1^2 l_2^2} = 2s\sqrt{1 - 4m_e^2/s} = 2s\sigma_e(s)$  and  $d\Phi_n$  is the  $n$ -body phase-space differential defined in appendix B. The total cross section is obtained by integrating over the full phase space.

Concerning the exclusive process  $e^+e^- \rightarrow \pi^+\pi^-$ , the amplitude can be written as an expansion in the fine-structure constant  $\alpha$  with respect to the lowest-order amplitude,

$$M = M_0 + \alpha M_1 + \mathcal{O}(\alpha^2). \quad (6.4)$$

$M_1$  contains all the corrections from one virtual-photon exchange to the lowest-order contribution  $M_0$ . Note that  $M_1$  is an infrared-divergent quantity and therefore needs to be regularized, as will be explained later. Using this notation, we can calculate the amplitude squared entering the cross section (6.3) as

$$|M^2| = |M_0|^2 + 2\alpha \text{Re}(M_0 M_1^*) + \mathcal{O}(\alpha^2). \quad (6.5)$$

Similarly, the exclusive cross section is written as the sum of a bare cross section and a correction one order higher in  $\alpha$ :

$$\sigma(e^+e^- \rightarrow \pi^+\pi^-) = \sigma_0(e^+e^- \rightarrow \pi^+\pi^-) + \alpha \sigma_1(e^+e^- \rightarrow \pi^+\pi^-) + \mathcal{O}(\alpha^2). \quad (6.6)$$

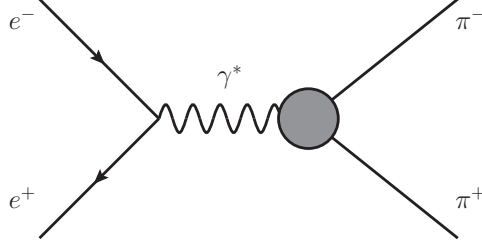


Figure 6.1: Tree-level diagram contributing to the process  $e^+e^- \rightarrow \pi^+\pi^-$ . The grey blob represents the purely hadronic pion vector form factor  $F_v^\pi(s)$ .

Concerning the process  $e^+e^- \rightarrow \pi^+\pi^-\gamma$ , the corresponding lowest-order amplitude carries an additional factor of  $e$  and the lowest-order cross section appears one order higher in  $\alpha$  than in the previous case:

$$\sigma(e^+e^- \rightarrow \pi^+\pi^-\gamma) = \alpha \sigma_1(e^+e^- \rightarrow \pi^+\pi^-\gamma) + \mathcal{O}(\alpha^2). \quad (6.7)$$

This quantity is also infrared divergent. This is a consequence of the photon becoming soft in the phase space of (6.3). It can be regularized by introducing a photon mass  $m_\gamma$  and using the method explained in appendix C.

### 6.3 Leading-order cross section

The lowest-order contribution to the process  $e^+e^- \rightarrow \pi^+\pi^-$  is given by the diagram depicted in figure 6.1. It is a tree-level diagram mediated by a virtual photon. The amplitude can thus directly be written as

$$M_0 = \bar{v}(l_2)(-ie\gamma_\mu)u(l_1)\frac{(k_1 - k_2)^\mu}{s}F_\pi^V(s). \quad (6.8)$$

In this expression,  $u$  and  $v$  are the electron and positron spinors where the spin indices were omitted. We defined the center-of-mass energy as  $\sqrt{s} = \sqrt{(l_1 + l_2)^2} = \sqrt{(k_1 + k_2)^2}$ . The presence of the pion vector form factor  $F_v^\pi(s)$  is due to the matrix element between the virtual photon and the pair of charged on-shell pions according to (5.1). Note that this would not be the case if the pions were off-shell.

In order to calculate the leading-order cross-section  $\sigma_0$ , we plug this expression into (6.3). Note that we must not forget about the factor  $1/4$  in the squared amplitude due to the fact that we average over the spins of the incoming particles. Working out the Dirac structure, we find

$$\Gamma_D^{\mu\nu} := \frac{1}{4}\text{Tr}[\bar{v}(l_2)\gamma^\mu u(l_1)\bar{u}(l_1)\gamma^\nu v(l_2)] = g^{\mu\nu}[m_e^2 - (l_1 \cdot l_2)] + l_1^\mu l_2^\nu + l_2^\mu l_1^\nu. \quad (6.9)$$

Then, using the two-body phase-space differential derived in appendix B, we can write the differential cross-section as

$$d\sigma_0(e^+e^- \rightarrow \pi^+\pi^-) = \frac{e^4}{(2\pi)^2} \frac{\Gamma_D^{\mu\nu}(k_1 - k_2)^\mu(k_1 - k_2)^\nu}{2s\sigma_e(s)} \frac{|F_\pi^V(s)|^2}{s^2} \frac{\sigma_\pi(s)}{8} d\Omega_2. \quad (6.10)$$

Finally, neglecting the electron mass allows one to write the total cross section in the following compact form

$$\begin{aligned}\sigma_0(e^+e^- \rightarrow \pi^+\pi^-) &= \frac{\pi\alpha^2}{3} \frac{2m_e^2 + s}{\sigma_e(s)} \frac{\sigma_\pi(s)^3}{s^2} |F_\pi^V(s)|^2 \\ &\approx \frac{\pi\alpha^2}{3} \frac{\sigma_\pi(s)^3}{s} |F_\pi^V(s)|^2.\end{aligned}\tag{6.11}$$

## 6.4 Types of radiative correction

When considering the radiative corrections to the process  $e^+e^- \rightarrow \pi^+\pi^-$ , there are three different types of radiation: initial-state radiation (ISR), final-state radiation (FSR) and interferences. We briefly discuss those in what follows.

### 6.4.1 Initial-state radiation

The ISR corresponds to any real- or virtual-photon exchange exclusively between the external electrons and positrons. In this case, the photons are always attached to leptons. The interactions between photons and leptons are described by the QED Lagrangian

$$\mathcal{L}_{QED} = \bar{\psi}(i\not{D} - m_e)\psi - \frac{1}{4}F_{\mu\nu}F^{\mu\nu}.\tag{6.12}$$

The spin-1/2 spinors are defined by  $\psi$  and the four-potential of the electromagnetic field  $A_\mu$ . We have defined the covariant derivative  $D_\mu = \partial_\mu + ieA_\mu$  and the field-strength tensor  $F_{\mu\nu} = \partial_\mu A_\nu - \partial_\nu A_\mu$ . Note also the use of the Dirac slashed convention  $\not{a} = a_\mu \gamma^\mu$ .

The corresponding Feynman diagrams are depicted in figure 6.2. Diagrams 6.2a and 6.2b correspond to the virtual-photon contribution. They both carry an ultraviolet as well as an infrared divergence. More specifically, (6.2b) contributes to the electron self energy. Note that the infrared divergence appears in the residue of the renormalized propagator only when summing all 1-particle irreducible leg corrections in a Dyson series

$$\begin{aligned}\frac{i}{\not{p} - m} &\rightarrow \frac{i}{\not{p} - m - \Sigma(m_{phys}) - \frac{\partial \Sigma}{\partial \not{p}}|_{\not{p}=m_{phys}}(\not{p} - m_{phys})} \\ &= \frac{i}{(\not{p} - m_{phys})(1 - \frac{\partial \Sigma}{\partial \not{p}}|_{\not{p}=m_{phys}})} \\ &\sim \frac{i}{\not{p} - m_{phys}}(1 + \delta Z_1),\end{aligned}\tag{6.13}$$

where  $\Sigma$  is the one-loop correction to diagram 6.2b. The residue contains a term proportional to the derivative of  $\Sigma$ :

$$\delta Z_1 := \frac{\partial \Sigma^{1-loop}}{\partial \not{p}} \Big|_{\not{p}=m_l}.\tag{6.14}$$

This term is infrared divergent, whereas  $\Sigma$  is not. The infrared divergence is cancelled in the total cross-section by the contribution from diagram 6.2c that represents the real-photon emission. Also, the Ward identity implies that the ultraviolet divergence in the

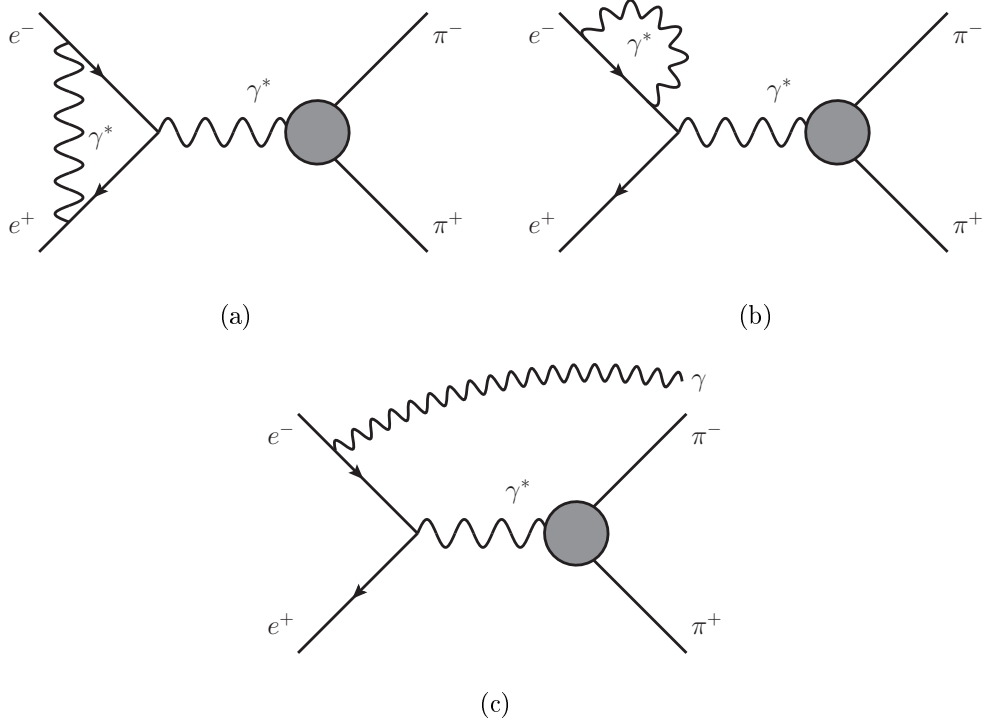


Figure 6.2: Virtual- (6.2a and 6.2b) and real- (6.2c) photon exchanges contributing to initial-state radiation of the process  $e^+e^- \rightarrow \pi^+\pi^-$ . All vertices are point-like.

residue  $Z_1 = 1 + \delta Z_1$  is cancelled by the residue of the vertex [73].

All of these corrections can be calculated unambiguously using perturbative methods. The contribution from virtual-photon exchange is

$$M_1^{\text{ISR}} = \bar{v}(p_2)(-ie\Gamma_\mu)u(p_1)\frac{(k_1 - k_2)^\mu}{s}F_\pi^V(s). \quad (6.15)$$

$\Gamma_\mu$  accounts for the resulting Dirac structure. In general, as already mentioned in (1.9), we can decompose the Lorentz structure in the following way:

$$\Gamma_\mu = F_1(s)\gamma_\mu - iF_2(s)\frac{\sigma_{\mu\nu}(p_1 + p_2)^\nu}{2m_e}. \quad (6.16)$$

As in the case of the lowest-order contribution, the hadronic interactions are contained in the purely hadronic pion vector form factor and can be factored out. The same is true for the real emission of figure 6.2c, the difference being that the argument of the pion vector form factor is the pion-pair energy. The calculation of the initial-state radiation contribution thus requires no non-perturbative method. The calculation has been carried out in [74]. We do not treat this matter further in this thesis.

#### 6.4.2 Final-state radiation

The final-state radiation corresponds to photon exchanges between any of the final hadronic states. The virtual-photon exchange is depicted in figure 6.3a and the real-photon emission in figure 6.3b. In those figures, the grey blob represents all possible hadronic interactions

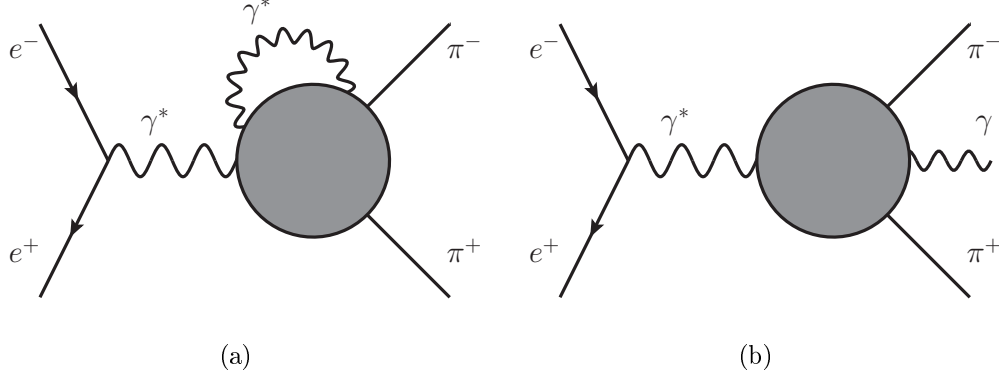


Figure 6.3: Virtual- and real-photon contribution to the final-state radiation. The grey blobs represent purely hadronic interactions.

contributing to the process  $\gamma^* \rightarrow \pi\pi$  and  $\gamma^* \rightarrow \pi\pi\gamma$  respectively. The difficulty in this case is that the use of perturbative methods is obsolete, due to the nature of strong interactions. A treatment of the final-state correction similar to the one in the previous section is thus not possible and we must find other methods to be able to predict the size of those contributions.

These final-state radiative corrections are the central point of this thesis. In what follows, we will explain the different methods used for their estimation in more detail.

### 6.4.3 Interference contribution

The interference contributions account for photon exchanges between one of the incoming fermions and an outgoing pion. The virtual-photon exchange to this contribution is depicted in figure 6.4a. By approximating the amplitude for the process  $\gamma^*\gamma^* \rightarrow \pi^+\pi^-$  with a pion pole, we end up with the two boxes 6.4b and 6.4c. Since in this approximation, photons are attached to external pion legs, the contribution is infrared divergent. The divergence is cancelled in any observable, once the product of the real-photon emission diagram 6.2c and the pion-pole approximation of 6.3b is taken into account.

An important feature of the sum of the two boxes 6.4b and 6.4c is that the corresponding amplitude is antisymmetric under exchange of the two crossed Mandelstam variables  $t$  and  $u$ . A direct consequence of this is that this contribution vanishes in the total cross-section where the scattering angle is integrated over. The interference terms therefore have no influence on the radiative corrections to the pion vector form factor. This kind of corrections contributing only to scattering-angle dependent observable are thus ignored in what follows.



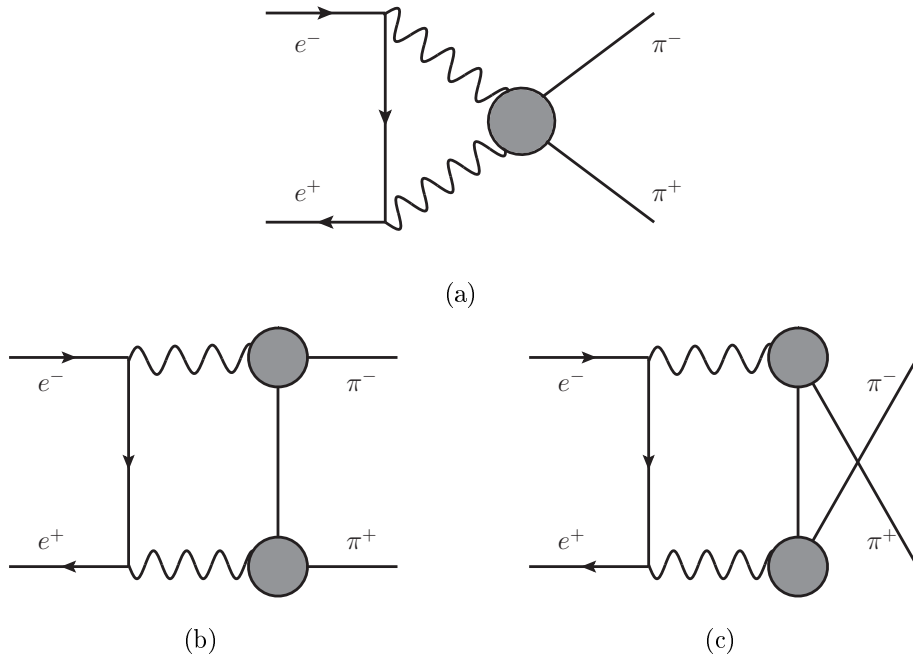


Figure 6.4: Interference contribution to  $e^+e^- \rightarrow \pi^+\pi^-$ . Diagram 6.4a represents the general case. The grey blob accounts for all hadronic contributions to  $\gamma^*\gamma^* \rightarrow \pi^+\pi^-$ . Diagrams 6.4b and 6.4c represent the pion-pole approximation to the hadronic blob in diagram 6.4a. The grey blobs account for hadronic interactions in the process  $\gamma^* \rightarrow \pi\pi^*$ .

## Chapter 7

# Final-state radiation

In this chapter we explain the method used for the calculation of the FSR to the process  $e^+e^- \rightarrow \pi^+\pi^-$ . So far, those have only been calculated in a model-dependent framework based on scalar QED. In this thesis, we are aiming at a completely model-independent description of the final-state radiative corrections. This is the first time that such a calculation is attempted for this process and we must therefore set up the new framework.

As we can see on figure 6.3a, the FSR to the process  $e^+e^- \rightarrow \pi^+\pi^-$  at order  $\alpha$  from virtual-photon exchange can be reduced to the correction to the pion vector form factor. The latter can be expanded in powers of  $\alpha$  as

$$F_\pi^V(s) = F_\pi^{V,0}(s) + F_\pi^{V,\alpha}(s) + \mathcal{O}(\alpha^2). \quad (7.1)$$

The quantity  $F_\pi^{V,0}(s)$  is the purely hadronic pion vector form factor where the electromagnetic interactions have been turned off. In this thesis, we are aiming for a calculation of the radiative corrections to the pion vector form factor at order  $\alpha$ ,  $F_\pi^{V,\alpha}(s)$ . This means that only one-photon exchanges are considered both in the virtual- and real-photon contributions. At the level of  $(g-2)_\mu$ , this corresponds to a correction at  $\mathcal{O}(\alpha^3)$ , i.e. the same order as the HLbL correction. Concerning the next order ( $\alpha^2$ ) in the  $\alpha$  expansion of  $F_\pi^V$ , it is hard to estimate such a contribution. We expect that it is suppressed by at least one or two orders of magnitude compared to the correction at order  $\alpha$ . Note that in the case of HVP at NNLO, the size of the contribution calculated in [75] is suppressed only by a factor 1/8 compared to the contribution from HVP at NLO [23]. In the case of HLbL at NLO, however, the contribution has been estimated in [76] to correspond to only a few percent of the LO contribution.

### 7.1 Model-dependent estimation

Let us start with a summary of the method used so far for the estimation of the radiative corrections to the pion vector form factor at order  $\alpha$ . The calculation has been carried out in [6]. It is based on scalar quantum electrodynamics [77] (sQED) applied on pions. This means that the pions are assumed to behave as point-like particles. Their substructure is therefore ignored. The Lagrangian of such a theory can be written as

$$\mathcal{L}_{\text{sQED}} = \mathcal{L}_{\text{QED}} + \mathcal{L}_\pi \quad (7.2)$$

where  $\mathcal{L}_{\text{QED}}$  is the QED Lagrangian defined in (6.12). The part of the Lagrangian containing information about the hadronic interactions is given by

$$\mathcal{L}_\pi = (\partial_\mu \Phi)(\partial_\mu \Phi^*) - ie(\Phi^* \partial_\mu \Phi - m_\pi^2 \Phi \Phi^* - \Phi \partial_\mu \Phi^*)A^\mu + e^2 g_{\mu\nu} \Phi \Phi^* A^\mu A^\nu. \quad (7.3)$$

where  $\Phi$  corresponds to the complex scalar field. The corresponding Feynman rules in momentum space are

$$\rightarrow -ie(p_1 - p_2)^\mu, \quad (7.4)$$

$$\rightarrow 2ie^2 g^{\mu\nu}. \quad (7.5)$$

Note that in this particular case, there is no  $\Phi^4$  term in the Lagrangian. Consequently there is also no four-pion vertex and therefore no rescattering effect is taken into account. From the Lagrangian above, the contribution from virtual-photon exchange is calculated via the diagrams of figure 7.1. Those diagrams are calculated perturbatively using Feynman parametrization, regularizing and renormalizing the infrared and ultraviolet divergences in the usual way. The real-photon contribution needed to that end is depicted in the diagrams of figure 7.2.

In order to take the non-trivial substructure of the pions into account, those radiative corrections are then dressed with a pion vector form factor by a simple multiplication. Schematically, we have

$$\Rightarrow \quad (7.6)$$

The argument behind this prescription is that the contribution from diagrams with an exchange of virtual photon in sQED are large in the soft-photon limit. In this limit, the pions in the loop are almost on-shell and the hadronic blob can be assumed to be close to the actual vector form factor. The second argument is that the FSR in QED are ultraviolet-finite. This is due to the Ward identity that implies the cancellation of divergences between diagram 7.1a and 7.1c similarly to the situation of the initial-state radiation in QED. Therefore, there are no ultraviolet cut-offs and no large logarithms due to high-energy effects.

Of course, those arguments are not formally proving that this prescription is good. The model dependence of this framework may have a large effect on the calculation. Additionally to the tiny theoretical uncertainty of this calculation, model uncertainty may be larger than expected. In the following chapters of this thesis, we intend to use a new model-independent method based on the general properties of the transition amplitude to analyse the radiative corrections. We will then be able to compare both of them.

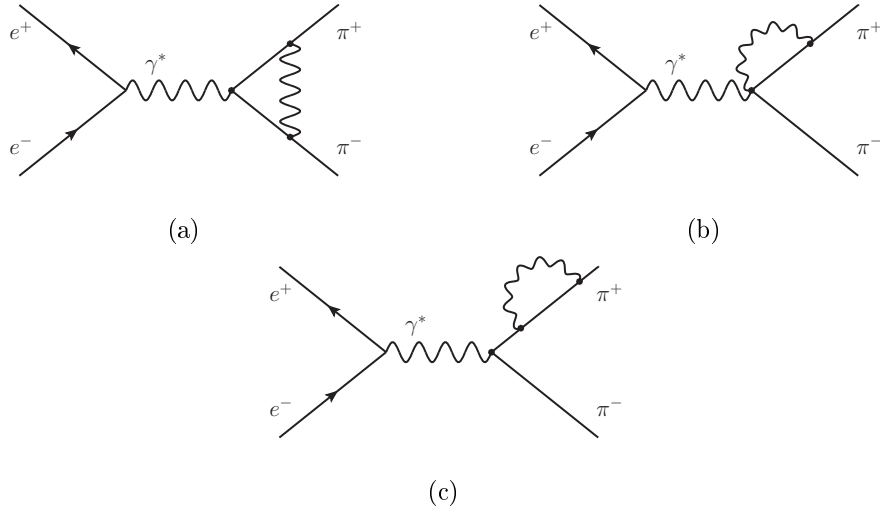


Figure 7.1: Virtual-photon exchange in scalar QED.

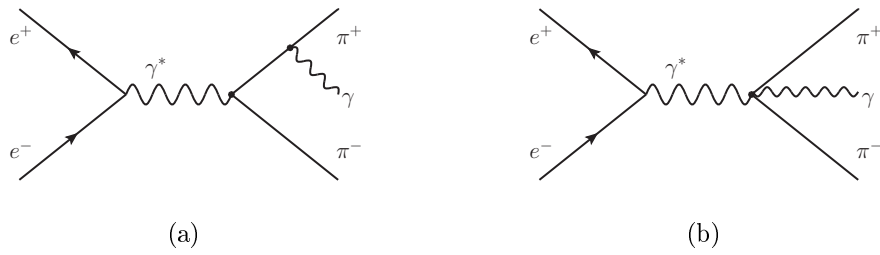


Figure 7.2: Real-photon emission in scalar QED.

## 7.2 Dispersive method

Let us now explain how we use the dispersive framework in this calculation. In order to assess those radiative corrections to the pion vector form factor, we rely on two general properties mentioned above: analyticity and unitarity. We have seen that once the analytic structure of an amplitude is known, its real part can be obtained from a dispersion relation. The latter is expressed as an integral of its imaginary part along a cut. In order to determine the branch points and the discontinuity of the amplitude along this cut, we rely on unitarity. It allows to specify which hadronic states are taken into account in the hadronic blob of figure 6.3a. As explained above, unitarity relates the imaginary part of a transition amplitude to all intermediate states consistent with the initial and final states of the process. There are a priori an infinite number of such intermediate states. In practice, we must truncate the series by restricting those to only the ones contributing the most to the correction. The imaginary part of a transition amplitude is closely related to its discontinuity along a cut in the complex plane of its center-of-mass energy squared  $s$ . This cut is determined by the intermediate states contributing to the amplitude. It starts from the creation threshold of the corresponding state and goes up to infinity. The principle of maximal analyticity ensures that the only discontinuities are those related to these intermediate states. From these analytic properties, the real part of the amplitude can be calculated once the imaginary part of  $F_\pi^{V,\alpha}$  is known:

$$\text{Re}F_\pi^V(s) = 1 + \frac{s}{\pi} P \int_{4m_\pi^2}^{\infty} ds' \frac{\text{Im}F_\pi^V(s')}{s'(s' - s)}, \quad (7.7)$$

where  $F_\pi^V(s)$  can be decomposed according to (7.1).

Our prescription in this thesis is to limit ourselves to intermediate states with at most two pions and a photon. All intermediate states with heavier particles or a larger number of pions are thus neglected. The justification of why this is a good approximation is that the energy threshold related to such states is higher. Such states therefore contribute less to the dispersive integrals evaluated in the energy range  $s \in [4m_\pi^2, 1\text{GeV}^2]$  that we are considering. Also, multi-particle states undergo a strong suppression near threshold because of the centrifugal barrier. For instance, pole contributions from heavier states with mass  $M$  would scale as  $1/M^2$ . Such contributions would therefore be suppressed compared to the exchange of two light pions. Note that this assumption has been made in a variety of other projects (see for instance [78]).

Also, diagrams consisting of self-energy corrections to the pion mass are not calculated explicitly. Instead, we directly consider the physical-pion masses throughout the whole calculation. We must not forget however, that those carry an infrared divergence when summing all the one-particle irreducible diagrams similarly to (6.14). The corresponding counter-part from soft-photon real emission must therefore be excluded by hand.

As we will see, the  $\pi\pi$  rescattering is omnipresent in our calculation. We thus need a good description of the  $\pi\pi$  scattering amplitudes. The latter can be expanded in partial waves according to (4.18). For the energy range of interest, the S and P waves are dominant and we neglect higher waves (D, F, ...).

Despite these approximations, we stress that the treatment of the corrections is done exactly, without relying on any prescription similar to (7.6). The two central hadronic



Figure 7.3: Pictorial representation of the purely hadronic pion vector form factor (7.3a) and  $\pi\pi$ -scattering amplitude (7.3b).

quantities used in the calculation are the pion vector form factor and  $\pi\pi$ -scattering amplitude in the isospin limit. In what follows, we display those hadronic objects according to the description of figure 7.3.

In summary, the important points are the following:

- We calculate the radiative corrections to the pion vector form factor at order  $\alpha$ .
- The center-of-mass energy range of interest is  $s \in [4m_\pi^2, 1\text{GeV}^2]$ .
- We only consider states with at most two pions and a photon in the intermediate states.
- The calculation is carried out with physical pion masses.
- Partial waves  $t_\ell^I(s)$  of the  $\pi\pi$ -scattering amplitude with  $\ell \geq 2$  are neglected.

We emphasize that this is the first time that such a model-independent calculation of those radiative corrections is done. In what follows we show that the calculation is tractable, which was not obvious to us at the start of the project. To that end a central point is the determination of all the topologies contributing to the radiative corrections. Some of those lead to an implicit integral equation that we will encounter in the corresponding section. The latter are also equations that had never been encountered before to our knowledge. A numerical method has been developed for the determination of their solution.

### 7.3 General unitarity relation

As stated above, the discontinuity of  $F_\pi^{V,\alpha}(s)$  along the real axis is obtained by cutting the diagram in figure 6.3a in all possible ways. Schematically, those cuts can be expressed as

a sum of three terms:

$$\text{Disc} = \text{blob} = \text{blob with cut 1} + \text{blob with cut 2} + \text{blob with cut 3} \quad (7.8)$$

Note that each dashed line represents a cut. According to our prescription above, each cut can consist of intermediate states with at most two pions. This means that we can translate this schematic representation into a sum of product of well-defined subamplitudes by replacing the hadronic blob with a two-pion state. Those are integrated over a two or three-body phase space as:

$$\begin{aligned} \frac{\text{Disc} F_{\pi}^{V,\alpha}(s)}{2i} &= \frac{(2\pi)^4}{2} \int d\Phi_2 F_{\pi}^V(s) \times T_{\pi\pi}^{\alpha*}(s, t) + \frac{(2\pi)^4}{2} \int d\Phi_2 F_{\pi}^{V,\alpha}(s) \times T_{\pi\pi}^*(s, t) \\ &+ \frac{(2\pi)^4}{2} \int d\Phi_3 F_{\pi}^{V,\gamma}(s, t) T_{\pi\pi}^{\gamma*}(s, \{t_i\}) \end{aligned} \quad (7.9)$$

Each term corresponds to a cut in (7.8). The first term is the product of the purely hadronic form factor with the  $\mathcal{O}(\alpha)$  correction to the  $\pi\pi$  scattering amplitude  $T_{\pi\pi}^{\alpha}(s, t)$ . The second term is the product of  $F_{\pi}^{V,\alpha}(s)$  with the purely hadronic  $\pi\pi$ -scattering amplitude. In the last term,  $F_{\pi}^{V,\gamma}(s, t)$  and  $T_{\pi\pi}^{\gamma}(s, \{t_i\})$  are the transition amplitudes respectively related to the process  $\gamma^* \rightarrow \pi^+\pi^-\gamma$  and  $\pi^+\pi^- \rightarrow \pi^+\pi^-\gamma$ . Note that the latter involves five external particles, which means that the amplitudes depends on five variables ( $s$  and  $t_i$ ,  $i \in \{1, 2, 3, 4\}$ ). The three-body phase-space integral is due to the additional presence of the photon in the intermediate state, in contrary to the two first terms.

An important feature of this equation is that the initial amplitude  $F_{\pi}^{V,\alpha}(s)$  also appears as a subamplitude in the two-body phase-space integral of the first term. Therefore, we are facing an implicit equation. Finding the solution of this equation is a large part of the project and will be explained in more details in the next chapters.

As is clear from (7.9), the calculation of the imaginary part of  $F_{\pi}^{V,\alpha}(s)$  requires the knowledge of other subamplitudes. We refer to these as building blocks. Those are either radiative corrections to the  $\pi\pi$ -scattering amplitude  $T_{\pi\pi}^{\alpha}(s, t)$  or real-photon emissions  $F_{\pi}^{V,\gamma}$  and  $T_{\pi\pi}^{\gamma}$ . In the following, we will explain how we calculate each of them before being able to use them as input in (7.9).

## Chapter 8

### Building block $\gamma^* \rightarrow \pi\pi\gamma$

The first building block that we discuss in this chapter is the amplitude for the process  $\gamma^*(q_1) \rightarrow \pi^+(p_1)\pi^-(p_2)\gamma(-q_2)$ . This amplitude is present in both the virtual- and real-photon contribution. In the first case, this amplitude enters the unitarity relation of the pion vector form factor (7.9). In the second case, it contributes directly to the cross section  $\sigma(e^+e^- \rightarrow \pi^+\pi^-\gamma)$  with a real photon in the final state. This process has been treated exhaustively in the literature and we only summarize the situation here. We can decompose the corresponding transition amplitude into a contribution from the pion pole and a contribution from two-pion exchanges. The corresponding diagrams are respectively depicted in figures 8.1a and 8.1b.

#### 8.1 Pion-pole contribution

Concerning the pion-pole contribution depicted in figure 8.1a, it has been shown in [19] that the tensorial amplitude in the dispersive formalism was identical to the one from scalar QED multiplied with the corresponding pion vector form factors at the vertices. Note that the presence of this hadronic object is due to the fact that the pion in the intermediate state of the unitarity relation is on-shell. The explicit expression for the amplitude is

$$W_\pi^{\mu\nu} = F_v^\pi(q_2^2)F_v^\pi(q_1^2) \left[ \frac{(2p_1^\mu - q_1^\mu)(2p_2^\nu - q_2^\nu)}{(p_1 - q_1)^2 - m_\pi^2} + \frac{(2p_2^\mu - q_1^\mu)(2p_1^\nu - q_2^\nu)}{(p_1 - q_2)^2 - m_\pi^2} + 2g^{\mu\nu} \right]. \quad (8.1)$$

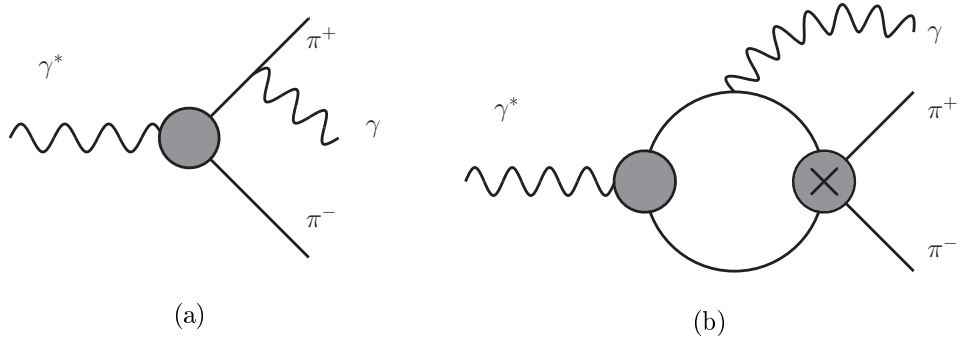


Figure 8.1: pion-pole and two-pion contribution to the process  $\gamma^* \rightarrow \pi^+\pi^-\gamma$



Note that in our case, one of the two photons is on-shell, which means  $F_v^\pi(q_2^2) = F_v^\pi(0) = 1$ .

## 8.2 Two-pion contribution

The two-pion contribution depicted in figure 8.1b is a rescattering effect of the previous one. This has been calculated in the literature for different kinematic regions. We are interested in the process where the incoming photon has a positive virtuality (time-like) and the outgoing one is on-shell. This contribution has been calculated in [79] based on an Omnès-Muskhelishvili method for the helicity amplitude of the process. The calculation is valid in the elastic region, below the  $K\bar{K}$  threshold, that is  $q_1^2 < 1\text{GeV}^2$ .

The helicity amplitudes of the process  $H^{\lambda_1\lambda_2}(s, q_1^2, \theta)$  are related to the transition amplitude  $W^{\mu\nu}$  via the relation

$$e^{i(\lambda_2 - \lambda_1)\phi} H_{\lambda_1, \lambda_2}(s, q_1^2, \theta) \equiv -W_{\mu\nu}(\{q_i, p_i\}) \epsilon_1^{*\mu}(q_1, \lambda_1) \epsilon_2^\nu(q_2, \lambda_2). \quad (8.2)$$

In this expression,  $s$  is the energy squared of the two-pion or two-photon system and  $q_1^2$  is the virtuality of the off-shell photon.  $\theta$  and  $\phi$  are the polar and azimuthal angles between a photon and a pion in the center-of-mass frame of  $s$ . Also,  $\epsilon_i^\mu(q_i, \lambda_i)$  with  $\lambda_i \in \{+, 0, -\}$  are the polarization vectors corresponding to each photon.

An additional superscript  $I$  corresponding to the isospin of the pion-pair state can be added, in order to expand the helicity amplitude in partial waves:

$$H_{\lambda_1\lambda_2}^I(s, q_1^2, \theta) = \sum_J (2J+1) h_{J, \lambda_1\lambda_2}^I(s, q_1^2) d_{\lambda_1 - \lambda_2, 0}^J(\theta). \quad (8.3)$$

The relation between the amplitude in the isospin basis and in the physical basis is

$$\begin{pmatrix} H_{\lambda\lambda'}^0 \\ H_{\lambda\lambda'}^2 \end{pmatrix} = C \begin{pmatrix} \sqrt{2} H_{\lambda\lambda'}^c \\ H_{\lambda\lambda'}^n \end{pmatrix}, \quad C = C^{-1} = \begin{pmatrix} -\sqrt{\frac{2}{3}} & -\sqrt{\frac{1}{3}} \\ -\sqrt{\frac{1}{3}} & \sqrt{\frac{2}{3}} \end{pmatrix}. \quad (8.4)$$

where  $H_{\lambda\lambda'}^c$  and  $H_{\lambda\lambda'}^n$  are respectively the helicity amplitude in the case of a pair of charged and neutral pions. Because of parity and the property of the Wigner function

$$d_{j,0}^J = (-1)^j d_{-j,0}^J, \quad (8.5)$$

there are dependences among the different helicity amplitudes:

$$H_{++}^I = H_{--}^I, \quad H_{+-}^I = H_{-+}^I, \quad H_{+0}^I = -H_{-0}^I. \quad (8.6)$$

Moreover, the helicity amplitudes where the on-shell photon has polarization 0 always vanishes. This means that there are only three independent helicity amplitudes that are chosen as  $H_{++}$ ,  $H_{+-}$  and  $H_{+0}$ .

The calculation is valid in the region  $s, q_1^2 \in [4m_\pi^2, 1\text{GeV}^2]$ . As we will see later, the amplitude for  $s$  larger than  $1\text{GeV}^2$  is not particularly important in our case. This is due to the fact that this quantity eventually contributes to an imaginary part that is integrated dispersively. The tail of this imaginary part is always suppressed by subtractions and the

contribution from the energy above the  $K\bar{K}$  threshold are less important.

The code generating the helicity amplitudes  $H_{++}$ ,  $H_{+-}$  and  $H_{+0}$  has been kindly provided by B. Moussallam. In practice, we choose a set of energy points  $\{s_i\}$ . Then for each  $s_i$ , we evaluate  $H^{\lambda_1\lambda_2}(s_i, \tilde{s}_j, \theta_k)$  for a finite number of points  $\{\tilde{s}_j, \theta_k\}$  on the whole phase space and interpolate between those. We end up with a function defined on the full phase space for each of the values of  $s_i$  originally chosen. The helicity amplitudes can then be used to calculate the phase-space integral of the amplitude squared in (7.9).

In order to give an idea of the size of this contribution relatively to the pion-pole term, we display the contribution to the anomalous magnetic moment calculated in [79]. The result is

$$a_\mu^{\text{Born}} = 42.9 \times 10^{-11}, \quad (8.7)$$

$$\hat{a}_\mu^{[\gamma\pi^+\pi^-]} = (1.47 \pm 0.40) \times 10^{-11}, \quad (8.8)$$

$$\hat{a}_\mu^{[\gamma\pi^0\pi^0]} = (0.33 \pm 0.05) \times 10^{-11}. \quad (8.9)$$

In this notation,  $a_\mu^{\text{Born}}$  corresponds to the pion pole and  $\hat{a}_\mu$  to rescattering effects. We see that the size of the latter is smaller than the first one by almost two orders of magnitude. Similarly, the part coming from the rescattering effect is subdominant in the unitarity relation (7.9).

## Chapter 9

# Building block $\pi\pi \rightarrow \pi\pi\gamma$

In this chapter, we calculate the pion-pole contribution to the process  $\pi(k_2)\pi(k_1) \rightarrow \gamma(k)\pi(p_2)\pi(p_1)$  and its rescattering effects. This process has been studied in the framework of ChPT at the one-loop level in [80]. It has also been extended to the hadronic scale where the low-energy expansion of ChPT breaks down using resonance exchanges in [60]. Our approach is to calculate the pion-pole contribution in terms of the purely hadronic  $\pi\pi$ -scattering amplitude.

In the first section, we derive the gauge-invariant amplitude in the dispersive framework. The latter is written in terms of the  $\pi\pi$ -scattering amplitudes that depends on the external kinematics of the process. In the second section, we explain the ambiguity appearing in the choice of the argument of the  $\pi\pi$ -scattering amplitudes. This ambiguity is due to the pion-pole approximation of the discontinuity and should a priori be resolved by higher state contributions. Finally we use a modified Omnès-Muskhelishvili method to calculate the rescattering effects and display our results for the cross section of the process  $\gamma\pi \rightarrow 3\pi$ .

### 9.1 Derivation of the gauge-invariant amplitude

In general this kind of  $2 \rightarrow 3$  process is hard to treat dispersively, since one needs to work with 10 different scalar products, 5 of which are independent kinematic variables (analogously to  $(s, t, u) \rightarrow (s, t, u(s, t))$  in a  $2 \rightarrow 2$  scattering processes [30]). The calculation is easier once we focus on poles only.

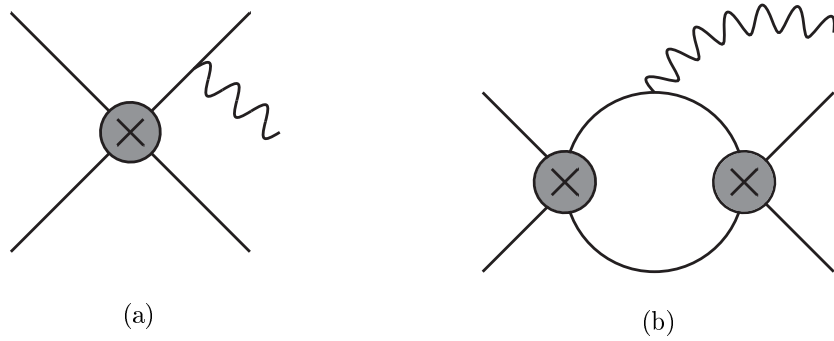


Figure 9.1: pion-pole and two-pion contribution to the process  $\pi^+\pi^- \rightarrow \pi^+\pi^-\gamma$

Let us start with the pion-pole contribution to the neutral channel ( $\pi^+(k_2)\pi^-(k_1) \rightarrow \gamma(k)\pi^0(p_2)\pi^0(p_1)$ ). We define this amplitude as  $M_{cn}^\mu$ . The subscript stands for the charges of the pions in the process. As we will see later, the amplitude for the fully-charged channel,  $M_c^\mu$ , can be obtained from the neutral one in the isospin limit.

In this case, only the charged external legs can emit a photon. The amplitude consists of the sum of two diagrams similar to 9.1a, where the photon is emitted by either of the two incoming legs. Because of energy and momentum conservation, there are four independent Lorentz structures for this process. We choose those as  $\{l_i^\mu\} = \{k^\mu, k_1^\mu, k_2^\mu, k_3^\mu := (p_2 - p_1)^\mu\}$ . In general, the transition amplitude of the process can be decomposed as

$$M_{cn}^\mu = k^\mu A_k + k_1^\mu A_{k_1} + k_2^\mu A_{k_2} + k_3^\mu A_{k_3} = \sum_i l_i^\mu A_{l_i}, \quad (9.1)$$

where  $A_{l_i}$  are scalar functions multiplying the corresponding Lorentz structures. The conservation of current under the form of the Ward identity

$$k_\mu M_{cn}^\mu = 0 \quad (9.2)$$

leads to dependences among the scalar functions, such that some linear combinations of them have to vanish. This leads to kinematic zeros and singularities. To circumvent this issue, we follow the recipe by Bardeen and Tung [81] also used in the case of the processes  $\gamma^{(*)}\gamma^* \rightarrow \pi\pi$  and  $\gamma\gamma^* \rightarrow \gamma^*\gamma^*$  in [19]. We introduce a projector

$$I^{\mu\nu}(\tilde{p}) := g^{\mu\nu} - \frac{\tilde{p}^\mu k^\nu}{\tilde{p} \cdot k}. \quad (9.3)$$

This object has the following properties:

$$k_\mu I^{\mu\nu} = 0, \quad (9.4)$$

$$I^\mu_\nu M_n^\nu = M_n^\mu. \quad (9.5)$$

It is important to note that choosing  $\tilde{p} = k_1$  in (9.5) would break the symmetry of the system, since the amplitude must obey

$$M_{cn}^\mu(k_1, k_2, k, k_3) = -M_{cn}^\mu(k_2, k_1, k, k_3), \quad (9.6)$$

that is, it must be antisymmetric under exchange of  $(k_1 \leftrightarrow k_2)$ . For this reason, we define our projector as

$$\bar{I}^{\mu\nu} := \frac{1}{2} (I^{\mu\nu}(k_1) + I^{\mu\nu}(k_2)), \quad (9.7)$$

which obviously fulfils the two properties above. From (9.5), we can write the amplitude as

$$M_{cn}^\mu = \bar{I}^\mu_\nu M_{cn}^\nu = \sum_i (\bar{I}^\mu_\nu l_i^\nu) A_{l_i} = \sum_i L_{l_i}^\mu A_{l_i} \quad (9.8)$$

where the tensor structures are given by

$$\begin{aligned}
L_k^\mu &= k^\mu - k^2 \left( \frac{1}{2k_1 \cdot k} k_1^\mu + \frac{1}{2k_2 \cdot k} k_2^\mu \right) = k^\mu, \\
L_{k_1}^\mu &= \frac{1}{2} \left( k_1^\mu - \frac{k_1 \cdot k}{k_2 \cdot k} k_2^\mu \right), \\
L_{k_2}^\mu &= \frac{1}{2} \left( k_2^\mu - \frac{k_2 \cdot k}{k_1 \cdot k} k_1^\mu \right), \\
L_{k_3}^\mu &= k_3^\mu - \frac{1}{2} \left( \frac{k_3 \cdot k}{k_1 \cdot k} k_1^\mu + \frac{k_3 \cdot k}{k_2 \cdot k} k_2^\mu \right).
\end{aligned} \tag{9.9}$$

It is not possible to get rid of the pole in  $(k_1 \cdot k)$  and  $(k_2 \cdot k)$  by using linear combinations of (9.9) without introducing further singularities. We therefore multiply the structures by their respective poles and rewrite the amplitude as

$$M_{cn}^\mu = \sum_i \tilde{L}_i^\mu \tilde{A}_i \tag{9.10}$$

where

$$\begin{aligned}
\tilde{L}_1^\mu &= k^\mu, \\
\tilde{L}_2^\mu &= (k_1 \cdot k) k_2^\mu - (k_2 \cdot k) k_1^\mu, \\
\tilde{L}_3^\mu &= (k_1 \cdot k)(k_2 \cdot k) k_3^\mu - \frac{(k_3 \cdot k)(k_2 \cdot k)}{2} k_1^\mu - \frac{(k_3 \cdot k)(k_1 \cdot k)}{2} k_2^\mu, \\
\tilde{A}_1 &= A_k, \\
\tilde{A}_2 &= \frac{A_{k_2}}{2(k_1 \cdot k)} - \frac{A_{k_1}}{2(k_2 \cdot k)}, \\
\tilde{A}_3 &= \frac{A_{k_3}}{(k_1 \cdot k)(k_2 \cdot k)}.
\end{aligned} \tag{9.11}$$

Note that since  $L_{k_1}^\mu$  and  $L_{k_2}^\mu$  transform into the same structure, we end up with only 3 tensor structures.

Let us now calculate the pion-pole contribution to the process. The discontinuity along the cut of the corresponding channel is simply proportional to a Dirac  $\delta$ -function. We define the channels in which the pole can appear as  $s_{p_1} := (p_1 + k)^2$ ,  $s_{p_2} := (p_2 + k)^2$ ,  $t_{k_1} := (k_1 - k)^2$  and  $t_{k_2} := (k_2 - k)^2$ . In our case, we only consider photons attached to the incoming pions and thus

$$\begin{aligned}
\frac{1}{2i} \text{Disc}_{\pi}^{s_{p_1}} M_{cn}^\mu &= 0, \\
\frac{1}{2i} \text{Disc}_{\pi}^{s_{p_2}} M_{cn}^\mu &= 0, \\
\frac{1}{2i} \text{Disc}_{\pi}^{t_{k_1}} M_{cn}^\mu &= e\pi \delta(t_{k_1} - m_\pi^2) \bar{T}_{\pi\pi}^{cn}(k_1) (2k_1^\mu - k^\mu), \\
\frac{1}{2i} \text{Disc}_{\pi}^{t_{k_2}} M_{cn}^\mu &= e\pi \delta(t_{k_2} - m_\pi^2) \bar{T}_{\pi\pi}^{cn}(k_2) (-2k_2^\mu + k^\mu).
\end{aligned} \tag{9.12}$$

In this notation,  $\bar{T}_{\pi\pi}^{cn}(l_i)$  is the pure hadronic  $\pi\pi$ -scattering amplitude for the process  $\pi^-(k_1)\pi^+(k_2) \rightarrow \pi^0(p_1)\pi^0(p_2)$ , where the momentum  $l_i$  is replaced by  $l_i - k$ . After the projection, we have

$$\begin{aligned}\frac{1}{2i}\text{Disc}_{\pi}^{t_{k_1}}\tilde{A}_1 &= -\pi e \delta(t_{k_1} - m_{\pi}^2)\bar{T}_{\pi\pi}^{cn}(k_1), \\ \frac{1}{2i}\text{Disc}_{\pi}^{t_{k_1}}\tilde{A}_2 &= -2\frac{\pi e \delta(t_{k_1} - m_{\pi}^2)\bar{T}_{\pi\pi}^{cn}(k_1)}{2(k_2 \cdot k)}, \\ \frac{1}{2i}\text{Disc}_{\pi}^{t_{k_2}}\tilde{A}_1 &= \pi e \delta(t_{k_2} - m_{\pi}^2)\bar{T}_{\pi\pi}^{cn}(k_2), \\ \frac{1}{2i}\text{Disc}_{\pi}^{t_{k_2}}\tilde{A}_2 &= -2\frac{\pi e \delta(t_{k_2} - m_{\pi}^2)\bar{T}_{\pi\pi}^{cn}(k_2)}{2(k_1 \cdot k)},\end{aligned}\tag{9.13}$$

while all others are zero. Therefore, the pion-pole contributions to the scalar functions are

$$\begin{aligned}\tilde{A}_1^{\pi} &= e \left( \frac{\bar{T}_{\pi\pi}^{cn}(k_1)}{t_{k_1} - m_{\pi}^2} - \frac{\bar{T}_{\pi\pi}^{cn}(k_2)}{t_{k_2} - m_{\pi}^2} \right), \\ \tilde{A}_2^{\pi} &= \frac{e}{2(k_1 \cdot k)} \left( 2\frac{\bar{T}_{\pi\pi}^{cn}(k_2)}{t_{k_2} - m_{\pi}^2} \right) \\ &\quad + \frac{e}{2(k_2 \cdot k)} \left( 2\frac{\bar{T}_{\pi\pi}^{cn}(k_1)}{t_{k_1} - m_{\pi}^2} \right), \\ \tilde{A}_3^{\pi} &= 0.\end{aligned}\tag{9.14}$$

The amplitude is now gauge-invariant by construction because of the properties of the tensor structures. After some algebra, we can express the amplitude in a convenient form

$$\begin{aligned}M_{cn,\pi}^{\mu} &= \sum_{i=1}^3 \tilde{L}_i \tilde{A}_i^{\pi} \\ &= e \frac{k^{\mu}}{2} \left( -\frac{\bar{T}_{\pi\pi}^{cn}(k_1)}{k_1 \cdot k} + \frac{\bar{T}_{\pi\pi}^{cn}(k_2)}{k_2 \cdot k} \right) \\ &\quad + e \left( \frac{k_1^{\mu}}{k_1 \cdot k} - \frac{k_2^{\mu}}{k_2 \cdot k} \right) \left( \frac{\bar{T}_{\pi\pi}^{cn}(k_1) + \bar{T}_{\pi\pi}^{cn}(k_2)}{2} \right)\end{aligned}\tag{9.15}$$

This amplitude is obviously antisymmetric under  $k_1 \leftrightarrow k_2$  and is gauge-invariant by construction.

## 9.2 Charged channels

To calculate the amplitude for the charged channel, we refer to [60]. In the isospin limit, there is a relation between the neutral and charged channel:

$$\begin{aligned}\langle \pi^0(l_1)\pi^0(l_2)\pi^-(l_3)\pi^+(l_4)|J_{e.m.}^{\mu}(0)|0 \rangle &=: J^{\mu}(l_1, l_2, l_3, l_4) \\ \langle \pi^-(l_1)\pi^+(l_2)\pi^-(l_3)\pi^+(l_4)|J_{e.m.}^{\mu}(0)|0 \rangle &= J^{\mu}(l_1, l_2, l_3, l_4) + J^{\mu}(l_1, l_4, l_3, l_2) \\ &\quad + J^{\mu}(l_3, l_4, l_1, l_2) + J^{\mu}(l_3, l_2, l_1, l_4).\end{aligned}\tag{9.16}$$

We can directly use the result above for the processes  $\pi^+(k_1)\pi^-(k_2) \rightarrow \pi^+(p_1)\pi^-(p_2)\gamma(k)$  and  $\pi^+(k_1)\pi^+(k_2) \rightarrow \pi^+(p_1)\pi^+(p_2)\gamma(k)$ . In the first case, the corresponding matrix element is

$$\begin{aligned} \langle \pi^-(-p_2)\pi^+(-p_1)\pi^-(k_1)\pi^+(k_2) | J_{e.m.}^\mu(0) | 0 \rangle &= J^\mu(-p_2, -p_1, k_1, k_2) \\ &+ J^\mu(-p_2, k_2, k_1, -p_1) \\ &+ J^\mu(k_1, k_2, -p_2, -p_1) \\ &+ J^\mu(k_1, -p_1, -p_2, k_2). \end{aligned} \quad (9.17)$$

We define the amplitude for this charged process as  $M_c^\mu$ . We also use the already introduced functions,  $A := T_{\pi\pi}^{cn}(s, t, u)$ ,  $B := T_{\pi\pi}^{cn}(t, s, u)$ ,  $C := T_{\pi\pi}^{cn}(u, t, s)$  and the bar notation introduced above. Plugging in the result of the neutral amplitude (9.15) leads to

$$\begin{aligned} M_c^\mu &= e \frac{k^\mu}{2} \left( -\frac{\bar{A}(k_1)}{k_1 \cdot k} + \frac{\bar{A}(k_2)}{k_2 \cdot k} - \frac{\bar{B}(k_1)}{k_1 \cdot k} - \frac{\bar{B}(-p_1)}{p_1 \cdot k} \right. \\ &\quad \left. - \frac{\bar{A}(-p_1)}{p_1 \cdot k} + \frac{\bar{A}(-p_2)}{p_2 \cdot k} + \frac{\bar{B}(-p_2)}{p_2 \cdot k} + \frac{\bar{B}(k_2)}{k_2 \cdot k} \right) \\ &+ e \frac{k_1^\mu}{k_1 \cdot k} \left( \frac{\bar{A}(k_1) + \bar{A}(k_2) + \bar{B}(k_1) + \bar{B}(-p_1)}{2} \right) \\ &- e \frac{k_2^\mu}{k_2 \cdot k} \left( \frac{\bar{A}(k_1) + \bar{A}(k_2) + \bar{B}(-p_2) + \bar{B}(k_2)}{2} \right) \\ &- e \frac{p_1^\mu}{p_1 \cdot k} \left( \frac{\bar{A}(-p_1) + \bar{A}(-p_2) + \bar{B}(-p_1) + \bar{B}(k_1)}{2} \right) \\ &+ e \frac{p_2^\mu}{p_2 \cdot k} \left( \frac{\bar{A}(-p_1) + \bar{A}(-p_2) + \bar{B}(-p_2) + \bar{B}(k_2)}{2} \right) \\ &= e \frac{k^\mu}{2} \left( -\frac{\bar{T}_{\pi\pi}^c(k_1)}{k_1 \cdot k} + \frac{\bar{T}_{\pi\pi}^c(k_2)}{k_2 \cdot k} - \frac{\bar{T}_{\pi\pi}^c(-p_1)}{p_1 \cdot k} + \frac{\bar{T}_{\pi\pi}^c(-p_2)}{p_2 \cdot k} \right) \\ &+ e \frac{k_1^\mu}{k_1 \cdot k} \left( \frac{\bar{T}_{\pi\pi}^c(k_1) + \bar{T}_{\pi\pi}^c(k_2) + \bar{B}(-p_1) - \bar{B}(k_2)}{2} \right) \\ &- e \frac{k_2^\mu}{k_2 \cdot k} \left( \frac{\bar{T}_{\pi\pi}^c(k_1) + \bar{T}_{\pi\pi}^c(k_2) + \bar{B}(-p_2) - \bar{B}(k_1)}{2} \right) \\ &- e \frac{p_1^\mu}{p_1 \cdot k} \left( \frac{\bar{T}_{\pi\pi}^c(-p_1) + \bar{T}_{\pi\pi}^c(-p_2) + \bar{B}(k_1) - \bar{B}(-p_2)}{2} \right) \\ &+ e \frac{p_2^\mu}{p_2 \cdot k} \left( \frac{\bar{T}_{\pi\pi}^c(-p_1) + \bar{T}_{\pi\pi}^c(-p_2) + \bar{B}(k_2) - \bar{B}(-p_1)}{2} \right), \end{aligned} \quad (9.18)$$

where we used  $\bar{A} + \bar{B} = \bar{T}_{\pi\pi}^c$ , the purely hadronic  $\pi^+\pi^-$ -scattering amplitude. As we can see, the expression looks very similar to the neutral amplitude (9.15) above. The difference is the fact that the photon can be emitted from all four legs and the  $\bar{B}(l_i) - \bar{B}(l_j)$  terms. The latter turn out to be numerically very small and do not play an important role in the calculation. We will neglect them in the following.

We can apply a similar procedure for the process  $\pi^+(k_1)\pi^+(k_2) \rightarrow \pi^+(p_1)\pi^+(p_2)$ . In

this case, the matrix-element of interest is

$$\begin{aligned}
\langle \pi^-(-p_2)\pi^+(k_1)\pi^-(-p_1)\pi^+(k_2)|J_{e.m.}^\mu(0)|0\rangle &= J^\mu(-p_2, k_1, -p_1, k_2) \\
&+ J^\mu(-p_2, k_2, -p_1, k_1) \\
&+ J^\mu(-p_1, k_2, -p_2, k_1) \\
&+ J^\mu(-p_1, k_1, -p_2, k_2).
\end{aligned} \tag{9.19}$$

From there we do the same as before and get

$$\begin{aligned}
M_+^\mu &= e \frac{k^\mu}{2} \left( \frac{\bar{C}(-p_1)}{p_1 \cdot k} + \frac{\bar{C}(k_2)}{k_2 \cdot k} + \frac{\bar{B}(-p_1)}{p_1 \cdot k} + \frac{\bar{B}(k_1)}{k_1 \cdot k} \right. \\
&\quad \left. + \frac{\bar{C}(-p_2)}{p_2 \cdot k} + \frac{\bar{C}(k_2)}{k_2 \cdot k} + \frac{\bar{B}(-p_2)}{p_2 \cdot k} + \frac{\bar{B}(k_2)}{k_2 \cdot k} \right) \\
&+ e \frac{p_1^\mu}{p_1 \cdot k} \left( \frac{\bar{C}(-p_1) + \bar{C}(k_2) + \bar{B}(-p_1) + \bar{B}(k_1)}{2} \right) \\
&- e \frac{k_2^\mu}{k_2 \cdot k} \left( \frac{\bar{C}(-p_1) + \bar{C}(k_2) + \bar{B}(-p_2) + \bar{B}(k_2)}{2} \right) \\
&- e \frac{k_1^\mu}{k_1 \cdot k} \left( \frac{\bar{B}(-p_1) + \bar{B}(k_1) + \bar{C}(-p_2) + \bar{C}(k_1)}{2} \right) \\
&+ e \frac{p_2^\mu}{p_2 \cdot k} \left( \frac{\bar{C}(-p_2) + \bar{C}(k_1) + \bar{B}(-p_2) + \bar{B}(k_2)}{2} \right) \\
&= e \frac{k^\mu}{2} \left( \frac{\bar{T}_{\pi\pi}^{++}(-p_1)}{p_1 \cdot k} + \frac{\bar{T}_{\pi\pi}^{++}(k_2)}{k_2 \cdot k} + \frac{\bar{T}_{\pi\pi}^{++}(k_1)}{k_1 \cdot k} + \frac{\bar{T}_{\pi\pi}^{++}(-p_2)}{p_2 \cdot k} \right) \\
&+ e \frac{p_1^\mu}{p_1 \cdot k} \left( \frac{\bar{T}_{\pi\pi}^{++}(-p_1) + \bar{T}_{\pi\pi}^{++}(k_2) + \bar{B}(k_1) - \bar{B}(k_2)}{2} \right) \\
&- e \frac{k_2^\mu}{k_2 \cdot k} \left( \frac{\bar{T}_{\pi\pi}^{++}(k_2) + \bar{T}_{\pi\pi}^{++}(-p_1) + \bar{B}(-p_2) - \bar{B}(-p_1)}{2} \right) \\
&- e \frac{k_1^\mu}{k_1 \cdot k} \left( \frac{\bar{T}_{\pi\pi}^{++}(k_1) + \bar{T}_{\pi\pi}^{++}(-p_2) + \bar{B}(-p_1) - \bar{B}(-p_2)}{2} \right) \\
&+ e \frac{p_2^\mu}{p_2 \cdot k} \left( \frac{\bar{T}_{\pi\pi}^{++}(-p_2) + \bar{T}_{\pi\pi}^{++}(k_1) + \bar{B}(k_2) - \bar{B}(k_1)}{2} \right), \tag{9.20}
\end{aligned}$$

where we used  $\bar{B} + \bar{C} = \bar{T}^{++}$ , the purely hadronic  $\pi\pi$ -scattering amplitudes with exclusively positively-charged pions.

### 9.3 Ambiguity in the pion-pole contribution

The  $\pi\pi$  scattering amplitude  $\bar{T}_{\pi\pi}(l_i)$ ,  $l_i \in \{k_1, k_2, p_1, p_2\}$  is well-defined only when the four external legs are on-shell pions. In other words, defining  $s, t$  and  $u$  as the three Mandelstam variables of the corresponding process, the on-shell relation

$$s + t + u = 4m_\pi^2 \tag{9.21}$$

must be valid. In this case, the kinematic point can be located unambiguously on the Mandelstam plane.



In our case, however, it seems that the scattering amplitudes depend on the external kinematics and therefore do not fulfil the on-shell relation, but rather the "off-shell" relation

$$s + t + u = \hat{s} + 3m_\pi^2, \quad (9.22)$$

where  $\hat{s}$  is the sum of the momentum of the photon and of the pion to which it is attached,  $\hat{s} \in \{s_{p_1}, s_{p_2}, t_{k_1}, t_{k_2}\}$ , depending on the topology.

The solution to this puzzle is to choose which two of the three Mandelstam variables that are argument of the  $\pi\pi$ -scattering amplitude have to be fixed in (9.13), before integrating dispersively. This way, the third Mandelstam variable is determined by the on-shell relation (9.21) and the  $\pi\pi$ -scattering amplitude is well-defined. This a priori arbitrary choice causes an ambiguity in the definition of the pion pole .

Let us calculate the difference between an amplitude in (9.14) with fixed  $s$  and  $t$  and one with fixed  $s$  and  $u$ . We have for  $s = (p_1 + p_2)^2$ ,  $t = (k_2 - p_2)^2$  and  $u = (k_2 - p_1)^2$

$$\begin{aligned} & \bar{T}_{\pi\pi}(k_1)|_{s,t} - \bar{T}_{\pi\pi}(k_1)|_{s,u} \\ = & T_{\pi\pi}(s, t, 4m_\pi^2 - s - t) - T_{\pi\pi}(s, 4m_\pi^2 - s - u, u) \\ = & T_{\pi\pi}(s, t, 4m_\pi^2 - s - t) - T_{\pi\pi}(s, t + (m_\pi^2 - t_{k_1}), 4m_\pi^2 - s - t - (m_\pi^2 - t_{k_1})) \\ \xrightarrow{t_{k_1} \rightarrow m_\pi^2} & 0 \end{aligned} \quad (9.23)$$

In the last line, we used relation (9.22). We conclude that the difference between the two choices is not due to the pion pole, since it vanishes as  $t_{k_1}$  approaches  $m_\pi^2$ , but to higher intermediate states. Indeed, the dispersion relation should be unambiguously defined, once all intermediate states are taken into account.

At this point, the question is which choice is physically better motivated, such that the corresponding pion pole contribution leads to a good description of the process  $\gamma\pi\pi \rightarrow \pi\pi$ . Let us consider the  $\pi\pi$ -scattering amplitude in ChPT at tree-level:

$$T_c^{\text{ChPT, tree}}(s, t, u) = \frac{s - m_\pi^2}{f_\pi^2} + \frac{t - m_\pi^2}{f_\pi^2} = \frac{s + (t - u)}{2f_\pi^2}, \quad (9.24)$$

$$T_{cn}^{\text{ChPT, tree}}(s, t, u) = \frac{s - m_\pi^2}{f_\pi^2}. \quad (9.25)$$

The charged channel has a symmetric and an antisymmetric part in  $t$  and  $u$ . The neutral channel is completely symmetric in  $t$  and  $u$ . When  $s > 4m_\pi^2$  is the center-of-mass energy squared of the process, it is important to keep the symmetry of the amplitude in  $t$  and  $u$ . Therefore, we define new variables  $\nu := t + u$  and  $\bar{\nu} := t - u$ . Note that both (9.24) and (9.25) can be written in terms of  $s$  and  $\bar{\nu}$  exclusively. We choose to fix in both channels  $s$  and  $\bar{\nu}$  and express the third one as  $\nu = 4m_\pi^2 - s$ . This implies that the Mandelstam relation is fulfilled for the three variables  $\{s, \nu, \bar{\nu}\}$  and that the symmetry of the system is not spoiled by this choice.

## 9.4 Rescattering effects

The one-loop correction of figure 9.1b is more problematic to calculate, because of the points mentioned above. It is unrealistic to aim for a full dispersive treatment of the amplitude taking into account the singularities in the ten different kinematic variables. Things

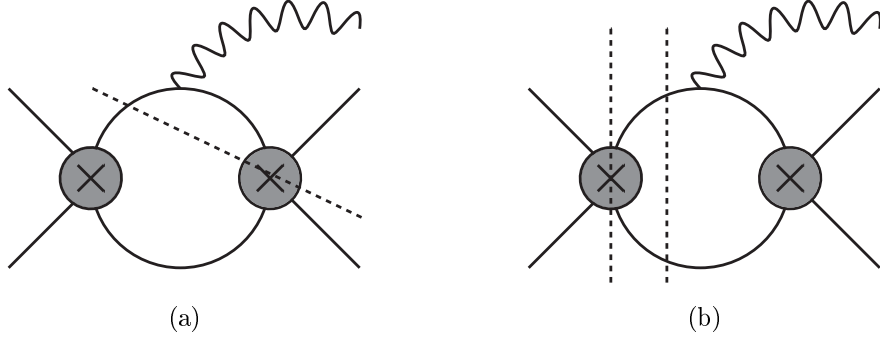


Figure 9.2: Different kind of cuts represented by the dashed line relevant in our choice of variables.

become much simpler if we only take into account the singularity in the  $s$ -channel. This is consistent with our prescription to only select intermediate states with at most two pions, since a cut in the four other channels would only start at the three-pion creation threshold. This case is depicted in diagram 9.2a. On the other hand, the cut in the  $s$ -channel depicted in diagram 9.2b starts at the two-pion threshold and must therefore be taken into account.

We are mostly interested in the case where the external pion pair (two pions on the left-hand side of figure 9.1b) is in a P-wave. In this case, the internal pion pair is in a wave with even angular momentum. Since waves with  $\ell \geq 2$  are neglected, we only consider the S-wave.

The kinematics in this case is simplified, since the corresponding  $\pi\pi$ -scattering amplitude only depends on the center-of-mass energy  $q^2$  of the internal two-pion system. The process of interest is  $\pi^+(k_2)\pi^-(k_1) \rightarrow \gamma(k)\Pi(q)$  where  $\Pi(q)$  represents the internal two-pion system. The kinematic situation is described in appendix A.

In order to calculate this object, we must first contract the tensorial amplitude with the three polarization vectors  $\epsilon^{\lambda_i}$ , in order to end up with a scalar helicity amplitude

$$H_c^\lambda := \epsilon_\mu^\lambda M_c^\mu. \quad (9.26)$$

For a photon whose 3-momentum points in the direction of the third spatial axis, the explicit representation of the polarization vectors are

$$\epsilon^\pm = \mp \frac{1}{\sqrt{2}}(0, 1, \pm i, 0), \quad (9.27)$$

$$\epsilon^0 = \frac{1}{\sqrt{2}}(1, 0, 0, 1). \quad (9.28)$$

The helicity amplitude can be expanded in partial waves. Similarly to (8.3), since the photon has a non-zero spin, the expansion is more general than in the case of zero-spin particles and Wigner functions must be considered instead of Legendre polynomials. Consider a scattering amplitude where the incoming particles have spins  $\mu_{1,2}$  and the outgoing ones  $\mu'_{1,2}$  and  $\mu = \mu_1 - \mu_2$  and  $\mu' = \mu'_1 - \mu'_2$ . Then, the corresponding helicity amplitude can be expanded as

$$H_{\mu\mu'}(s, q^2, \theta) = \sum_J (2J+1) d_{\mu\mu'}^J(\cos\theta) h^J(s, q^2). \quad (9.29)$$

In this expression,  $d_{\mu\mu'}^J$  is the Wigner  $d$ -function. In the limit  $\mu, \mu' = 0$ , this function is identical to the Legendre polynomial:  $d_{00}^J(\cos\theta) = P_J(\cos\theta)$ . In our case, we have  $\mu = 1$ ,  $\mu' = 0$ . This corresponds to the function

$$d_{10}^J = \frac{-\sin\theta P_J'(\cos\theta)}{\sqrt{J(J+1)}} = \frac{-\sin\theta}{\sqrt{2}}. \quad (9.30)$$

The helicity amplitude can therefore be written as

$$H_c^\lambda(s, q^2, \theta) = \sum_J (2J+1) d_{10}^J(\cos\theta) h_c^{\lambda,J}(s, q^2), \quad (9.31)$$

and the projection on the partial-wave amplitudes is

$$h_c^{\lambda,J}(s, q^2) = \frac{1}{2} \int_{-1}^1 dz H_c^\lambda(s, q^2, \theta) d_{10}^J(\cos\theta). \quad (9.32)$$

We can now consider the discontinuity of the helicity amplitude along its  $s$ -channel cut. The latter is given by the two cuts in figure 9.2b. Defining  $h_{c,\pi}^{\lambda,J}$  as the pion-pole contribution and  $h_{c,\pi\pi}^{\lambda,J}$  the rescattering contribution projected on the partial wave with angular momentum  $J$ , we have

$$\begin{aligned} \frac{\text{Disc } h_c^{\lambda,1}(s, q^2)}{2i} &= \frac{\text{Disc} \left( h_{c,\pi\pi}^{\lambda,1}(s, q^2) + h_{c,\pi}^{\lambda,1}(s, q^2) \right)}{2i} \\ &= \sigma_\pi(s) \left( h_{c,\pi\pi}^{\lambda,1}(s, q^2) + h_{c,\pi}^{\lambda,1}(s, q^2) \right) t_1^{1*}(s). \end{aligned} \quad (9.33)$$

Thus, the P-wave of the  $\pi\pi$ -scattering amplitude is multiplying the whole imaginary part. This is a typical case of Watson's theorem. In order to calculate the real part of the helicity amplitude from this relation, we rely on a modified Omnès-Muskhelishvili method. The latter has been used in several works (see for instance [79, 82, 83] and in particular [84] for a detailed derivation). The general idea is to define

$$\bar{h}_c^{\lambda,1}(s, q^2) := \frac{h_c^{\lambda,1}(s, q^2) - h_{c,\pi}^{\lambda,1}(s, q^2)}{\Omega_1^1(s)} \quad (9.34)$$

with the Omnès function defined above as

$$\Omega_1^1(s) = \exp \left( \frac{s}{\pi} \int_{4m_\pi^2}^{\infty} ds' \frac{\delta_1^1(s')}{s'(s' - s)} \right). \quad (9.35)$$

The particularity of this newly-defined function (9.34) is that the  $s$ -channel cut in the first term of the numerator is exactly cancelled by the cut of the Omnès function. This is obvious from (9.33). Moreover, as already mentioned, cuts from other channels are neglected. The second term in the numerator, the pion-pole contribution, has no cut in the  $s$ -channel. Therefore the discontinuity on the right-hand cut is

$$\begin{aligned} \text{Disc } \bar{h}_c^{\lambda,1}(s, q^2) &= -h_{c,\pi}^{\lambda,1}(s, q^2) \text{Disc} \left( \Omega_1^1(s) \right)^{-1} \\ &= h_{c,\pi}^{\lambda,1}(s, q^2) \frac{2i \sin \delta_1^1(s)}{|\Omega_1^1(s)|} \end{aligned} \quad (9.36)$$

Once the discontinuity of  $\bar{h}_c^{\lambda,1}(s, q^2)$  is known, we can reconstruct it dispersively using a once-subtracted dispersion relation. To that end, it is convenient to define

$$h_{c,\pi}^{\lambda,1}(s, q^2) := T_{\pi\pi}^0(q^2) \frac{\tilde{h}_{c,\pi}^{\lambda,1}(s, q^2)}{s - q^2} \quad (9.37)$$

where  $T_{\pi\pi}^0(q^2)$  is the  $S$ -wave contribution to the  $\pi\pi$ -scattering amplitude in (9.18). Note that it only depends on  $q^2$ .

The Omnès function is assumed to have its phase going asymptotically to  $\pi$  and therefore goes itself as  $\Omega_1^1(s) \xrightarrow{s \rightarrow \infty} s^{-1}$ . Also, the projected pion-pole contribution goes as  $h_{c,\pi}^{\lambda,1} \xrightarrow{s \rightarrow \infty} \sqrt{s}$ . This allows us to calculate  $h_c^{\lambda,1}(s, q^2)$  as a once-subtracted dispersive integral.

$$h_c^{\lambda,1}(s, q^2) = h_{c,\pi}^{\lambda,1}(s, q^2) + \Omega_1^1(s) \left[ c(q^2) + T_{\pi\pi}^0(q^2) \frac{J^\pi(s) - J^\pi(q^2)}{s - q^2} \right] \quad (9.38)$$

$$J^\pi(s) = \frac{s}{\pi} \int_{4m_\pi^2}^{\infty} ds' \frac{\sin \delta_1^1(s') \tilde{h}_{c,\pi}^{\lambda,1}(s', q^2)}{|\Omega_1^1(s')| s'(s' - s)}. \quad (9.39)$$

Note that we have used the relation

$$\frac{1}{(s' - s)(s' - q^2)} = \frac{1}{s - q^2} \left( \frac{1}{s' - s} - \frac{1}{s' - q^2} \right) \quad (9.40)$$

to rewrite the dispersive integral as the difference in  $s$  and  $q^2$ . Also, there is no contribution from the other channels since all of them start at least at the three-pion threshold. Note that the subtraction function depends on  $q^2$ . The latter is expected to have a cut at the two-pion creation threshold  $q^2 = 4m_\pi^2$ . In order to fix it, we rely on the general soft-photon theorem of Low [85]. The general structure (9.11) implies that only the pion-pole contribution survives in the soft-photon limit. This happens when  $q^2 \rightarrow s$ . We thus impose that the rescattering contribution exactly vanishes when the photon becomes soft. The constraint is therefore

$$c(q^2) + T_{\pi\pi}^0(q^2) \frac{d}{ds} J^\pi(s) \Big|_{s \rightarrow q^2} = 0. \quad (9.41)$$

Numerically, the contribution of the rescattering effect is almost negligible compared to the pion-pole term. This is due to the fact that when there are two pion-pole amplitudes in a phase-space product, the latter is infrared divergent and thus enhanced. On the other hand, the presence of such a rescattering amplitude implies that there is no infrared divergence. The situation is similar to the one in the case of  $\gamma^* \gamma \rightarrow \pi\pi$ . We therefore do not include the contribution from this amplitude in our calculation, but just as part of the uncertainty.

## 9.5 Cross section $\sigma(\gamma\pi \rightarrow 3\pi)$

To check the consistency of the formalism, we compare the cross section  $\sigma(\gamma\pi \rightarrow 3\pi)$  calculated from our amplitude to the one from tree-level and one-loop ChPT. This calculation has been done in [80].

In order to take into account the higher intermediate states, we include in the uncertainty the contribution from resonances. Either a  $\omega(782)$  or a  $a_1(1260)$  resonance could

indeed replace the pion in the topology depicted in figure 9.1a. The amplitude for such processes has been derived in [60]. The uncertainty on the partial waves of the  $\pi\pi$ -scattering amplitude are also included.

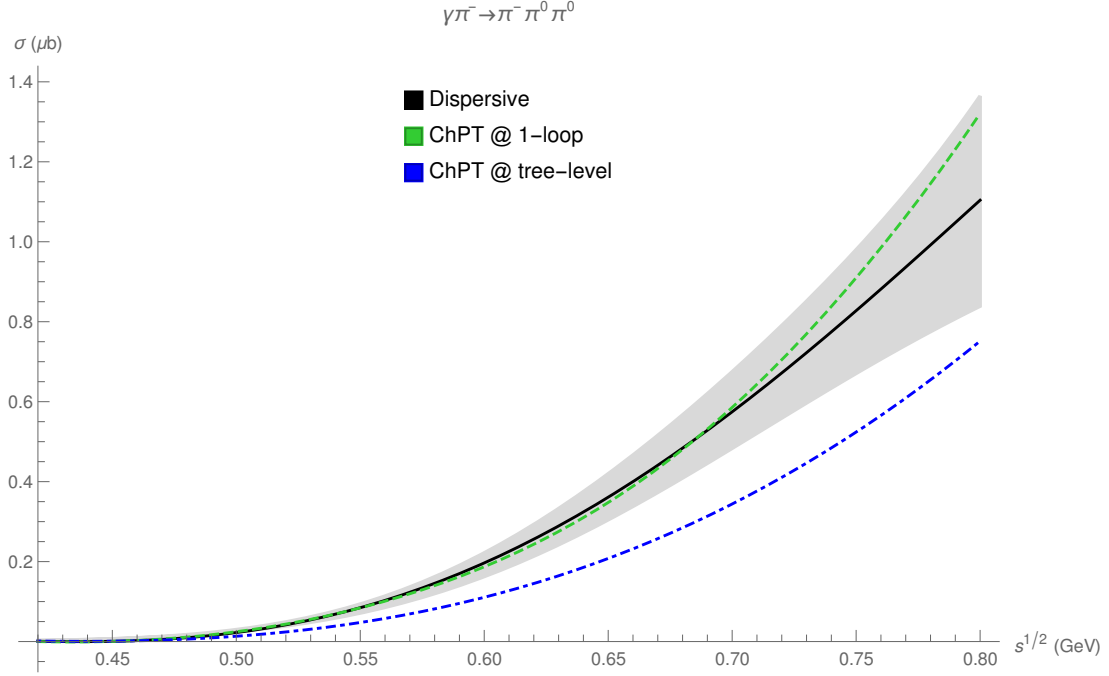


Figure 9.3: Cross section for the process  $\gamma\pi^- \rightarrow \pi^-\pi^0\pi^0$

Concerning the process  $\gamma\pi^- \rightarrow \pi^-\pi^0\pi^0$ , the result is depicted on the plot of figure 9.3. Concerning the process  $\gamma\pi^- \rightarrow \pi^-\pi^+\pi^-$ , a measurement has been performed by COMPASS [86]. We can therefore include the data points in the plot as well. The latter is depicted in figure 9.4.

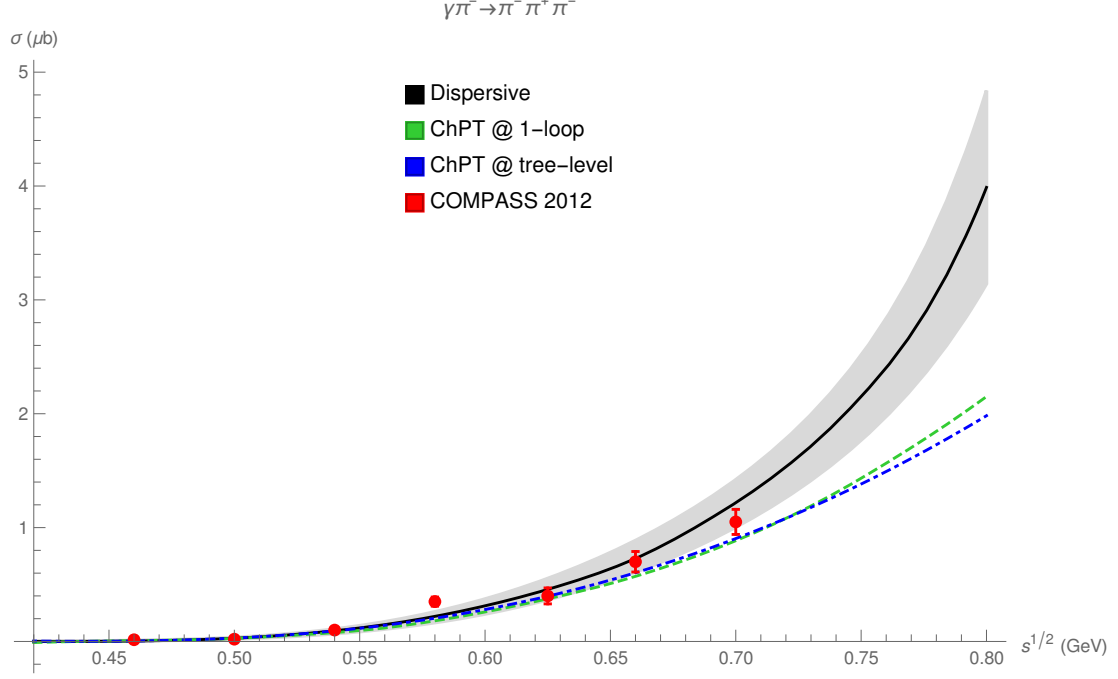


Figure 9.4: Cross section for the process  $\gamma\pi^- \rightarrow \pi^- \pi^+ \pi^-$

We can see that in the first case, the dispersive result is very close to ChPT at one loop. In the second case, there is a large enhancement of the cross section at higher energy compared to the result from ChPT. This can be caused by the  $\rho(770)$  exchange in the  $\pi^+ \pi^-$  channel that is not present in the case of a neutral-pion pair.

In both cases, the result agrees well with ChPT at low energy.

# Chapter 10

## Building block $T_{\pi\pi}^\alpha$

In this chapter, we calculate the contribution from virtual-photon exchanges to the  $\pi\pi$ -scattering amplitude,  $T_{\pi\pi}^\alpha(s, t)$ . Such corrections have been calculated in ChPT in the presence of electromagnetism at the one-loop level including charged and neutral pions in [7, 8]. This calculation is explained in section 4.6. In order to extend the calculation to a scale at which the low-energy expansion of ChPT breaks down, we apply the prescription discussed in section 7.2 based on unitarity and analyticity on the  $\pi\pi$ -scattering amplitude. In what follows, we explain the different dispersive methods used in the calculation. We stress that this is the first time that such a formalism is used for the calculation of those radiative corrections.

### 10.1 Topologies

The two-pion prescription at order  $\alpha$  explained in section 7.2 leads to a finite number of topologies, depending on the pion legs between which the photon is exchanged and how many occurrences of  $\pi\pi$  rescattering are present. Those topologies are depicted in figures 10.1. The notation that we use for the corresponding amplitudes is  $T_{(i)}(s, t)$ ,  $i \in \{0, \dots, 4\}$  and is summarized in appendix G. Note that those diagrams must be understood as unitarity diagrams. By unitarity diagram we mean that the imaginary part is obtained by cutting them in all possible ways. The pion and photon lines cut in that fashion are automatically on-shell. This implies that the hadronic blobs at the vertices of the diagrams are the purely hadronic amplitudes. The grey ones represent the pion vector form factor and the crossed ones the  $\pi\pi$ -scattering amplitudes, as shown in figure 7.3. The most convenient choice of pion basis is the physical basis defined by the charge of the pions.

At very low energy, the chiral ordering scheme implies that each occurrence of  $\pi\pi$  rescattering is suppressed by  $p^2$ . This means that, in that regime, there is a hierarchy between the diagrams of figure 10.1. The dominant one is diagram 10.1a, only consisting of a photon exchange between two pion legs. Diagrams 10.1b - 10.1d contain one additional occurrence of  $\pi\pi$  rescattering and are therefore suppressed by an additional  $p^2$ . Finally, diagrams 10.1e - 10.1f and diagram 10.1g are even less important, since they contain respectively two and three  $\pi\pi$  rescatterings and are suppressed by  $p^4$  and  $p^6$ . As we increase energy, however, the chiral expansion gradually loses its validity. To extend the calculation up to an energy as large as 1 GeV, we rely on the dispersive framework. In that framework, each grey blob in figure 10.1 contains an a priori infinite number of  $\pi\pi$  rescatterings and

there is no more hierarchy between the different diagrams. There is therefore no particular reason for the diagrams 10.1e - 10.1g to be suppressed compared to the others and all of them must be calculated by solving the dispersion relation. Note that an exact solution of the dispersion relation means a resummation of local interaction vertices.

An important feature of the dispersive framework is that, in order to calculate the discontinuity from the unitarity relation of a particular topology, one has to cut through hadronic blobs too when possible. This has an interesting consequence for diagrams 10.1e - 10.1g, since their unitarity relation leads to an implicit integral equation. To solve such an equation, we have to rely on numerical methods that will be explained in the corresponding section.

The contributions are projected on the  $s$ -channel P-wave, since those enter the unitarity relation of the pion vector form factor. In what follows, we write the partial-wave amplitude of the different corrections as

$$T_{(i)}(s, t) = \sum_j \tilde{T}_{(i)}^j(s) P_j \left( 1 + \frac{2t}{s - 4m_\pi^2} \right), \quad i \in \{0, 1, 2, 3, 4\}. \quad (10.1)$$

The main difference with the analytic properties of the pion vector form factor is the presence of a left-hand cut. This means that additionally to the  $s$ -channel P-wave projection of those topologies for the process  $\pi^+\pi^- \rightarrow \pi^+\pi^-$ , we also need to calculate the S-wave projection for the processes  $\pi^+\pi^- \rightarrow \pi^+\pi^-$  and  $\pi^+\pi^+ \rightarrow \pi^+\pi^+$ . Consider as an illustration diagram 10.1e, where the two incoming and outgoing pions are a pair of charged pions. The right-hand cut is obtained by cutting the diagram in the  $s$ -channel. Moreover, the same diagram rotated by 90 degrees contributes as well to the process. This could correspond either to the process  $\pi^+\pi^- \rightarrow \pi^+\pi^-$  in the  $t$ -channel or to  $\pi^+\pi^+ \rightarrow \pi^+\pi^+$  in the  $u$ -channel.

## 10.2 Tree-level photon exchange (topology 10.1a)

Let us start with the diagram of figure 10.1a. The hadronic blobs are described by pion vector form factors because the external pions are on-shell. The  $t$ -channel photon exchange is calculated as

$$T_{(0)}(s, t) = 4\pi\alpha \frac{2s + t - 4m_\pi^2}{t} F_\pi^V(t)^2. \quad (10.2)$$

Note that in the case where the bottom pion line has the same charge as the one at the top, the amplitude gets an additional minus sign due to the photon interaction.

The goal is to project the amplitude on partial waves (S or P) to allow one to use those directly in the unitarity relation as a building block. Note that we are not interested in the case where the photon is exchanged in the  $s$ -channel which only contributes to the hadronic polarization of the photon.

The amplitude has a pole when the virtuality of the photon vanishes. This is due to the photon exchange in the  $t$ -channel. This singularity happening at zero momentum transfer is physical and referred to as Coulomb pole. Because of this feature, when projecting the amplitude on partial waves, the result is divergent. Therefore, it does not make sense to



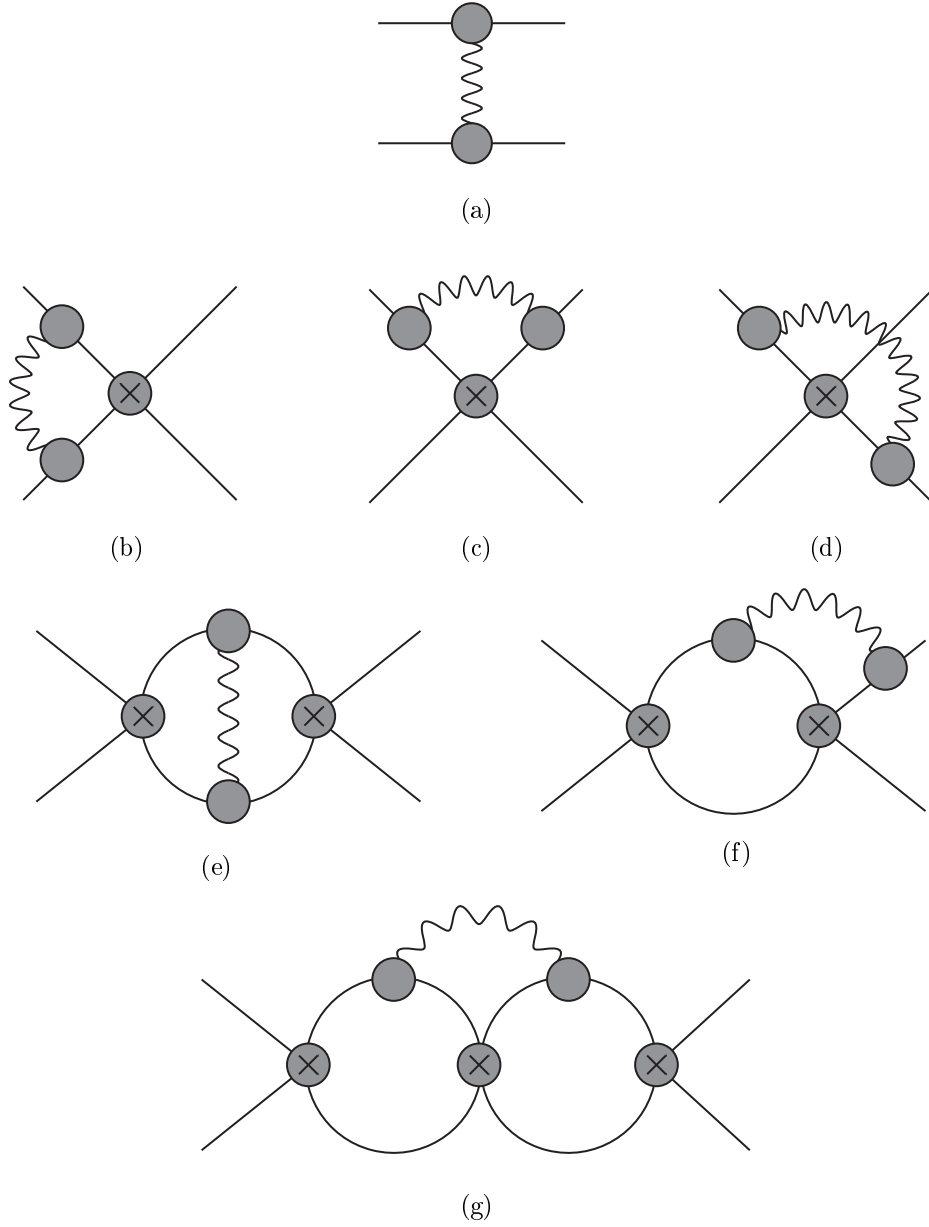


Figure 10.1: Topologies contributing to the radiative correction to the  $\pi\pi$ -scattering amplitude. Note that they are classified according to the number of occurrences of  $\pi\pi$  rescattering. There is none in diagram 10.1a, one in 10.1b - 10.1d, two in 10.1e - 10.1f and three in 10.1g.

take this contribution as a correction to the different partial waves. At the level of the cross-section, this contribution would also make the total cross section diverge when integrating over the full phase space. However, this happens when the two pairs of pions are exactly collinear and this can not be observed experimentally.

In our case, the diagram of figure 10.1a is used as a subamplitude in the unitarity relation of different topologies. This will be the case for instance in diagram 10.1c. In such diagrams, the divergence due to the projection is of infrared nature and is cancelled by the soft-photon emission corresponding to the topology it contributes to. Thus, we need to regularize this amplitude with a finite photon mass  $m_\gamma$ . At the level of diagram 10.1a, this means that we must carry out the calculation analytically and isolate the term proportional to  $\log(m_\gamma^2)$ . This is however not trivial because of the form factors present at each of the two  $\pi\pi\gamma$  vertices. In practice, what we do is to subtract it with the same amplitude expressed in the soft-photon limit, that is, where the hadronic vertices represented by the black blobs are replaced by 1. We write the partial-wave amplitude as follows:

$$\begin{aligned}
\tilde{T}_{(0)}^l(s) &= \frac{2l+1}{2} \int_{-1}^1 dz P_l(z) T_{(0)}(s, z) \\
&= \frac{2l+1}{2} \int_{-1}^1 dz P_l(z) \left( T_{(0)}(s, z) - T_{(0)}(s, z)|_{F_\pi^V(t) \rightarrow 1} \right) \\
&\quad + \frac{2l+1}{2} \int_{-1}^1 dz P_l(z) T_{(0)}(s, z)|_{F_\pi^V(t) \rightarrow 1} \\
&=: \tilde{T}_{(0),\text{fin}}^l + \tilde{T}_{(0),\text{IR}}^l
\end{aligned} \tag{10.3}$$

It is convenient to express the partial wave in that way, since the term in brackets is infrared-finite and the integral can be carried out numerically. Also, the second term does not contain any hadronic object and can be integrated analytically. The infrared divergence can thus be regularized and identified explicitly. The explicit projection on the S- and P-wave are

$$\begin{aligned}
\tilde{T}_{(0),\text{IR}}^0(s) &= \frac{1}{2} \int_{-1}^1 dz P_0(z) T_{(0)}(s, z)|_{F_\pi^V(t) \rightarrow 1} \\
&= \frac{1}{2} \int_{-1}^1 dz e^2 \frac{s(z+3) - 4m_\pi^2(z+1)}{2m_\gamma^2 + (z-1)(4m_\pi^2 - s)} \\
&= -e^2 \frac{(2s - 4m_\pi^2) \log\left(\frac{1}{(s-4m_\pi^2)}\right) + s - 4m_\pi^2}{(s - 4m_\pi^2)} \\
&\quad - e^2 \frac{(2s - 4m_\pi^2) \log(m_\gamma^2)}{(s - 4m_\pi^2)} + \mathcal{O}(m_\gamma^2).
\end{aligned} \tag{10.4}$$

$$\begin{aligned}
\tilde{T}_{(0),\text{IR}}^1(s) &= \frac{3}{2} \int_{-1}^1 dz P_1(z) T_{(0)}(s, z)|_{F_\pi^V(t) \rightarrow 1} \\
&= \frac{3}{2} \int_{-1}^1 dz z e^2 \frac{s(z+3) - 4m_\pi^2(z+1)}{2m_\gamma^2 + (z-1)(4m_\pi^2 - s)} \\
&= -e^2 \frac{3(2s - 4m_\pi^2) \left[ \log\left(\frac{1}{(s-4m_\pi^2)}\right) + 2 \right]}{(s - 4m_\pi^2)} \\
&\quad - \frac{(3e^2(2s - 4m_\pi^2) \log(m_\gamma^2))}{(s - 4m_\pi^2)} + \mathcal{O}(m_\gamma^2).
\end{aligned} \tag{10.5}$$

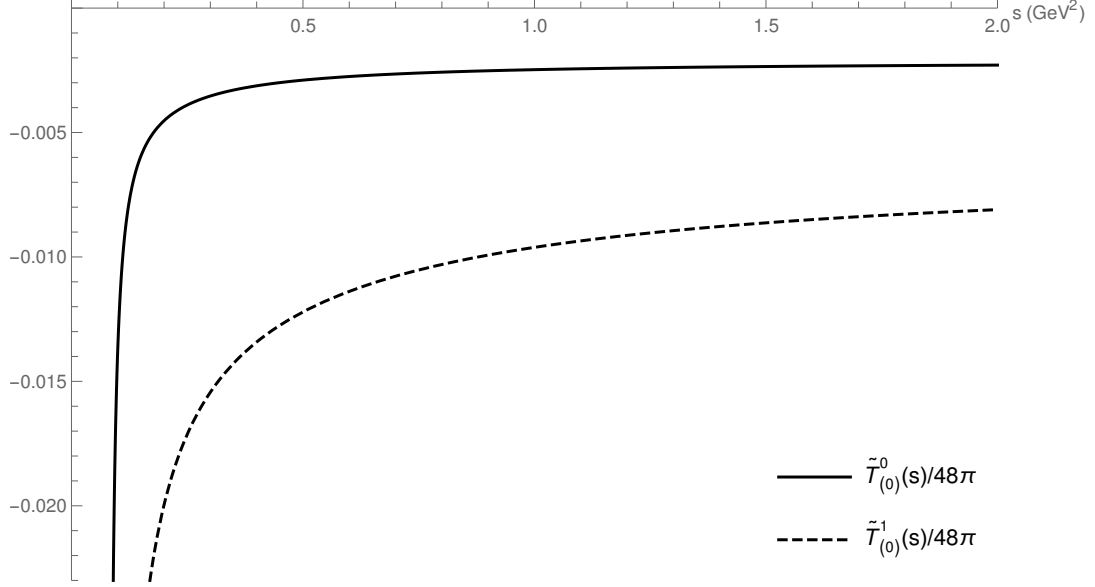


Figure 10.2: Infrared-finite part of the S- and P-wave projection of  $T_{(0)}(s, t)$

In both cases, the divergent part proportional to  $\log m_\gamma^2$  has been singled out. Note that the remaining part behaves as  $\frac{\log(s-4m_\pi^2)}{s-4m_\pi^2}$  as  $s \rightarrow 4m_\pi^2$  and thus diverges at the two-pion threshold. This behaviour is shown in the plot of figure 10.2 in the case of the S- and P-wave projections.

### 10.3 Direct triangle (topology 10.1b)

In principle, the topologies 10.1b - 10.1d are all related by crossing symmetry and should be calculated in the same framework. In practice, however, an implicit dependence in the unitarity relation makes the calculation more involved. We therefore decided to treat differently the contributions from diagram 10.1b that we call *direct triangle* and diagrams 10.1c - 10.1d that we call *crossed triangles*.

Let us first define the  $\pi\pi$ -scattering amplitudes in the physical basis. We consider the three processes:  $\pi^+\pi^- \rightarrow \pi^+\pi^-$ ,  $\pi^+\pi^- \rightarrow \pi^0\pi^0$  and  $\pi^0\pi^0 \rightarrow \pi^0\pi^0$ . According to chapter 4, those can be expanded in partial waves as

$$\begin{aligned} T_{\pi\pi}^c(s, t) &= T(\pi^+\pi^- \rightarrow \pi^+\pi^-) \\ &= 32\pi \sum_{\ell} (2\ell + 1) t_c^\ell(s) P_\ell \left( 1 + \frac{2t}{s - 4m_\pi^2} \right), \end{aligned} \quad (10.6)$$

$$\begin{aligned} T_{\pi\pi}^{cn}(s, t) &= T(\pi^+\pi^- \rightarrow \pi^0\pi^0) \\ &= 32\pi \sum_{\ell} (2\ell + 1) t_{cn}^\ell(s) P_\ell \left( 1 + \frac{2t}{s - 4m_\pi^2} \right), \end{aligned} \quad (10.7)$$

$$\begin{aligned} T_{\pi\pi}^n(s, t) &= T(\pi^0\pi^0 \rightarrow \pi^0\pi^0) \\ &= 32\pi \sum_{\ell} (2\ell + 1) t_n^\ell(s) P_\ell \left( 1 + \frac{2t}{s - 4m_\pi^2} \right). \end{aligned} \quad (10.8)$$

where the partial waves in the physical basis are defined as

$$t_A^\ell(s) = c_\ell^{A,I} t_\ell^I(s) \quad A \in \{c, cn, n\}. \quad (10.9)$$

The coefficients  $c_I^{c,j}$ ,  $c_I^{cn,j}$  and  $c_I^{n,j}$  correspond to the coefficients in the decomposition of the amplitudes of the corresponding processes in the isospin basis (4.10).

The diagram in figure 10.1a only contributes to the fully charged process  $\pi^+\pi^- \rightarrow \pi^+\pi^-$ . On the other hand, both  $\pi^+\pi^- \rightarrow \pi^+\pi^-$  and  $\pi^+\pi^- \rightarrow \pi^0\pi^0$  get a contribution from the topology of figure 10.1b. We define those corrections respectively as  $T_{(1)}^c(s, t)$  and  $T_{(1)}^{cn}(s, t)$ . Those corrections have two cuts in the  $s$ -channel. The first one goes through the two-pion state and the second one through the hadronic blob. While the cut through the two-pion state only involves charged pions in the intermediate state, neutral pions must also be taken into account in the cut through the hadronic blob. The discontinuity in the case of the fully-charged channel is

$$\begin{aligned} \frac{\text{Disc}_s T_{(1)}^c(s, t)}{2i} &= \frac{(2\pi)^4}{2} \int d\Phi_2 \left( T_{(0)}(s, t_1) + T_{(1)}^c(s, t_1) \right) T_{\pi\pi}^{c*}(s, t_2) \\ &\quad + \frac{(2\pi)^4}{4} \int d\Phi_2 T_{(1)}^{cn}(s, t_1) T_{\pi\pi}^{cn*}(s, t_2) \\ &= 2\sigma_\pi(s) \sum_{I,j} \left( \tilde{T}_{(0)}^j(s) + \tilde{T}_{(1)}^{c,j}(s) \right) c_j^{c,I} P_j \left( 1 + \frac{2t}{s - 4m_\pi^2} \right) t_j^I(s)^* \\ &\quad + \sigma_\pi(s) \sum_{I,j} \left( \tilde{T}_{(1)}^{cn,j}(s) \right) c_j^{cn,I} P_j \left( 1 + \frac{2t}{s - 4m_\pi^2} \right) t_j^I(s)^*. \end{aligned} \quad (10.10)$$

On the other hand, the discontinuity contributing to the process  $\pi^+\pi^- \rightarrow \pi^0\pi^0$  is

$$\begin{aligned} \frac{\text{Disc}_s T_{(1)}^{cn}(s, t)}{2i} &= \frac{(2\pi)^4}{2} \int d\Phi_2 \left( T_{(0)}(s, t_1) + T_{(1)}^c(s, t_1) \right) T_{\pi\pi}^{cn*}(s, t_2) \\ &\quad + \frac{(2\pi)^4}{4} \int d\Phi_2 T_{(1)}^{cn}(s, t_1) T_{\pi\pi}^{n*}(s, t_2) \\ &= 2\sigma_\pi(s) \sum_{I,j} \left( \tilde{T}_{(0)}^j(s) + \tilde{T}_{(1)}^{c,j}(s) \right) c_j^{cn,I} P_j \left( 1 + \frac{2t}{s - 4m_\pi^2} \right) t_j^I(s)^* \\ &\quad + \sigma_\pi(s) \sum_{I,j} \left( \tilde{T}_{(1)}^{cn,j}(s) \right) c_j^{n,I} P_j \left( 1 + \frac{2t}{s - 4m_\pi^2} \right) t_j^I(s)^*. \end{aligned} \quad (10.11)$$

The phase-space differential is defined in appendix B and the kinematics of the process  $2 \rightarrow 2 \rightarrow 2$  is described in appendix A. Note also the additional factor 1/2 in the case of neutral pions in the intermediate state. This is due to the fact that the two particles are identical and only half of the phase-space must be integrated over. In the last line, we expanded the discontinuity in partial waves.

### 10.3.1 P-wave contribution

In the case of the P-wave projection of the fully-charged process, there is no contribution from two neutral pions since they are always in a wave with even angular momentum and the second term in (10.10) vanishes. We project the discontinuity that can be related to the imaginary part on the cut and find

$$\text{Im} \tilde{T}_{(1)}^1(s) = \sigma_\pi(s) \left( \tilde{T}_{(0)}^1(s) + \tilde{T}_{(1)}^1(s) \right) t_1^1(s)^*. \quad (10.12)$$

Note that we dropped the index  $c$ , since there is no P-wave in the neutral channel. This equation implies that the phase of  $\tilde{T}_{(0)}^1(s) + \tilde{T}_{(1)}^1(s)$  must be identical to the phase of the  $\pi\pi$ -scattering P-wave. This is a manifestation of the Watson's final state theorem. In order to find a solution satisfying the theorem, we use a modified Omnès-Muskhelishvili method. We define

$$\bar{T}^1(s) := \frac{\left(\tilde{T}_{(0)}^1(s) + \tilde{T}_{(1)}^1(s)\right) - \tilde{T}_{(0)}^1(s)}{\Omega_1^1(s)}, \quad (10.13)$$

where the Omnès function is the one defined in (9.35). In this way, the discontinuity on the right-hand cut of the term in brackets is exactly cancelled by the Discontinuity of the Omnès function. Note also that  $\tilde{T}_{(0)}^1(s)$  is purely real on the right-hand cut. Therefore, the discontinuity is

$$\begin{aligned} \text{Disc } \bar{T}^1(s) &= \text{Disc } (\Omega_1^1)^{-1} \left( -\tilde{T}_{(0)}^1(s) \right) \\ &= \frac{2i \sin \delta_1^1(s)}{|\Omega_1^1(s)|} \tilde{T}_{(0)}^1(s). \end{aligned} \quad (10.14)$$

In order to reconstruct the real part, we express  $\tilde{T}_{(1)}^1(s)$  as a twice-subtracted dispersive integral. In principle only one subtraction should be sufficient. However, in this case the contribution from the high-energy tail of the integrand turned out to be rather large. The second subtraction allows us to suppress this contribution. The drawback is the introduction of two subtraction constants. We write the amplitude as

$$\tilde{T}_{(1)}^1(s) = \Omega_1^1(s) \left( c_{(1),0}^1 + c_{(1),1}^1 s + \frac{s^2}{\pi} \int_{4m_\pi^2}^{\infty} ds' \frac{\sin \delta_1^1(s') \tilde{T}_{(0)}^1(s')}{|\Omega_1^1(s')|(s' - s)s'^2} \right). \quad (10.15)$$

In order to fix the subtraction constants  $c_{(1),0}^1$  and  $c_{(1),1}^1$ , we use the ChPT result presented in section 4.6. We project the part of the ChPT amplitude that has a dependence on  $e^2$  on the P-wave. Note that the term proportional to the pion vector form factor in (4.31) accounts for diagram (10.1a) and is not taken into account in the subtraction constant. Note also that we ignore the part of the amplitude consisting of loop functions  $G_{+-\gamma}$  and  $\bar{J}$  explicitly depending on the crossed variables  $t$  and  $u$ . This is because we are essentially interested in the diagram of figure 10.1b that only related to the  $s$ -dependent loop functions. Concerning the contact terms, there is no unambiguous way to distinguish between those contributing to the topology of interest. We therefore simply select 1/6 of the contribution, thereby equally distributing among the triangles.

It is possible to match the amplitude (10.15) to the ChPT amplitude (4.31) by expanding the Omnès function and the phase-shift  $\delta_1^1(s)$  in (10.15) in  $s$ . For  $s > 4m_\pi^2$  near threshold, the partial waves can be expanded as [87]

$$\text{Ret}_\ell^I(s) = \left( \frac{s - 4m_\pi^2}{4} \right) \left[ a_\ell^I + b_\ell^I \left( \frac{s - 4m_\pi^2}{4} \right) + \dots \right] \quad (10.16)$$

where the  $a_\ell^I$  are the scattering lengths and the  $b_\ell^I$  the effective ranges. At order  $p^2$  in ChPT, the P-wave is given by

$$t_1^1(s)_2 = \frac{s - 4m_\pi^2}{96\pi F^2}. \quad (10.17)$$

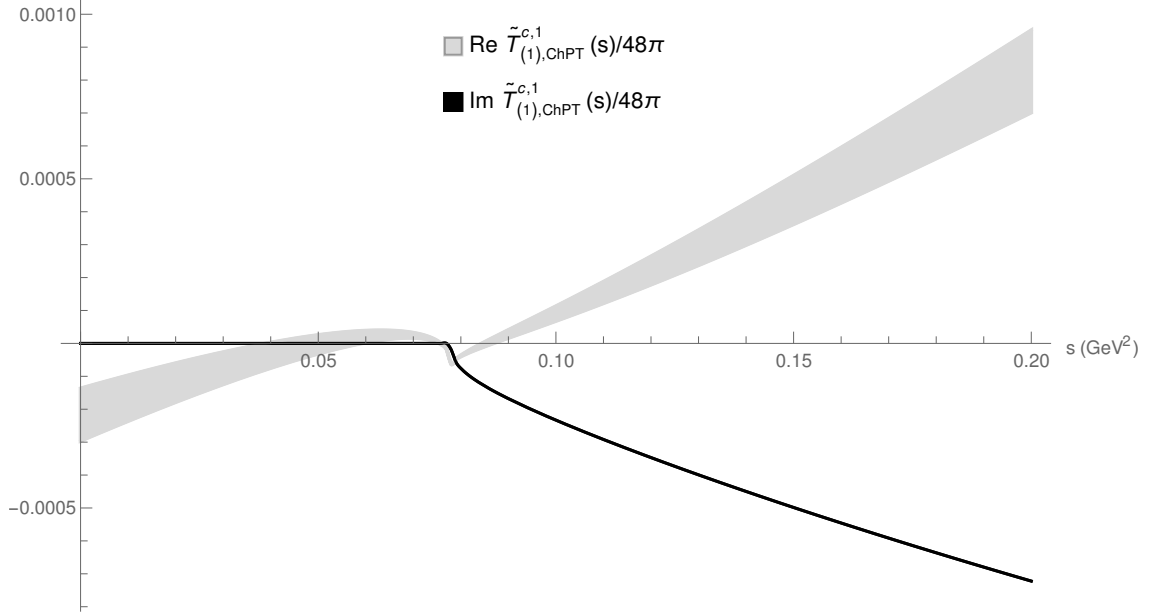


Figure 10.3: Real and imaginary part of the ChPT amplitude 4.31 projected on the P-wave and evaluated near threshold

We therefore identify  $a_1^1 = 1/(24\pi F^2)$ . Using relation (4.22) leads to the following expression for the P-wave phase-shift expanded around threshold:

$$\delta_1^1(s) = a_1^1 \sigma_\pi(s) \frac{s - 4m_\pi^2}{4} + \mathcal{O}((s - 4m_\pi^2)^2). \quad (10.18)$$

After some algebra, we find the following relation between the loop functions present in the ChPT expression and the expanded dispersive integral:

$$\frac{a_1^1}{4\pi} \int_{4m_\pi^2}^{\infty} ds' \sigma_\pi(s') \frac{\tilde{T}_{(0)}^1(s')}{(s' - s)(s' - 2m_\pi^2)} = -\frac{2e^2}{F^2} \left( G_{+-\gamma}(s) - 2 \frac{J(s)}{s - 4m_\pi^2} \right) \quad (10.19)$$

and the unitarity contribution from both sides agree. What remains on the dispersive side is a polynomial of order one whose coefficients are fixed by the ChPT amplitude. Note that the latter has a large uncertainty due to the presence of the quantities  $K^{+-;+-}$  and  $K^{++;++}$  whose numerical value are given in (4.37) and (4.38). The amplitude is displayed in figure 10.3. At threshold, the dependence on those low-energy constants exactly vanishes. For this reason, we match the subtraction polynomial to ChPT precisely at that point.

Note that until this point, we completely ignored the discontinuity along the left-hand cut. In order to estimate the size of this contribution, we calculate the discontinuity in the  $t$ - and  $u$ -channel by cutting diagram 10.1b through the photon line and the hadronic blob. We have

$$\begin{aligned} \frac{\text{Disc}_t T_{(1)}(s, t)}{2i} &= \frac{(2\pi)^4}{2} \int d\Phi_3 M_\pi^{c,\text{ext}}(t, \{s_i\}) \cdot M_\pi^{c,\text{ext}*}(t, \{\tilde{s}_i\}) \\ &\quad + \frac{(2\pi)^4}{4} \int d\Phi_3 M_\pi^{cn,\text{ext}}(t, \{s_i\}) \cdot M_\pi^{cn,\text{ext}*}(t, \{\tilde{s}_i\}), \end{aligned} \quad (10.20)$$

$$\frac{\text{Disc}_u T_{(1)}(s, u)}{2i} = \frac{(2\pi)^4}{4} \int d\Phi_3 M_\pi^{+,\text{ext}}(t, \{s_i\}) \cdot M_\pi^{+,\text{ext}*}(t, \{\tilde{s}_i\}). \quad (10.21)$$

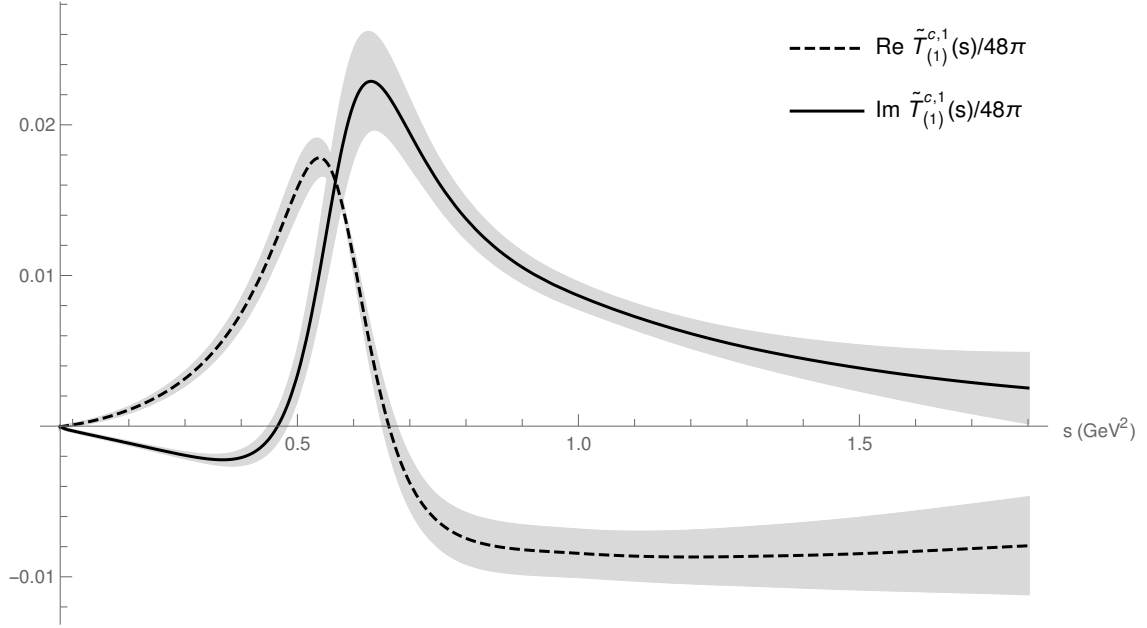


Figure 10.4: Real and imaginary part of the P-wave projection of  $T_{(1)}^c(s, t)$ .

The additional index in  $M_\pi^{c,\text{ext}}$  means that we only select the part corresponding to the pion-pole contribution where the photon is emitted from the external pions. From this discontinuity, we calculate dispersively the real part in the respective channel and project the result on the  $s$ -channel P-wave. We then insert the result in  $\tilde{T}^1$  of equation (10.13), additionally to  $T_{(0)}^1$ . Numerically, this left-hand cut contribution is very small compared to  $T_{(0)}^1$ . Since this is only a rough estimate, the result will be incorporated in the uncertainty.

The result is depicted in figure 10.4. Note that the imaginary part vanishes at threshold. This is due to the fact that close to this point, the P-wave behaves as

$$\begin{aligned} \text{Re}t_1^1(s) &\sim \sigma_\pi(s)^2, \\ \text{Im}t_1^1(s) &\sim \sigma_\pi(s)^5. \end{aligned} \quad (10.22)$$

Therefore, the cut through the two-pion state is finite, even though it involves the tree-level photon exchange amplitude of figure 10.1a that diverges at that point. In fact, the behaviour of the imaginary part near threshold is proportional to  $\sigma_\pi(s) \times \sigma_\pi(s)^2 \times \sigma_\pi(s)^{-2} = \sigma_\pi(s)$ , where the first threshold function comes from the phase-space and the second and third ones come from the  $\pi\pi$ -scattering P-wave and the photon-exchange amplitude  $\tilde{T}_{(0)}^1(s)$ .

### 10.3.2 S-wave contribution

When projecting relations (10.10) and (10.11) on the S-wave, we notice that the two channels are coupled. We can therefore not directly solve the system as in the case of the

P-wave. Let us define the two-dimensional vectors

$$\tilde{\mathbf{T}}_{(1)}^0(s) = \begin{pmatrix} \tilde{T}_{(1)}^{c,0}(s) \\ \tilde{T}_{(1)}^{cn,0}(s) \end{pmatrix}, \quad (10.23)$$

$$\tilde{\mathbf{T}}_{(0)}^0(s) = \begin{pmatrix} \tilde{T}_{(0)}^0(s) \\ 0 \end{pmatrix}. \quad (10.24)$$

Each of the two components corresponds to one of the two processes. In the isospin limit where all pion masses are equal, this notation allows us to write the unitarity relations (10.10) and (10.11) projected on the S-wave in a very compact form:

$$\text{Im}\tilde{\mathbf{T}}_{(1)}^0(s) = T^*\Sigma \left( \tilde{\mathbf{T}}_{(1)}^0(s) + \tilde{\mathbf{T}}_{(0)}^0(s) \right) \quad (10.25)$$

$$T^*\Sigma = 2\sigma_\pi(s) \begin{pmatrix} t_c^{0*}(s) & t_{cn}^{0*}(s)/2 \\ t_{cn}^{0*}(s) & t_n^{0*}(s)/2 \end{pmatrix} \quad (10.26)$$

where  $t_c^0(s)$ ,  $t_{cn}^0(s)$  and  $t_n^0$  are the partial S-waves of the corresponding channels, as defined in relations (10.6), (10.7) and (10.8). The factor 1/2 in the second column of the matrix is due to the identical neutral pions in the phase space.

Note that the consistency of this unitarity relation can be checked by replacing  $\tilde{\mathbf{T}}_{(1)}^0(s)$  by the purely hadronic amplitudes  $\pi\pi$ -scattering amplitude. We can express the partial waves in the isospin basis

$$t_c^0(s) = 1/3 t_0^0(s) + 1/6 t_0^2(s), \quad (10.27)$$

$$t_{cn}^0(s) = 1/3 t_0^0(s) - 1/3 t_0^2(s), \quad (10.28)$$

$$t_n^0(s) = 1/3 t_0^0(s) + 2/3 t_0^2(s), \quad (10.29)$$

and the unitarity relation (10.25) leads directly to the usual relation (4.21).

In general, this kind of problem is hard to solve. It requires the solution of a coupled Omnès-Muskhelishvili problem. The generalization of the Omnès function in this case is a  $n \times n$  matrix where  $n$  is the number of channels. The system is not analytically solvable and one has to rely on a numerical solution (see for instance [84]). In our case, however, we can take a shortcut. The reason is that this matrix is diagonalizable. We can therefore decouple the problem by rewriting

$$T^*\Sigma = P\Lambda P^{-1}, \quad (10.30)$$

$$\Lambda = \sigma_\pi(s) \text{diag} (t_0^{2*}(s), t_0^{0*}(s)), \quad (10.31)$$

$$P = \begin{pmatrix} -1/2 & 1 \\ 1 & 1 \end{pmatrix}, \quad (10.32)$$

$$P^{-1} = \begin{pmatrix} -2/3 & 2/3 \\ 2/3 & 1/3 \end{pmatrix}, \quad (10.33)$$

and define

$$\tilde{\mathbf{G}}_{(1)}^0(s) := P^{-1} \tilde{\mathbf{T}}_{(1)}^0(s), \quad (10.34)$$

$$\tilde{\mathbf{G}}_{(0)}^0(s) := P^{-1} \tilde{\mathbf{T}}_{(0)}^0(s). \quad (10.35)$$



In this way, the unitarity relation is diagonal and we end up with two independent single-channel problems. The two corresponding unitarity relations are

$$\text{Im}\tilde{G}_{(1),1}^0(s) = \sigma_\pi(s)t_0^{2*}(s) \left( \tilde{G}_{(1),1}^0(s) + \tilde{G}_{(0),1}^0(s) \right), \quad (10.36)$$

$$\text{Im}\tilde{G}_{(1),2}^0(s) = \sigma_\pi(s)t_0^{0*}(s) \left( \tilde{G}_{(1),2}^0(s) + \tilde{G}_{(0),2}^0(s) \right). \quad (10.37)$$

This kind of equation can be solved analytically using the Omnès-Muskhelishvili method already used in the previous section. The difference is the phase of the partial waves in (10.36) and (10.37). We write

$$\bar{G}_1^0(s) := \frac{\left( \tilde{G}_{(0),1}^0(s) + \tilde{G}_{(1),1}^0(s) \right) - \tilde{G}_{(0),1}^0(s)}{\Omega_0^2(s)}, \quad (10.38)$$

$$\bar{G}_2^0(s) := \frac{\left( \tilde{G}_{(0),2}^0(s) + \tilde{G}_{(1),2}^0(s) \right) - \tilde{G}_{(0),2}^0(s)}{\Omega_0^0(s)}. \quad (10.39)$$

Again, the denominator has exactly the same discontinuity as the first term in brackets in the numerator. The discontinuities are therefore

$$\text{Disc } \bar{G}_1^0(s) = \frac{2i \sin \delta_0^2(s)}{|\Omega_0^2(s)|} \tilde{G}_{(0),1}^0(s) = -\frac{2}{3} \frac{2i \sin \delta_0^2(s)}{|\Omega_0^2(s)|} \tilde{T}_{(0)}^0(s), \quad (10.40)$$

$$\text{Disc } \bar{G}_2^0(s) = \frac{2i \sin \tilde{\delta}_0^0(s)}{|\Omega_0^0(s)|} \tilde{G}_{(0),2}^0(s) = \frac{2}{3} \frac{2i \sin \tilde{\delta}_0^0(s)}{|\Omega_0^0(s)|} \tilde{T}_{(0)}^0(s). \quad (10.41)$$

Note that  $\tilde{\delta}_0^0$  is the phase of the amplitude  $t_0^0(s)$  including the inelasticity, as explained in appendix D. Similarly to (10.15), we write the dispersion relations

$$\begin{aligned} \tilde{G}_{(1),1}^0(s) &= \Omega_0^2(s) \frac{1}{\pi} \int_{4m_\pi^2}^{\infty} ds' \frac{\sin \delta_0^2(s') \tilde{G}_{(0),1}^0(s')}{|\Omega_0^2(s')|(s' - s)}, \\ \tilde{G}_{(1),2}^0(s) &= \Omega_0^0(s) \left( c_{(1),1}^0 + c_{(1),2}^0 s + \frac{s^2}{\pi} \int_{4m_\pi^2}^{\infty} ds' \frac{\sin \tilde{\delta}_0^0(s') \tilde{G}_{(0),2}^0(s')}{|\Omega_0^0(s')|(s' - s)s'^2} \right). \end{aligned} \quad (10.42)$$

Note that there is no need for subtractions in the first case, since we assume  $\delta_0^2(s) \xrightarrow{s \rightarrow \infty} 0$ . On the other hand, two subtractions have been used in the second case. Again, the subtraction constant is fixed from the ChPT amplitude of chapter 4. To that end, we make the transformation of the amplitude in the physical basis to the isospin basis using relation (10.43). The high-energy tail may have a sizeable effect, but this is not too important in our calculation, since the S-wave projection of the amplitude only enters the calculation via a left-hand cut contribution and is therefore small.

Once the solution is found for the two components, we reconstruct the two original triangle topologies in the respective channels from

$$\tilde{T}_{(1)}^0(s) = P \tilde{G}_{(1)}^0(s). \quad (10.43)$$

We can then check explicitly that the final solution is consistent with the unitarity relation, in the sense that it reproduces exactly the imaginary part.

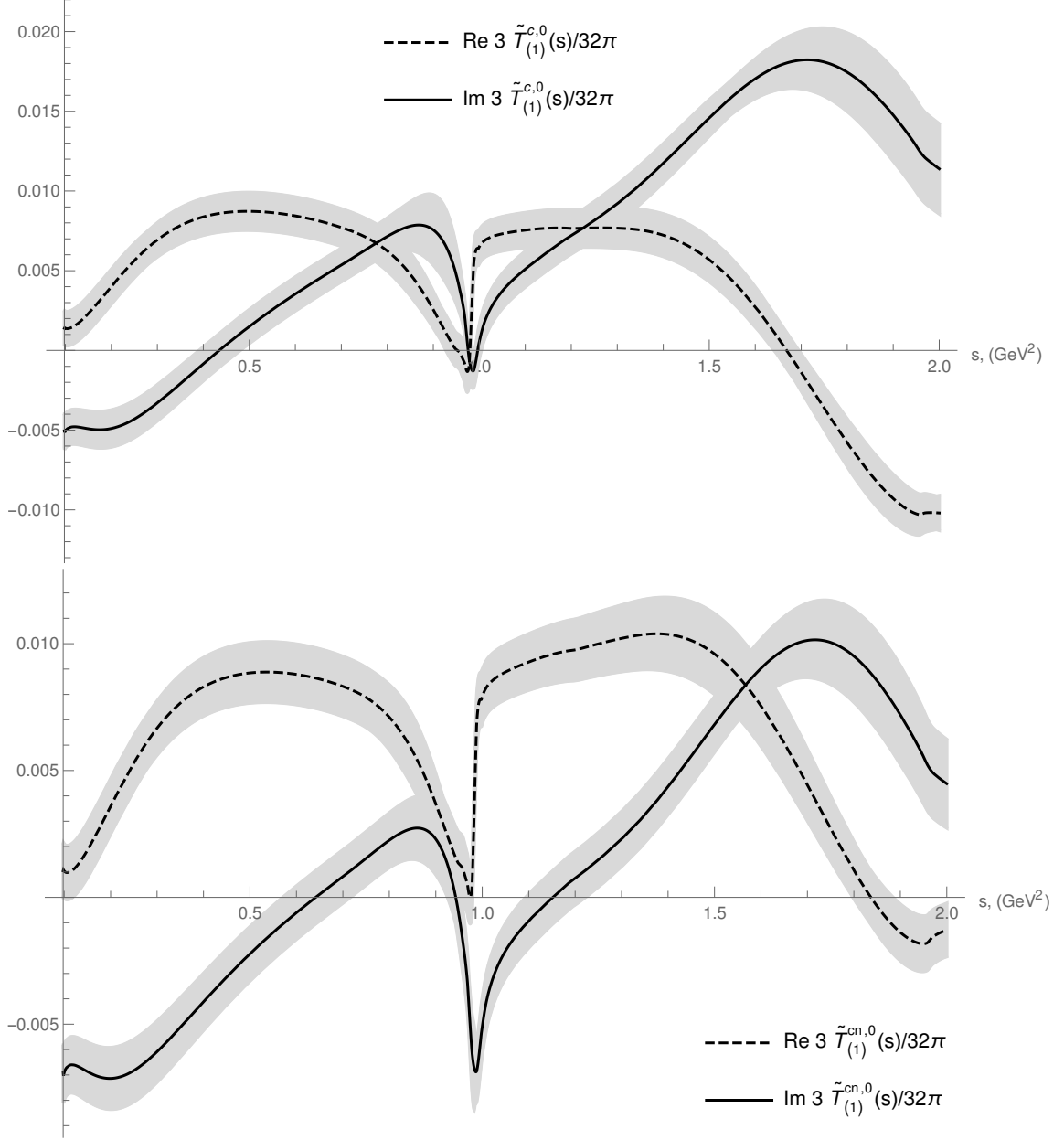


Figure 10.5: S-wave projection of the real and imaginary part of topology 10.1b contributing to the process  $\pi^+\pi^- \rightarrow \pi^+\pi^-$  and  $\pi^+\pi^- \rightarrow \pi^0\pi^0$ .

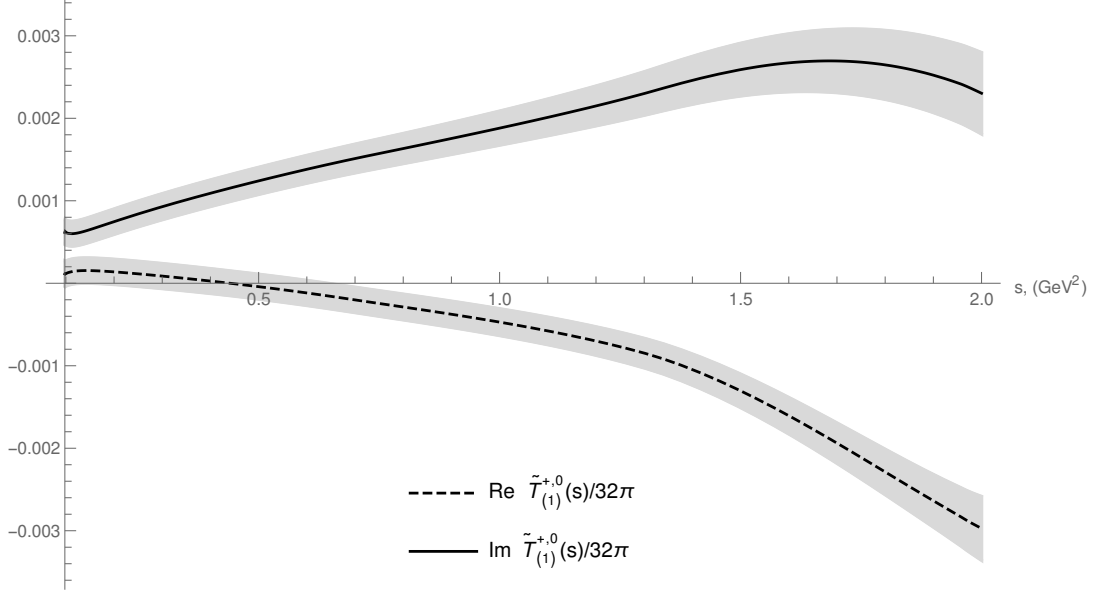


Figure 10.6: S-wave projection of the real and imaginary part of topology 10.1b contributing to the process  $\pi^+\pi^+ \rightarrow \pi^+\pi^+$ .

The result for the two different channels is depicted in figure 10.5. It is important to notice that, in this case, the amplitude diverges at threshold, as in the case of the tree-level photon exchange 10.1a. This is due to the fact that near threshold, the partial waves behave as

$$\text{Re} t_0^I(s) \sim \sigma_\pi(s)^0 \quad I \in \{0, 2\}, \quad (10.44)$$

$$\text{Im} t_0^I(s) \sim \sigma_\pi(s)^1 \quad I \in \{0, 2\}. \quad (10.45)$$

Therefore, the cut through the two-pion state behaves as  $\sigma_\pi(s) \times \sigma_\pi(s)^0 \times \sigma_\pi(s)^{-2} = \sigma_\pi(s)^{-1}$ .

### 10.3.3 The process $\pi^+\pi^+ \rightarrow \pi^+\pi^+$

The topology of figure 10.1b also contributes to the process  $\pi^+\pi^+ \rightarrow \pi^+\pi^+$ . We define this contribution as  $T_{(1)}^+$ . In this case, there is no P-wave since  $T(\pi^+\pi^+ \rightarrow \pi^+\pi^+) = T^2(s, t)$ . Equation (10.10) is simplified to

$$\begin{aligned} \frac{\text{Disc}_s T_{(1)}^+(s, t)}{2i} &= \frac{(2\pi)^4}{2} \int d\Phi_2 \left( -T_{(0)}(s, t_1) + T_{(1)}^+(s, t_1) \right) T^2(s, t_2) \\ &= \sigma_\pi(s) \sum_{j=0} \left( -\tilde{T}_{(0)}^{2j}(s) + \tilde{T}_{(1)}^{+,2j}(s) \right) P_{2j} \left( 1 + \frac{2t}{s - 4m_\pi^2} \right) t_{2j}^2(s)^* \end{aligned} \quad (10.46)$$

Again, the factor 1/2 is due to the fact that the two  $\pi^+$  in the intermediate state are identical. Following the same steps as above, we end up with the same kind of dispersion relation:

$$\tilde{T}_{(1)}^{+,0}(s) = -\Omega_0^2(s) \frac{1}{\pi} \int_{4m_\pi^2}^{\infty} ds' \frac{\sin \delta_0^2(s') \left( \tilde{T}_{(0)}^0(s') \right)}{|\Omega_0^2(s')|(s' - s)}, \quad (10.47)$$

The result is depicted in figure 10.6. Concerning the behaviour of the amplitude at threshold, the same remark as in the previous section is valid in this case.

## 10.4 Crossed triangles (topologies 10.1c and 10.1d)

Since the  $\pi\pi$ -scattering amplitude has a branch cut in each of the three Mandelstam variables, some diagrams account for different topologies. As can be seen in figure 10.7, by replacing the purely hadronic blob in the triangle diagram by the two-pion exchange in any of the three channels, we end up with three distinct topologies for each of the three diagrams 10.1b - 10.1d. Diagram 10.7c only has a discontinuity in one particular channel. The others, however are boxes and have two discontinuities in two distinct channels. More specifically, diagrams 10.7a and 10.7b have a  $s$ -channel cut starting at the  $\pi$ - $\pi$  threshold. This is precisely what we intend to calculate using a double-spectral representation. The contribution from diagram 10.7c is also taken into account using a method similar to the one used in previous section in the crossed channel and projecting the result on the  $s$ -channel P-wave. As we will see, however, the amplitude is dominated by the contribution from the right-hand cut.

The limiting factor is our knowledge of the  $\pi\pi$ -scattering amplitude in the Mandelstam plane. While it is well known outside of the double-spectral region, from the solution of a system of Roy equations, it is a priori unknown inside of it. We must therefore be careful about the region in which the  $\pi\pi$ -scattering amplitude is evaluated. Nevertheless, it is possible to analytically continue the amplitude outside of the physical region. The prescription we use is the one from [66] presented in section 4.5. It is a phenomenological representation expressed as sum of single-variable functions depending on either of the three Mandelstam variables.

The method we use follows from [36]. We first calculate the discontinuity in the  $t$ -channel by cutting through the two-pion state. Then, the two sub-amplitudes for the process  $\pi\pi \rightarrow \pi\pi$  are replaced by their dispersive expressions. That way, the dependence in the crossed-variable of the sub-amplitude only appears in the Cauchy pole and the angular integral of the two-body phase space in the discontinuity can be solved analytically. It is re-expressed as a dispersive integral in  $s$ , thus providing a double-spectral representation. This is schematically displayed in figure 10.8. Note that we must also be careful about the IR divergences present in each of those boxes.

Let us start with diagrams 10.7a for the process  $\pi^+\pi^- \rightarrow \pi^+\pi^-$ . All the others are analogous. We use again the convention  $\text{Im}f(s) \equiv \text{Disc}f(s)/2i$  on the right-hand cut and the different variables used for the process  $\pi^-(l_1)\pi^+(l_2) \rightarrow \pi^-(k_1)\pi^+(k_2)$  are

$$\begin{aligned} s &= (l_1 + l_2)^2 = (k_1 + k_2)^2 = P^2 \\ t &= (l_1 - k_1)^2 = (l_2 - k_2)^2 \\ u &= (l_2 - k_1)^2 = (l_1 - k_2)^2 \end{aligned} \tag{10.48}$$

The tree-level photon exchange can be written as a sum of a photon pole and a dispersive integral along the cut starting at  $4m_\pi^2$  where the discontinuity comes from the cut through either of the pion vector form factors:

$$T_{(0)}(s, t) = \frac{e^2(4m_\pi^2 - 2t)}{s} + \frac{1}{2\pi i} \int_{4m_\pi^2}^{\infty} ds_2 \frac{\text{Disc}T_{(0)}(s_2, t)}{s_2 - s}. \tag{10.49}$$

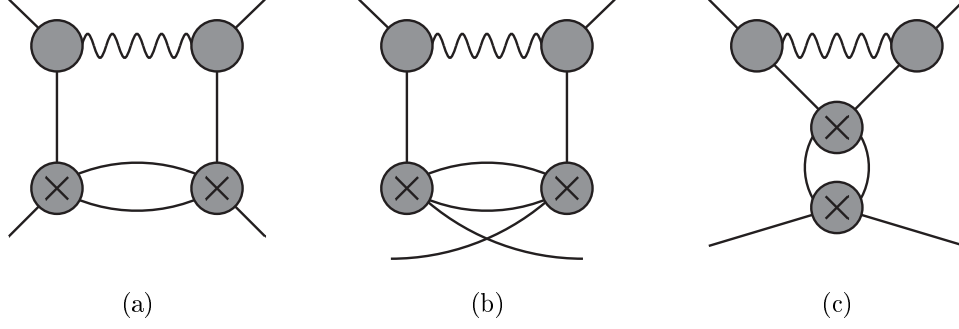


Figure 10.7: Decomposition of the internal  $\pi\pi$ -scattering amplitude of diagram 10.1b that gives rise to three different diagrams.

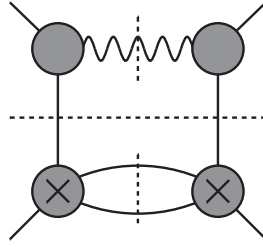


Figure 10.8: Cuts applied on the box and leading to the density of the double-spectral representation

The  $\pi\pi$ -scattering amplitude can be written as a once-subtracted dispersive integral where the Mandelstam variable  $t$  is fixed:

$$\begin{aligned}
 T_{\pi\pi}(s, t) = c_0(t) &+ \frac{1}{2\pi i} \int_{4m_\pi^2}^{\infty} ds_1 \frac{\text{Disc} T_{\pi\pi}(s_1, t)}{(s_1 - s)} - \frac{1}{2\pi i} \int_{4m_\pi^2}^{\infty} ds_1 \frac{\text{Disc} T_{\pi\pi}(s_1, t)}{s_1} \\
 &+ \frac{1}{2\pi i} \int_{4m_\pi^2}^{\infty} du_1 \frac{\text{Disc} T_{\pi\pi}(u_1, t)}{(u_1 - u)} - \frac{1}{2\pi i} \int_{4m_\pi^2}^{\infty} du_1 \frac{\text{Disc} T_{\pi\pi}(u_1, t)}{u_1}.
 \end{aligned} \tag{10.50}$$

For convenience, the subtraction has been expressed using the relation

$$\frac{s}{(s_1 - s)s_1} = \frac{1}{s_1 - s} - \frac{1}{s_1} \tag{10.51}$$

in order to have the dependence in  $s$  only in the denominator of the first term.

We can now write the contribution from diagram 10.1c,  $T_{(2)}^{10.1c}(s, t)$ , as a dispersive integral in  $t$  with  $s$  fixed:

$$\begin{aligned}
 T_{(2)}^{10.1c}(s, t) &= T_{(2)}^{10.1c}(s, 0) + \frac{t}{2\pi i} \int d\tilde{t} \frac{\text{Disc} T_{(2)}^{10.1c}(s, \tilde{t})}{(\tilde{t} - t)\tilde{t}}, \\
 \frac{\text{Disc} T_{(2)}^{10.1c}(s, \tilde{t})}{2i} &= \frac{1}{2} (2\pi)^4 \int d\Phi_2 T_{\pi\pi}^c(s', \tilde{t}) T_{(0)}^*(s'', \tilde{t}) \\
 &= \frac{1}{2} \frac{1}{(2\pi)^2} \frac{\sigma_\pi(\tilde{t})}{8} \int d\Omega' T_{\pi\pi}^c(s', \tilde{t}) T_{(0)}^*(s'', \tilde{t}).
 \end{aligned} \tag{10.52}$$

Depending on which one of the two terms in (10.49) and (10.50) is considered in the photon exchange and the purely-hadronic  $\pi\pi$ -scattering amplitude, the angular integral can take several forms. According to our prescription of only selecting up to two pions in the intermediate state, we neglect the cut in the photon-exchange amplitude and only consider the photon pole (first term in (10.49)). The different angular integrals that we must calculate are

$$\int d\Omega' \frac{1}{s'' - m_\gamma^2} = -4\pi \frac{\log(t - 4m_\pi^2) - \log(m_\gamma^2)}{t - 4m_\pi^2}, \quad (10.53)$$

$$\int d\Omega' \frac{1}{s' - s_1} \frac{1}{s'' - m_\gamma^2} = \frac{8\pi}{t - 4m_\pi^2} \int_{s^+}^{\infty} \frac{d\tilde{s}}{\tilde{s} - s} \frac{1}{\sqrt{(\tilde{s} - s^+)(\tilde{s} - s^-)}}, \quad (10.54)$$

$$\int d\Omega' \frac{1}{u' - u_1} \frac{1}{s'' - m_\gamma^2} = \frac{8\pi}{t - 4m_\pi^2} \int_{u^+}^{\infty} \frac{d\tilde{u}}{\tilde{u} - u} \frac{1}{\sqrt{(\tilde{u} - u^+)(\tilde{u} - u^-)}}. \quad (10.55)$$

The explicit calculation of the two last angular integrals are explained in appendix E.

The  $s$ - and  $u$ -independent terms in (10.50) lead to the first angular integral. As we can see, it only depends on  $t$  and the term proportional to  $\log m_\gamma^2$  is the infrared-divergent term. Since the angular integral does not depend on  $s$ , the result is a single-variable dispersive integral in  $t$ .

The second angular integral, however, has been re-expressed as a dispersive integral in  $s$ , giving rise to a double-spectral function. When  $m_\gamma \rightarrow 0$ , we have  $s^+ = s^- = s_1$  and there is an end-point singularity responsible for the infrared divergence. In order to extract it, we regularize the process with a photon mass  $m_\gamma$ . We note that

$$\begin{aligned} s^+ &= s_1 + m_\gamma \Delta(s_1) = s_1 + \mathcal{O}(m_\gamma), \\ s^- &= s_1 - m_\gamma \Delta(s_1) = s_1 + \mathcal{O}(m_\gamma), \\ \sqrt{(s - s^+)(s - s^-)} &= s - s_1 + \mathcal{O}(m_\gamma^2) \\ \Delta(s_1) &= 2\sqrt{\frac{s_1(s_1 + t - 4m_\pi^2)}{t - 4m_\pi^2}}. \end{aligned} \quad (10.56)$$

Keeping the correction at order  $m_\gamma$ , we can switch the order of the integrals as

$$\int_{4m_\pi^2}^{\infty} ds_1 \int_{s_1 + m_\gamma \Delta(s_1)}^{\infty} d\tilde{s} = \int_{4m_\pi^2}^{\infty} d\tilde{s} \int_{4m_\pi^2}^{\tilde{s} - m_\gamma \Delta(\tilde{s})} ds_1. \quad (10.57)$$

Then, in order to extract analytically the term proportional to  $\log(m_\gamma)$ , we subtract

$$\begin{aligned} \int_{4m_\pi^2}^{\tilde{s} - m_\gamma \Delta(\tilde{s})} ds_1 \frac{f(s_1)}{\tilde{s} - s_1} &= \int_{4m_\pi^2}^{\tilde{s} - m_\gamma \Delta(\tilde{s})} ds_1 \frac{(f(s_1) - f(\tilde{s})) + f(\tilde{s})}{\tilde{s} - s_1} \\ &= \int_{4m_\pi^2}^{\tilde{s}} ds_1 \frac{(f(s_1) - f(\tilde{s}))}{\tilde{s} - s_1} + \left[ -\frac{\log(m_\gamma^2)}{2} + \log\left(\frac{\tilde{s} - 4m_\pi^2}{\Delta(\tilde{s})}\right) \right] f(\tilde{s}). \end{aligned} \quad (10.58)$$

The first term is infrared-finite because the pole is cancelled by the numerator at  $s_1 = \tilde{s}$ . The second term is the infrared divergent part that is removed. The third term is the finite

logarithm corresponding to the infrared divergence.

The infrared-safe double-spectral density is

$$\rho_{ts}(s, t) = -\frac{e^2(4m_\pi^2 - 2t)}{8\pi t\sqrt{1-4m_\pi^2/t}} \left\{ \left[ \int_{4m_\pi^2}^s ds_1 \frac{\text{Im}T_{\pi\pi}^c(s_1, t) - \text{Im}T_{\pi\pi}^c(s, t)}{s - s_1} \right] + \log \left( \frac{s - 4m_\pi^2}{\Delta(s)} \right) \text{Im}T_{\pi\pi}^c(s, t) \right\} \quad (10.59)$$

$$\rho_{tu}(u, t) = -\frac{e^2(4m_\pi^2 - 2t)}{8\pi t\sqrt{1-4m_\pi^2/t}} \left\{ \left[ \int_{4m_\pi^2}^u du_1 \frac{\text{Im}T_{\pi\pi}^+(u_1, t) - \text{Im}T_{\pi\pi}^+(u, t)}{u - u_1} \right] + \log \left( \frac{u - 4m_\pi^2}{\Delta(u)} \right) \text{Im}T_{\pi\pi}^+(u, t) \right\} \quad (10.60)$$

The calculation of diagram 10.1d is completely analogous. We simply write a fixed- $s$  dispersion relation in  $u$  instead of  $t$  and obtain similar densities  $\rho_{us}$  and  $\rho_{ut}$ . Eventually, the sum of diagrams 10.1c and 10.1d can be expressed as

$$\begin{aligned} T_{(2)}(s, t, u) &= T_{(2)}^{10.1c}(s, t, u) + T_{(2)}^{10.1d}(s, t, u) \\ &= \frac{st}{\pi^2} \int_{4m_\pi^2}^\infty ds' \int_{4m_\pi^2}^\infty dt' \frac{\rho_{ts}(t', s')}{(s' - s)(t' - t)t's'} \\ &\quad + \frac{us}{\pi^2} \int_{4m_\pi^2}^\infty ds' \int_{4m_\pi^2}^\infty du' \frac{\rho_{us}(s', u')}{(s' - s)(u' - u)s'u'} \\ &\quad + \frac{ut}{\pi^2} \int_{4m_\pi^2}^\infty du' \int_{4m_\pi^2}^\infty dt' \frac{\rho_{tu}(t', u') + \rho_{ut}(u', t')}{(u' - u)(t' - t)t'u'} \\ &\quad + \frac{s}{\pi} \int_{4m_\pi^2}^\infty ds' \frac{\rho_s(s')}{(s' - s)s'} + \frac{t}{\pi} \int_{4m_\pi^2}^\infty dt' \frac{\rho_t(t')}{(t' - t)t'} + \frac{u}{\pi} \int_{4m_\pi^2}^\infty du' \frac{\rho_u(u')}{(u' - u)u'} \\ &\quad + T_{(2)}(0, 0). \end{aligned} \quad (10.61)$$

The first three terms are the double-spectral functions integrated over the  $s$ - $t$ ,  $s$ - $u$  or  $t$ - $u$  regions. The single-variable dispersive integrals are caused by the subtraction in the double-spectral representation and by the subtraction terms in (10.50). The first of them is  $t$ - and  $u$ -independent and thus vanishes under projection on the  $s$ -channel P-wave. The last term is a subtraction constant that also vanishes when projected on the  $s$ -channel P-wave.

In order to calculate the density of the single-variable dispersive integrals caused by the subtraction in the double-spectral representation, we cut the boxes (10.7) in the corresponding channel, fixing the other variable to 0. In the case of the box (10.7a), there are two types of cuts. In the  $t$ -channel, the intermediate state is a pion pair and in the  $s$ -channel, the intermediate state is a pion pair and a photon.

In the first case, the discontinuity in  $t$  at fixed  $s = 0$  is almost identical to the expression (10.52). The only difference is the angular integration when fixing  $s = 0$ . In this particular case the scattering angle in the  $t$ -channel center-of-mass frame is  $z_t = 1$ . Therefore, the internal angles are  $z'' = z'z_t + \cos\phi\sqrt{1-z'^2}\sqrt{1-z_t^2} = z'$  and consequently  $s'' = s'$ . The

corresponding  $s$ -independent angular integral is

$$\int d\Omega' \frac{1}{s' - m_\gamma^2} \frac{1}{s_1 - s'} = 4\pi \frac{\log\left(\frac{s_1+t-4m_\pi^2}{s_1(t-4m_\pi^2)}\right) + \log(m_\gamma^2)}{s_1(t-4m_\pi^2)}. \quad (10.62)$$

In the second situation, fixing  $t = 0$  and cutting in  $s$ , there are three particles in the phase space. The discontinuity is proportional to the three-body phase space of the product of two pion-pole contribution derived in chapter 9. The details of how we deal with the infrared divergence of such three-body phase-space integrals are explained in the next section.

Finally, a last comment about the term containing the subtraction constant of the  $\pi\pi$ -scattering amplitude,  $c_0(t) = T_{\pi\pi}^c(0, t)$ . Since this function is evaluated in the region where  $t > 4m_\pi^2$ , it receives an imaginary part from the  $t$ -channel right-hand cut. This implies that the discontinuity is not a real quantity any more. This is due to the fact that the cut through the blob in the  $t$ -channel has been ignored, since we only considered the cut through the two-pion propagators. Once this part is included, the discontinuity should be real, as in the calculation of diagram 10.1b. The problem is that the cut through the blob leads to an implicit integral equation that can not be solved easily. Therefore, we decide to replace  $c_0(t)$  by the pure left-hand cut contribution. This is done by performing the same calculation as for diagram 10.7c for the S- and P-waves in the  $t$ -channel and project the result on the  $s$ -channel P-wave. The higher waves are neglected.

The result can then be projected on the P-wave using

$$\tilde{T}_{(2)}^1(s) = \frac{3}{2} \int_{-1}^1 dz z T_{(2)}(s, t(z), u(z)). \quad (10.63)$$

Doing this, we notice that the P-wave contribution of the internal  $\pi\pi$ -scattering amplitude completely vanishes. Hence, the structure of the correction is similar to the  $\pi\pi$ -scattering S-wave. This is confirmed by calculating the imaginary part with a direct cut in the  $s$ -channel through the hadronic blob.

An important remark is that all of the left-hand cut contributions are small compared to the contributions from the right-hand cut that dominates. Therefore, even though we had to rely on an approximation to assess them, we expect this to be quite accurate.

## 10.5 Many-loop topologies (10.1e - 10.1g)

The last topologies of figure 10.1 remaining are the multi-loop topologies 10.1e - 10.1g. Note that those diagrams also account for their crossed versions, where the photon can be attached either to the top or to the bottom pion. Contrary to the diagram in figure 10.7, a particularity of those topologies is that all cuts in the crossed channels ( $t$  or  $u$ ) start at least at the four-pion creation threshold. Their left-hand cuts are thus ignored and only the cuts in the  $s$ -channel are considered.

For each of the topologies, there are three types of cuts in the  $s$ -channel. Let us illustrate this with the diagram of figure 10.1e. The imaginary part that can be related to the discontinuity is schematically given by



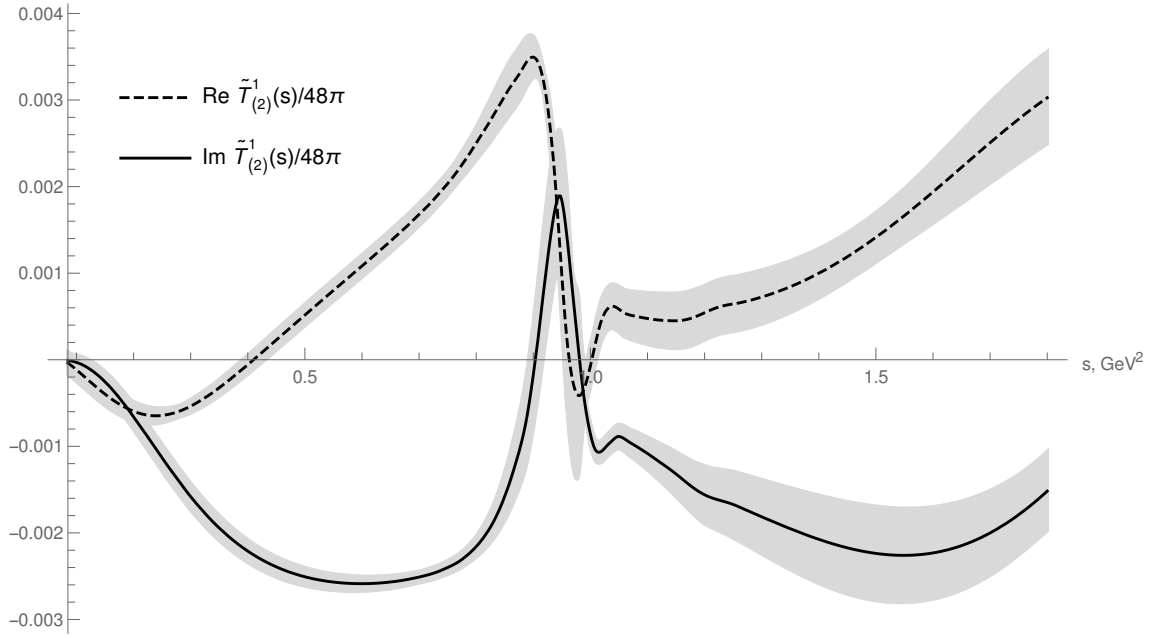


Figure 10.9: Real and imaginary part of the sum of diagrams 10.7a and 10.7b projected on the P-wave

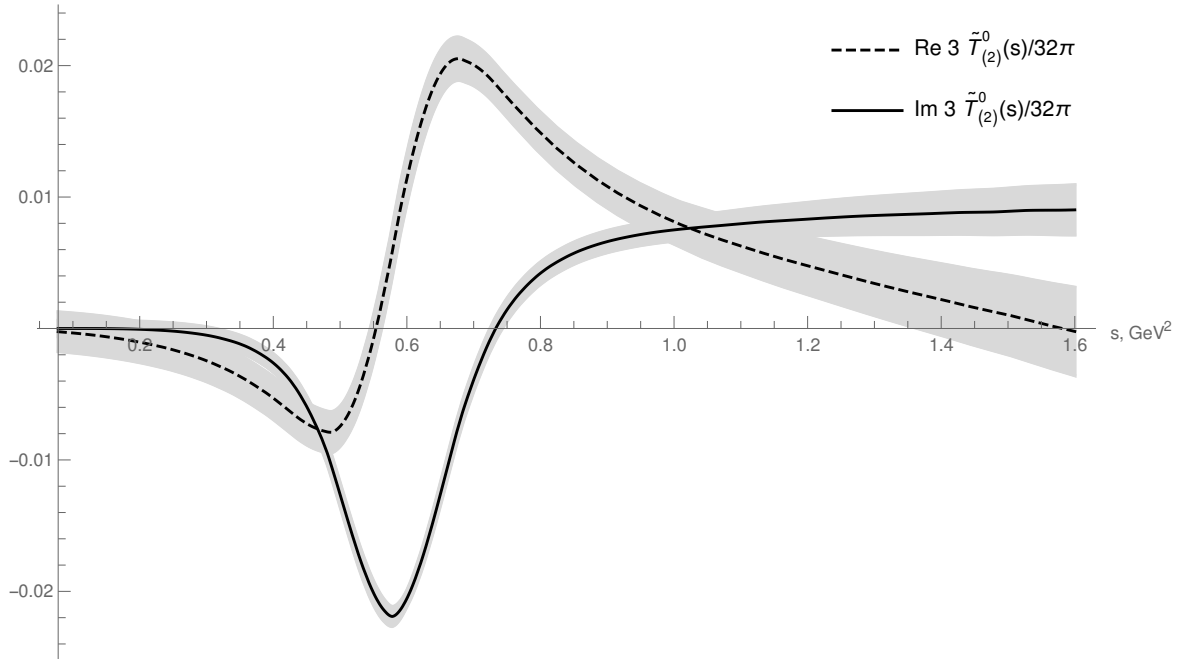


Figure 10.10: Real and imaginary part of the sum of diagrams 10.7a and 10.7b projected on the S-wave

$$\text{Disc} = \text{Diagram 1} + \text{Diagram 2} + \text{Diagram 3} + \text{Diagram 4}, \quad (10.64)$$

where each dashed line corresponds to one possible cut. Hence, there are two cuts through the pion lines, two cuts through the hadronic blobs and two cuts through the photon and pion lines. The discontinuities of the different channels of diagram 10.1e are therefore

$$\begin{aligned} \frac{\text{Disc} T_{(3)}^c}{2i} &= \frac{(2\pi)^4}{2} \int d\Phi_2 \, 2\text{Re} \left[ T_{(1)}^c(s, t_1) \times T_{\pi\pi}^{c*}(s, t_2) \right] \\ &+ \frac{(2\pi)^4}{2} \int d\Phi_2 \, 2\text{Re} \left[ T_{(3)}^c(s, t_1) \times T_{\pi\pi}^{c*}(s, t_2) + \frac{1}{2} T_{(3)}^{cn}(s, t_1) \times T_{\pi\pi}^{cn*}(s, t_2) \right] \\ &+ \frac{(2\pi)^4}{2} \int d\Phi_3 \, M_{\pi}^{c,\text{int}}(s, \{t_i\}) \cdot M_{\pi}^{c,\text{int}*}(s, \{\tilde{t}_i\}) \end{aligned} \quad (10.65)$$

$$\begin{aligned} \frac{\text{Disc} T_{(3)}^{cn}}{2i} &= \frac{(2\pi)^4}{2} \int d\Phi_2 \, \text{Re} \left[ T_{(1)}^{cn}(s, t_1) \times T_{\pi\pi}^{c*}(s, t_2) + T_{(1)}^c(s, t_1) \times T_{\pi\pi}^{cn*}(s, t_2) \right] \\ &+ \frac{(2\pi)^4}{2} \int d\Phi_2 \, \text{Re} \left[ T_{(3)}^{cn}(s, t_1) \times T_{\pi\pi}^{c*}(s, t_2) + \frac{1}{2} T_{(3)}^n(s, t_1) \times T_{\pi\pi}^{cn*}(s, t_2) \right] \\ &+ \frac{(2\pi)^4}{2} \int d\Phi_2 \, \text{Re} \left[ T_{(3)}^c(s, t_1) \times T_{\pi\pi}^{cn*}(s, t_2) + \frac{1}{2} T_{(3)}^{cn}(s, t_1) \times T_{\pi\pi}^{n*}(s, t_2) \right] \\ &+ \frac{(2\pi)^4}{2} \int d\Phi_3 \, \text{Re} \left[ M_{\pi}^{cn,\text{int}}(s, \{t_i\}) \cdot M_{\pi}^{c,\text{int}*}(s, \{\tilde{t}_i\}) \right] \end{aligned} \quad (10.66)$$

$$\begin{aligned} \frac{\text{Disc} T_{(3)}^n}{2i} &= \frac{(2\pi)^4}{2} \int d\Phi_2 \, 2\text{Re} \left[ T_{(1)}^{cn}(s, t_1) \times T_{\pi\pi}^{cn*}(s, t_2) \right] \\ &+ \frac{(2\pi)^4}{2} \int d\Phi_2 \, 2\text{Re} \left[ T_{(3)}^{cn}(s, t_1) \times T_{\pi\pi}^{cn*}(s, t_2) + \frac{1}{2} T_{(3)}^n(s, t_1) \times T_{\pi\pi}^{n*}(s, t_2) \right] \\ &+ \frac{(2\pi)^4}{2} \int d\Phi_3 \, M_{\pi}^{cn,\text{int}}(s, \{t_i\}) \cdot M_{\pi}^{cn,\text{int}*}(s, \{\tilde{t}_i\}) \end{aligned} \quad (10.67)$$

All the internal pion lines are charged in the three channels. When cutting the hadronic blobs, however, contributions from pairs of neutral pions must be included. This is the case in the second term of (10.64). Also, for convenience, we used the time invariance property of the amplitude to write  $F^{cn} = 1/2(F^{cn} + F^{nc})$ . This will turn out to be useful later. Note also that the additional index in the fully-charged  $M_{\pi}^{c,\text{int},\text{ext}}$  subamplitudes means that we only select the part corresponding to the pion-pole contribution where the photon is emitted either from the internal or from the external pions. This is due to the fact that

we distinguish between the different topologies.

The two other diagrams 10.1f and 10.1g are regrouped together. This is a natural choice, since the cut through the two pion lines of diagram 10.1g is the product of diagram 10.1f and a purely hadronic  $\pi\pi$ -scattering amplitude. The corresponding discontinuities are

$$\begin{aligned} \frac{\text{Disc}T_{(4)}^c}{2i} &= \frac{(2\pi)^4}{2} \int d\Phi_2 \, 2\text{Re} \left[ T_{(2)}^c(s, t_1) \times T_{\pi\pi}^{c*}(s, t_2) \right] \\ &+ \frac{(2\pi)^4}{2} \int d\Phi_2 \, 2\text{Re} \left[ T_{(4)}^c(s, t_1) \times T_{\pi\pi}^{c*}(s, t_2) + \frac{1}{2} T_{(4)}^{cn}(s, t_1) \times T_{\pi\pi}^{cn*}(s, t_2) \right] \\ &+ \frac{(2\pi)^4}{2} \int d\Phi_3 \, 2\text{Re} \left[ M_{\pi,\pi\pi}^{c,\text{int}}(s, \{t_i\}) \cdot M_{\pi,\pi\pi}^{c,\text{ext}*}(s, \{\tilde{t}_i\}) \right] \end{aligned} \quad (10.68)$$

$$\begin{aligned} \frac{\text{Disc}T_{(4)}^{cn}}{2i} &= \frac{(2\pi)^4}{2} \int d\Phi_2 \, \text{Re} \left[ T_{(2)}^c(s, t_1) \times T_{\pi\pi}^{cn*}(s, t_2) \right] \\ &+ \frac{(2\pi)^4}{2} \int d\Phi_2 \, \text{Re} \left[ T_{(4)}^{cn}(s, t_1) \times T_{\pi\pi}^{c*}(s, t_2) + \frac{1}{2} T_{(4)}^n(s, t_1) \times T_{\pi\pi}^{cn*}(s, t_2) \right] \\ &+ \frac{(2\pi)^4}{2} \int d\Phi_2 \, \text{Re} \left[ T_{(4)}^c(s, t_1) \times T_{\pi\pi}^{cn*}(s, t_2) + \frac{1}{2} T_{(4)}^{cn}(s, t_1) \times T_{\pi\pi}^{n*}(s, t_2) \right] \\ &+ \frac{(2\pi)^4}{2} \int d\Phi_3 \, \text{Re} \left[ M_{\pi,\pi\pi}^{cn,\text{int}}(s, \{t_i\}) \cdot M_{\pi,\pi\pi}^{c,\text{ext}*}(s, \{\tilde{t}_i\}) \right] \end{aligned} \quad (10.69)$$

$$\begin{aligned} \frac{\text{Disc}T_{(4)}^n}{2i} &= \frac{(2\pi)^4}{2} \int d\Phi_2 \, 2\text{Re} \left[ T_{(4)}^{cn}(s, t_1) \times T_{\pi\pi}^{cn*}(s, t_2) \right] \\ &+ \frac{(2\pi)^4}{2} \int d\Phi_2 \, 2\text{Re} \left[ T_{(4)}^{cn}(s, t_1) \times T_{\pi\pi}^{cn*}(s, t_2) + \frac{1}{2} T_{(4)}^n(s, t_1) \times T_{\pi\pi}^{n*}(s, t_2) \right] \\ &+ \frac{(2\pi)^4}{2} \int d\Phi_3 \, M_{\pi\pi}^{cn,\text{int}}(s, \{t_i\}) \cdot M_{\pi\pi}^{cn,\text{int}*}(s, \{\tilde{t}_i\}) \end{aligned} \quad (10.70)$$

Note that the amplitude  $M_{\pi,\pi\pi}^{c,\text{int}}$  is the sum of the pion-pole contribution and of the rescattering effect. The amplitude  $M_{\pi\pi}^{c,\text{int}}$  accounts only for the rescattering effect.

Note also that, despite the fact that the different discontinuities above consist of infrared divergent quantities as for instance  $T_{(1)}^c(s)$ , they are themselves infrared finite. The reason is that the infrared divergence coming from those cuts is exactly cancelled by the cuts involving a photon in the phase space. The latter can be regularized using the method explained in appendix C.

### 10.5.1 P-wave projection

Projecting the discontinuities above on the P-wave leads to a great simplification, since all the terms involving a pair of neutral pions (without photon) in the  $s$ -channel vanish. This

means that the discontinuities become

$$\frac{\text{Disc}\tilde{T}_{(3)}^{c,1}(s)}{2i} = \sigma_\pi(s) 2\text{Re} \left[ \tilde{T}_{(3)}^{c,1}(s) t_1^{1*}(s) \right] + \Delta_{(3)}^{c,1}(s), \quad (10.71)$$

$$\frac{\text{Disc}\tilde{T}_{(3)}^{cn,1}(s)}{2i} = 0, \quad (10.72)$$

$$\frac{\text{Disc}\tilde{T}_{(3)}^{n,1}(s)}{2i} = 0. \quad (10.73)$$

The inhomogeneity  $\Delta_{(3)}^{c,1}(s)$  contains all the terms that do not depend on  $\tilde{T}_{(3)}^{c,1}(s)$  projected on the P-wave. It is therefore calculable explicitly. The more problematic part is the term that depends on  $\tilde{T}_{(3)}^{c,1}(s)$  leading to an implicit equation. Such an equation can not be solved using an Omnès-Muskhelishvili method similarly to the situations above. The first reason is that the Watson's final-state theorem can not be invoked in (10.71), since the imaginary part of  $\tilde{T}_{(3)}^{c,1}(s)$  is already a real quantity by construction. Also, the inhomogeneity does have a right-hand cut contrary to the case above. We must therefore use another method to solve this equation.

By expressing the discontinuity on the cut in terms of the imaginary part and expanding the term  $\text{Re} \left[ \tilde{T}_{(3)}^{c,1}(s) t_1^{1*}(s) \right]$ , (10.71) can be written as

$$\text{Im}\tilde{T}_{(3)}^{c,1}(s) = \frac{\Delta_{(3)}^{c,1}(s) + 2\sigma_\pi(s)\text{Re}t_1^1(s)\text{Re}\tilde{T}_{(3)}^{c,1}(s)}{1 - 2\sigma_\pi(s)\text{Im}t_1^1(s)}. \quad (10.74)$$

Note that the situation is almost the same for the other topology. The only difference is the inhomogeneity  $\Delta_{(4)}^{c,1}(s)$ . Once the latter is calculated, the problem is formally identical and we can write

$$\text{Im}\tilde{T}_{(4)}^{c,1}(s) = \frac{\Delta_{(4)}^{c,1}(s) + 2\sigma_\pi(s)\text{Re}t_1^1(s)\text{Re}\tilde{T}_{(4)}^{c,1}(s)}{1 - 2\sigma_\pi(s)\text{Im}t_1^1(s)}. \quad (10.75)$$

The first noticeable feature of this equation is that the denominator of the term on the right-hand side has two zeros  $s_1$  and  $s_2$ . At those points, the following relation is exact:

$$2\sigma_\pi(s_{1,2})\text{Re}t_1^1(s_{1,2}) = 2\sigma_\pi(s_{1,2})\text{Im}t_1^1(s_{1,2}) = 1. \quad (10.76)$$

This is due to the unitarity relation (4.21), since

$$\begin{aligned} 1 = 2\sigma_\pi(s_{1,2})\text{Im}t_1^1(s_{1,2}) &= 2\sigma_\pi(s_{1,2})^2(\text{Im}t_1^1(s_{1,2})^2 + \text{Re}t_1^1(s_{1,2})^2) \\ &= \frac{1}{2}(1 + (2\sigma_\pi(s_{1,2})\text{Re}t_1^1(s_{1,2}))^2) \end{aligned} \quad (10.77)$$

Of course, there is no reason why the imaginary part should diverge at those "special" points. This means that the numerator has to vanish as well, in order to cancel these poles. This provides a constraint for the real part at those two points:

$$\text{Re}\tilde{T}_{(i)}^{c,1}(s_{1,2}) = -\Delta_{(i)}^{c,1}(s_{1,2}), \quad i \in \{3, 4\}. \quad (10.78)$$

Because of this, we can thus write the real part as a dispersive integral subtracted at those two points. For reasons explained later, we also subtract at  $s = 0$ , imposing the function

to vanish at this point. We have in case  $i \in \{3, 4\}$

$$\text{Re}\tilde{T}_{(i)}^{c,1}(s) = P_{(i)}^{c,1}(s) + D_{(i)}^{c,1}(s) \quad (10.79)$$

$$D_{(i)}^{c,1}(s) = \frac{s^3}{\pi} P \int_{4m_\pi^2}^{\infty} ds' \frac{\text{Im}\tilde{F}_{(i)}^{c,1}(s')}{s'^3(s' - s)} \quad (10.80)$$

$$\begin{aligned} P_{(i)}^{c,1}(s) &= (\text{Re}\tilde{F}_{(i)}^{c,1}(s_1) - D_{(i)}^{c,1}(s_1)) \frac{(s - s_2)s}{(s_1 - s_2)s_1} \\ &\quad + (\text{Re}\tilde{F}_{(i)}^{c,1}(s_2) - D_{(i)}^{c,1}(s_2)) \frac{(s - s_1)s}{(s_2 - s_1)s_2}. \end{aligned} \quad (10.81)$$

This way, the real part is exclusively expressed in terms of the imaginary part and equations (10.74) and (10.75) become implicit integral equations for the imaginary part.

Assuming that the real part goes asymptotically at most as a constant, we can write the two following sum-rules:

$$\frac{\text{Re}\tilde{T}_{(i)}^{c,1}(s_1)}{s_1} - \frac{\text{Re}\tilde{T}_{(i)}^{c,1}(s_2)}{s_2} = \frac{s_1 - s_2}{\pi} \int \frac{ds'}{s'} \frac{\text{Im}\tilde{T}_{(i)}^{c,1}(s')}{(s' - s_1)(s' - s_2)}, \quad (10.82)$$

$$\frac{s_2 \text{Re}\tilde{T}_{(i)}^{c,1}(s_1)}{s_1} - \frac{s_1 \text{Re}\tilde{T}_{(i)}^{c,1}(s_2)}{s_2} = \frac{s_1 - s_2}{\pi} \int \frac{ds'}{s'} \frac{(s_1 + s_2 - s') \text{Im}\tilde{T}_{(i)}^{c,1}(s')}{(s' - s_1)(s' - s_2)}. \quad (10.83)$$

Note that the resolution of such an equation with poles at those "special points" is completely new to our knowledge. The elaboration of a numerical method capable of solving this equation was therefore a benchmark of this project. The latter is explained in appendix F. Relation (10.79) as well as the sum rules (10.82) and (10.83) must be implemented into the parametrization of the solution in the numerical method. The numerical results are depicted in figures 10.11 and 10.12.

### 10.5.2 S-wave projection

The situation is more involved in the case of the projection of the S-wave. The unitarity relations expressed above involve three different channels and are coupled. The projection on the S-wave does not decouple the problem as in the P-wave projection. We therefore use the same strategy as in section 10.3.2 and define

$$\tilde{\mathbf{T}}_{(3)}^0(s) = \begin{pmatrix} \tilde{T}_{(3)}^{c,0}(s) \\ \tilde{T}_{(3)}^{cn,0}(s) \\ \tilde{T}_{(3)}^{n,0}(s) \end{pmatrix}, \quad (10.84)$$

$$\Delta_{(3)}^0(s) = \begin{pmatrix} \Delta_{(3)}^{c,0}(s) \\ \Delta_{(3)}^{cn,0}(s) \\ \Delta_{(3)}^{n,0}(s) \end{pmatrix}. \quad (10.85)$$

Note that we still use the symmetrized version of the two channels  $\pi^+\pi^- \rightarrow \pi^0\pi^0$  and  $\pi^0\pi^0 \rightarrow \pi^+\pi^-$ :

$$\tilde{T}_{(3)}^{cn,0}(s) = \tilde{T}_{(3)}^{nc,0}(s) = 1/2(\tilde{T}_{(3)}^{cn,0}(s) + \tilde{T}_{(3)}^{nc,0}(s)). \quad (10.86)$$

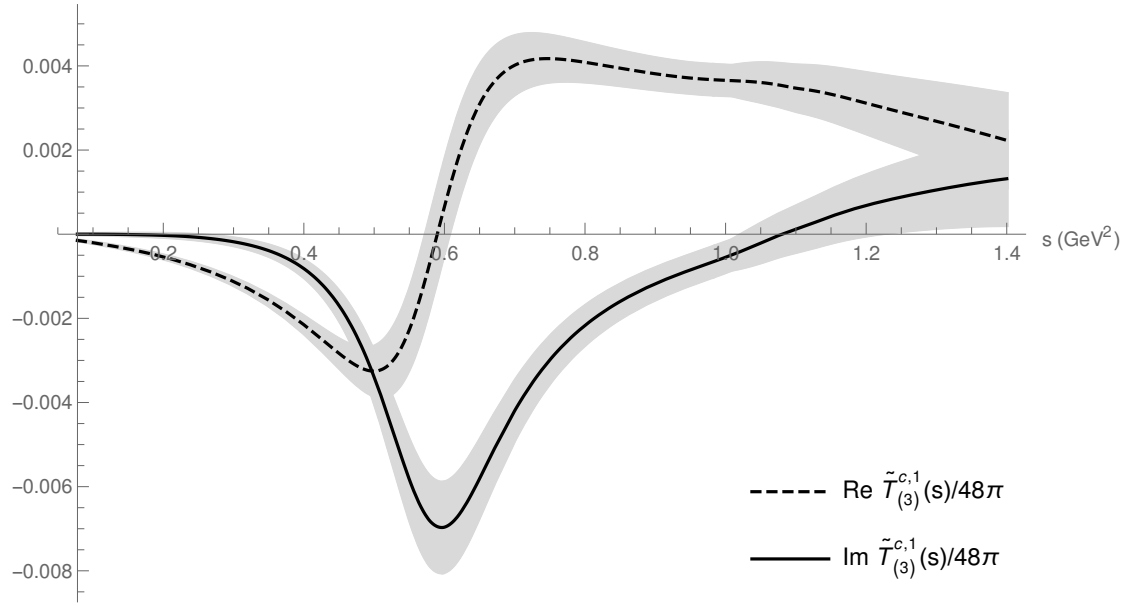


Figure 10.11: Real and imaginary parts of the solution of the implicit integral equation (10.74)

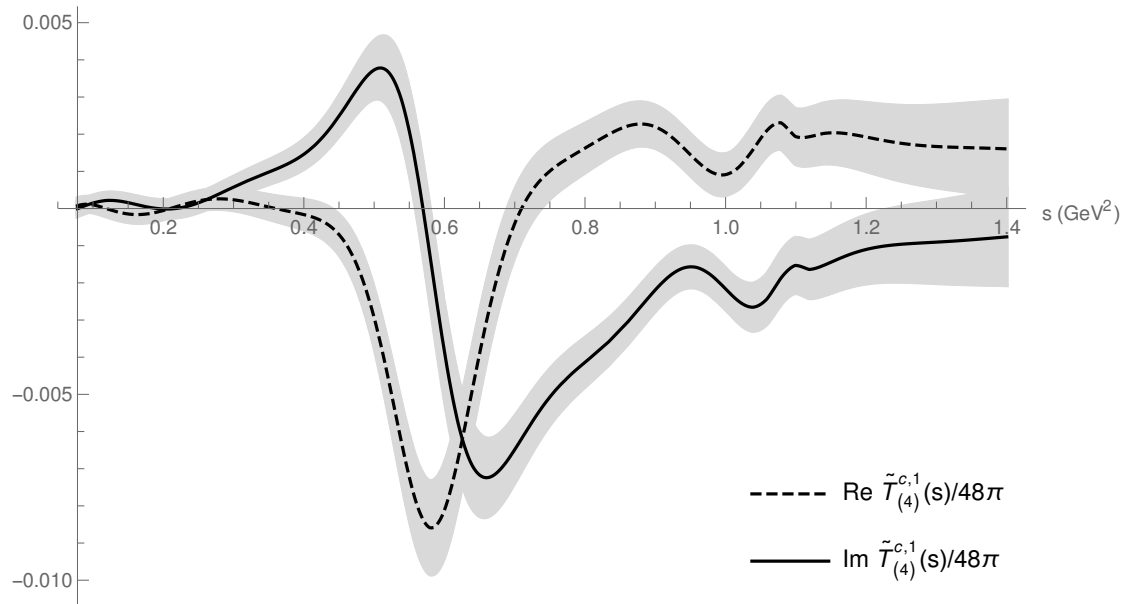


Figure 10.12: Real and imaginary parts of the solution of the implicit integral equation (10.75)

Using this relation, we can write the unitarity relation as the following matrix equation

$$\begin{aligned}\text{Im}\tilde{\mathbf{T}}_{(3)}^0(s) &= T^*\Sigma\tilde{\mathbf{T}}_{(3)}^0(s) + T\Sigma\tilde{\mathbf{T}}_{(3)}^{0*}(s) + \mathbf{\Delta}_{(3)}^0(s) \\ &= 2\text{Re}\left(T^*\Sigma\tilde{\mathbf{T}}_{(3)}^0(s)\right) + \mathbf{\Delta}_{(3)}^0(s)\end{aligned}\quad (10.87)$$

where the matrix product  $T^*\Sigma$  can be written in the chiral limit as

$$T^*\Sigma = 2\sigma_\pi(s) \begin{pmatrix} t_c^{0*}(s) & t_{cn}^{0*}(s)/2 & 0 \\ t_{cn}^{0*}(s)/2 & t_c^{0*}(s)/2 + t_n^{0*}(s)/4 & t_{cn}^{0*}(s)/4 \\ 0 & t_{cn}^{0*}(s) & t_n^{0*}(s)/2 \end{pmatrix}. \quad (10.88)$$

Note that the factor  $1/2$  in the second line of the matrix is due to the definition of the symmetrized amplitude in (10.86). The other  $1/2$  factors are due to the indistinguishable pair of neutral pions in the intermediate state. As in the two-dimensional case above, this matrix is diagonalizable. We can write

$$T^*\Sigma = P\Lambda P^{-1}, \quad (10.89)$$

$$\Lambda = \sigma_\pi(s) \text{diag}\left(t_0^{0*}(s), t_0^{2*}(s), 1/2(t_0^{0*}(s) + t_0^{2*}(s))\right), \quad (10.90)$$

$$P = \begin{pmatrix} 1 & 1/4 & -1/2 \\ 1 & -1/2 & 1/4 \\ 1 & 1 & 1 \end{pmatrix}, \quad (10.91)$$

$$P^{-1} = \begin{pmatrix} 4/9 & 4/9 & 1/9 \\ 4/9 & -8/9 & 4/9 \\ -8/9 & 4/9 & 4/9 \end{pmatrix}. \quad (10.92)$$

Again, we define

$$\mathbf{G}_{(3)}^0(s) := P^{-1}\tilde{\mathbf{T}}_{(3)}^0(s), \quad (10.93)$$

$$\mathbf{\Gamma}_{(3)}^0(s) := P^{-1}\tilde{\mathbf{\Delta}}_{(3)}^0(s). \quad (10.94)$$

Each component of this vector fulfils a single-channel implicit integral equation similar to those in the case of the P-wave projection. The only difference is the partial-wave present in the diagonal matrix (10.90). We have

$$\begin{aligned}\text{Im}G_{(3),1}^0(s) &= \frac{\Gamma_{(3),1}(s) + 2\sigma_\pi(s)\text{Re}t_0^0(s)\text{Re}G_{(3),1}^0(s)}{1 - 2\sigma_\pi(s)\text{Im}t_0^0(s)}, \\ \text{Im}G_{(3),2}^0(s) &= \frac{\Gamma_{(3),2}(s) + 2\sigma_\pi(s)\text{Re}t_0^2(s)\text{Re}G_{(3),2}^0(s)}{1 - 2\sigma_\pi(s)\text{Im}t_0^2(s)}, \\ \text{Im}G_{(3),3}^0(s) &= \frac{\Gamma_{(3),3}(s) + \sigma_\pi(s)\text{Re}(t_0^0(s) + t_0^2(s))\text{Re}G_{(3),3}^0(s)}{1 - \sigma_\pi(s)\text{Im}(t_0^0(s) + t_0^2(s))}.\end{aligned}\quad (10.95)$$

Formally, the equation is evidently the same for the two other topologies and we can write

$$\begin{aligned}\text{Im}G_{(4),1}^0(s) &= \frac{\Gamma_{(4),1}(s) + 2\sigma_\pi(s)\text{Re}t_0^0(s)\text{Re}G_{(4),1}^0(s)}{1 - 2\sigma_\pi(s)\text{Im}t_0^0(s)}, \\ \text{Im}G_{(4),2}^0(s) &= \frac{\Gamma_{(4),2}(s) + 2\sigma_\pi(s)\text{Re}t_0^2(s)\text{Re}G_{(4),2}^0(s)}{1 - 2\sigma_\pi(s)\text{Im}t_0^2(s)}, \\ \text{Im}G_{(4),3}^0(s) &= \frac{\Gamma_{(4),3}(s) + \sigma_\pi(s)\text{Re}(t_0^0(s) + t_0^2(s))\text{Re}G_{(4),3}^0(s)}{1 - \sigma_\pi(s)\text{Im}(t_0^0(s) + t_0^2(s))}.\end{aligned}\quad (10.96)$$

The denominator in the equation for the first component has three zeros at  $s_1^0$ ,  $s_2^0$  and  $s_3^0$ . Similarly to the case before, we add the constraint that the real part vanishes at  $s = 0$ . We write a four-times subtracted dispersion relation for the real part as ( $i \in \{3, 4\}$ )

$$\text{Re}\tilde{G}_{(i),1}^0(s) = P_{(i),1}^0(s) + D_{(i),1}^0(s) \quad (10.97)$$

$$D_{(i),1}^0(s) = \frac{s^4}{\pi} P \int_{4m_\pi^2}^{\infty} ds' \frac{\text{Im}\tilde{G}_{(i),1}^0(s')}{s'^4(s' - s)} \quad (10.98)$$

$$\begin{aligned} P_{(i),1}^0(s) = & (\text{Re}\tilde{G}_{(i),1}^0(s_1^0) - D_{(i),1}^{c,1}(s_1^0)) \frac{(s - s_2^0)(s - s_3^0)s}{(s_1^0 - s_2^0)(s_1^0 - s_3^0)s_1^0} \\ & + (\text{Re}\tilde{G}_{(i),1}^0(s_2^0) - D_{(i),1}^0(s_2^0)) \frac{(s - s_1^0)(s - s_3^0)s}{(s_2^0 - s_1^0)(s_2^0 - s_3^0)s_2^0} \\ & + (\text{Re}\tilde{G}_{(i),1}^0(s_3^0) - D_{(i),1}^0(s_3^0)) \frac{(s - s_1^0)(s - s_2^0)s}{(s_3^0 - s_1^0)(s_3^0 - s_2^0)s_3^0}. \end{aligned} \quad (10.99)$$

The denominator of the second component, on the other hand has no zero. We can simply write a once-subtracted dispersion relation

$$\text{Re}\tilde{G}_{(i),2}^0(s) = \frac{s}{\pi} P \int_{4m_\pi^2}^{\infty} ds' \frac{\text{Im}\tilde{G}_{(i),2}^0(s')}{s'(s' - s)}. \quad (10.100)$$

Again, the subtraction constant is set to 0. Finally, the denominator of the third component has four zeros,  $s_{(j)}^2$ ,  $j \in \{1, 2, 3, 4\}$ . However, the first one also corresponds to a zero of  $\sigma_\pi(s)\text{Re}(t_0^0(s) + t_0^2(s))$ . This means that at this point, there is a constraint on the inhomogeneity  $\Gamma_{(i),3}(s)$  that must exactly vanish. The fact that it does is a good check of consistency in our case. We can write the real part as

$$\text{Re}\tilde{G}_{(i),3}^0(s) = P_{(i),3}^0(s) + D_{(i),3}^0(s) \quad (10.101)$$

$$D_{(i),3}^0(s) = \frac{s^4}{\pi} P \int_{4m_\pi^2}^{\infty} ds' \frac{\text{Im}\tilde{G}_{(i),3}^0(s')}{s'^4(s' - s)} \quad (10.102)$$

$$\begin{aligned} P_{(i),3}^0(s) = & (\text{Re}\tilde{G}_{(i),3}^0(s_2^2) - D_{(i),3}^{c,1}(s_2^2)) \frac{(s - s_3^2)(s - s_4^2)s}{(s_2^2 - s_3^2)(s_2^2 - s_4^2)s_2^2} \\ & + (\text{Re}\tilde{G}_{(i),3}^0(s_3^2) - D_{(i),3}^0(s_3^2)) \frac{(s - s_2^2)(s - s_4^2)s}{(s_3^2 - s_2^2)(s_3^2 - s_4^2)s_3^2} \\ & + (\text{Re}\tilde{G}_{(i),3}^0(s_4^2) - D_{(i),3}^0(s_4^2)) \frac{(s - s_2^2)(s - s_3^2)s}{(s_4^2 - s_2^2)(s_4^2 - s_3^2)s_4^2}. \end{aligned} \quad (10.103)$$

Note that in this case, we do not impose any sum-rule on the imaginary part of the components of  $\tilde{\mathbf{G}}_{(i)}^0(s)$ . The reason is that we only solve the equation in the interval  $s \in [4m_\pi^2, 1\text{GeV}^2]$ . This way, the  $K\bar{K}$  does not interfere and we are able to find a stable solution.

Also, we notice that the size of the components of the inhomogeneity  $\mathbf{\Gamma}_{(4)}$  is one to two orders of magnitude smaller than those of  $\mathbf{\Gamma}_{(3)}$ . Therefore, we treat  $\tilde{\mathbf{G}}_{(4)}^0(s)$  as an uncertainty and only care about the contribution from diagram 10.1e.

The same method as in the case of the P-wave is used for each of the components. Once the solution is found for each of them, we go back to the physical basis by inverting relation (10.93). The numerical solutions are depicted in figure 10.13.



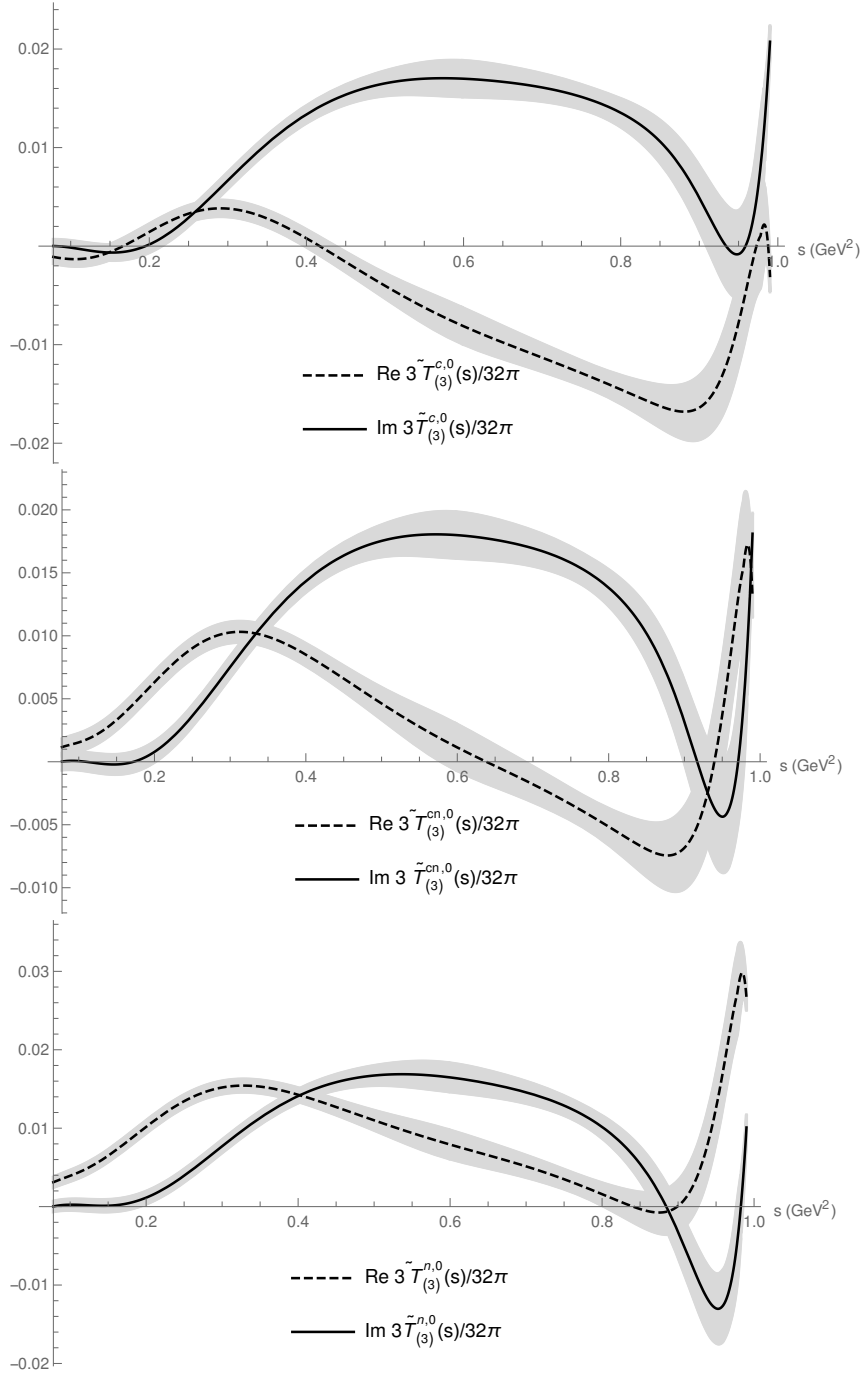


Figure 10.13: Real and imaginary parts of the solution to the implicit integral equation (10.95). The three plots correspond respectively to the corrections to the processes  $\pi^+\pi^- \rightarrow \pi^+\pi^-$ ,  $\pi^+\pi^- \rightarrow \pi^0\pi^0$  and  $\pi^0\pi^0 \rightarrow \pi^0\pi^0$

### 10.5.3 Contribution to the process $\pi^+\pi^+ \rightarrow \pi^+\pi^+$

The contribution from the many-loop topologies 10.1e - 10.1g to the process  $\pi^+\pi^+ \rightarrow \pi^+\pi^+$  is completely analogous. In this case, there is only one channel and the unitarity relation can be expressed as

$$\begin{aligned} \frac{\text{Disc}T_{(3)}^+}{2i} &= \frac{(2\pi)^4}{2} \int d\Phi_2 \text{Re} \left[ T_{(1)}^+(s, t_1) \times T_{\pi\pi}^{+*}(s, t_2) \right] \\ &+ \frac{(2\pi)^4}{2} \int d\Phi_2 \text{Re} \left[ T_{(3)}^+(s, t_1) \times T_{\pi\pi}^{+*}(s, t_2) \right] \\ &+ \frac{1}{2} \frac{(2\pi)^4}{2} \int d\Phi_3 M_{\pi}^{+, \text{int}}(s, \{t_i\}) \cdot M_{\pi}^{+, \text{int}*}(s, \{\tilde{t}_i\}) \end{aligned} \quad (10.104)$$

$$\begin{aligned} \frac{\text{Disc}T_{(4)}^+}{2i} &= \frac{(2\pi)^4}{2} \int d\Phi_2 \text{Re} \left[ T_{(2)}^+(s, t_1) \times T_{\pi\pi}^{+*}(s, t_2) \right] \\ &+ \frac{(2\pi)^4}{2} \int d\Phi_2 \text{Re} \left[ T_{(4)}^+(s, t_1) \times T_{\pi\pi}^{+*}(s, t_2) \right] \\ &+ \frac{(2\pi)^4}{2} \int d\Phi_3 \text{Re} \left[ M_{\pi, \pi\pi}^{+, \text{int}}(s, \{t_i\}) \cdot M_{\pi, \pi\pi}^{+, \text{ext}*}(s, \{\tilde{t}_i\}) \right] \end{aligned} \quad (10.105)$$

Note that once again, only half of the phase-space is integrated over, since the two positively-charged pions are identical particles.

Only even waves contribute to this process. We can project this amplitude on the S-wave as

$$\frac{\text{Disc}\tilde{T}_{(i)}^{+,0}(s)}{2i} = 2\sigma_{\pi}(s) \text{Re} \left[ \tilde{T}_{(i)}^{+,0}(s) t_2^{2*}(s) \right] + \Delta_{(i)}^{+,0}(s) \quad (10.106)$$

Again, the inhomogeneity  $\Delta_{(i)}^{+,0}(s)$  consists of the terms that do not depend on  $T_{(i)}^+$  in (10.105). This single-channel unitarity relation for the S-wave is very similar to (10.71) and so is the implicit integral equation:

$$\text{Im}\tilde{T}_{(i)}^{+,0}(s) = \frac{\Delta_{(i)}^{+,0}(s) + 2\sigma_{\pi}(s) \text{Re}t_2^2(s) \text{Re}\tilde{T}_{(i)}^{+,0}(s)}{1 - 2\sigma_{\pi}(s) \text{Im}t_2^2(s)}. \quad (10.107)$$

The denominator in this case has no zero between threshold and  $2\text{GeV}^2$ . We can simply write a once-subtracted dispersion relation

$$\text{Re}\tilde{T}_{(i)}^{+,0}(s) = \frac{s}{\pi} P \int_{4m_{\pi}^2}^{\infty} ds' \frac{\text{Im}\tilde{T}_{(i)}^{+,0}(s')}{s'(s' - s)}. \quad (10.108)$$

where the subtraction constant has been set to 0 conformally to the chiral ordering discussed above.

### 10.5.4 Ambiguity due to homogeneous solution

The numerical method used to calculate the inhomogeneous solution of the implicit integral equation is explained in appendix F. It is important to notice that an homogenous solution

to the implicit integral equation may also exist. Let us define such a solution to equation (10.74) in the case  $\Delta_{(3)}^{c,1}(s) = 0$  as  $\tilde{T}_{(3),0}^{c,1}(s)$ , such that

$$\text{Im}\tilde{T}_{(3),0}^{c,1}(s) = \frac{2\sigma_\pi(s)\text{Ret}_1^1(s)\text{Re}\tilde{T}_{(3),0}^{c,1}(s)}{1 - 2\sigma_\pi(s)\text{Im}t_1^1(s)}. \quad (10.109)$$

This would directly lead to an ambiguity in our solution of the inhomogeneous problem. The reason is that one can add to the inhomogeneous solution  $\tilde{T}_{(3)}^{c,1}(s)$  the product of the homogeneous solution with any constant  $c$  and the implicit integral equation would still be satisfied:

$$\text{Im}\left[\tilde{T}_{(3)}^{c,1}(s) + c\tilde{T}_{(3),0}^{c,1}(s)\right] = \frac{\Delta_{(3)}^{c,1} + 2\sigma_\pi(s)\text{Ret}_1^1(s)\text{Re}\left[\tilde{T}_{(3)}^{c,1}(s) + c\tilde{T}_{(3),0}^{c,1}(s)\right]}{1 - 2\sigma_\pi(s)\text{Im}t_1^1(s)}. \quad (10.110)$$

In order to illustrate this feature, we first consider the diagram of figure 10.1b again. Because of time invariance, we can write the amplitude schematically as

$$2T_{(1)}^c(s, t) = \text{diagram 1} + \text{diagram 2}. \quad (10.111)$$

Then, following the same steps as the the derivation for the multi-loop topologies above, we find the following implicit equation for the P-wave projection:

$$\text{Im}\tilde{T}_{(1)}^{c,1}(s) = \frac{\Delta_{(1)}^{c,1}(s) + \sigma_\pi(s)\text{Ret}_1^1(s)\text{Re}\tilde{T}_{(1)}^{c,1}(s)}{1 - \sigma_\pi(s)\text{Im}t_1^1(s)} \quad (10.112)$$

Note that formally, the difference with equation (10.74) is the factor 2 multiplying the threshold functions in the numerator and denominator. The homogeneous solution to this implicit equation, that is, in the case where the inhomogeneity is set to 0 is

$$\tilde{T}_{(1),0}^{c,1}(s) = t_1^1(s). \quad (10.113)$$

This can be easily verified using relation (4.21). The inhomogeneity comes solely from the cut through the two-pion state and is the product of diagram 10.1a with a  $\pi\pi$ -scattering P-wave:

$$\Delta_{(1)}^{c,1}(s) = 2\sigma_\pi(s)\tilde{T}_{(0)}^1(s)\text{Ret}_1^1(s). \quad (10.114)$$

In this case, the denominator has a zero of order two at the  $\rho$  mass  $s^* = m_\rho^2$ . Consequently, both the numerator and its derivative must vanish at that point. The first constraint is trivially satisfied, because both terms are proportional to  $\text{Ret}_1^1(s)$  that vanishes precisely at that point. The second constraint leads to

$$\text{Re}\tilde{T}_{(1)}^{c,1}(s^*) = -2\tilde{T}_{(0)}^1(s^*). \quad (10.115)$$

Note that this constraint is numerically satisfied by the result from the method derived in section 10.3.1. This is a good check of consistency.

Using this constraint and imposing that it vanishes at  $s = 0$ , we can write the real part of  $\tilde{T}_{(1)}^{c,1}$  as a twice-subtracted dispersive integral

$$\text{Re}\tilde{T}_{(1)}^{c,1}(s) = P_{(1)}^{c,1}(s) + D_{(1)}^{c,1}(s) \quad (10.116)$$

$$D_{(1)}^{c,1}(s) = \frac{s^2}{\pi} \int_{4m_\pi^2}^{\infty} ds' \frac{\text{Im}\tilde{T}_{(1)}^{c,1}(s')}{s'^2(s' - s)} \quad (10.117)$$

$$P_{(1)}^{c,1}(s) = \left( \text{Re}\tilde{T}_{(1)}^{c,1}(s^*) - D_{(1)}^{c,1}(s^*) \right) \frac{s}{s^*} \quad (10.118)$$

We can then apply the method of the previous section to equation (10.112). The difference is that in this case, we use the ansatz

$$\text{Im}\tilde{T}_{(1)}^{c,1}(s) = P(s)\text{Ret}_1^1(s) + c\sigma_\pi(s) \quad (10.119)$$

where  $c$  is an additional coefficient. This term is added because of the zero of the real part of  $t_1^1(s)$ . Without this term, the ansatz would have a fixed zero that would add a wrong constraint to the system. Also, the presence of  $\sigma_\pi(s)$  is due to the known behaviour of the imaginary part near threshold. This can be read off from the implicit equation (10.112) and the explicit expression of the inhomogeneity (10.114). Note that the photon exchange behaves as  $\tilde{T}_{(0)}^1 \sim \sigma_\pi(s)^{-2}$  close to threshold. Also, we implement the sum rule

$$\frac{s^*}{\pi} \int_{4m_\pi^2}^{\infty} ds' \frac{\text{Im}\tilde{T}_{(1)}^{c,1}(s')}{s'(s' - s^*)} = \text{Im}\Delta_{(1)}^{c,1}(s^*). \quad (10.120)$$

into the parametrization. Once the numerical solution is found, we can check that it differs from the solution of the Omnès-Muskhelishvili method (10.15) only by a multiple of the homogeneous solution (10.113).

In the case of the implicit integral equations of the multi-loop topologies, there is also an ambiguity due to the homogeneous solution. We can not rely on any ChPT estimate corresponding to those topologies to fix the ambiguity. As explained in section 10.1, we know that those diagrams would be at least one order higher in  $p^2$  than the one-loop diagrams in the chiral ordering scheme. The consequence is that we set the amplitude corresponding to those topologies to 0 at  $s = 0$ . The possible deviation from this approximation are then accounted for as uncertainties.

As a last remark, we add that an implicit integral equations of the form

$$\text{Im}T(s) = \frac{\Delta(s) + 2\sigma_\pi(s)\text{Re}t_j^I(s)\text{Re}T(s)}{1 - 2\sigma_\pi(s)\text{Im}t_j^I(s)}, \quad (10.121)$$

like equations (10.74) or (10.75), has an homogeneous solution given by

$$\text{Im}T_0(s) = \text{Im}[t_j^I(s)^2] \quad (10.122)$$

as can be checked easily using relation (4.21).

## 10.6 Contribution from many-loop topologies in the crossed channels

The multi-loop topologies of figure 10.1 have been calculated in the direct channel,  $s$ , and for the process  $\pi^+\pi^- \rightarrow \pi^+\pi^-$ . Additionally, those also contribute in the form of a

crossed-channel loop, that is, when the diagrams are rotated by 90 degrees. In this case, the relevant crossed-channel processes are  $\pi^+\pi^- \rightarrow \pi^+\pi^-$  and  $\pi^+\pi^+ \rightarrow \pi^+\pi^+$ . In the previous sections, we calculated the S- and P-wave projection of the amplitude evaluated in the corresponding channel. Those can then be projected on the  $s$ -channel P-wave using the usual Legendre polynomial orthogonality property.

Additionally to those topologies evaluated in the crossed channels, we must also take into account their  $\pi\pi$  rescattering. The resulting topology is depicted in figure 10.14. Note that this process of evaluating a many-loop topology in a crossed channel, projecting it on  $s$  and considering the rescattering effects is infinitely repeatable. That way, one would find at each iteration a new topology. However, it must also be noted that in the unitarity relation of these new topologies, one of the two subamplitudes is small, since a cut in the  $s$ -channel would start at least at the four-pion creation threshold. This is also checked numerically. All next iterations of this procedure are thus neglected and this is the reason why the diagram of figure 10.14 has not been taken into account in the topologies listed in figure 10.1.

The method to calculate the topology of figure 10.14 is very similar to the method used for diagram 10.1b. The only difference is that we replace the tree-level photon exchange diagram 10.1a by the multi-loop diagrams of figure 10.1 evaluated in the crossed channel and projected on the  $s$ -channel P-wave. We define this amplitude as

$$\tilde{T}_{(i)}^{tu,\ell}(s) = \frac{2\ell+1}{2} \int_{-1}^1 dz P_\ell(z) \left( T_{(i)}^c(t(z), s) + T_{(i)}^+(u(z), s) \right), \quad i \in \{3, 4\}. \quad (10.123)$$

This is due to the fact that the right-hand cut of the latter is neglected and the Omnès-Muskhelishvili method can be used. Note that the projected amplitudes in (10.123) are evaluated at negative  $t$  and  $u$ . We therefore use the dispersive expressions above to analytically continue the amplitude in this region of the Mandelstam plane.

In the case of the fully-charged process, the discontinuity along the right-hand cut is given by

$$\begin{aligned} \frac{\text{Disc}_s T_{(5)}^c(s, t)}{2i} &= \frac{(2\pi)^4}{2} \int d\Phi_2 \left( T_{(3)}^c(t_1, s) + T_{(4)}^c(t_1, s) + T_{(5)}^c(s, t_1) \right) T_{\pi\pi}^{c*}(s, t_2) \\ &\quad + \frac{(2\pi)^4}{2} \int d\Phi_2 \left( T_{(3)}^{cn}(t_1, s) + T_{(4)}^{cn}(t_1, s) + T_{(5)}^{cn}(s, t_1) \right) T_{\pi\pi}^{cn*}(s, t_2) \\ &= 2\sigma_\pi(s) \sum_{I,j} \left( \tilde{T}_{(3)}^{tu,j}(s) + \tilde{T}_{(4)}^{tu,j}(s) + \tilde{T}_{(5)}^{c,j}(s) \right) c_j^{c,I} P_j(z) t_j^I(s)^* \\ &\quad + \sigma_\pi(s) \sum_{I,j} \left( \tilde{T}_{(3),cn}^{tu,j}(s) + \tilde{T}_{(4),cn}^{tu,j}(s) + \tilde{T}_{(5)}^{cn,j}(s) \right) c_j^{cn,I} P_j(z) t_j^I(s)^*. \end{aligned} \quad (10.124)$$

Note that the partial waves  $\tilde{T}_{(i),cn}^{tu,j}(s)$  are defined similarly to (10.123), but for the process  $\pi^+\pi^- \rightarrow \pi^0\pi^0$  instead of  $\pi^+\pi^- \rightarrow \pi^+\pi^-$ . Those do not matter in our case, since we are only interested in the  $s$ -channel P-wave projection of this amplitude. The S-wave projection is not taken into account, since it would only contribute to the next iteration that is neglected in our case. Projecting on the P-wave, we get

$$\text{Im} \tilde{T}_{(5)}^1(s) = \sigma_\pi(s) \left( \tilde{T}_{(3)}^{tu,1}(s) + \tilde{T}_{(4)}^{tu,1}(s) + \tilde{T}_{(5)}^1(s) \right) t_1^1(s)^*. \quad (10.125)$$

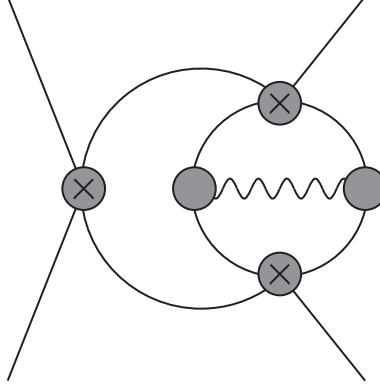


Figure 10.14: Topology consisting of a rescattering of the multi-loop topology of figure 10.1e

From here, the calculation is identical to the diagram of figure 10.1b and we can write

$$\tilde{T}_{(5)}^1(s) = \Omega_1^1(s) \left( c_{(5),0}^1 + c_{(5),1}^1 s + \frac{s^2}{\pi} \int_{4m_\pi^2}^{\infty} ds' \frac{\sin \delta_1^1(s') \left( \tilde{T}_{(3)}^{tu,1}(s') + \tilde{T}_{(4)}^{tu,1}(s') \right)}{|\Omega_1^1(s')|(s' - s)s'^2} \right). \quad (10.126)$$

The subtraction constants are set to 0 because of the higher chiral order of the topology and the fact that the low-energy behaviour of the amplitude has already been fixed by ChPT for the triangle topology.

## 10.7 Summary of the chapter

In this chapter, we have calculated the radiative corrections to the  $\pi\pi$ -scattering amplitude  $T_{\pi\pi}^\alpha$  projected on the S- and P-waves. The latter can be written as the sum of the different topologies of figure 10.1 and 10.14:

$$\tilde{T}_{\pi\pi}^{j,\alpha} = \sum_{i=0}^5 \tilde{T}_{(i)}^j(s). \quad (10.127)$$

The explicit expressions for each topology are the following:

- $\tilde{T}_{(0)}^0(s)$  and  $\tilde{T}_{(0)}^1(s)$  are given by (10.4) and (10.5).
- $\tilde{T}_{(1)}^1(s)$  is given by (10.15).
- $\tilde{T}_{(1)}^{c,0}(s)$  and  $\tilde{T}_{(1)}^{cn,0}(s)$  are given by (10.42) and (10.43).
- $\tilde{T}_{(1)}^{+,0}(s)$  is given by (10.47)
- $T_{(2)}(s, t)$  is given by (10.61).
- $\tilde{T}_{(3)}^1(s)$  and  $\tilde{T}_{(4)}^1(s)$  are given by the numerical solution of equations (10.74) and (10.75). Their dispersive representation is given by (10.79).

- $\tilde{T}_{(3)}^0(s)$  and  $\tilde{T}_{(4)}^0(s)$  are given by the numerical solution of equations (10.95) and (10.96). Their dispersive representations are given by (10.99), (10.100) and (10.103).
- $\tilde{T}_{(3)}^{+,0}(s)$  and  $\tilde{T}_{(4)}^{+,0}(s)$  are given by the numerical solution of equation (10.108). Their dispersive representation is given by (10.108) .
- $T_{(5)}^1(s)$  is given by (10.126).

## Chapter 11

# Radiative corrections to the pion vector form factor $F_\pi^{V,\alpha}$

In what follows, we calculate the radiative corrections to the pion vector form factor  $F_\pi^{V,\alpha}(s)$ . Those have been analysed in the framework of ChPT at the one-loop level in [3]. The details of the calculation are explained in section 5.3. Additionally, a representation of the pion vector form factor at two-loop accuracy in the low-energy expansion in the presence of isospin-breaking effects has been derived in [4]. There, the dispersive representation in the framework of the chiral expansion in the isospin limit [88] are extended to include isospin-breaking effects. Note however that those effects do not involve exchanges of virtual photons and only account for the mass difference between neutral and charged pions. In our case, we include photons in the intermediate state as well, as is clear from the unitarity relation (7.9). Note that all the ingredients needed as input in this relation have been treated in the previous chapters.

### 11.1 Topologies

Similarly to the case of the radiative corrections to the  $\pi\pi$ -scattering amplitude, we must identify the different topologies contributing to the process at order  $\alpha$ . The two-pion prescription explained in section 7.2 gives rise to all topologies where the hadronic blob of figure 6.3a can be substituted by a two-pion exchange. Those topologies are the ones depicted in figure 11.1. The corresponding amplitudes are defined as  $F_{(i)}(s)$ ,  $i \in \{1, 2, 3\}$ , as explained in appendix G. Again, those diagrams must be understood as unitarity diagrams. Note as well that the remarks of the previous section also apply in this case: the topology 11.1b accounts for all photon exchanges between the internal pion lines of the loop. The diagrams where the photon is emitted and reabsorbed by the same line must therefore also be taken into account. Similarly, diagram 11.1c accounts for all diagrams where a photon is exchanged between an internal and an external pion line. Hence, this topology represents four different diagrams. Finally, topology 11.1d accounts for all photon exchanges between an internal line of the first and of the second loop and has four different versions. The total radiative correction to the pion vector form factor is written as the sum of all those topologies:

$$F_\pi^{V,\alpha}(s) = \sum_{i=1}^3 F_{(i)}(s). \quad (11.1)$$



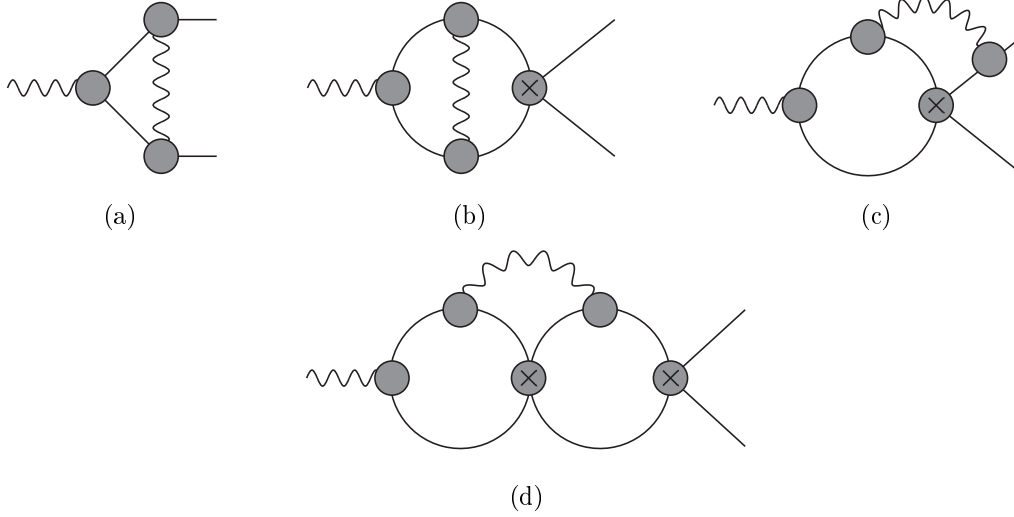


Figure 11.1: Topologies contributing to the radiative corrections to the pion vector form factor as a two-pion exchange. The full grey blobs account for the purely hadronic form factor. The crossed blobs account for the purely hadronic  $\pi\pi$  scattering amplitude.

The topologies of figure 11.1 can also be classified according to the number of occurrences of  $\pi\pi$  rescattering. The triangle diagram 11.1a has none of them. At very low energy, the chiral expansion implies that it must be the leading contribution. At higher energy, as explained in the previous section, this is not necessary the case any more and the dispersive framework is used to assess the size of the unitarity corrections from the different topologies. Similarly to the corrections to the  $\pi\pi$ -scattering amplitude, the unitarity relations of the multi-loop topologies 11.1b - 11.1d lead to an implicit integral equation due to the resummation of the local interaction vertices. This equation must be solved numerically, using the method explained in appendix F.

In practice, to calculate the discontinuity of the form factor along the cut caused by the different topologies, we must isolate the scalar part from the T-matrix element (5.1). To that end, we use the same contraction as in the purely hadronic case (5.8).

## 11.2 Triangle correction (diagram 11.1a)

We define the amplitude from diagram 11.1a as  $F_{(1)}(s)$ . There are two possible  $s$ -channel cuts in this diagram. The first one goes through the two-pion state and the second one through the hadronic blob. We calculate the discontinuity as

$$\frac{\text{Disc} F_{(1)}(s)}{2i} = \frac{\sigma_\pi(s)}{48\pi} F_\pi^V(s) \left( \tilde{T}_{(0)}^{1*}(s) + \tilde{T}_{(1)}^{1*}(s) \right) \quad (11.2)$$

One nice feature of this expression is that it is a real quantity by construction. This is due to the fact that the Omnès-Muskhelishvili method used to calculate the diagram (10.1b) is based on the Watson's theorem imposing that the phase of  $\left( \tilde{T}_{(0)}^1(s) + \tilde{T}_{(1)}^1(s) \right)$  is identical to the phase of the  $\pi\pi$ -scattering P-wave, and thus to the phase of the pion vector form factor as well.

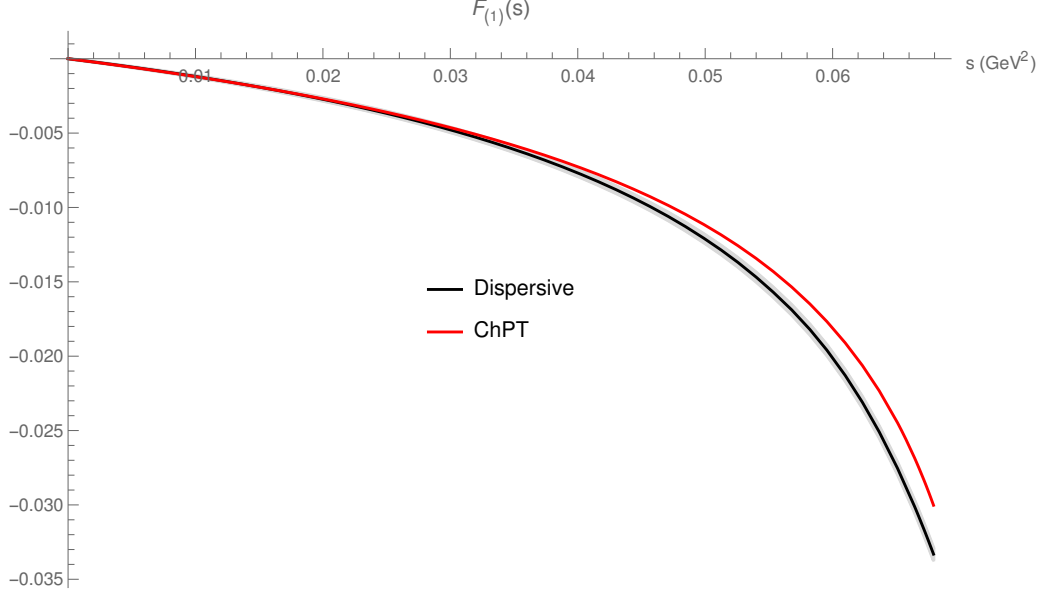


Figure 11.2: Comparison of the results from ChPT and from the dispersive result near  $s = 0$ .

The real part can be calculated from a once-subtracted dispersion relation

$$\text{Re}F_{(1)}(s) = c_{(1)} + \frac{s}{\pi} \int_{4m_\pi^2}^{\infty} ds' \frac{\text{Im}F_{(1)}(s')}{s'(s' - s)}. \quad (11.3)$$

The subtraction constant is fixed from the ChPT calculation (5.12) evaluated at  $s = 0$ . We find  $c_{(1)} = 0$ , in agreement with the current conservation in the isospin limit  $F_\pi^V(0) = 1$  that is already saturated by the purely hadronic form factor contribution. This condition is also in agreement with the radiative correction (5.10) calculated in ChPT. Near  $s = 0$ , both representations agree well, as can be seen from the plot of figure 11.2.

The numerical result in the energy range  $s \in [4m_\pi^2, 1.8 \text{ GeV}^2]$  is depicted in figure 11.3. Note the divergence at threshold due to the Coulomb pole. Once again, this has to be the case, because near threshold, the discontinuity (11.2) behaves as

$$\text{Disc}F_{(1)}(s) \sim \sigma_\pi(s) \times \sigma_\pi(s)^0 \times \sigma_\pi(s)^{-2} = \sigma_\pi(s)^{-1} \quad (11.4)$$

where the three terms correspond respectively to the phase-space, the behaviour of the pion vector form factor and of the photon-exchange amplitude.

Note that this diagram also enters the unitarity relation of the other topologies and is therefore also used as a building block in the calculation of their discontinuity.

### 11.3 Many-loop topologies

The unitarity relation of the many-loop topologies of figure 11.1 is very similar to the P-wave projection of the correction to the  $\pi\pi$ -scattering amplitude. We have schematically

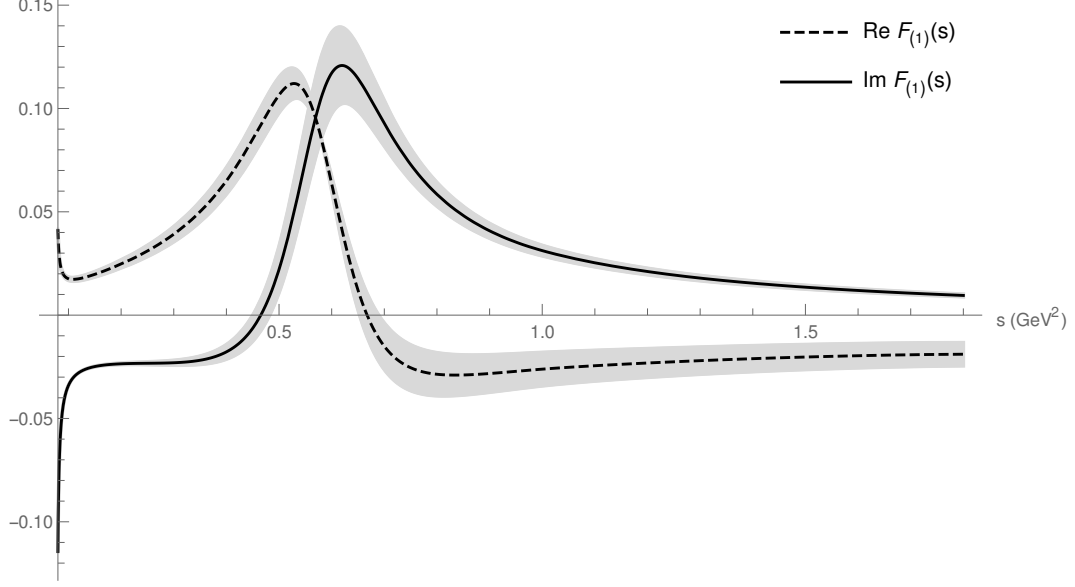


Figure 11.3: Real and imaginary part from the contribution of diagram 11.1a.

$$\text{Disc} \sim \text{wavy line} \sim \text{loop} \sim \text{vertex with cross} = \text{wavy line} \sim \text{loop with vertical dashed lines} \sim \text{vertex with cross} + \text{wavy line} \sim \text{loop with vertical dashed lines} \sim \text{vertex with cross} + \text{wavy line} \sim \text{loop with diagonal dashed lines} \sim \text{vertex with cross} . \quad (11.5)$$

This translates into

$$\begin{aligned} \frac{\text{Disc} F_{(2)}(s)}{2i} &= \frac{\sigma_\pi(s)}{48\pi} F_v^\pi(s) \times \left( \tilde{T}_{(1)}^{1*}(s) + \tilde{T}_{(3)}^{1*}(s) \right) \\ &+ \sigma_\pi(s) (F_{(1)}(s) + F_{(2)}(s)) \times t_1^{1*}(s) \\ &+ \frac{(2\pi)^4}{2} \int d\Phi_3 W_\pi(s, \{t_i\}) \cdot M_\pi^{c, \text{int}*}(s, \{\tilde{t}_i\}). \end{aligned} \quad (11.6)$$

Note the implicit dependence on  $F_{(2)}(s)$ . We define again the sum of all contributions in (11.6) that do not depend on  $F_{(2)}(s)$  as  $\Delta_{(2)}(s)$ . This quantity is the inhomogeneity of the problem. Note also that there is no neutral-pion pair in the intermediate state since all pions must be in a P-wave.

Similarly, we define the sum of the topologies 11.1c and 11.1d as  $F_{(3)}(s)$  and write the

corresponding unitarity relation as

$$\begin{aligned}
\frac{\text{Disc}F_{(3)}(s)}{2i} &= \frac{\sigma_\pi(s)}{48\pi} F_\pi^V(s) \times \left( \tilde{T}_{(2)}^{1*}(s) + \tilde{T}_{(4)}^{1*}(s) \right) \\
&+ \sigma_\pi(s) F_{(3)}(s) \times t_1^{1*}(s) \\
&+ \frac{(2\pi)^4}{2} \int d\Phi_3 W_\pi(s, \{t_i\}) \cdot M_{\pi,\pi\pi}^{c,\text{int}*}(s, \{\tilde{t}_i\}) \\
&+ \frac{(2\pi)^4}{2} \int d\Phi_3 W_{\pi\pi}(s, \{t_i\}) \cdot M_{\pi,\pi\pi}^{c*}(s, \{\tilde{t}_i\}). \tag{11.7}
\end{aligned}$$

The main difference with the implicit equation for the corrections to  $\pi\pi$  scattering is the fact that the inhomogeneities are not real quantities in this case. We can rewrite the unitarity relations for  $i \in \{2, 3\}$  as

$$\begin{aligned}
\text{Im}F_{(i)}(s) &= \Delta_{(i)}(s) + \sigma_\pi(s) F_{(i)}(s) t_1^{1*}(s) \\
&= \text{Re}\Delta_{(i)}(s) + \sigma_\pi(s) \text{Re}F_{(i)}(s) \text{Ret}_1^1(s) + \sigma_\pi(s) \text{Im}F_{(i)}(s) \text{Im}t_1^1(s) \\
&\quad + i \left( \text{Im}\Delta_{(i)}(s) - \sigma_\pi(s) \text{Re}F_{(i)}(s) \text{Im}t_1^1(s) + \sigma_\pi(s) \text{Im}F_{(i)}(s) \text{Ret}_1^1(s) \right). \tag{11.8}
\end{aligned}$$

In order for the imaginary part of  $F_{(i)}(s)$  to be a real quantity, we must impose that the term in brackets vanishes. This leads to two independent equations:

$$\text{Re}F_{(i)}(s) = \frac{\text{Im}\Delta_{(i)}(s) + \sigma_\pi(s) \text{Im}F_{(i)}(s) \text{Ret}_1^1(s)}{\sigma_\pi(s) \text{Im}t_1^1(s)}, \tag{11.9}$$

and

$$\text{Im}F_{(i)}(s) = \frac{\text{Re}\Delta_{(i)}(s) + \sigma_\pi(s) \text{Re}F_{(i)}(s) \text{Ret}_1^1(s)}{1 - \sigma_\pi(s) \text{Im}t_1^1(s)}. \tag{11.10}$$

We insert that first equation into (11.8) and get

$$\begin{aligned}
\text{Im}F_{(i)}(s) &= \text{Re}\Delta_{(i)}(s) + \frac{\text{Ret}_1^1(s)}{\text{Im}t_1^1(s)} \left( \text{Im}\Delta_{(i)}(s) + \sigma_\pi(s) \text{Im}F_{(i)}(s) \text{Ret}_1^1(s) \right) \\
&\quad + \sigma_\pi(s) \text{Im}F_{(i)}(s) \text{Im}t_1^1(s) \\
&= \text{Re}\Delta_{(i)}(s) + \frac{\text{Ret}_1^1(s)}{\text{Im}t_1^1(s)} \text{Im}\Delta_{(i)}(s) + \text{Im}F_{(i)}(s). \tag{11.11}
\end{aligned}$$

We used the relations

$$\begin{aligned}
\text{Im}t_1^1(s) &= \sigma_\pi(s) |t_1^1(s)|^2 = \sigma_\pi(s) \left( \text{Ret}_1^1(s)^2 + \text{Im}t_1^1(s)^2 \right) \\
&\Leftrightarrow \\
\text{Ret}_1^1(s)^2 &= \frac{\text{Im}t_1^1(s)}{\sigma_\pi(s)} - \text{Im}t_1^1(s)^2 \tag{11.12}
\end{aligned}$$

From here, we see that the term  $\text{Im}F_{(i)}(s)$  drops out and we end up with the equation

$$\frac{\text{Im}\Delta_{(i)}(s)}{\text{Re}\Delta_{(i)}(s)} = -\frac{\text{Im}t_1^1(s)}{\text{Ret}_1^1(s)}. \tag{11.13}$$

This means that the phase of the inhomogeneity  $\Delta_{(i)}(s)$  must be equal to the  $\pi\pi$ -scattering P-wave phase shift up to a minus sign. This new constraint seems curious at first, but this is a direct consequence of the unitarity relation.

As a side remark, we stress that the ambiguity in the solution of the multi-loop topologies contributing to the inhomogeneity does not have any effect on this constraint. This is due to the fact that, as explained above, the homogeneous solutions  $T_{(j),0}$  for  $j \in \{3, 4\}$  is proportional to  $t_1^1(s)^2$ , up to a real constant  $c$ . Its contribution to the inhomogeneity is therefore

$$\frac{\sigma_\pi(s)}{48\pi} F_\pi^V(s) \times \tilde{T}_{(j),0}^{1*} = c \frac{\sigma_\pi(s)}{48\pi} [F_\pi^V(s) t_1^{1*}(s)] t_1^{1*}(s). \quad (11.14)$$

The term in bracket is a real quantity. Therefore, the phase of this quantity is the phase of  $t_1^{1*}(s)$ , independently of the choice of the constant  $c$ .

In order to find  $\text{Im}F_{(i)}(s)$  and  $\text{Re}F_{(i)}(s)$ , we must solve (11.9). The latter can be recast into

$$\text{Im}F_{(i)}(s) = \frac{\sigma_\pi(s) \text{Im}t_1^1(s) \text{Re}F_{(i)}(s) - \text{Im}\Delta_{(i)}(s)}{\sigma_\pi(s) \text{Re}t_1^1(s)}. \quad (11.15)$$

This equation only has a simple pole at the  $\rho$ -mass  $s = s^* = m_\rho^2$ , instead of the double pole in (11.10). Note that at this point, the  $\pi\pi$ -scattering P-wave satisfies the following relation:

$$\text{Im}t_1^1(s^*) = \sigma_\pi(s^*) (\text{Im}t_1^1(s^*)^2 + \text{Re}t_1^1(s^*)^2) = \sigma_\pi(s^*) \text{Im}t_1^1(s^*)^2, \quad (11.16)$$

$$\Leftrightarrow$$

$$\sigma_\pi(s^*) \text{Im}t_1^1(s^*) = 1. \quad (11.17)$$

In order for  $\text{Im}F_{(i)}(s)$  to be well-defined at  $s = s^*$ , we must impose that the numerator also vanishes at this point. We get a condition for  $\text{Re}F_{(i)}(s)$ :

$$\text{Re}F_{(i)}(s^*) = \frac{\text{Im}\Delta_{(i)}(s^*)}{\sigma_\pi(s^*) \text{Im}t_1^1(s^*)} = \text{Im}\Delta_{(i)}(s^*). \quad (11.18)$$

Note that equation (11.10) does not lead to any further constraint on  $\text{Re}F_{(i)}(s)$ , when imposing analogous regularity condition. There are actually two conditions, because the denominator as well as its derivative vanish at  $s = s^*$ . However, this leads to constraints on  $\Delta_{(i)}(s)$  only:

$$\text{Re}\Delta_{(i)}(s^*) = \text{Re}F_{(i)}(s^*) \sigma_\pi(s^*) \text{Re}t_1^1(s^*) = 0 \quad (11.19)$$

$$\begin{aligned} \frac{\partial}{\partial s} [\text{Re}\Delta_{(i)}(s)]_{s=s^*} &= -\sigma_\pi(s^*) \text{Re}t_1^1(s^*) \frac{\partial}{\partial s} [\text{Re}F_{(i)}(s)]_{s=s^*} \\ &\quad - \text{Re}F_{(i)}(s^*) \frac{\partial}{\partial s} [\sigma_\pi(s) \text{Re}t_1^1(s)]_{s=s^*} \\ &= -\text{Im}\Delta_{(i)}(s^*) \frac{\partial}{\partial s} [\sigma_\pi(s) \text{Re}t_1^1(s)]_{s=s^*}. \end{aligned} \quad (11.20)$$

In order to solve equation (11.15), we can express the real part of  $F_{(i)}(s)$  as a twice-subtracted dispersive integral, imposing that the numerator of the equation has a zero at

$s = s^*$  and vanishes at  $s = 0$ :

$$\text{Re}F_{(i)}(s) = P_{(i)}(s) + D_{(i)}(s) \quad (11.21)$$

$$D_{(i)}(s) = \frac{s^2}{\pi} \int_{4m_\pi^2}^{\infty} ds' \frac{\text{Im}F_{(i)}(s')}{s'^2(s' - s)} \quad (11.22)$$

$$\begin{aligned} P_{(i)}(s) &= (\text{Re}F_{(i)}(s^*) - D_{(i)}(s^*)) \frac{(s - 0)}{(s^* - 0)} + (\text{Re}F_{(i)}(0) - D_{(i)}(0)) \frac{(s - s^*)}{(0 - s^*)} \\ &= (\text{Im}\Delta_{(i)}(s^*) - D_{(i)}(s^*)) \frac{s}{s^*} \end{aligned} \quad (11.23)$$

Also, assuming that  $\text{Re}F_{(i)}(s)$  goes asymptotically at most as a constant leads to the following sum rule

$$\frac{s^*}{\pi} \int_{4m_\pi^2}^{\infty} ds' \frac{\text{Im}F_{(i)}(s')}{s'(s' - s^*)} = \text{Im}\Delta_{(i)}(s^*). \quad (11.24)$$

As in the case of the radiative corrections to the  $\pi\pi$ -scattering amplitude, we stress that this special kind of implicit integral equation is new. To find a solution, we use a method similar to the one explained in appendix F.

## 11.4 Numerical solution of the implicit integral equation

Since we know that the phase of  $\Delta_{(i)}(s)$  must be equal to  $-\delta_1^1(s)$ , it is reasonable to assume that the imaginary part  $\text{Im}\Delta_{(i)}(s)$  behaves like the imaginary part of  $t_1^1(s)$ . This assumption is also confirmed numerically. Let us write

$$\text{Im}\Delta_{(i)}(s) = \alpha \text{Im}t_1^1(s). \quad (11.25)$$

The solution of this implicit integral equation is  $F_{(i)}(s) = \text{Re}F_{(i)}(s) + i \text{Im}F_{(i)}(s) = -i\alpha t_1^1(s)$ <sup>1</sup>. To understand why, let's choose another real constant  $\beta$  and assume that the solution is  $F_{(i)}(s) = -i\beta t_1^1(s)$ . This means  $\text{Im}F_{(i)}(s) = -\beta \text{Ret}_1^1(s)$  and  $\text{Re}F_{(i)}(s) = \beta \text{Im}t_1^1(s)$ . The implicit integral equation becomes

$$\begin{aligned} -\beta \sigma_\pi(s) (\text{Ret}_1^1(s)^2 + \text{Im}t_1^1(s)^2) &= -\text{Im}\Delta_{(i)}(s) \\ -\beta \text{Im}t_1^1(s) &= -\alpha \text{Im}t_1^1(s) \\ \beta &= \alpha. \end{aligned}$$

The conclusion is that under the assumption (11.25), the solution is exactly  $F_{(i)}(s) = -i\alpha t_1^1(s)$ . We therefore use the same numerical method explained in appendix F applied to the correction to  $\pi\pi$  scattering. In this case, the ansatz we start with is

$$\text{Im}F_{(2,3)}(s) = P(s) \text{Ret}_1^1(s) + c \sigma_\pi(s)^2 \quad (11.26)$$

Again,  $c$  is an additional parameter and the corresponding term gives the freedom to the solution to shift the zero of  $\text{Ret}_1^1(s)$ . The  $\sigma_\pi(s)^2$  in front is due to the behaviour of the imaginary part near threshold. It can be obtained from (11.10), where the dominant

---

<sup>1</sup>Note that such a representation is only valid above the two-pion threshold. In the case where  $s < 4m_\pi^2$ , the imaginary part of this expression vanishes and is therefore not anymore proportional to  $\text{Ret}_1^1(s)$ . The real part, on the contrary, does not vanish and is defined by its analytic continuation below threshold.

term in the inhomogeneity near threshold is the contribution from  $F_{(1)}(s)$  in (11.6). The behaviour of the  $\pi\pi$ -scattering P-wave near threshold is given by (10.22) and therefore

$$F_{(1)}(s) \sim \sigma_\pi(s)^{-1}, \quad (11.27)$$

$$F_{(2)}(s), F_{(3)}(s) \sim \sigma_\pi(s)^2. \quad (11.28)$$

Concerning the homogeneous implicit equation (11.15), it is easily found that the solution is (similarly to (10.113))

$$F_{(i),0}(s) = t_1^1(s). \quad (11.29)$$

The real part is set to zero at  $s = 0$  by construction via the dispersion relation (11.21). This convention is due to the fact that the corrections of those topologies appear at higher order in the chiral ordering scheme. The contribution from the homogeneous solution is then accounted for as an uncertainty.

The numerical result for the sum of the amplitudes  $F_{(2)}(s)$  and  $F_{(3)}(s)$  is depicted in figure 11.4. As we can see, it is small near threshold, as expected by chiral counting. An important point, as we will see in the next chapter, is that its contribution to the cross section  $\sigma(e^+e^- \rightarrow \pi^+\pi^-)$  is much less important than the contribution from the amplitude  $F_{(1)}(s)$  calculated above. The first reason is that the size of the amplitude is smaller. The second reason is that, as expected, the solution is close to  $\bar{F}_{(2+3)}(s) = -ict_1^1(s)$  where  $c$  is a real constant. Such a solution does however not contribute to the cross section, because according to (6.5), the contribution from such a solution would be

$$\bar{\sigma}(e^+e^- \rightarrow \pi^+\pi^-) \propto 2\text{Re} [i F_\pi^V(s) t_1^{1*}(s)] = 0 \quad (11.30)$$

On the other hand, the product of the purely hadronic pion vector form factor with the conjugate of the homogeneous solution (11.29) contributes to the cross section. This is the cause of an additional uncertainty due to the ambiguity in the solution of the implicit integral equation.

## 11.5 Contribution from many-loop topologies in the crossed channels

Similarly to section 10.6, the multi-loop diagrams 10.1e - 10.1g evaluated in the crossed channel and projected on the  $s$ -channel P-wave appear in the unitarity relation of the pion vector form factor. The corresponding diagram is depicted in figure 11.5. The latter has not been taken into account in the topologies of figure 11.1 since, as we have already seen in the previous chapter, the process is infinitely repeatable. The difference with the correction to the  $\pi\pi$ -scattering amplitude is that there is no implicit dependence in this case. The unitarity relation is very similar to the unitarity relation of diagram 11.1a given in (11.2). The difference is that the photon exchange is replaced by the multi-loop diagram in the corresponding channel and the box diagram 10.1b is replaced by diagram 10.14. The discontinuity is

$$\frac{\text{Disc} F_{(4)}(s)}{2i} = \frac{\sigma_\pi(s)}{48\pi} F_\pi^V(s) \left( \tilde{T}_{(3)}^{tu,1}(s) + \tilde{T}_{(4)}^{tu,1}(s) + \tilde{T}_{(5)}^{1*}(s) \right). \quad (11.31)$$

Then, the real part can directly be calculated using a once-subtracted dispersion relation:

$$\text{Re} F_{(4)}(s) = c_{(4)} + \frac{s}{\pi} \int_{4m_\pi^2}^{\infty} ds' \frac{\text{Im} F_{(4)}(s')}{s'(s' - s)}. \quad (11.32)$$

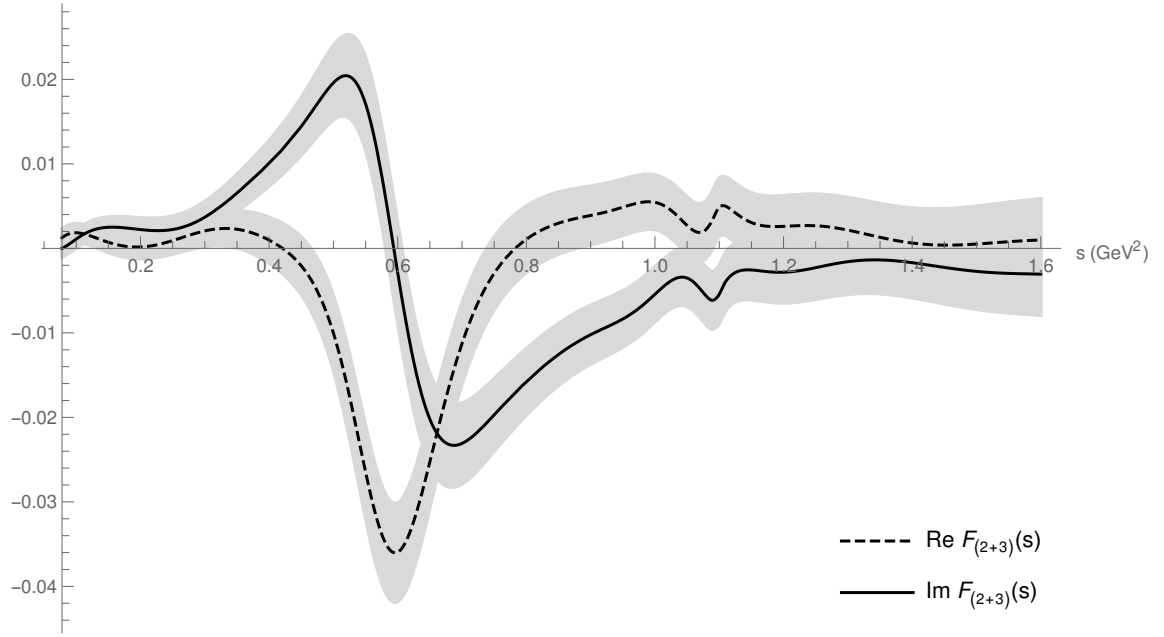


Figure 11.4: Real and imaginary part of the numerical solution of the implicit integral equation for the sum of the amplitudes  $F_{(2)}(s)$  and  $F_{(3)}(s)$ .

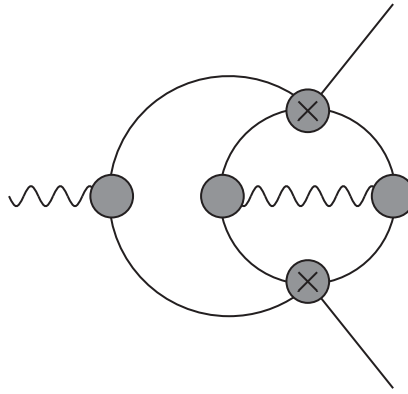


Figure 11.5: Topology consisting of the multi-loop topology of figure 10.1e in the  $t$ -channel



The subtraction constant  $c_{(4)}$  is set to 0 due to the higher order in the chiral counting of such a topology. Given the very small size of the building blocks in (11.31), the result can be incorporated into the uncertainty as well.

## 11.6 Summary of the chapter

In this chapter, we have calculated the radiative corrections to the pion vector form factor  $F_\pi^{V,\alpha}$ . The latter can be written as the sum of the different topologies of figure 11.1 and 11.5:

$$F_\pi^{V,\alpha}(s) = \sum_{i=1}^4 F_{(i)}(s) \quad (11.33)$$

The explicit expressions corresponding to each topology are the following:

- $F_{(1)}(s)$  is given by (11.2) and (11.3).
- $F_{(2)}(s)$  and  $F_{(3)}(s)$  are found by solving equation (11.15). Their dispersive representation is given by (11.21).
- $F_{(4)}(s)$  is given by (11.31) and (11.32).

## Chapter 12

# Impact on $(g - 2)_\mu$

Having now calculated all corrections due to virtual-photon exchange, we have all the elements needed to calculate the effect on the total cross section  $\sigma(e^+e^- \rightarrow \pi^+\pi^-(\gamma))$  and consequently estimate the impact on  $(g - 2)_\mu$ .

### 12.1 Corrections to the cross section

The effect of the FSR contribution on the cross section is calculated from (6.6), (6.7) and (6.11) as

$$\sigma^\alpha(e^+e^- \rightarrow \pi^+\pi^-) := \alpha\sigma_1(e^+e^- \rightarrow \pi^+\pi^-) + \alpha\sigma_1(e^+e^- \rightarrow \pi^+\pi^-\gamma). \quad (12.1)$$

Note that both the virtual- and real-photon exchanges are taken into account and lead to an infrared-finite quantity. The result can then be compared to the prescription explained in section 7.1.

The first plot of figure 12.1 represents the relative cross section  $\sigma^\alpha/\sigma_0$  when considering only the topology of figure 11.1a,  $F_{(1)}(s)$ , as the virtual photon exchange contribution. As we can see, both results agree within the uncertainty of our prediction. The latter is large and essentially due to the uncertainty in the low-energy constants of ChPT that are used as input to determine the subtraction constants. Note that as in the scalar QED calculation, there is a large cancellation between the infrared-finite contribution from virtual- and real-photon exchange. This explains why the relative correction  $\sigma^\alpha(s)/\sigma_0(s)$  is relatively small (only about 2% between  $0.2 \text{ GeV}^2$  and  $1 \text{ GeV}^2$ ) for both curves.

The second plot of figure 12.1 consists of the full correction, including the multi-loop topologies of figure 11.1b, 11.1c and 11.1d. The larger uncertainty is due to the homogeneous solution of the implicit integral equation (11.29). It is hard to estimate precisely the size of the uncertainty coming from this additional source, but we set it proportional to the size of the numerical solution of the equation. As we can see, the inclusion of those topologies has a noticeable effect on the curve.

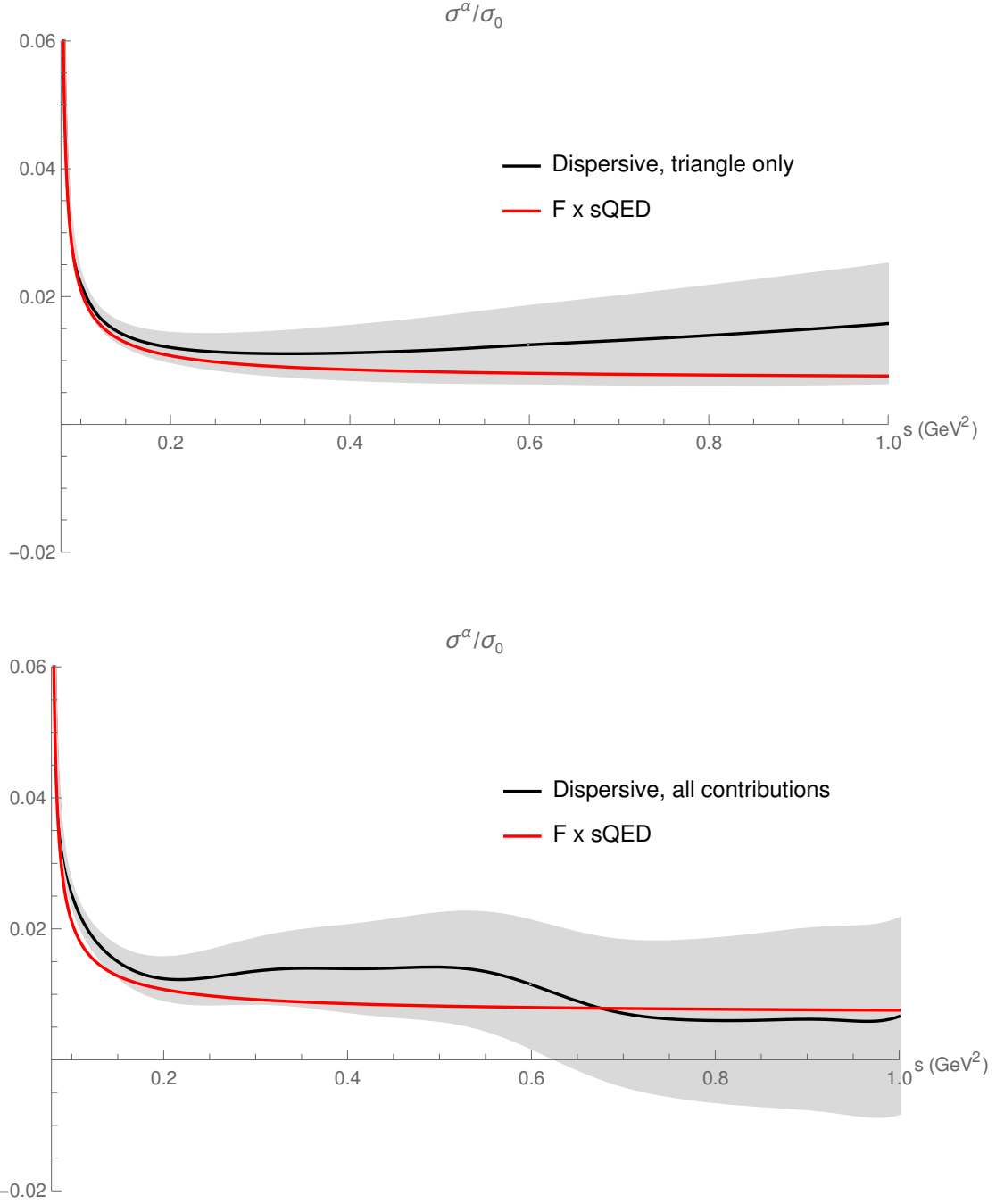


Figure 12.1: Correction from the FSR on the total cross section  $\sigma(e^+e^- \rightarrow \pi^+\pi^-)$  (black) compared to the prescription explained in section 7.1 (red). Only the triangle topology is taken into account in the first plot. The full FSR correction is taken into account in the second one.

## 12.2 Ambiguity in the extraction of FSR

In principle, assuming that the experiment could measure exactly the one-photon-inclusive cross section, there would be no need for the calculation of the FSR. One could simply plug the experimental data into the master formula for the HVP contribution to  $a_\mu$ . However,

there are two obstacles. First of all, experimental setups do not allow a coverage of the full solid angle because of various practical reasons. In general, one therefore needs a theoretical representation of the amplitude including radiative corrections to be able to extrapolate the measured cross section to the full  $4\pi$  coverage. Doing this requires knowledge of the detector details, including energy resolution and efficiency as well as its geometry. For doing this, the calculations worked out here need to be integrated in the codes used for data analysis. The other reason is that it is desirable to extract the purely hadronic part of the pion vector form factor and fit it with a dispersive representation. This is done for instance in [22].

The problem is that radiative corrections are contained by default in any observable in nature. Thus there is an ambiguity in the splitting of the purely hadronic quantity in the isospin limit and its radiative correction contributing to the isospin breaking effect. This ambiguity has been pointed out in other contexts. In particular, the purely hadronic pion decay constant can not be unambiguously extracted from the measurement of the decay rate  $\Gamma(\mu \rightarrow \pi \nu_\mu(\gamma))$  because of a dependence on a matching scale [89, 90]. However, this dependence is very weak and the extraction can still be carried out in a way which is precise enough for all practical purposes. In the case of the pion vector form factor, the situation is similar. The measurement of the photon-inclusive cross section  $\sigma(e^+e^- \rightarrow \pi^+\pi^-(\gamma))$  also accounts for all types of radiative corrections. Note that the method explained in section 7.1 allows an unambiguous distinction between the purely hadronic form factor and its radiative corrections. Of course, the drawback is the loss of model independence. In our case, as for the pion decay constant, we can rely on a convention for this extraction. We will show that the final results will not suffer significantly from this arbitrariness.

Let us identify the source of the ambiguity in our case. To that end, we analyse the dependence on the subtraction constants coming from the direct-triangle topology  $\tilde{T}_{(1)}^1(s)$  that can be written from (10.15) as

$$\tilde{T}_{(1)}^1(s) = \Omega_1^1(s) \left( c_{(1),0}^1 + s c_{(1),1}^1 \right) + \tilde{T}_{(1),\text{disp}}^1(s). \quad (12.2)$$

Once introduced in the unitarity relation of the pion vector form factor (11.2), we have

$$\begin{aligned} \text{Im} F_{(1)}(s) &= \frac{\sigma_\pi(s)}{48\pi} F_\pi^V(s) \Omega_1^{1*}(s) \left( c_{(1),0}^1 + s c_{(1),1}^1 \right) + \text{Im} F_{(1)}^{\text{disp}}(s) \\ &= \frac{\sigma_\pi(s)}{48\pi} |F_\pi^V(s)|^2 \left( c_{(1),0}^1 + s c_{(1),1}^1 \right) + \text{Im} F_{(1)}^{\text{disp}}(s). \end{aligned} \quad (12.3)$$

Note that  $F_{(1)}^{\text{disp}}(s)$  refers to all terms that do not depend on a subtraction constant. Then, the full amplitude is reconstructed from (11.3), where the subtraction constant  $c_{(1)}$  is exactly zero:

$$\begin{aligned} F_{(1)}(s) &= \frac{s}{48\pi^2} \int_{4m_\pi^2}^\infty ds' \frac{\sigma_\pi(s') |F_\pi^V(s')|^2 \left( c_{(1),0}^1 + s' c_{(1),1}^1 \right)}{s'(s' - s)} + F_{(1)}^{\text{disp}}(s) \\ &= \frac{s}{48\pi^2} \int_{4m_\pi^2}^\infty ds' \frac{\text{Im} \Pi_{2\pi}(s') \left( \tilde{c}_{(1),0}^1 + s' \tilde{c}_{(1),1}^1 \right)}{s'(s' - s)} + F_{(1)}^{\text{disp}}(s) \\ &= \frac{1}{48\pi} \left[ \left( \tilde{c}_{(1),0}^1 + s \tilde{c}_{(1),1}^1 \right) \Pi_{2\pi}(s) - \tilde{c}_{(1),0}^1 \Pi_{2\pi}(0) \right] + F_{(1)}^{\text{disp}}(s), \end{aligned} \quad (12.4)$$

where  $\Pi_{2\pi}(s)$  is the two-pion polarization function.

The second source of ambiguity is the homogeneous solution of the implicit integral equation (11.29). We write the amplitude as a sum of the homogeneous and inhomogeneous solutions:

$$\begin{aligned} F_{(2+3)}(s) &= c_{(2+3)} F_{(2+3),0}(s) + F_{(2+3)}^{\text{incho}}(s) \\ &= c_{(2+3)} t_1^1(s) + F_{(2+3)}^{\text{incho}}(s) \end{aligned} \quad (12.5)$$

Finally, from (11.1), the full radiative correction to the pion vector form factor can be written as

$$\begin{aligned} F_\pi^{V,\alpha}(s) &= \frac{1}{48\pi} \left[ \left( \tilde{c}_{(1),0}^1 + s \tilde{c}_{(1),1}^1 \right) \Pi_{2\pi}(s) - \tilde{c}_{(1),0}^1 \Pi_{2\pi}(0) \right] + c_{(2+3)} t_1^1(s) \\ &\quad + F_{(1)}^{\text{disp}}(s) + F_{(2+3)}^{\text{incho}}(s) \\ &= \Omega_1^1(s) F_s(s) + F_r(s), \end{aligned} \quad (12.6)$$

$$\begin{aligned} F_s(s) &= \frac{1}{\Omega_1^1(s)} \left\{ \frac{1}{48\pi} \left[ \left( \tilde{c}_{(1),0}^1 + s \tilde{c}_{(1),1}^1 \right) \Pi_{2\pi}(s) - \tilde{c}_{(1),0}^1 \Pi_{2\pi}(0) \right] + c_{(2+3)} t_1^1(s) \right\} \\ &= \frac{1}{\Omega_1^1(s)} \left\{ \frac{1}{48\pi} \left[ \left( \tilde{c}_{(1),0}^1 + s \tilde{c}_{(1),1}^1 \right) \Pi_{2\pi}(s) \right] + c_{(2+3)} t_1^1(s) \right\}, \end{aligned} \quad (12.7)$$

$$F_r(s) = F_{(1)}^{\text{disp}}(s) + F_{(2+3)}^{\text{incho}}(s). \quad (12.8)$$

We have used the fact that the polarization function must exactly vanish at  $s = 0$ . Note that  $F_s(s)$  is a smooth, complex function independently of the actual value of the real constants.  $F_r(s)$  contains the part that is calculated unambiguously. The specific form of the first term in (12.6) has been written such that it is identical to the representation used in the dispersive fit of the purely hadronic part of the form factor in [22]. That is, an Omnès function multiplying a function accounting for the  $\rho - \omega$ -mixing and a smooth conformal polynomial:

$$F_\pi^V(s) = \Omega_1^1(s) G_\omega(s) G_{\text{in}}^N(s). \quad (12.9)$$

We have explicitly checked numerically that the function  $F_s(s)$  can be well described by a conformal polynomial of the form used in  $G_{\text{in}}^N(s)$ , after appropriately adjusting the parameters in the latter. It would therefore be impossible to separate the function  $F_s(s)$ , which contains all the dependence on the poorly known constants, from the inelastic contributions described by  $G_{\text{in}}^N(s)$ . The idea is therefore to include  $F_s(s)$  in the hadronic contribution, having a priori subtracted  $F_r(s)$  from the experimental data in which the FSR are included. One can then find the best fit for the polynomial and add back  $F_r(s)$  into the full result. Of course, in order to do so, one would need to know exactly how the analysis is conducted on the experimental side. More work will therefore be needed in that direction.

### 12.3 Numerical contribution to $(g - 2)_\mu$

Despite the ambiguity explained in the previous section, we can still calculate an estimate of the effect of the FSR on  $(g - 2)_\mu$ . To do so, we consider the photon-inclusive cross section  $\sigma(e^+e^- \rightarrow \pi^+\pi^-(\gamma))$  and subtract it with our numerical expression for the radiative corrections

$$\sigma_0(e^+e^- \rightarrow \pi^+\pi^-) = \sigma(e^+e^- \rightarrow \pi^+\pi^-(\gamma)) - \sigma^\alpha(e^+e^- \rightarrow \pi^+\pi^-). \quad (12.10)$$

A fit of the subtracted data can then be performed with the dispersive representation of the form factor. The machinery in [22] can be used to that end<sup>1</sup>. The data come from  $e^+e^-$  experiments based on both energy scan [91, 92] and radiative return measurement [93, 71, 94]. Once this is done, the contribution from FSR is added back to the fitted purely hadronic cross section and the two-pion HVP contribution to  $(g-2)_\mu$  can be calculated. The latter consists of the expression (1.19) and (1.22) where the integral runs from the two-pion creation threshold to  $1\text{GeV}^2$  and the photon-inclusive cross section is limited to the two-pion state:

$$a_\mu^{\text{HVP}} := \left(\frac{\alpha m_\mu}{3\pi}\right)^2 \int_{4m_\pi^2}^1 \frac{ds}{s^2} \hat{K}_\mu(s) R_{\pi\pi}(s), \quad (12.11)$$

$$R_{\pi\pi}(s) = \frac{3s}{4\pi\alpha^2} \frac{s\sigma_e(s)}{s+2m_e^2} \sigma(e^+e^- \rightarrow \pi^+\pi^-(\gamma)). \quad (12.12)$$

The result can then be compared to the value obtained from the bare photon-inclusive cross section  $a_{\mu,0}^{\text{HVP}}$ . That is, the calculation of  $a_\mu^{\text{HVP}}$  directly from the experimental data, without subtracting and adding back any FSR effect. Using the model-dependent method based on sQED to determine the FSR, the result is [95]

$$\Delta a_{\mu,\text{sQED}}^{\text{HVP}} = a_{\mu,\text{sQED}}^{\text{HVP}} - a_{\mu,0}^{\text{HVP}} = (1.02 \pm 0.05 \pm 0.51) \times 10^{-10}. \quad (12.13)$$

Note that the first error comes from the error propagation in the fitting procedure and the second one is an estimation of the systematic uncertainty due to model dependence taken as 50% of the central value. When using the result from our dispersive method, only including the triangle diagram, the result is [95]

$$\Delta a_{\mu,(1)}^{\text{HVP}} = a_{\mu,(1)}^{\text{HVP}} - a_{\mu,0}^{\text{HVP}} = (1.05 \pm 0.05) \times 10^{-10}. \quad (12.14)$$

Finally, including the full virtual-photon correction, the result is [95]

$$\Delta a_\mu^{\text{HVP}} = a_\mu^{\text{HVP}} - a_{\mu,0}^{\text{HVP}} = (1.32 \pm 0.05) \times 10^{-10}. \quad (12.15)$$

In those two cases, the only source of uncertainty comes from the propagated error in the fit. As we can see, the result from sQED and the triangle topology of the dispersive method are in good agreement. Moreover, including the full result amounts to an increase of about 30%. This effect is comparable to the contribution (8.8). The most important remark is that the uncertainty on the result coming out of this analysis is very small, whereas the systematic uncertainty on the prediction from sQED is impossible to assess exactly.

Another conclusion that we can draw is that it is really unlikely that the tension between the data-driven approach and the lattice mentioned in section 1.7 is essentially due to radiative corrections.

Of course, we must recall that this is just an estimation and a more careful analysis as explained above should still be conducted.

---

<sup>1</sup>I thank Martin Hoferichter and Peter Stoffer for running this analysis.

# Chapter 13

## Outlook

The aim of this thesis is to calculate the final-state radiations to the process  $e^+e^- \rightarrow \pi^+\pi^-$ . In particular, we calculate the electromagnetic corrections to the pion vector form factor  $F_\pi^V(s)$  in the energy range  $s \in [4m_\pi^2, 1\text{GeV}^2]$  and their effect on  $a_\mu$ .

The method is based on unitarity and analyticity. We calculate transition amplitudes whose analytic properties are defined by the unitarity relation where only two-pion intermediate states are considered. This then allows us to calculate the full amplitude using dispersion relations in the form of integrals of well-defined hadronic quantities. Those are the purely hadronic pion vector form factor and the  $\pi\pi$ -scattering amplitude. We emphasize that this is the first model-independent calculation of those radiative corrections.

The unitarity relation considered for the calculation of the radiative corrections to the pion vector form factor involves different building blocks. Some of them are unknown and need to be calculated beforehand. They are therefore a byproduct of the analysis.

The amplitude for the process  $\gamma^*\gamma \rightarrow \pi\pi$  can be split into a pion-pole and a two-pion rescattering contribution. Both of them have been analysed in the literature. The first one is dominant compared to the second one, once inserted into a unitarity relation.

The process  $\pi\pi \rightarrow \pi\pi\gamma$  has only been analysed in ChPT so far and therefore only known at low energy. In order to extend its range of validity to higher energy, we have written the amplitude as a sum of terms with gauge-invariant Lorentz structures and calculated the pion-pole contribution to the scalar functions. We also have analysed the rescattering effects that turn out to be negligible once inserted in the unitarity relation of interest.

The radiative corrections to the  $\pi\pi$ -scattering amplitude itself is also needed as a building block. This quantity has also been calculated in ChPT and this result is used to fix the subtraction constants of the dispersive integrals. The two-pion prescription leads to a finite set of topologies that we calculate separately and then project on partial waves. Some of them can be calculated unambiguously using well-known techniques such as the Omnès-Muskhelishvili method. Others lead to a new type of implicit integral equation and numerical methods must be used to find stable solutions or local minima. The S-wave projection is special, since the unitarity relation leads to a coupled-channel problem, but the latter can be diagonalised and split into independent single-channel problems which can be solved with standard techniques.

Finally, once all building blocks are known, the unitarity relation for the radiative corrections to the pion vector form factor can be evaluated. Similarly to the case of the corrections to the  $\pi\pi$ -scattering amplitudes, different topologies are identified. Some of them also lead to an implicit integral equation and the same kind of numerical methods must be used to find a solution.

In this thesis, we have set up a new framework to calculate this type of radiative corrections. We have seen that the resulting correction at order  $\alpha$  to the cross section for the process  $e^+e^- \rightarrow \pi^+\pi^-$  carries a large uncertainty reflecting the error on the electromagnetic low-energy constants of ChPT. In the calculation of  $a_\mu^{\text{HVP}}$ , this uncertainty can be significantly reduced by subtracting the FSR and fitting the purely hadronic data to then add back the FSR. The final result is

$$\Delta a_\mu^{\text{HVP}} = a_\mu^{\text{HVP}} - a_{\mu,0}^{\text{HVP}} = (1.32 \pm 0.05) \times 10^{-10},$$

where  $a_{\mu,0}^{\text{HVP}}$  is the value obtained from the bare cross section. This represents an increase of about 30% of the model-dependent prediction based on sQED. The rather large size of the correction shows the level of remaining uncertainties one has to fight with if one relies on a model-dependent approach to estimate the FSR. With the approach developed here, we had to rely on approximations too, but were able to estimate that their effect is most likely negligible. Higher order QED effects are expected to be about two orders of magnitude smaller and therefore negligible too. We conclude that there is no significant systematic uncertainty beyond the one shown above. This represents one of the most important improvements brought about by the model-independent approach we have adopted. This shows that the current tension between the predictions of the lattice and the data-driven approach can not be explained by FSR. Future improvements will require to integrate the calculations described here directly into the data analysis. Work in this direction will be undertaken soon.



# Appendix A

## Kinematics

In this appendix, we give the technical details about the kinematics of the different processes entering the calculation. To generally describe the angular dependences of the processes we define the rotation matrices

$$R_1(\theta) = \begin{pmatrix} \cos \theta & 0 & \sin \theta \\ 0 & 1 & 0 \\ -\sin \theta & 0 & \cos \theta \end{pmatrix}, \quad (\text{A.1})$$

$$R_2(\phi) = \begin{pmatrix} \cos \phi & -\sin \phi & 0 \\ \sin \phi & \cos \phi & 0 \\ 0 & 0 & 1 \end{pmatrix}, \quad (\text{A.2})$$

### A.1 $2 \rightarrow 2$ process

We consider a process  $\phi_1(p_1)\phi_2(p_2) \rightarrow \phi_3(p_3)\phi_4(p_4)$ . We choose the center-of-mass frame of  $s = (p_1 + p_2)^2 = (p_3 + p_4)^2$ . the kinematic situation is depicted in figure A.1. Each of the four particles has a mass  $m_i$ . In this frame, the four-momenta can be expressed as

$$p_i = (E_i, \mathbf{p}_i) \quad (\text{A.3})$$

The energy and momentum of the different particles are expressed in terms of  $s$ , the different particle masses and the scattering angle  $\theta$  defined between  $p_1$  and  $p_3$ :

$$E_{1,2} = \frac{s \pm m_1^2 \mp m_2^2}{2\sqrt{s}} \quad (\text{A.4})$$

$$E_{3,4} = \frac{s \pm m_3^2 \mp m_4^2}{2\sqrt{s}} \quad (\text{A.5})$$

$$\mathbf{p}_{1,2} = \pm \frac{\lambda^{1/2}(s, m_1^2, m_2^2)}{2\sqrt{s}} (0, 0, 1)^T \quad (\text{A.6})$$

$$\begin{aligned} \mathbf{p}_{3,4} &= \pm \frac{\lambda^{1/2}(s, m_3^2, m_4^2)}{2\sqrt{s}} R_1(\theta) (0, 0, 1)^T \\ &= \pm \frac{\lambda^{1/2}(s, m_3^2, m_4^2)}{2\sqrt{s}} (\sin \theta, 0, \cos \theta)^T \end{aligned} \quad (\text{A.7})$$

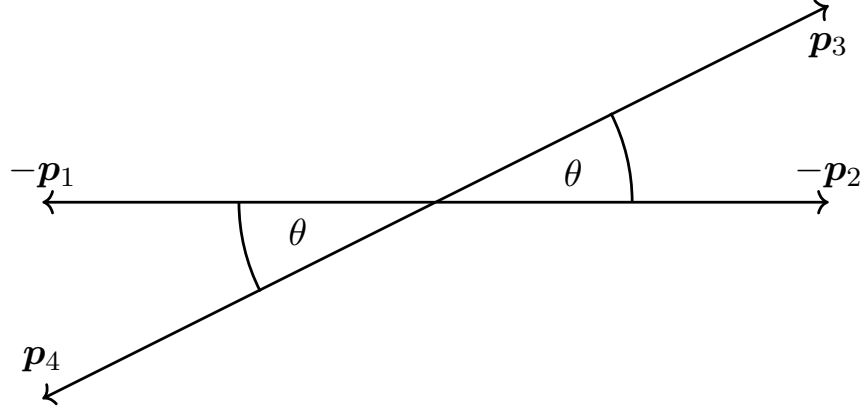


Figure A.1: kinematic situation of the  $2 \rightarrow 2$  process in the  $s$ -center-of-mass frame

## A.2 $2 \rightarrow 2 \rightarrow 2$ process

We consider a process  $\phi_1(p_1)\phi_2(p_2) \rightarrow \phi_3(p_3)\phi_4(p_4) \rightarrow \phi_5(p_5)\phi_6(p_6)$ . We choose the center-of-mass frame of  $s = (p_1 + p_2)^2 = (p_3 + p_4)^2 = (p_5 + p_6)^2$ . the kinematic situation is depicted in figure A.2. There, only one of the two pions of each pair is displayed. Each of the six particles has a mass  $m_i$ . In this frame, the four-momenta can be expressed as

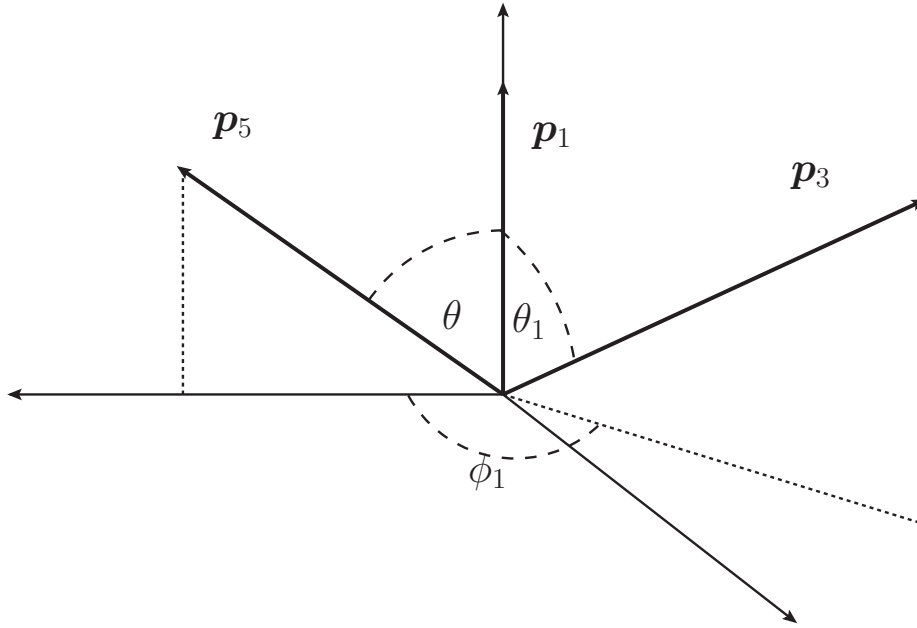


Figure A.2: kinematic situation of the process  $2 \rightarrow 2 \rightarrow 2$  in the  $s$ -center-of-mass frame

$$E_{1,2} = \frac{s \pm m_1^2 \mp m_2^2}{2\sqrt{s}} \quad (\text{A.8})$$

$$E_{3,4} = \frac{s \pm m_3^2 \mp m_4^2}{2\sqrt{s}} \quad (\text{A.9})$$

$$E_{5,6} = \frac{s \pm m_5^2 \mp m_6^2}{2\sqrt{s}} \quad (\text{A.10})$$

$$\mathbf{p}_{1,2} = \pm \frac{\lambda^{1/2}(s, m_1^2, m_2^2)}{2\sqrt{s}} (0, 0, 1)^T \quad (\text{A.11})$$

$$\begin{aligned} \mathbf{p}_{3,4} &= \pm \frac{\lambda^{1/2}(s, m_3^2, m_4^2)}{2\sqrt{s}} R_2(\phi_1) R_1(\theta_1) (0, 0, 1)^T \\ &= \pm \frac{\lambda^{1/2}(s, m_3^2, m_4^2)}{2\sqrt{s}} (\sin \theta_1 \cos \phi_1, \sin \theta_1 \sin \phi_1, \cos \theta_1)^T \end{aligned} \quad (\text{A.12})$$

$$\begin{aligned} \mathbf{p}_{5,6} &= \pm \frac{\lambda^{1/2}(s, m_5^2, m_6^2)}{2\sqrt{s}} R_1(\theta) (0, 0, 1)^T \\ &= \pm \frac{\lambda^{1/2}(s, m_3^2, m_4^2)}{2\sqrt{s}} (\sin \theta, 0, \cos \theta)^T \end{aligned} \quad (\text{A.13})$$

Note also that defining the angle between  $\mathbf{p}_3$  and  $\mathbf{p}_5$  as  $\theta_2$ , we have

$$\cos \theta_2 = \frac{\mathbf{p}_3 \cdot \mathbf{p}_5}{|\mathbf{p}_3| |\mathbf{p}_5|} = \cos \theta \cos \theta_1 + \sin \theta_1 \sin \theta \cos \phi_1 \quad (\text{A.14})$$

### A.3 $2 \rightarrow 3 \rightarrow 2$ process

We consider a process  $\phi_1(p_1)\phi_2(p_2) \rightarrow \chi_1(k_1)\chi_2(k_2)\phi_4(p_4) \rightarrow \phi_5(p_5)\phi_6(p_6)$ . We choose the center-of-mass frame of  $s = (p_1 + p_2)^2 = (k_1 + k_2 + p_4)^2 = (p_5 + p_6)^2$ . The masses of particles is defined by

$$p_i^2 = m_i^2 \quad (\text{A.15})$$

$$k_i^2 = \tilde{m}_i^2 \quad (\text{A.16})$$

Once the two-particle system  $\chi_1(k_1)\chi_2(k_2)$  is considered as one virtual particle of mass  $q^2 = (k_1 + k_2)^2$ , the situation is identical to the one depicted in A.2 for  $m_3^2 = q^2$ .

In order to specify the two-body system, we use the Lorentz transformation matrix

$$\Lambda = \begin{pmatrix} \gamma & 0 & 0 & -\beta\gamma \\ 0 & 1 & 0 & 0 \\ 0 & 0 & 1 & 0 \\ -\beta\gamma & 0 & 0 & \gamma \end{pmatrix} = \begin{pmatrix} \frac{s+q^2-m_4^2}{2\sqrt{s}\sqrt{q^2}} & 0 & 0 & -\frac{\lambda^{1/2}(s, q^2, m_4^2)}{2\sqrt{s}\sqrt{q^2}} \\ 0 & 1 & 0 & 0 \\ 0 & 0 & 1 & 0 \\ -\frac{\lambda^{1/2}(s, q^2, m_4^2)}{2\sqrt{s}\sqrt{q^2}} & 0 & 0 & \frac{s+q^2-m_4^2}{2\sqrt{s}\sqrt{q^2}} \end{pmatrix} \quad (\text{A.17})$$

where  $\beta = |\mathbf{q}|/E_q$  and  $\gamma = 1/\sqrt{1-\beta^2} = E_q/\sqrt{q^2}$ . This transformation boosts the system from the  $q^2$ -center-of-mass frame to the  $s$ -center-of-mass frame, provided  $\mathbf{q}$  points in the direction of the third axis. We define

$$\tilde{k}_{1,2} = \Lambda(1, R_2(\tilde{\phi}_1))(1, R_1(\tilde{\theta}_1))\left(\frac{q^2 \pm \tilde{m}_1^2 \mp \tilde{m}_2^2}{2\sqrt{q^2}}, 0, 0, \pm \frac{\lambda^{1/2}(q^2, \tilde{m}_1^2, \tilde{m}_2^2)}{2\sqrt{q^2}}\right). \quad (\text{A.18})$$

Then, taking into account the rotation of the three-vector  $\mathbf{q}$  as defined above, those two vectors become

$$E_{k_{1,2}} = \tilde{E}_{k_{1,2}} \quad (\text{A.19})$$

$$\mathbf{k}_{1,2} = R_2(\phi_1)R_1(\theta_1)\tilde{\mathbf{k}}_{1,2}. \quad (\text{A.20})$$

## Appendix B

# Phase-space differentials

We explain here the convention we use regarding the phase-space differentials. The  $n$ -body phase-space differential for  $n$  particles with momenta  $\{k_1, \dots, k_n\}$  and  $P = \sum_{i=1}^n k_i$  is defined as follows ([72]):

$$d\Phi_n(P; k_1, \dots, k_n) := \delta^{(4)}\left(P - \sum_n k_n\right) \prod_{i=1}^n \frac{d^3 k_i}{(2\pi)^3 2k_i^0}. \quad (\text{B.1})$$

The two-body phase space can be calculated directly for any two-particle states with momenta  $k_1$  and  $k_2$  as

$$\begin{aligned} d\Phi_2(P; k_1, k_2) &:= \delta^{(4)}(P - k_1 - k_2) \frac{d^3 k_1}{(2\pi)^3 2k_1^0} \frac{d^3 k_2}{(2\pi)^3 2k_2^0} \\ &= \frac{1}{(2\pi)^6} \frac{d\Omega(\hat{\mathbf{k}}_1) d|\mathbf{k}_1| |\mathbf{k}_1|^2}{2k_1^0} \delta^{(1)}((P - k_1)^2 - k_2^2) \\ &= \frac{1}{(2\pi)^6} \frac{d\Omega(\hat{\mathbf{k}}_1) dk_1^0 |\mathbf{k}_1|}{4P_0} \delta^{(1)}\left(k_1^0 - \frac{P^2 + k_1^2 - k_2^2}{2P^0}\right) \\ &= \frac{1}{(2\pi)^6} \frac{d\Omega(\hat{\mathbf{k}}_1) |\mathbf{k}_1^*|}{4P_0} = \frac{1}{(2\pi)^6} d\Omega(\hat{\mathbf{k}}_1) \frac{\lambda(P^2, k_1^2, k_2^2)}{8P^2}, \end{aligned} \quad (\text{B.2})$$

where we introduced the Källén function  $\lambda(a, b, c) := a^2 + b^2 + c^2 - 2(ab + ac + bc)$  and  $\vec{k}_1^*$  is the three-vector evaluated in the center-of-mass frame of  $P$ . Also,  $d\Omega$  is the solid-angle differential

$$\int d\Omega(\theta, \phi) = \int_0^\pi d\theta \int_0^{2\pi} d\phi \sin \theta = \int_{-1}^1 dz \int_0^{2\pi} d\phi \quad (\text{B.3})$$

where  $\theta$  and  $\phi$  are the polar and azimuthal angles and the variable transformation  $z = \cos \theta$  has been done.

In order to calculate the phase-space differentials with  $n > 2$ , we use a very convenient formulation. It allows to write the  $n$ -body phase space as a convolution of a  $j$ -body phase space and a  $(n - j + 1)$ -body phase space ( $2 \leq j < n$ ):

$$d\Phi_n(P, k_1, \dots, k_n) = d\Phi_j(q; k_1, \dots, k_j) d\Phi_{n-j+1}(P; q, k_{j+1}, \dots, k_n) (2\pi)^3 dq^2. \quad (\text{B.4})$$

We can express the three-body phase space as a convolution of two two-body phase spaces and obtain, using the formula derived above

$$\begin{aligned} d\Phi_3(P, k_1, k_2, k_3) &= d\Phi_2(q; k_1, k_2) d\Phi_2(P; q, k_3) (2\pi)^3 dq^2 \\ &= \frac{1}{(2\pi)^9} d\Omega(k_1) d\Omega(k_3) dq^2 \frac{\lambda(q^2, k_1^2, k_2^2)}{8q^2} \frac{\lambda(P^2, q^2, k_3^2)}{8P^2}. \end{aligned} \quad (\text{B.5})$$

In case  $k_{1,2}^2 > 0$ ,  $q^2$  must then be integrated from  $q_{\min}^2 = (\sqrt{k_1^2} + \sqrt{k_2^2})^2$  to  $q_{\max}^2 = P^2 + k_3^2 - 2\sqrt{P^2}\sqrt{k_3^2}$ . The lower bound corresponds to the kinematic situation where both sub-particles are at rest in the center-of-mass frame of  $q$ . Note that if one of the two sub-particles is massless, this situation is impossible. One must therefore be careful, in case there is a photon in the sub-system of  $q$ . The upper bound corresponds to the kinematic situation where  $q$  is at rest in the center-of-mass frame of  $P$ . It is therefore the solution to the equation  $|\vec{q}| = \frac{\lambda(P^2, q^2, k_3^2)^{1/2}}{2\sqrt{P^2}} = 0$ .

## Appendix C

# Regularization of the infrared phase-space integrals

Let us explain the details of the calculation of the infrared-divergent phase-space integrals. When we cut through a photon line attached to two on-shell pion legs, infrared divergences arise. The reason is the following: defining the momentum of the real photon by  $k$  ( $k^2 = 0$ ) and the momenta of the external legs by  $p_1$  and  $p_2$  the discontinuity has the form

$$\frac{\text{Disc} F_{IR}}{2i} = \int d\Phi_3(P, k_1, k_2, k) \frac{\tilde{F}_{IR}(P, k_1, k_2, \dots)}{(p_1 \cdot k)(p_2 \cdot k)}. \quad (\text{C.1})$$

We have  $k = P - q$  and  $(p_1 \cdot k)(p_2 \cdot k) \sim (P^2 - q^2)^2$ . The 3-body phase space is written as in appendix B and involves an integration of  $q^2$  from threshold to  $q_{max}^2 = P^2$ . Thus, the integral has an end-point singularity at its upper bound.

In order to extract analytically the divergent term, we separate the phase space into two regions. In the first one, the photon is soft ( $k^0 < \Delta\epsilon$ ) and, in the other one, it is hard ( $k^0 > \Delta\epsilon$ ). The arbitrary cut-off  $\Delta\epsilon$  is chosen to be very small and the full amplitude must not have any more dependence on it after summing the soft and hard regions together.

We approximate the three-body phase-space of the soft region by slicing away the Lorentz-invariant measure of the photon momentum off the two-pion phase space:

$$\begin{aligned} d\Phi_3(P, k_1, k_2, k)|_{k^0 < \Delta\epsilon} &= \frac{d^3k_1}{(2\pi)^3 2k_1^0} \frac{d^3k_2}{(2\pi)^3 2k_2^0} \frac{d^3k}{(2\pi)^3 2k^0} \delta^{(4)}(P - k_1 - k_2 - k)|_{k^0 < \Delta\epsilon} \\ &\approx (2\pi)^4 \frac{d^3k_1}{(2\pi)^3 2k_1^0} \frac{d^3k_2}{(2\pi)^3 2k_2^0} \delta^{(4)}(P - k_1 - k_2) \times \frac{d^3k}{(2\pi)^3 2k^0} \end{aligned} \quad (\text{C.2})$$

This approximation is good as long as  $\Delta\epsilon$  is small relatively to the energy of the system. The integral of two propagators over the photon momentum is well known in the literature. We find in [96] that if the two momenta are identical ( $p_1 = p_2$ )

$$\int_{|\mathbf{k}| < \Delta\epsilon} \frac{d^3\mathbf{k}}{(2\pi)^3 2k^0} \frac{1}{(p_1 \cdot k)^2} = \frac{1}{8\pi^2} \frac{1}{k^2} \left\{ 2 \log \left( \frac{2\Delta\epsilon}{m_\gamma} \right) - \frac{k^0}{|\mathbf{k}|} \log \left( \frac{k^0 + |\mathbf{k}|}{k^0 - |\mathbf{k}|} \right) \right\} + \mathcal{O}(m_\gamma^2). \quad (\text{C.3})$$

In the case where the two momenta are different ( $p_1 \neq p_2$ ), the integral becomes

$$\int_{|\mathbf{k}| < \Delta\epsilon} \frac{d^3\mathbf{k}}{(2\pi)^3 2k^0} \frac{1}{p_1 \cdot \mathbf{k}} \frac{1}{p_2 \cdot \mathbf{k}} = \frac{\alpha}{8\pi^2} \left( \frac{1}{p_2^2 - \kappa^2} \log \left( \frac{p_1^2}{\kappa^2} \right) \log \left( \frac{4\Delta\epsilon^2}{m_\gamma^2} \right) + \tilde{I}(p_1, p_2) \right) + \mathcal{O}(m_\gamma^2) \quad (\text{C.4})$$

where

$$\tilde{I}(p_1, p_2) = \frac{1}{p_1^0 - \kappa^0} \frac{1}{v} \left\{ \frac{1}{4} \log^2 \left( \frac{u^0 - |\mathbf{u}|}{u^0 + |\mathbf{u}|} \right) + \text{Li}_2 \left( \frac{v - u^0 + |\mathbf{u}|}{v} \right) + \text{Li}_2 \left( \frac{v - u^0 - |\mathbf{u}|}{v} \right) \right\} \Big|_{u=\kappa}^{u=p_1} \quad (\text{C.5})$$

and

$$v = \frac{p_1^2 - \kappa^2}{2(p_1^0 - \kappa^0)}. \quad (\text{C.6})$$

In these formulae, we used  $\kappa = \alpha p_2$ , with  $\alpha$  defined, such that  $(p_1 - \alpha p_2)^2 = 0$  and  $\kappa^0 - p_1^0$  has the same sign as  $p_1^0$ . We see that the soft contribution gets a logarithmic divergence as the photon mass approaches 0.

The full three-body phase space with a hard photon ( $|\mathbf{k}| > \Delta\epsilon$ ) can easily be calculated as well. The expression is identical to the one in appendix B, but we have to change the upper integration limit in  $q^2$  to  $q_{max}^2 = P^2 - 2\sqrt{P^2}\Delta\epsilon$ . When summing both regions, we must find a result that is independent of the cut-off  $\Delta\epsilon$ .



## Appendix D

### Omnès functions

In this thesis, we encounter situations where the phase of an amplitude is known to be equal to the phase of one of the  $\pi\pi$ -scattering partial waves. The Omnès functions in the case of the  $S_0$ -,  $S_2$ - and  $P$ -waves are depicted in figure D.1. In order to calculate those quantities, the phase-shift  $\delta_\ell^I(s)$  must be evaluated in the range  $s \in [4m_\pi^2, \infty]$ . However, the latter is known only up to  $s = 2 \text{ GeV}^2$  from the analysis of [65]. Nevertheless, it is reasonable to assume that those phases converge asymptotically to a multiple of  $\pi$ , namely

$$\delta_0^0(s) \xrightarrow{s \rightarrow \infty} 2\pi =: n_0^0 \pi \quad (\text{D.1})$$

$$\delta_1^1(s) \xrightarrow{s \rightarrow \infty} \pi =: n_1^1 \pi \quad (\text{D.2})$$

$$\delta_0^2(s) \xrightarrow{s \rightarrow \infty} 0 =: n_0^2 \pi \quad (\text{D.3})$$

We use the same parametrization as in [97] to extend the behaviour of the phase-shift above  $2 \text{ GeV}^2$ . The central phase-shift is parametrized as

$$\delta_\ell^I(s)^{asympt} = \begin{cases} \delta_\ell^I(s) & s < s_a \\ n_\ell^I \pi + (\delta_\ell^I(s_a) - n_\ell^I \pi) \frac{2}{1 + (s/s_a)^{3/4}} & s > s_a \end{cases} \quad (\text{D.4})$$

where  $s_a = 1.3 \text{ GeV}^2$ . One can also choose a point at which the phase reaches exactly  $\pi$  and stays constant from there. To vary the point, we use the prescription

$$\delta_\ell^I(s)^{asympt} = \begin{cases} \delta_\ell^I(s) & s < s_1 \\ \delta_\ell^I(s) + (n_\ell^I \pi - \delta_\ell^I(s)) f(s) & s_1 \leq s < s_b \\ \delta_\ell^I(s) + (n_\ell^I \pi - \delta_\ell^I(s_b)) f(s) & s_b \leq s < s_2 \\ \pi & s \geq s_2 \end{cases} \quad (\text{D.5})$$

$$f(s) = \frac{(s - s_1)^2 (3s_2 - 2s - s_1)}{(s_2 - s_1)^3} \quad (\text{D.6})$$

We follow the same convention as in [97] and set  $s_b = 2.25 \text{ GeV}^2$  and  $s_1 = 1.32 \text{ GeV}^2$ . Also, we choose  $s_2 = 3 \text{ GeV}^2$

One comment must be added regarding the Omnès function  $\Omega_0^0(s)$ . As is shown in figure 4.1, the phase-shift  $\delta_0^0$  raises very rapidly at the  $K\bar{K}$ -threshold. This would therefore result in a huge peak in the Omnès function. Such a peak is however not seen in a coupled-channel analysis, including the  $K\bar{K}$ -channel. In order to fix this behaviour, we therefore use the

phase of the partial wave including the inelasticity (4.23) instead of just  $\delta_0^0(s)$ :

$$\begin{aligned} t_0^0(s) &= \frac{\eta_0^0(s)e^{2i\delta_0^0(s)} - 1}{2i\sigma_\pi(s)} \\ &= |t_0^0(s)|e^{i\tilde{\delta}_0^0(s)}. \end{aligned} \tag{D.7}$$

The Omnès function is then calculated as

$$\Omega_0^0(s) = \exp \frac{s}{\pi} \int_{4m_\pi^2}^{\infty} ds' \frac{\tilde{\delta}_0^0(s')}{s'(s' - s)}. \tag{D.8}$$

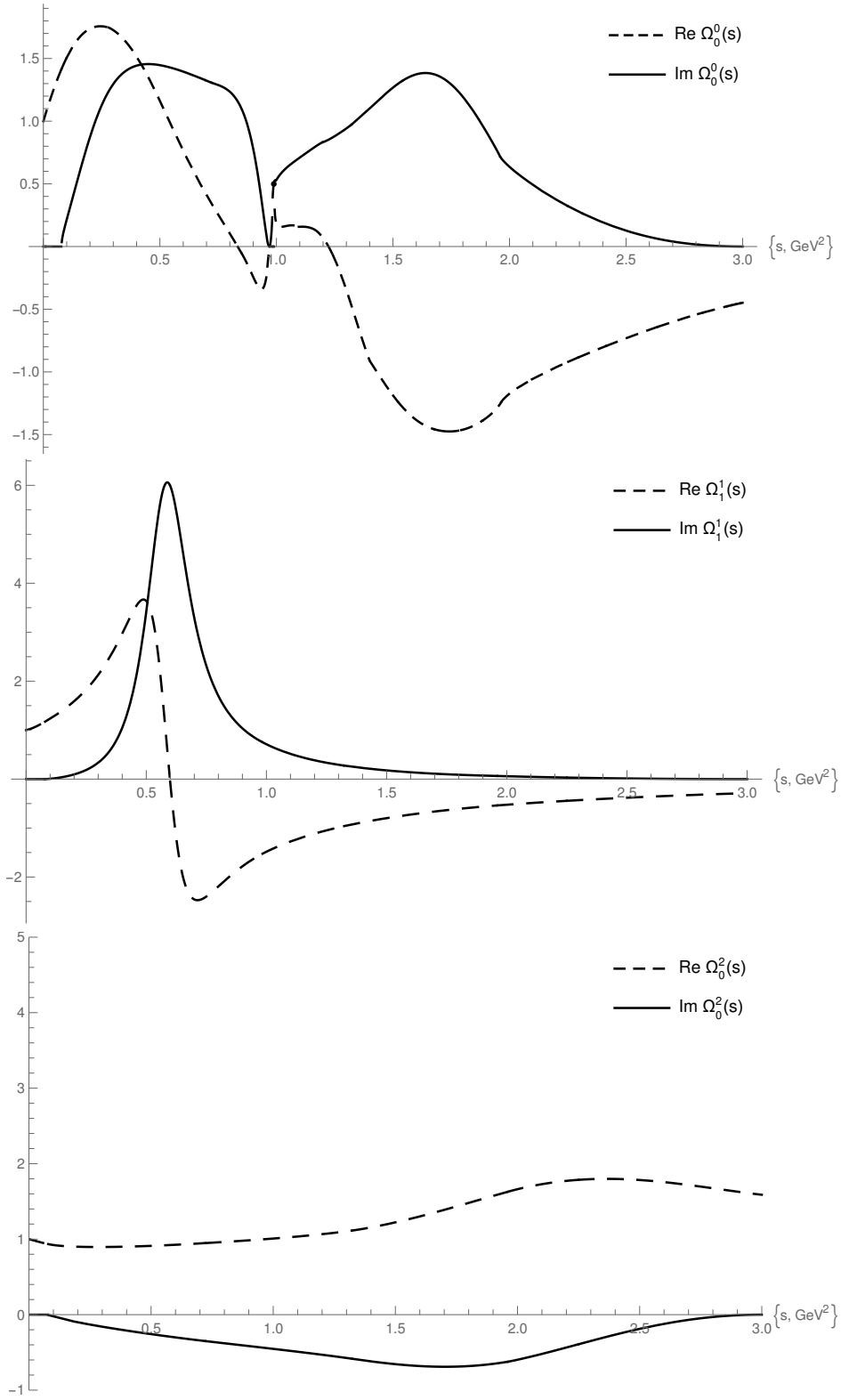


Figure D.1: Central values of the real and imaginary part of the Omnès functions  $\Omega_0^0$ ,  $\Omega_1^1$  and  $\Omega_0^2$

## Appendix E

### Angular integration

In this appendix, we explain in more details the calculation of the angular integral of the two propagators leading to the double-spectral representation. The calculation of such angular integrals is explained in detail in [98]. We follow the same method here. Consider a situation similar to A.2 but where the direct channel is defined as  $t$  instead of  $s$ :

$$\begin{aligned}
t &= (p_1 + p_2)^2 = (p_3 + p_4)^2 = (p_5 + p_6)^2 \\
s &= (p_1 - p_5)^2 = (p_2 - p_6)^2 \\
s' &= (p_1 - p_3)^2 = (p_2 - p_4)^2 \\
s'' &= (p_5 - p_3)^2 = (p_6 - p_4)^2 \\
u &= (p_1 - p_6)^2 = (p_2 - p_5)^2 \\
u' &= (p_1 - p_4)^2 = (p_2 - p_3)^2 \\
u'' &= (p_3 - p_6)^2 = (p_4 - p_5)^2
\end{aligned} \tag{E.1}$$

The quantities of interest are

$$\begin{aligned}
&\int d\Omega \frac{1}{s' - a} \frac{1}{s'' - b} \\
&\int d\Omega \frac{1}{u' - a} \frac{1}{u'' - b} \\
&\int d\Omega \frac{1}{s' - a} \frac{1}{u'' - b} \\
&\int d\Omega \frac{1}{u' - a} \frac{1}{s'' - b}
\end{aligned}$$

We start by expressing the crossed Mandelstam variables  $s'$  and  $s''$  in terms of the invariants of the process and the scattering angles in the  $t$  center-of-mass frame. We define  $z'$  and  $z''$  as the cosinus between respectively  $p_1$  and  $p_3$  and  $p_3$  and  $p_5$ . We have

$$\begin{aligned}
s &= \frac{\Sigma_{12} + \Sigma_{56} - t}{2} - \frac{\Delta_{12}\Delta_{56}}{2t} + \frac{\lambda_{12}^{1/2}\lambda_{56}^{1/2}}{2t}z_t \\
s' &= \frac{\Sigma_{12} + \Sigma_{34} - t}{2} - \frac{\Delta_{12}\Delta_{34}}{2t} + \frac{\lambda_{12}^{1/2}\lambda_{34}^{1/2}}{2t}z'_t \\
s'' &= \frac{\Sigma_{34} + \Sigma_{56} - t}{2} - \frac{\Delta_{34}\Delta_{56}}{2t} + \frac{\lambda_{34}^{1/2}\lambda_{56}^{1/2}}{2t}z''_t \\
u &= \frac{\Sigma_{12} + \Sigma_{56} - t}{2} - \frac{\Delta_{12}\Delta_{56}}{2t} - \frac{\lambda_{12}^{1/2}\lambda_{56}^{1/2}}{2t}z_t \\
u' &= \frac{\Sigma_{12} + \Sigma_{34} - t}{2} - \frac{\Delta_{12}\Delta_{34}}{2t} - \frac{\lambda_{12}^{1/2}\lambda_{34}^{1/2}}{2t}z'_t \\
u'' &= \frac{\Sigma_{34} + \Sigma_{56} - t}{2} - \frac{\Delta_{34}\Delta_{56}}{2t} - \frac{\lambda_{34}^{1/2}\lambda_{56}^{1/2}}{2t}z''_t
\end{aligned} \tag{E.2}$$

with  $\Sigma_{ij} = m_i^2 + m_j^2$ ,  $\Delta_{ij} = m_i^2 - m_j^2$  and  $\lambda_{ij} = \lambda(t, m_i^2, m_j^2)$ . Using this and a Feynman parametrization, we find

$$\begin{aligned}
\int d\Omega \frac{1}{s' - a} \frac{1}{s'' - b} &= \frac{4t^2}{\lambda_{12}^{1/2}\lambda_{34}\lambda_{56}^{1/2}} \int d\Omega \frac{1}{z'_t - \alpha_1} \frac{1}{z''_t - \alpha_2} \\
&= \frac{4t^2}{\lambda_{12}^{1/2}\lambda_{34}\lambda_{56}^{1/2}} \int d\Omega \int_0^1 dx (x\alpha_1 + (1-x)\alpha_2 - (xz'_t + (1-x)z''_t))^{-2} \\
&= \frac{4t^2}{\lambda_{12}^{1/2}\lambda_{34}\lambda_{56}^{1/2}} \int_0^1 dx \int d\Omega \left( x\alpha_1 + (1-x)\alpha_2 - \left( x \frac{\mathbf{p}_1}{|\mathbf{p}_1|} + (1-x) \frac{\mathbf{p}_5}{|\mathbf{p}_5|} \right) \cdot \frac{\mathbf{p}_3}{|\mathbf{p}_3|} \right)^{-2} \\
&= \frac{4t^2}{\lambda_{12}^{1/2}\lambda_{34}\lambda_{56}^{1/2}} 4\pi \int_0^1 dx \left( (x\alpha_1 + (1-x)\alpha_2)^2 - \left| x \frac{\mathbf{p}_1}{|\mathbf{p}_1|} + (1-x) \frac{\mathbf{p}_5}{|\mathbf{p}_5|} \right|^2 \right)^{-1} \\
&= \frac{4t^2}{\lambda_{12}^{1/2}\lambda_{34}\lambda_{56}^{1/2}} 4\pi \int_0^1 dx ((x\alpha_1 + (1-x)\alpha_2)^2 - (1 - 2x(1-x)(1 - z_t)))^{-1} \\
&= \frac{4t^2}{\lambda_{12}^{1/2}\lambda_{34}\lambda_{56}^{1/2}} 4\pi I(z_t) = \frac{4t^2}{\lambda_{12}^{1/2}\lambda_{34}\lambda_{56}^{1/2}} 4\pi \int_0^1 dx \frac{1}{D(x, z_t)}, \tag{E.3}
\end{aligned}$$

where  $z_t$  is the angle between  $\mathbf{p}_1$  and  $\mathbf{p}_5$  and

$$\begin{aligned}
\alpha_1 &= \frac{2t}{\lambda_{12}^{1/2}\lambda_{34}^{1/2}} \left( \frac{-\Sigma_{12} - \Sigma_{34} + t}{2} + \frac{\Delta_{12}\Delta_{34}}{2t} + a \right) \\
\alpha_2 &= \frac{2t}{\lambda_{34}^{1/2}\lambda_{56}^{1/2}} \left( \frac{-\Sigma_{34} - \Sigma_{56} + t}{2} + \frac{\Delta_{34}\Delta_{56}}{2t} + b \right). \tag{E.4}
\end{aligned}$$

From here, we note that the denominator of the integrand  $D(x, z_t)$  vanishes for

$$x_{1,2} = \frac{\pm \sqrt{\alpha_1^2 - 2\alpha_1\alpha_2 z_t + \alpha_2^2 + z_t^2 - 1 + z_t - 1 - \alpha_1\alpha_2 + \alpha_2^2}}{(\alpha_1 - \alpha_2)^2 - 2(1 - z_t)}, \tag{E.5}$$

and that there is an endpoint singularity for  $z_t \rightarrow \pm\infty$  ( $x_1 \rightarrow 1, 0$ ,  $x_2 \rightarrow 0, 1$ ) and a pinched

singularity when  $x_1 = x_2$ , that is when the square root term vanishes or

$$\begin{aligned} z_t^\pm &= \alpha_1 \alpha_2 \pm \sqrt{(\alpha_1^2 - 1)(\alpha_2^2 - 1)} \\ x_1^\pm &= x_2^\pm = \frac{1}{1 \pm \sqrt{\frac{\alpha_1^2 - 1}{\alpha_2^2 - 1}}}. \end{aligned} \quad (\text{E.6})$$

As we can see, the singularity at  $z_t^-$  is irrelevant since  $x^-$  is not in its integration domain any more. However there is a branch cut between  $z_t = z_t^+$  and  $z_t = \infty$ . By slightly shifting  $z_t$  above or under the real axis, we get a discontinuity with respect to  $z_t$  as

$$\begin{aligned} I(z_t + i\epsilon) - I(z_t - i\epsilon) &= 2\pi i \left( \text{Res} \left( \frac{1}{D}, x_1 \right) - \text{Res} \left( \frac{1}{D}, x_2 \right) \right) \\ &= \frac{2\pi i}{\sqrt{\alpha_1^2 - 2\alpha_1 \alpha_2 z_t + \alpha_2^2 + z_t^2 - 1}} = \frac{2\pi i}{\sqrt{(z_t - z_t^+)(z_t - z_t^-)}}. \end{aligned} \quad (\text{E.7})$$

This allows us to write a dispersion relation for  $I(z_t)$  and to express it as a function of  $s$  as

$$\begin{aligned} I(z_t) &= \int_{z_t^+}^{\infty} \frac{dz}{(z - z_t) \sqrt{(z - z_t^+)(z - z_t^-)}} \\ &= \frac{\lambda_{12}^{1/2} \lambda_{56}^{1/2}}{2t} \int_{s^+}^{\infty} \frac{ds'}{(s' - s) \sqrt{(s' - s^+)(s' - s^-)}} \end{aligned} \quad (\text{E.8})$$

where we expressed the angles in terms of the invariant quantities of the system similarly to (E.2)

$$z_t = \frac{2t}{\lambda_{12}^{1/2} \lambda_{56}^{1/2}} \left( s - \frac{\Sigma_{12} + \Sigma_{56} - t}{2} + \frac{\Delta_{12} \Delta_{56}}{2t} \right) \quad (\text{E.9})$$

$$z_t^\pm = \frac{2t}{\lambda_{12}^{1/2} \lambda_{56}^{1/2}} \left( s^\pm - \frac{\Sigma_{12} + \Sigma_{56} - t}{2} + \frac{\Delta_{12} \Delta_{56}}{2t} \right) \quad (\text{E.10})$$

$$z = \frac{2t}{\lambda_{12}^{1/2} \lambda_{56}^{1/2}} \left( s' - \frac{\Sigma_{12} + \Sigma_{56} - t}{2} + \frac{\Delta_{12} \Delta_{56}}{2t} \right) \quad (\text{E.11})$$

We then recover the result used above:

$$\int d\Omega \frac{1}{s' - a} \frac{1}{s'' - b} = \frac{8\pi t}{\lambda(t, m_3^2, m_4^2)} \int_{s^+}^{\infty} \frac{ds'}{(s' - s) \sqrt{(s' - s^+)(s' - s^-)}} \quad (\text{E.12})$$

where  $s^\pm$  are written in terms of  $z_t^\pm$ :

$$s^\pm = \frac{\Sigma_{12} + \Sigma_{56} - t}{2} + \frac{\Delta_{12} \Delta_{56}}{2t} + \frac{\lambda_{12}^{1/2} \lambda_{56}^{1/2}}{2t} z_t^\pm. \quad (\text{E.13})$$

and  $z_t^\pm$  and  $\alpha_{1,2}$  are given by (E.6) and (E.4).

The calculation of the three other phase-space integrals is completely similar, we have

$$\int d\Omega \frac{1}{u' - a} \frac{1}{u'' - b} = \frac{8\pi t}{\lambda(t, m_3^2, m_4^2)} \int_{s^+}^{\infty} \frac{ds'}{(s' - s) \sqrt{(s' - s^+)(s' - s^-)}} \quad (\text{E.14})$$

$$\int d\Omega \frac{1}{u' - a} \frac{1}{s'' - b} = \frac{8\pi t}{\lambda(t, m_3^2, m_4^2)} \int_{u^+}^{\infty} \frac{du'}{(u' - u) \sqrt{(u' - u^+)(u' - u^-)}} \quad (\text{E.15})$$

$$\int d\Omega \frac{1}{s' - a} \frac{1}{u'' - b} = \frac{8\pi t}{\lambda(t, m_3^2, m_4^2)} \int_{u^+}^{\infty} \frac{du'}{(u' - u) \sqrt{(u' - u^+)(u' - u^-)}} \quad (\text{E.16})$$

with

$$u^{\pm} = \frac{\Sigma_{12} + \Sigma_{56} - t}{2} + \frac{\Delta_{12}\Delta_{56}}{2t} - \frac{\lambda_{12}^{1/2}\lambda_{56}^{1/2}}{2t} z_t^{\pm}. \quad (\text{E.17})$$

## Appendix F

# Numerical solution of the implicit integral equation

In this appendix, we explain the method used to solve the numerical problem encountered in the previous section.

In order to find a solution to the different implicit integral equations above, different numerical methods based for instance on iterative procedures or Gauss-Legendre quadrature have been implemented. It was unfortunately not possible to find a good solution with those and it was found that the most efficient method is based on a singular-value decomposition of a matrix equation constructed from a well-chosen ansatz. To illustrate the method, we consider the specific case of the implicit integral equation in (10.74) and (10.75)

Before explaining the details of the method, we must make a remark about the inhomogeneities of the different implicit integral equations. Let us assume that the inhomogeneity behaves similarly to the imaginary part of the  $\pi\pi$ -scattering P-wave, that is

$$\Delta_{(i)}^{c,1}(s) = \alpha \text{Im}t_1^1(s), \quad (\text{F.1})$$

where  $\alpha$  is a constant. In this case, the solution of the implicit integral equation would be  $\tilde{T}_{(i)}^{c,1}(s) = -\alpha t_1^1(s)$ . To see that, let us choose an other constant,  $\beta$  and define

$$\tilde{T}_{(i)}^{c,1}(s) = \beta t_1^1(s). \quad (\text{F.2})$$

Then plugging this and (F.1) into the implicit equation leads to

$$\begin{aligned} \beta \text{Im}t_1^1(s)(1 - 2\sigma_\pi(s)\text{Im}t_1^1(s)) &= \alpha \text{Im}t_1^1(s) + 2\beta\sigma_\pi(s)\text{Re}t_1^1(s)^2 \\ \Leftrightarrow \\ -\beta &= \alpha. \end{aligned} \quad (\text{F.3})$$

Note that relation (4.21) has been used again. This confirms our previous statement.

Based on this and the fact that numerically, (F.1) is a good approximation, we choose to parametrize the solution as

$$\text{Im}\tilde{T}_{(i)}^{c,1}(s) = -P(s)\Delta_{(i)}^{c,1}(s). \quad (\text{F.4})$$

The quantity  $P(s)$  is a polynomial defined as

$$P(s) = \sum_{k=0}^{N_+} c_k s^k \quad (\text{F.5})$$



Note that all the coefficients  $c_k$  are pure constants. Moreover, we must also include the sum-rules (10.83) into the parametrization of the imaginary part. Each of them corresponds to a constraint among the coefficients. In order to calculate explicitly the integral, we calculate the contribution from each power of  $s$  in the polynomial. For instance, the sum-rule (10.82) becomes

$$\frac{\text{Re}\tilde{T}_{(3)}^{c,1}(s_1)}{s_1} - \frac{\text{Re}\tilde{T}_{(3)}^{c,1}(s_2)}{s_2} = - \sum_j c_j \frac{s_1 - s_2}{\pi} \int \frac{ds'}{s'} \frac{\Delta_{(3)}^{c,1}(s')s'^j}{(s' - s_1)(s' - s_2)}. \quad (\text{F.6})$$

Hence, the initial set of coefficients  $\{c_j\}$  is reduced to a smaller number of independent coefficients  $\{\tilde{c}_j\}$ .

At this point, the problem consists of finding the best set of coefficients satisfying the implicit integral equation. In order to do so, we reduce the equation to a matrix equation for the coefficients. We choose a set of  $N$  energy points  $\{s_\ell\}$  between the threshold energy  $4m_\pi^2$  and  $s_{max} = 1.8\text{GeV}^2$ . For each of those, we calculate the dispersive integral of the corresponding problem for each power of  $s$  in the polynomial. For instance, equation (10.80) can be reduced to a linear combination of coefficients:

$$D_{(3)}^{c,1}(s_\ell) = \frac{s_\ell^3}{\pi} \sum_j \tilde{c}_j \int_{4m_\pi^2}^\infty ds' \frac{\Delta_{(3)}^{c,1}(s')s'^j}{s'^3(s' - s_\ell)}. \quad (\text{F.7})$$

By defining the vector made of all independent coefficients as

$$\mathbf{c} = \begin{pmatrix} \tilde{c}_1 \\ \vdots \\ \tilde{c}_{\tilde{N}} \end{pmatrix}, \quad (\text{F.8})$$

the implicit integral equation can be transformed into the following affine equation:

$$M\mathbf{c} = \mathbf{b} \quad (\text{F.9})$$

where  $M$  is  $N \times \tilde{N}$  matrix and  $\mathbf{b}$  a  $N$ -dimensional vector. In order to solve this system, we calculate the so-called pseudoinverse matrix  $\tilde{M}$ . The latter is a  $\tilde{N} \times N$  matrix that fulfils

$$\tilde{M}M = \mathbf{1}. \quad (\text{F.10})$$

Its calculation is based on a singular-value decomposition of  $M$ . Note that this kind of method is very often used to solve least-squares problems. The solution is then found by inserting the coefficients of

$$\mathbf{c} = \tilde{M}\mathbf{b} \quad (\text{F.11})$$

into the ansatz (F.4). We can then vary the number of energy points and check the quality of the solution by comparing the left- and right-hand side of (10.74). Note that the coefficients can be very large, which means that cancellations among the different terms of the polynomial occur. It is therefore crucial that the integrals evaluated numerically in (F.7) are calculated at a very high precision.

The solution is then cross-checked by the minimization program MINUIT from CERN [99]. To that end, we take the solution of the discretization method as a starting point and check that it is stable, in the sense that the minimization program does not find any other minimum in the phase space of the coefficients.

## Appendix G

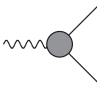
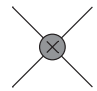
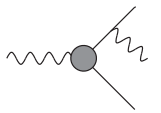
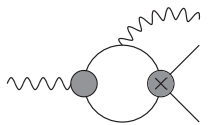
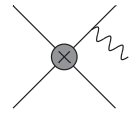
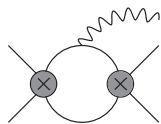
# Dictionary of the different topologies

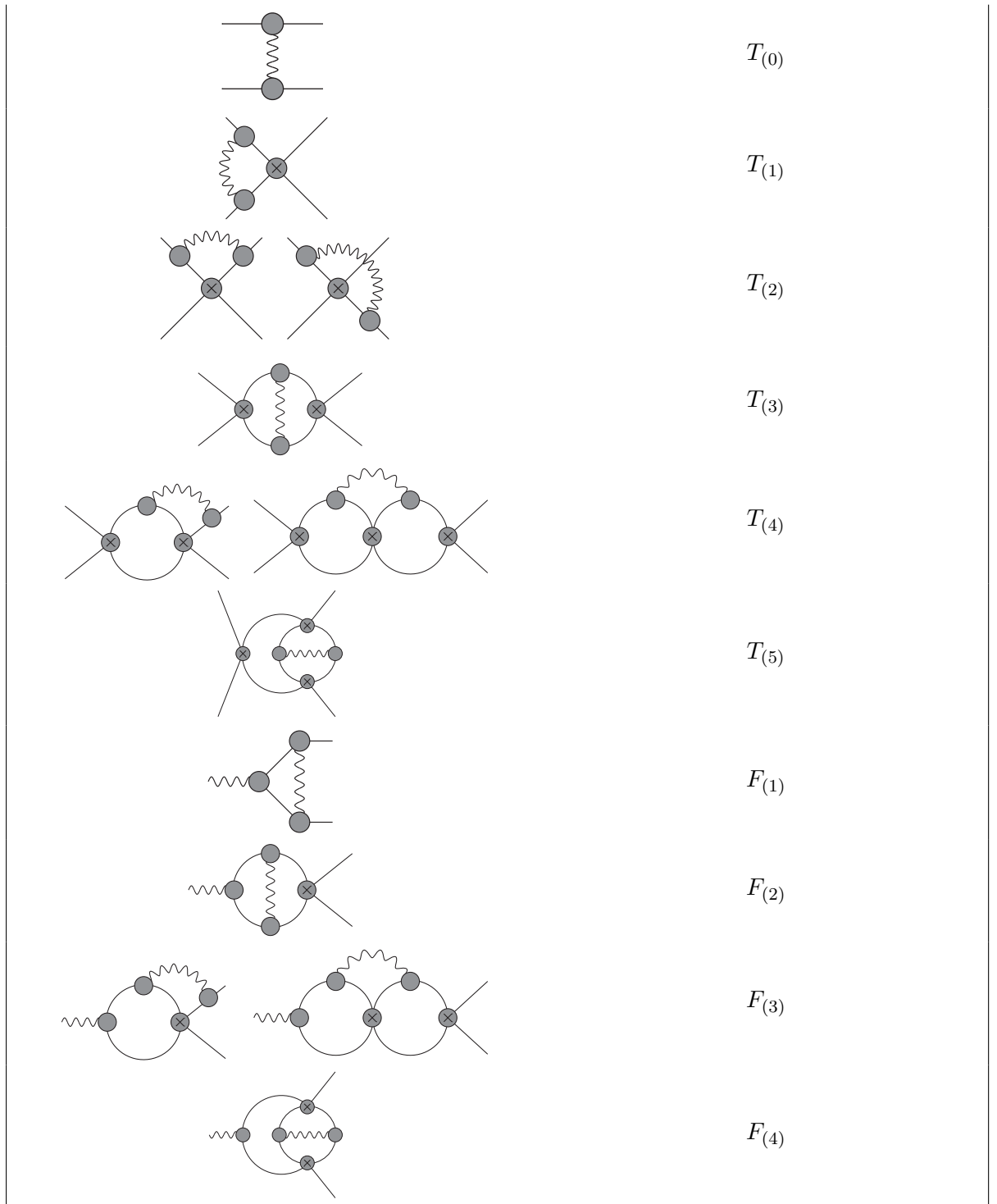
In this appendix, we list all the topologies of the different building blocks and contributions to  $F_\pi^{V,\alpha}$  as they are depicted in the different figures of the thesis.

Concerning the  $\pi\pi$ -scattering amplitude, the convention is the following:

channel	Amplitude
$\pi^+\pi^- \rightarrow \pi^+\pi^-$	$T_{\pi\pi}^c$
$\pi^+\pi^- \rightarrow \pi^0\pi^0$	$T_{\pi\pi}^{cn}$
$\pi^0\pi^0 \rightarrow \pi^0\pi^0$	$T_{\pi\pi}^n$
$\pi^+\pi^+ \rightarrow \pi^+\pi^+$	$T_{\pi\pi}^+$

The Different topologies are the following:

Topology	Amplitude
	$F_\pi^V$
	$T_{\pi\pi}$
	$W_\pi^{\mu\nu}$
	$W_{\pi\pi}^{\mu\nu}$
	$M_\pi^\mu$
	$M_{\pi\pi}^\mu$



# Bibliography

- [1] H. Neufeld and H. Rupertsberger. Isospin breaking in chiral perturbation theory and the decays  $\eta \rightarrow \pi \ell \nu$  and  $\tau \rightarrow \eta \pi \nu$ . *Z. Phys. C*, 68:91–102, 1995.
- [2] Res Urech. Virtual photons in chiral perturbation theory. *Nuclear Physics B*, 433(1):234–254, Jan 1995.
- [3] Bastian Kubis and Ulf-G. Meissner. Virtual photons in the pion form-factors and the energy momentum tensor. *Nucl. Phys. A*, 671:332–356, 2000. [Erratum: Nucl.Phys.A 692, 647–648 (2001)].
- [4] Sebastien Descotes-Genon and Marc Knecht. Two-loop representations of low-energy pion form factors and pi-pi scattering phases in the presence of isospin breaking. *Eur. Phys. J. C*, 72:1962, 2012.
- [5] Alexander Keshavarzi, Daisuke Nomura, and Thomas Teubner.  $g - 2$  of charged leptons,  $\alpha(M_Z^2)$ , and the hyperfine splitting of muonium. *Phys. Rev. D*, 101(1):014029, 2020.
- [6] A. Hoefer, J. Gluza, and F. Jegerlehner. Pion pair production with higher order radiative corrections in low energy  $e^+ e^-$  collisions. *Eur. Phys. J.*, C24:51–69, 2002.
- [7] Marc Knecht and Res Urech. Virtual photons in low-energy pi pi scattering. *Nucl. Phys. B*, 519:329–360, 1998.
- [8] M. Knecht and A. Nehme. Electromagnetic corrections to charged pion scattering at low-energies. *Phys. Lett. B*, 532:55–62, 2002.
- [9] Julian Schwinger. On quantum-electrodynamics and the magnetic moment of the electron. *Phys. Rev.*, 73:416–417, Feb 1948.
- [10] Tatsumi Aoyama, Masashi Hayakawa, Toichiro Kinoshita, and Makiko Nio. Tenth-order qed contribution to the electron  $g-2$  and an improved value of the fine structure constant. *Phys. Rev. Lett.*, 109:111807, Sep 2012.
- [11] Tatsumi Aoyama, Masashi Hayakawa, Toichiro Kinoshita, and Makiko Nio. Complete tenth-order qed contribution to the muon  $g-2$ . *Phys. Rev. Lett.*, 109:111808, Sep 2012.
- [12] W.S. Cowland. On schwinger’s theory of the muon. *Nuclear Physics*, 8:397–401, 1958.
- [13] Richard H. Parker, Chenghui Yu, Weicheng Zhong, Brian Estey, and Holger Müller. Measurement of the fine-structure constant as a test of the standard model. *Science*, 360(6385):191–195, Apr 2018.

- [14] G. W. *et al.* Bennett. Measurement of the negative muon anomalous magnetic moment to 0.7 ppm. *Phys. Rev. Lett.*, 92:161802, Apr 2004.
- [15] J. Grange *et al.* Muon (g-2) technical design report, 2018.
- [16] B. Abi, T. Albahri, S. Al-Kilani, D. Allspach, L. Alonzi, A. Anastasi, A. Anisenkov, F. Azfar, K. Badgley, and S. Baessler *et al.* Measurement of the positive muon anomalous magnetic moment to 0.46 ppm. *Physical Review Letters*, 126(14), Apr 2021.
- [17] Hiromi Iinuma *et al.* New approach to the muon g-2 and EDM experiment at j-PARC. *Journal of Physics: Conference Series*, 295:012032, may 2011.
- [18] T. Aoyama *et al.* The anomalous magnetic moment of the muon in the Standard Model. *Phys. Rept.*, 887:1–166, 2020.
- [19] Gilberto Colangelo, Martin Hoferichter, Massimiliano Procura, and Peter Stoffer. Dispersion relation for hadronic light-by-light scattering: theoretical foundations. *JHEP*, 09:074, 2015.
- [20] Gilberto Colangelo, Martin Hoferichter, Massimiliano Procura, and Peter Stoffer. Dispersion relation for hadronic light-by-light scattering: two-pion contributions. *JHEP*, 04:161, 2017.
- [21] Fred Jegerlehner and Andreas Nyffeler. The Muon g-2. *Phys. Rept.*, 477:1–110, 2009.
- [22] Gilberto Colangelo, Martin Hoferichter, and Peter Stoffer. Two-pion contribution to hadronic vacuum polarization. *Journal of High Energy Physics*, 2019(2), Feb 2019.
- [23] Alexander Kurz, Tao Liu, Peter Marquard, and Matthias Steinhauser. Hadronic contribution to the muon anomalous magnetic moment to next-to-next-to-leading order. *Phys. Lett. B*, 734:144–147, 2014.
- [24] Sz. Borsanyi *et al.* Leading hadronic contribution to the muon 2 magnetic moment from lattice QCD. 2 2020.
- [25] G. Abbiendi, C. M. Carloni Calame, U. Marconi, C. Matteuzzi, G. Montagna, O. Nicrosini, M. Passera, F. Piccinini, R. Tenchini, L. Trentadue, and *et al.* Measuring the leading hadronic contribution to the muon g-2 via muon-electron scattering. *The European Physical Journal C*, 77(3), Mar 2017.
- [26] Alexander Keshavarzi, Daisuke Nomura, and Thomas Teubner. Muon  $g - 2$  and  $\alpha(M_Z^2)$ : a new data-based analysis. *Phys. Rev. D*, 97(11):114025, 2018.
- [27] Denis Bernard. Measurement of  $e^+e^- \rightarrow$  hadrons cross sections at BABAR, and implication for the muon  $g - 2$ . *PoS, Hadron2013*:126, 2013.
- [28] T. Kinoshita. *Quantum Electrodynamics*. Advanced series on directions in high energy physics. World Scientific, 1990.
- [29] P.A. Zyla *et al.* Review of Particle Physics. *PTEP*, 2020(8):083C01, 2020.
- [30] Richard John Eden, Peter V. Landshoff, David I. Olive, and John Charlton Polkinghorne. *The analytic S-matrix*. Cambridge Univ. Press, Cambridge, 1966.
- [31] R.E. Cutkosky. Singularities and discontinuities of Feynman amplitudes. *J. Math. Phys.*, 1:429–433, 1960.

- [32] Ansgar Denner. Techniques for the calculation of electroweak radiative corrections at the one-loop level and results for w-physics at lep200, 2007.
- [33] Stanley Mandelstam. Analytic properties of transition amplitudes in perturbation theory. *Phys. Rev.*, 115:1741–1751, Sep 1959.
- [34] Peter Goddard. The Guiding Influence of Stanley Mandelstam, from S-Matrix Theory to String Theory. *Int. J. Mod. Phys. A*, 32(12):1740013, 2017.
- [35] José Antonio Oller. *A brief introduction to dispersion relations: with modern applications*. Springerbriefs in physics. Springer, Cham, 2019.
- [36] Alan Douglas Martin and Thomas D Spearman. *Elementary-particle theory*. North-Holland, Amsterdam, 1970.
- [37] Marcel Froissart. Asymptotic behavior and subtractions in the mandelstam representation. *Phys. Rev.*, 123:1053–1057, Aug 1961.
- [38] Paul Buettiker, S. Descotes-Genon, and B. Moussallam. A new analysis of pi K scattering from Roy and Steiner type equations. *Eur. Phys. J. C*, 33:409–432, 2004.
- [39] R. Omnes. On the Solution of certain singular integral equations of quantum field theory. *Nuovo Cim.*, 8:316–326, 1958.
- [40] N.I. Muskhelishvili. *Singular Integral Equations*. Noordhoff, Groningen, 1953.
- [41] F. J. Yndurain. Low-energy pion physics. 2002.
- [42] Steven Weinberg. Phenomenological Lagrangians. *Physica A*, 96(1-2):327–340, 1979.
- [43] J. Gasser and H. Leutwyler. Chiral Perturbation Theory to One Loop. *Annals Phys.*, 158:142, 1984.
- [44] J. Gasser and H. Leutwyler. Chiral Perturbation Theory: Expansions in the Mass of the Strange Quark. *Nucl. Phys. B*, 250:465–516, 1985.
- [45] Stefan Scherer. Introduction to chiral perturbation theory. *Adv. Nucl. Phys.*, 27:277, 2003. [,277(2002)].
- [46] Bastian Kubis. An Introduction to chiral perturbation theory. In *Workshop on Physics and Astrophysics of Hadrons and Hadronic Matter*, 3 2007.
- [47] Gilberto Colangelo and Gino Isidori. An Introduction to ChPT. *Frascati Phys. Ser.*, 18:333–376, 2000.
- [48] P. G. Harris, C. A. Baker, K. Green, P. Iaydjiev, S. Ivanov, D. J. R. May, J. M. Pendlebury, D. Shiers, K. F. Smith, M. van der Grinten, and P. Geltenbort. New experimental limit on the electric dipole moment of the neutron. *Phys. Rev. Lett.*, 82:904–907, Feb 1999.
- [49] J. S. Bell and R. Jackiw. A PCAC puzzle:  $\pi^0 \rightarrow \gamma\gamma$  in the  $\sigma$  model. *Nuovo Cim. A*, 60:47–61, 1969.
- [50] Stephen L. Adler. Axial vector vertex in spinor electrodynamics. *Phys. Rev.*, 177:2426–2438, 1969.

- [51] Murray Gell-Mann. The Eightfold Way: A Theory of strong interaction symmetry. 3 1961.
- [52] J. Goldstone. Field Theories with Superconductor Solutions. *Nuovo Cim.*, 19:154–164, 1961.
- [53] Murray Gell-Mann. The symmetry group of vector and axial vector currents. *Physics Physique Fizika*, 1:63–75, Jul 1964.
- [54] G. Colangelo, J. Gasser, and H. Leutwyler. The  $\pi\pi$  s-wave scattering lengths. *Physics Letters B*, 488(3-4):261–268, Sep 2000.
- [55] J. Gasser and H. Leutwyler. Quark Masses. *Phys. Rept.*, 87:77–169, 1982.
- [56] G. Ecker. Chiral perturbation theory. *Progress in Particle and Nuclear Physics*, 35:1 – 80, 1995.
- [57] Roger Dashen. Chiral  $SU(3) \otimes SU(3)$  as a symmetry of the strong interactions. *Phys. Rev.*, 183:1245–1260, Jul 1969.
- [58] J. Wess and B. Zumino. Consequences of anomalous Ward identities. *Phys. Lett. B*, 37:95–97, 1971.
- [59] G. Ecker, J. Gasser, A. Pich, and E. de Rafael. The Role of Resonances in Chiral Perturbation Theory. *Nucl. Phys.*, B321:311–342, 1989.
- [60] G. Ecker and R. Unterdorfer. Four pion production in  $e^+ e^-$  annihilation. *Eur. Phys. J.*, C24:535–545, 2002.
- [61] G. Ecker, J. Gasser, H. Leutwyler, A. Pich, and E. de Rafael. Chiral Lagrangians for Massive Spin 1 Fields. *Phys. Lett. B*, 223:425–432, 1989.
- [62] V. Cirigliano, G. Ecker, M. Eidemuller, Roland Kaiser, A. Pich, and J. Portoles. Towards a consistent estimate of the chiral low-energy constants. *Nucl. Phys.*, B753:139–177, 2006.
- [63] Karol Kampf and Jiri Novotny. Resonance saturation in the odd-intrinsic parity sector of low-energy QCD. *Phys. Rev.*, D84:014036, 2011.
- [64] B. R. Martin, D. Morgan, and Graham Shaw. *Pion Pion Interactions in Particle Physics*. 1976.
- [65] R. Garcia-Martin, R. Kaminski, J. R. Pelaez, J. Ruiz de Elvira, and F. J. Yndurain. The Pion-pion scattering amplitude. IV: Improved analysis with once subtracted Roy-like equations up to 1100 MeV. *Phys. Rev.*, D83:074004, 2011.
- [66] B. Ananthanarayan, G. Colangelo, J. Gasser, and H. Leutwyler. Roy equation analysis of  $\pi\pi$  scattering. *Phys. Rept.*, 353:207–279, 2001.
- [67] R. Kaminski, J. R. Pelaez, and F. J. Yndurain. The Pion-pion scattering amplitude. III. Improving the analysis with forward dispersion relations and Roy equations. *Phys. Rev. D*, 77:054015, 2008.
- [68] G. Colangelo, J. Gasser, and H. Leutwyler.  $\pi\pi$  scattering. *Nucl. Phys. B*, 603:125–179, 2001.

- [69] Glennys R. Farrar and Darrell R. Jackson. Pion form factor. *Phys. Rev. Lett.*, 43:246–249, Jul 1979.
- [70] F. Stollenwerk, C. Hanhart, A. Kupsc, U. G. Meissner, and A. Wirzba. Model-independent approach to  $\eta \rightarrow \pi^+ \pi^- \gamma$  and  $\eta' \rightarrow \pi^+ \pi^- \gamma$ . *Phys. Lett.*, B707:184–190, 2012.
- [71] Aubert et al. Precise measurement of the  $e^+e^- \rightarrow \pi^+\pi^-(\gamma)$  cross section with the initial state radiation method at babar. *Phys. Rev. Lett.*, 103:231801, Dec 2009.
- [72] C. Patrignani et al. Review of Particle Physics. *Chin. Phys.*, C40(10):100001, 2016.
- [73] Michael E. Peskin and Daniel V. Schroeder. *An Introduction to quantum field theory*. Addison-Wesley, Reading, USA, 1995.
- [74] A.Hoefer. *Radiative Corrections to Hadron Productions in  $e e$  Annihilations at DA NE Energies*. PhD thesis, Humboldt University at Berlin, 2001.
- [75] J. Calmet, S. Narison, M. Perrottet, and E. De Rafael. Higher order hadronic corrections to the anomalous magnetic moment of the muon. *Physics Letters B*, 61(3):283–286, 1976.
- [76] Gilberto Colangelo, Martin Hoferichter, Andreas Nyffeler, Massimo Passera, and Peter Stoffer. Remarks on higher-order hadronic corrections to the muon  $g-2$ . *Phys. Lett. B*, 735:90–91, 2014.
- [77] C. Itzykson and J. B. Zuber. *Quantum Field Theory*. International Series In Pure and Applied Physics. McGraw-Hill, New York, 1980.
- [78] Gilberto Colangelo, Martin Hoferichter, Massimiliano Procura, and Peter Stoffer. Dispersive approach to hadronic light-by-light scattering. *JHEP*, 09:091, 2014.
- [79] B. Moussallam. Unified dispersive approach to real and virtual photon-photon scattering at low energy. *Eur. Phys. J.*, C73:2539, 2013.
- [80] N. Kaiser. Chiral corrections to  $\pi^-\gamma \rightarrow 3\pi$  processes at low energies. *Nucl. Phys.*, A848:198–217, 2010.
- [81] William A. Bardeen and W. K. Tung. Invariant amplitudes for photon processes. *Phys. Rev.*, 173:1423–1433, 1968. [Erratum: *Phys. Rev.*D4,3229(1971)].
- [82] Igor Danilkin, Oleksandra Deineka, and Marc Vanderhaeghen. Dispersive analysis of the  $\gamma^*\gamma^* \rightarrow \pi\pi$  process. 2019.
- [83] Martin Hoferichter and Peter Stoffer. Dispersion relations for  $\gamma^*\gamma^* \rightarrow \pi\pi$ : helicity amplitudes, subtractions, and anomalous thresholds. *JHEP*, 07:073, 2019.
- [84] R. Garcia-Martin and B. Moussallam. MO analysis of the high statistics Belle results on  $\gamma\gamma \rightarrow \pi^+\pi^-, \pi^0\pi^0$  with chiral constraints. *Eur. Phys. J.*, C70:155–175, 2010.
- [85] F. E. Low. Bremsstrahlung of very low-energy quanta in elementary particle collisions. *Phys. Rev.*, 110:974–977, May 1958.
- [86] C. Adolph et al. First Measurement of Chiral Dynamics in  $\pi^-\gamma \rightarrow \pi^-\pi^-\pi^+$ . *Phys. Rev. Lett.*, 108:192001, 2012.



- [87] B. Ananthanarayan and Paul Buettiker. Scattering lengths and medium-energy and high-energy pi pi scattering. *Phys. Rev. D*, 54:5501–5508, 1996.
- [88] Gilberto Colangelo, Markus Finkemeier, and Res Urech. Tau decays and chiral perturbation theory. *Phys. Rev. D*, 54:4403–4418, 1996.
- [89] J. Gasser and G. R. S. Zarnauskas. On the pion decay constant. *Phys. Lett. B*, 693:122–128, 2010.
- [90] N. Carrasco, V. Lubicz, G. Martinelli, C. T. Sachrajda, N. Tantalo, C. Tarantino, and M. Testa. QED Corrections to Hadronic Processes in Lattice QCD. *Phys. Rev. D*, 91(7):074506, 2015.
- [91] R. R. Akhmetshin et al. Measurement of  $e^+e^- \rightarrow \pi^+\pi^-$  cross-section with CMD-2 around rho meson. *Phys. Lett. B*, 527:161–172, 2002.
- [92] M. N. Achasov et al. Study of the process  $e^+e^- \rightarrow \pi^+\pi^-$  in the energy region  $400 < s^{(1/2)} < 1000$ -MeV. *J. Exp. Theor. Phys.*, 101(6):1053–1070, 2005.
- [93] F. Ambrosino et al. Measurement of  $\sigma(e^+e^- \rightarrow \pi^+\pi^-\gamma(\gamma))$  and the dipion contribution to the muon anomaly with the KLOE detector. *Phys. Lett. B*, 670:285–291, 2009.
- [94] M. Ablikim et al. Measurement of the  $e^+e^- \rightarrow \pi^+\pi^-$  cross section between 600 and 900 MeV using initial state radiation. *Phys. Lett. B*, 753:629–638, 2016. [Erratum: *Phys.Lett.B* 812, 135982 (2021)].
- [95] Martin Hoferichter and Peter Stoffer. Private communication.
- [96] Gerard 't Hooft and M. J. G. Veltman. Scalar One Loop Integrals. *Nucl. Phys.*, B153:365–401, 1979.
- [97] Gilberto Colangelo, Martin Hoferichter, and Peter Stoffer. Two-pion contribution to hadronic vacuum polarization. *JHEP*, 02:006, 2019.
- [98] Peter Stoffer. *Dispersive Treatments of  $K_{\ell 4}$  Decays and Hadronic Light-by-Light Scattering*. PhD thesis, U. Bern, AEC, 2014.
- [99] F. James. MINUIT Function Minimization and Error Analysis: Reference Manual Version 94.1. 1994.



# Acknowledgements

I thank my supervisor Gilberto Colangelo for giving me the opportunity to see what it means to do research in theoretical particle physics. He proposed to me this interesting problem about radiative corrections and despite the difficulty, I had a lot of fun to tackle it. Gilberto always encouraged me and I thank him for his support, especially in the last stressful months of the PhD.

I also thank Jacobo Ruiz de Elvira for his constant support. He was always ready to sacrifice a lot of time to discuss the different problems I was facing. He has been a major motivator in times of doubt. I am really grateful to him for that.

I also want to thank all the PhD students of the institute for Theoretical Physics of the University of Bern. We had a great time together in the pre-Covid era. Special thanks go to Marcel Balsiger, Samuel Favrod, Greg Jackson, Laetitia Laub and Francesco Saturnino who formed the core of our group.

Finally I want to thank all my friends and family members who always encouraged me throughout my time as a PhD student. I would certainly never have made it so far without them and I am really grateful for their support.



# **Erklärung**

gemäss Art. 18 PromR Phil.-nat. 2019

Name/Vorname: Monnard Joachim

Matrikelnummer: 12-212-734

Studiengang: Theoretische Physik

Bachelor ☐ Master ☐ Dissertation ☒

Titel der Arbeit: Radiative corrections for the two-pion contribution to the hadronic vacuum polarization contribution to the muon  $g-2$

LeiterIn der Arbeit: Prof. Dr. Gilberto Colangelo

Ich erkläre hiermit, dass ich diese Arbeit selbständig verfasst und keine anderen als die angegebenen Quellen benutzt habe. Alle Stellen, die wörtlich oder sinn-gemäss aus Quellen entnommen wurden, habe ich als solche gekennzeichnet. Mir ist bekannt, dass andern-falls der Senat gemäss Artikel 36 Absatz 1 Buchstabe r des Gesetzes über die Universität vom 5. September 1996 und Artikel 69 des Universitätssta-tuts vom 7. Juni 2011 zum Entzug des Dokortitels be-rechtigt ist.

Für die Zwecke der Begutachtung und der Überprüfung der Einhaltung der Selbständigkeitserklärung bzw. der Reglemente betreffend Plagiate erteile ich der Univer-sität Bern das Recht, die dazu erforderlichen Perso-nendaten zu bearbeiten und Nutzungshandlungen vor-zunehmen, insbesondere die Doktorarbeit zu vervielfäl-tigen und dauerhaft in einer Datenbank zu speichern sowie diese zur Überprüfung von Arbeiten Dritter zu verwenden oder hierzu zur Verfügung zu stellen.

Ort/Datum

Unterschrift